2015

Using Trace Fossils to Determine the Role of Oceanic Anoxic Event II on the Cretaceous Western Interior Seaway Paleoenvironment

Jacob Frederick Grosskopf
Louisiana State University and Agricultural and Mechanical College

USING TRACE FOSSILS TO DETERMINE THE ROLE OF OCEANIC ANOXIC EVENT II ON THE CRETACEOUS WESTERN INTERIOR SEAWAY PALEOENVIRONMENT

A Dissertation

Submitted to the Graduate Faculty of the
Louisiana State University and
Agricultural and Mechanical College
in partial fulfillment of the
requirements for the degree of
Doctor of Philosophy

in

The Department of Geology and Geophysics

by
Jacob Frederick Grosskopf
B.S., Louisiana Tech University, 2007
M.S., Louisiana State University, 2010
May 2015

ACKNOWLEDGEMENTS

Funding for this PhD dissertation was provided by graduate assistantships from the Department of Geology and Geophysics at Louisiana State University as well as a Marathon Oil Company Geology Scholarship, the Mary Jo Klosterman Fellowship, and the Houston Energy Professorship.

I would like to thank my major advisor, Dr. Brooks Ellwood, for his help, advice, and expertise over the course of this research. I would like to thank Dr. Bruce Schumacher (United States Forest Service), geologist for the Comanche National Grasslands, La Junta, CO, for his expertise, access to field sites, and aid in correlation and data collection in the field at Site 4. I would also like to thank Dr. Art Donovan and Rand Gardner at BP, for access to the southern site field area. Thanks are extended to Dr. David Watkins at the University of Nebraska– Lincoln for help in locating and correlating Site 6. I would also like to thank the technicians at the United States Geological Survey Core Research Center in Denver, CO, for help during my multiple visits to the facility. Thanks to Ken Ratcliffe, director of Chemostrat, for running samples for geochemistry.

At Louisiana State University, I would like to thank Emad El Far for discussions about my project, and with help in the field and time-series work. Thanks to Ryan Ellis for his pictures and preliminary research on Lozier Canyon. Further, I would like to thank Rick Young for guidance on how to use lab equipment, and Amber Ellwood for help in the lab. Thanks to Tom Schramm for discussion about this project and all things geology. I would also like to thank Amy Cone, a former fellow graduate student, for her advice on all things, including editing. Lastly, thanks to my dissertation committee, Drs. Huiming Bao, Samuel Bentley, and Achim Herrmann, for their expertise across the many unique disciplines over which this project spans.

PREFACE

The dissertation work presented herein is formatted for publishing in academic journals. Each chapter represents a different paper to be published. Thus, each chapter should be considered its own separate element in that it addresses a different particular problem in the dissertation work. For this reason the separate, but complete chapters have unique abstract, introduction, methods, results, discussion, conclusion, and reference sections.

The main conclusions from each of these chapters are reported in a standalone conclusions section. Following the conclusions section, there is a reference summary section that lists all references used for the entire dissertation.

TABLE OF CONTENTS

ABSTRACT

Did well-oxygenated benthic conditions exist in all parts of the Cretaceous Western Interior Seaway (CWIS) during the deposition of Bed 63 at the onset Oceanic Anoxic Event II (OAE II), as suggested by findings from two cores from the central portion of the CWIS? This problem was approached by categorizing the bioturbation that is prevalent through Bed 63 into oxygen-related ichnofabrics (ORI) in order to describe benthic oxygen conditions. These data were collected from outcrop and core among seven different sites along West–East and North–South transects that traversed portions of the CWIS with differing depositional settings and proximities to the global ocean during OAE II. ORI results from both transects indicated oxygenated benthic conditions for the duration of Bed 63 throughout all parts of the CWIS.

Were these well-oxygenated benthic conditions consistent for the duration of OAE II in the CWIS? This problem was approached by examining ORIs from synchronous horizons, represented by laterally-extensive limestone beds found through the OAE II interval along the West–East transect. Among the six sites, it was determined that the limestone beds indicate well-oxygenated benthic conditions at the onset of and early into the OAE II interval, while ORIs slightly dropped up-section. Also, variable ORIs were recognized in thick limestone beds, which may have been controlled by precessional-scale orbitally-forced long-term climate effects. However, competing phases of climate-forced carbonate deposition limited the ability to determine the temporal variability among the ORIs.

Additionally, an alternate interpretation was established for the onset of OAE II at Antonio Canyon outcrop, near Langtry, TX, in southern portion of the CWIS. The onset of OAE II at this locality was correlated to Cenomanian–Turonian Boundary GSSP reference section and time-equivalent Portland Core using recognizable patterns in CWIS lithology, and χ, GRS, total

organic carbon, and $\delta^{13}C_{organic}$ and $\delta^{13}C_{carbonate}$ curves from the Antonio Canyon section. More work is needed to locate the Cenomanian–Turonian Boundary and the end of OAE II in the Antonio Canyon outcrop.

CHAPTER 1: BASAL BRIDGE CREEK LIMESTONE BED (BED 63) TRACE FOSSILS INDICATE OXYGENATED BOTTOM-WATERS THROUGHOUT THE CRETACEOUS WESTERN INTERIOR SEAWAY DURING OCEANIC ANOXIC EVENT II

ABSTRACT

The base of the limestone Bed 63, the basal bed of the Bridge Creek Limestone Member of the Greenhorn Formation, marks the onset of the Oceanic Anoxic Event II (OAE II) as identified by a positive shift in the $\delta^{13}C_{organic}$ signal in Cretaceous Western Interior Seaway (CWIS) strata. Previous paleoenvironmental work from three cores positioned in the central area of the CWIS suggests well-oxygenated benthic oxygen conditions for the duration of Bed 63 deposition, opposite of what is expected for that time. However, it is unknown if these same benthic conditions existed throughout the CWIS at the onset of OAE II. This study investigated benthic oxygen conditions throughout the CWIS by tracing the laterally-extensive Bed 63 limestone along a West–East transect reaching from the western margin of the CWIS in Utah, to the eastern margin in Kansas, and along a North–South transect reaching from north-central Montana to southwest Texas, the northern and southern termini of the CWIS.

Benthic oxygen interpretations for Bed 63 were derived from oxygen-related ichnofabrics (ORI) categorized by trace fossil fabric diversity, density, and maximum burrow diameter. Along both transects ORIs indicated, bottom-waters were well-oxygenated during the entirety of the onset of OAE II-time throughout the CWIS. This matched findings from previous CWIS studies. Also congruent with the prior studies, the trace fossil fabrics composing Bed 63 showed frequent, minor variations in benthic oxygen concentrations. Both the high oxygen concentration evidenced by the trace fossil fabrics, and the variation in the concentration of trace fossils within

Bed 63, result from decrease in terrigenous input into the basin and concomitant increase in carbonate production.

INTRODUCTION

Strata of the Cretaceous Western Interior Seaway (CWIS; Figures 1.1 and 1.2) have been extensively studied since the late 1970s, mainly due to their high total organic carbon content, and hydrocarbon potential (Arthur and Schlanger, 1979; DeMaison and Moore, 1980; Tyson and Pearson, 1991; Bowman and Bralower, 2005). Oceanic Anoxic Event II (OAE II) is responsible for high concentrations of total organic carbon in Late Cretaceous rocks. The onset of OAE II, recognized globally by positive $^{13}C_{organic}$ and $^{13}C_{carbonate}$ excursions (Schlanger and Jenkyns, 1976; Arthur and Schlanger, 1989), which occurred prior to the Cenomanian–Turonian Boundary (CTB). Recent research from Meyers et al. (2012) used a combination of $^{40}Ar/^{39}Ar$, U-Pb, and astronomic forcing dating techniques to determine the age of the CTB to be 93.90 ± 0.15 Ma. The ~600 kyr-long OAE II (Sageman et al., 2006) was brought about by an increase in global primary productivity as a result of magmatically-derived metals and micronutrients sourced from the submarine Caribbean Large Igneous Province (Snow et al., 2005). The positive shift in $\delta^{13}C_{organic}$ levels resulted from an increase in primary production and subsequent drawdown of atmospheric pCO_2 (Kump and Arthur, 1999).

The many stratigraphic, sedimentological, paleontological, paleoceanographic, paleoenvironmental, and geochemical analyses performed on CWIS strata that span the OAE II interval, including the Cenomanian–Turonian Global boundary Stratotype Section and Point (CTB GSSP), located at Site 3 in Figure 1.1, determine there was little-to-no impact to the oxygen concentration in the CWIS benthic environment during OAE II (Sageman et al., 1997; Pedersen and Calvert, 1990; Keller et al., 2004; Kennedy et al., 2005; Meyers et al., 2005). There

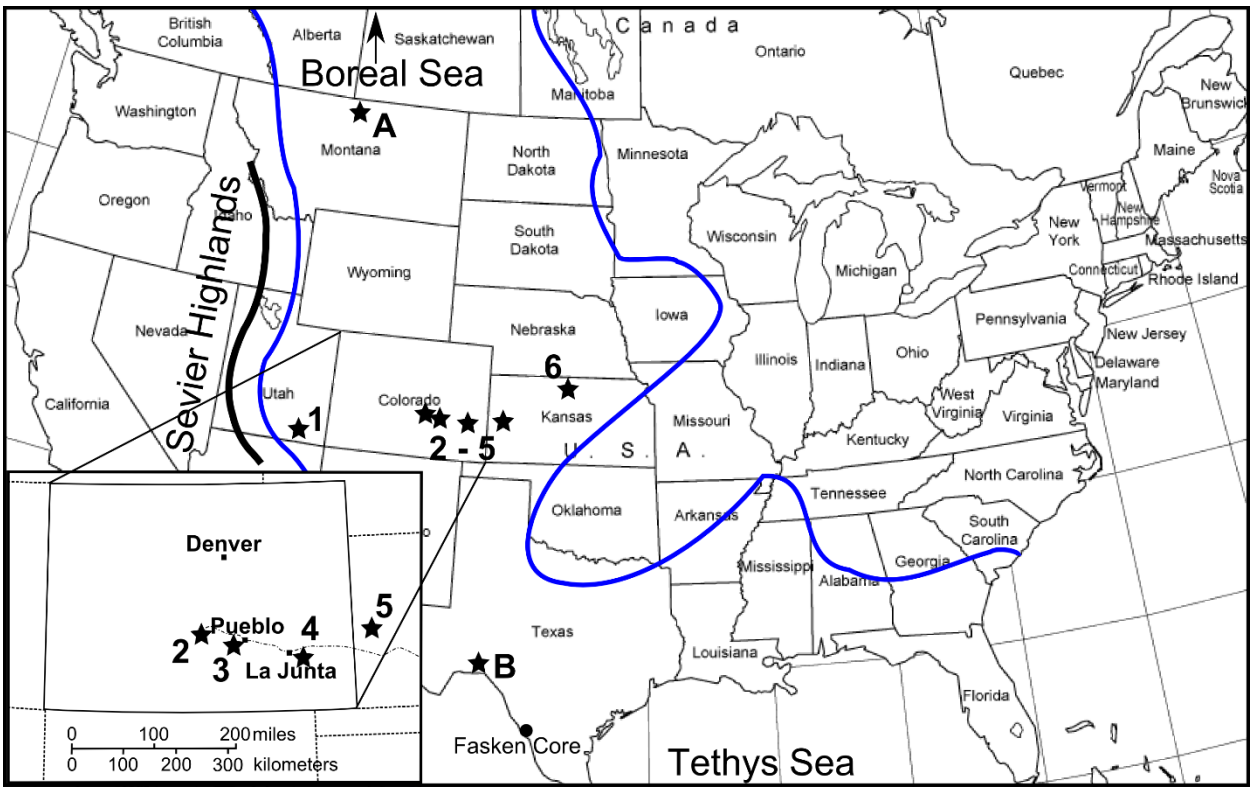

Figure 1.1 Location of field sites and cores along a West–East transect and North–South transect across the Cretaceous Western Interior Seaway (CWIS). Bold blue lines represent the CWIS shoreline at maximum transgression at ~94 Ma; modeled after Cobban et al. (1994) and Slingerland et al. (1996). Stars indicate field or core localities where: 1 – Waheap Wash outcrop outside of Big Water, UT and nearby USGS Escalante core from Garfield County, UT; 2 – USGS Portland core from Florence, CO; 3 – CTB GSSP railroad cut south of Pueblo, CO; 4 – outcrop on Comanche National Grassland southwest of La Junta, CO; 5 – Amoco Bounds core from Greeley County, KS; 6 – US Highway 36 roadcut outside of Cuba, KS; A – 2-21 Federal Core, Phillips County, MT; B – outcrop from offshoot of Lozier Canyon, near Langtry, TX.

do appear to be changes in benthic oxygen conditions in the CWIS independent of OAE II, however (Sageman et al., 1997; Savrda, 1998). It has been determined that at no time did anoxic (< 0.2 ml of O_2/l of H_2O [Tyson and Pearson, 1991]) benthic conditions prevail in the CWIS during this interval. Instead, benthic oxygen concentrations may have only dropped to dysoxic levels (2.0 – 0.2 ml of O_2/l of H_2O) rather than anoxic levels (Fisher and Arthur, 2002; Friedrich et al., 2009).

The hemipelagic facies that compose CWIS strata during OAE II-time represent an average dysoxic state. The changing paleoenvironments, represented by the binary bedding transitions of calcareous shale and limestone bed couplets, indicated that the CWIS experienced short-term variations from oxic–dysoxic, conditions for the duration of the OAE II interval.

The recognizable changes in benthic oxygen conditions are observed in oxygen-related trace fossil fabrics. Savrda and Bottjer (1994) and Savrda (1998) examined these variations in the Pueblo Core (from Pratt, 1984; Site 3, Figure 1.1), USGS Portland core (Site 2, Figure 1.1) and Amoco Bounds core (Site 5, Fig 1.1) for the duration of OAE II in the Bridge Creek Limestone Member of the Greenhorn Formation (Figure 1.2). Through the OAE II interval, long-term trends in interpreted oxygen levels were observed from assemblages of trace fossils whose tracemakers had varying levels of low-oxygen tolerance. The findings suggested the presence of a low- frequency high-amplitude variation between trace assemblages match the pattern of limestone and calcareous shale bed couplets. Sageman et al. (1997, 1998) calculated that the two major ichnofabrics observed in the Portland core from Savrda (1998), and consequently the two bedding types, showed variation on Milankovitch frequencies. They found cycles in CWIS sedimentation were brought about by orbitally-forced long-term changes in climate, with the obliquity portion (39 kyr [O1] – 50.5 kyr [O2] [calculated from data presented by Berger et al. (1992)] at 93.9 Ma), among others, being the most influential, at least in the Upper Bridge Creek Limestone.

Attributing basin-wide rhythmic stratal patterns preserved in the Bridge Creek Limestone Member to be from orbitally-influenced long-term changes to paleoclimatic and paleo-oceanographic conditions is not a novel concept for CWIS stratigraphy. Over the last century, these bedding couplets were surmised to derive from astronomical forces (e.g., Gilbert, 1895). In

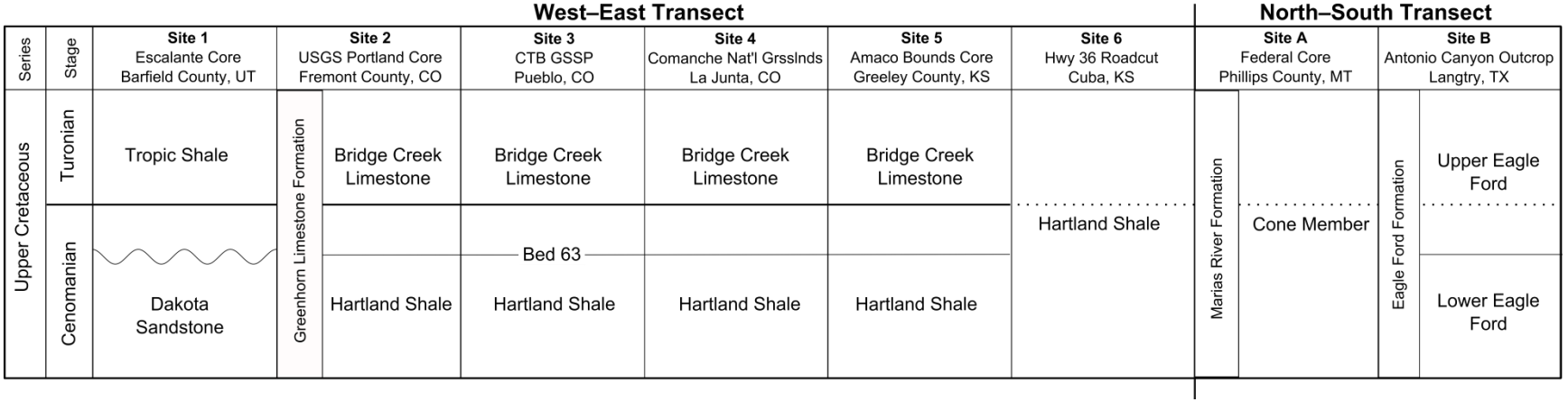

Figure 1.2 Simplified stratigraphic framework for CWIS strata spanning OAE II along West–East and North–South transects. Solid line represents where the CTB is known, and dotted line represents in what stratigraphic unit it is found when the exact placement is unknown. Note at Site 1 the Dakota Sandstone is time-equivalent to the Hartland Shale. At Site 6, the name "Hartland Shale" in Central and East Kansas comprises Hartland Shale and Bridge Creek Limestone members due to a facies shift west to east (Hattin, 1975).

the last half-century advances in CWIS stratigraphy established these bedding couplets as basin-wide synchronous horizons that pointed to regional-scale response to Milankovitch Effects (e.g. Hattin, 1971). Further work by Fischer (1980) and Fischer et al. (1985) linked control of Milankovitch Effects to the bedding type related to dilution and productivity altering the rate of carbonate deposition.

The work by Fischer (1980) attempted to link periodic paleoclimatic and paleo-oceanographic controls to two models that explain the presence of limestone and calcareous shale couplets that dominate the Bridge Creek Limestone stratigraphy. The first model, known as the "dilution model", as explained in Pratt (1984), attributed the calcareous shale component of the limestone-calcareous shale bed couplets of the Bridge Creek Limestone to be derived from terrigenous input during wetter periods. The increase in sediment delivery from fluvio-deltaic systems emptied detritus into the CWIS, and effectively diluted the carbonate content produced by the constant rain of microfossil tests. Pratt (1984) also related increased sediment delivery to carbon burial, as indicated by relatively higher organic content in the calcareous shale beds than the limestone beds. Higher concentrations of organic carbon in the calcareous shale bed component of the Bridge Creek Limestone were due to a decrease in bottom water oxygen brought about by effects of increased runoff. Increased runoff caused a sediment-laden freshwater surface layer to form over the CWIS waters. Density stratification slowed or stopped water column mixing, which ultimately resulted in bottom water stagnation. Thus, relative to limestone beds, the calcareous shale beds of the Bridge Creek Limestone exhibit higher organic carbon concentrations due to paucity of organic degradation under oxygen-poor conditions. In contrast, decreased runoff during drier years did not deliver the sediment load from the continent compared to what was produced in wetter years, and therefore lesser freshwater input and

sediment delivery resulted in a well-mixed CWIS water column. It was under these conditions that the limestone beds formed.

The second model, known as the "productivity model", as explained in Eicher and Diner (1989), attributed variations to the carbonate component were the result of changes in carbonate production from calcareous microorganisms. The limestone bed indicated increases in fertility of the water column due to vertical mixing between surface and bottom waters. Fluctuations in the carbonate productivity are explained by the influences of the Tethyan water mass on the CWIS. They argued rhythms between calcareous shale and limestone beds were caused by oscillations in productivity from the Tethyan water mass, which matched other similar bedding rhythms found in other marine environments during that time. Evidence from Eicher and Diner (1989) in favor of the productivity model was similar concentrations of planktonic foraminifera in calcareous shale and limestone beds, which would not occur if there were carbonate dilution effects. Further evidence for the productivity model reported in Eicher and Diner (1989) targeted the freshwater cap from the dilution model as means for increased organic carbon preservation. Organic carbon in the Bridge Creek Limestone increases west-to-east across the basin, which would trend opposite of the effects of sediment-rich freshwater flux from the western margin of the CWIS. Additionally, fossil assemblages indicated constant and normal marine salinities at central sites in the CWIS.

Sageman et al. (1997) and Watkins (1989), among others, concluded that the limestone and calcareous shale bed couplets in the Bridge Creek Limestone were derived from the combined effects of or more complicated effects than carbonate dilution and productivity. Orbital-forcing of the long-term climate component, for either model, was responsible for the resultant bedding couplets preserved in the Bridge Creek Limestone. The combined model was

used in Sageman et al. (1997) and incorporated in their time-series work, based off of work by Fischer et al. (1980), to interpret the role of orbital forcing for different components in the combined dilution-productivity model across different portions of the CWIS.

Purpose and approach

Basal Bridge Creek Limestone, Bed 63, representing a single synchronous horizon, was traced along West–East and North–South transects spanning across geographic regions in the CWIS that represent different paleoenvironmental extremes. Bed 63 was predicted to yield similar benthic oxygen conditions as those reported in Savrda and Bottjer (1994) and Savrda (1998) as a result of effects from combined dilution and productivity models. This research was new to CWIS literature because it focused on a single horizon in CWIS history from three uncollected locations, and examined oxygen-related trace fossil fabrics at a finer resolution than previous studies. Two additional outcrops with the Bed 63 horizon were added along the West–East transect to the three previous study areas (Portland and Bounds Cores, and CTB GSSP core; from Savrda and Bottjer, 1994), and, thus, expanded the transect from near the western margin in south central Utah (Site 1, Figure 1.1), to the stable eastern margin of the CWIS in north central Kansas (Site 6, Figure 1.1). Along the North–South transect, a Bridge Creek Limestone equivalent section from a north central Montana site (Site A, 2-21 Federal Core; Figure 1.1) was studied, and an outcrop at the southern site located in Antonio Canyon, an off shoot of Site B (Figure 1.1), near Langtry, TX, was added. These North–South transect sites were added to determine the effects of water mixing at high and low latitudes, and water mixing proximal to Boreal and Tethys Seas. Bed 63 among sites that represented four different paleoenvironmental extremes located along both transects was used to test effects of the combined dilution-productivity model. 1) Site 1, with proximity to Sevier Highlands along the western margin; 2)

Site 6, on the eastern margin, far removed from dilution effects of terrigenous input; 3) Site A, proximal to Boreal Sea; and 4) Site B, in the southern portion of the CWIS from a restricted platform most proximal to Tethyan water masses.

METHODS

For CWIS paleoenvironmental analyses, in Savrda and Bottjer (1994) and Savrda (1998) it was established that benthic oxygen concentrations can be interpreted from transitioning of trace fossil tiering patterns in Portland and Bounds Cores (drilled in 1992 by the USGS in Fremont County, Colorado and drilled in 1988 by Amoco Production Company in Greeley County, Kansas, respectively). The amount of benthic oxygen and rate of change among benthic oxygen conditions throughout the section can also be extracted (Sageman et al., 1997, 1998). Further, trace fossil tiering patterns among different locations provide a spatial representation of the effect OAE II had on different CWIS regions.

Trace fossils are remnants of ancient organisms' behavior, making the traces of those organisms that are sensitive to changing benthic oxygen conditions good indicators of bottom-water conditions (Bromley and Ekdale, 1984). Trace characteristics that vary due to changes in oxygen levels include burrow diameter, burrow depth, diversity of traces, and concentration of traces (Savrda 2007). Categorizing and comparing these parameters in trace fossil fabrics in order to track changes to the benthic environment is the concept behind oxygen-related ichnofabrics (ORIs) (Savrda and Bottjer, 1994; Savrda, 1998; Savrda, 1998b, Savrda, 2007).

Chondrites, *Planolites*, *Taenidium*, *Zoophycus*, *Thalassinoides*, and *Teichichnus* are trace fossils found in CWIS strata spanning OAE II (Figure 1.3), and each depicts varying levels of oxygen tolerance in the tracemaker (Ekdale, 1985; Ekdale and Mason, 1988; Savrda and Bottjer,

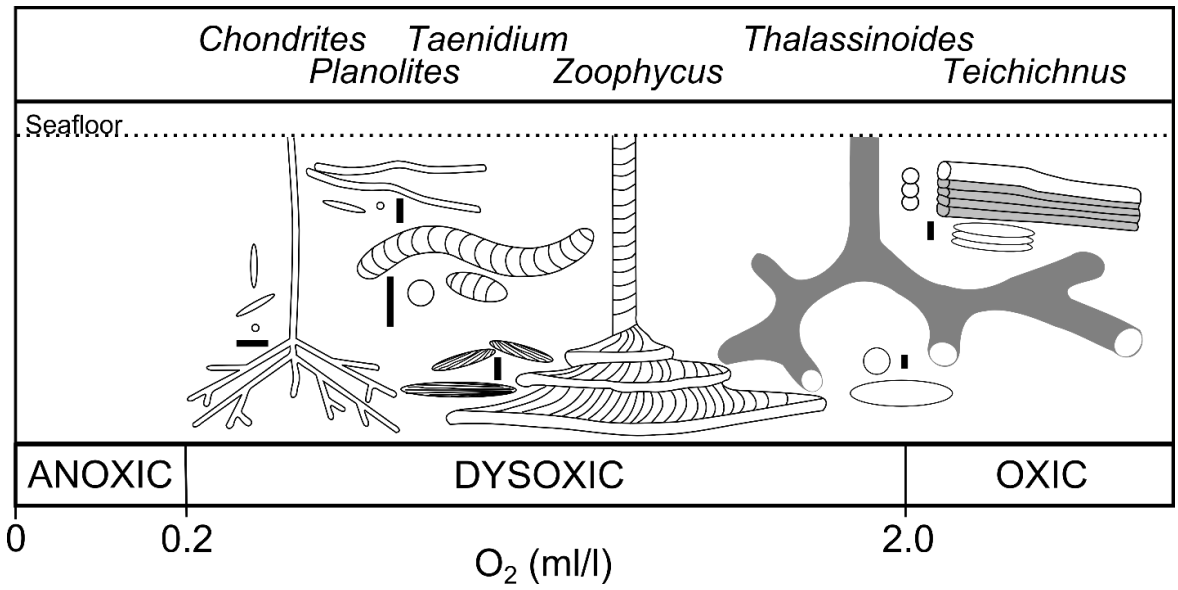

ORI Zone	Traces Present	Diversity (relative)	Burrow Diameter (mm)	Oxygen Content
ORI Zone 1	*Chondrites* *Planolites*	Lowest	2 – 6 range; 3 – 4 average	**Lowest**
ORI Zone 2	*Chondrites* *Planolites* *Taenidium* *Zoophycus*	Medium	3 – 8 range; 4 – 5 average	**Low**
ORI Zone 3	Same as ORI Zone 2	Medium	6 – 10 range; 8 average	**Medium**
ORI Zone 4	Same as ORI zone 3 *Thalassonoides* *Teichichnus*	High	8 – 20 range; 12 average	**High**

Figure 1.3 Trace fossils and how they appear in cuttings and their corresponding oxygen-related ichnofabric (ORI) ranks. Black scale bars represent 1 cm for each trace fossil type. Descriptions: *Chondrites* – feeding/dwelling behavior; a complex system of small branching tunnels with uniform diameter; positioned vertically in substrate. *Planolites* – deposit-feeding trace; unbranched, straight, or curved cylindrical burrows; positioned horizontally to sub-horizontally in substrate. *Taenidium* – deposit-feeding trace; cylindrical burrows with marked miniscate backfill; positioned horizontally or vertically in the substrate. *Zoophycus* – complex feeding/dwelling spreiten structure (corkscrew) with shallowly inclined horizontal structures that have chevron-shaped surfaces on and meniscate lamination within the trace. *Thalassonoides* – feeding/dwelling structure of crustaceans; relatively large unlined burrows linked in a 3D branching network. *Teichichnus* – feeding/dwelling structure; series of stacked longitudinally-nested tubes that are spreiten in shape; positioned vertically or horizontally in substrate (Savrda, 1998). Oxygen Related Ichnofabrics (ORIs) 1 – 4 and how they indicate benthic oxygen content in relation to the trace fossils present, diversity of traces present, burrow diameter, and burrow depth.

1994; Savrda, 1998). Categorization of a trace fossil fabric as an ORI is determined by the diversity and density of trace fossils (bioturbation), as well as the ranges of burrow diameters present. Put simply, as benthic oxygen increases from ORI 1(low oxygen) to ORI 4 (high oxygen), trace diversity and burrow diameters increase (Figure 1.3).

Representative sections from the laterally-continuous, highly correlatable basal Bridge Creek Limestone Bed 63, were used from seven sites (four outcrops [Sites 1, 3, 4, and B], and three cores [Sites 1, 2, 5, and A]) along a West–East transect and wider-spaced North-South transect (Figure 1.1).

In the laboratory, blocks of Bed 63 from outcrop were cut and photographed. Observations on ichnofabrics were taken every 0.02 m on the flat, slabbed surface of each block (Figures 1.4, 1.5a). Interpretations for Site 2 (Portland Core) and Site 5 (Bounds Core) were derived from Savrda (1998), and were made every 0.05 m on both calcareous shale and limestone beds (Figures 1.5b, 1.5c). Interpretations from Site 1 (Escalante Core) were made at the USGS Core Research Center in Denver, CO. Trace fossil data were recorded from the working-half of the core (Figure 1.5c).

Magnetic susceptibility (χ) and field gamma-ray spectroscopy (GRS) data were used to correlate Bed 63 among sites without clear marker beds (Bed 63 or bentonite marker beds from Elder et al., 1988). Bed 63, for the West–East transect is the thickest bed at each section that registers low χ and GRS values, making it a good marker bed. The low χ values for Bed 63 are due to the bed being mostly comprised of limestone. Limestone is mainly composed of the diamagnetic mineral calcite, therefore, when placed in an inducing magnetic field, samples acquire a low, negative induced moment. Paramagnetic materials acquire a low positive induced moment in an inducing magnetic field. Examples of paramagnetic minerals are biotite and illite,

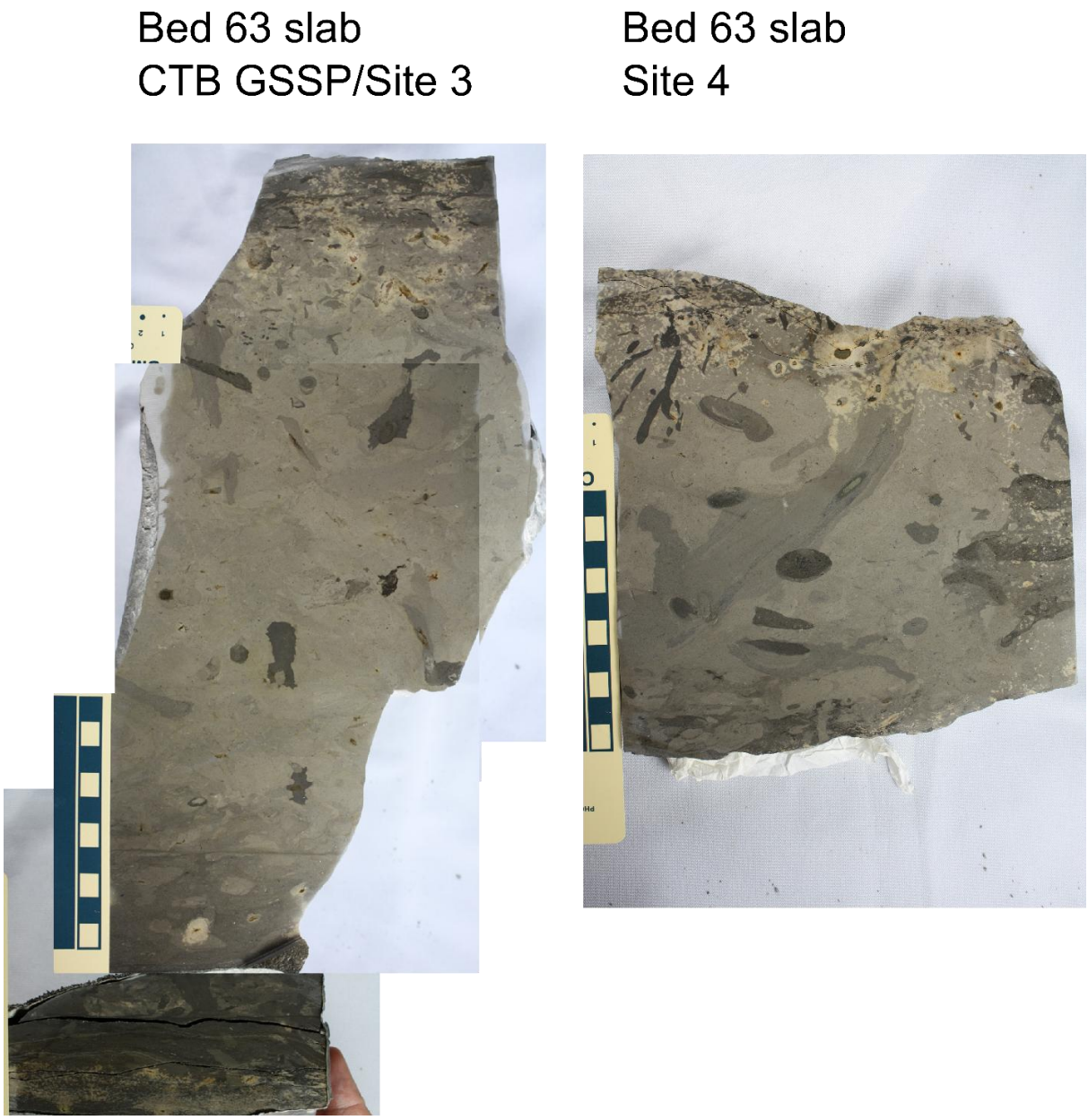

Figure 1.4 Photographs of slabbed Bed 63 samples revealing trace fossils. Scale to the left of each slab is 10 cm. Photographs by J. Grosskopf.

which are derived from terrigenous sources. Calcareous shales represent more detrital input from the continent relative to limestones, and consequently register higher χ values than limestones (Figure 1.5b; Ellwood et al., 2006; Ellwood et al., 2013). Ferrimagnetic materials, such as magnetite, exhibit high χ values in an inducing magnetic field. However, in the marine

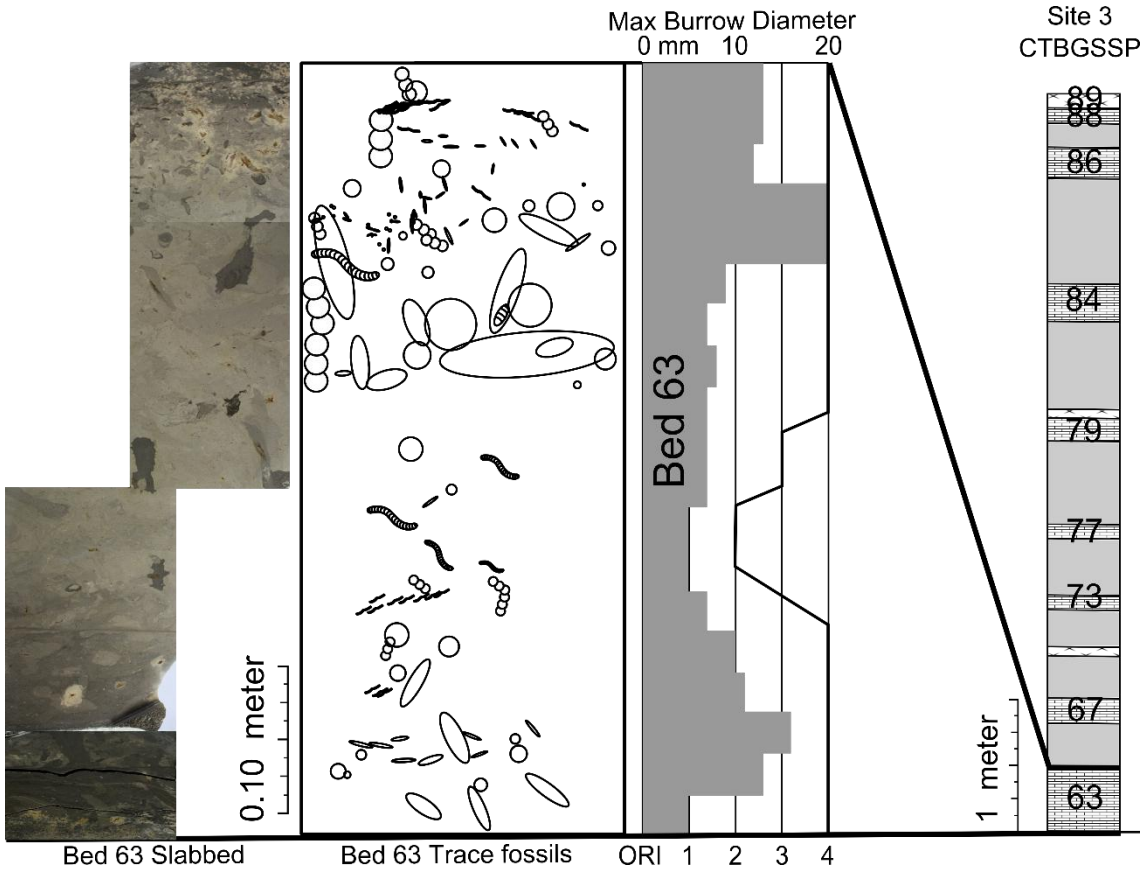

Figure 1.5a Bed 63 and CTB GSSP/Site 3 benthic oxygen variation. Left to right: slab from CTB GSSP/Site 3 Bed 63 and cartoon of trace fossil fabric; expanded interpreted oxygen curve from maximum burrow diameter (MBD) and oxygen-related ichnofabric (ORI) trace data; lithology for the CTB GSSP/Site section.

environment, magnetite is usually destroyed due to metabolization by sulfate-reducers (Karlin and Levi, 1983; Karlin and Levi, 1985). The Willams Magnetic Susceptibility Bridge at Louisiana State University is very sensitive and operates at very low, alternating magnetic fields. Single and pseudo-single domain magnetite grains would not acquire an induced magnetization in such fields, and therefore do not contribute to the χ value unless concentrations of such grains are very high (Ellwood et al., 2006).

Similar to χ values, GRS data represent detrital input from the continent. The gamma ray spectrometer field instrument was used to derive field GRS data from outcrop, by directly

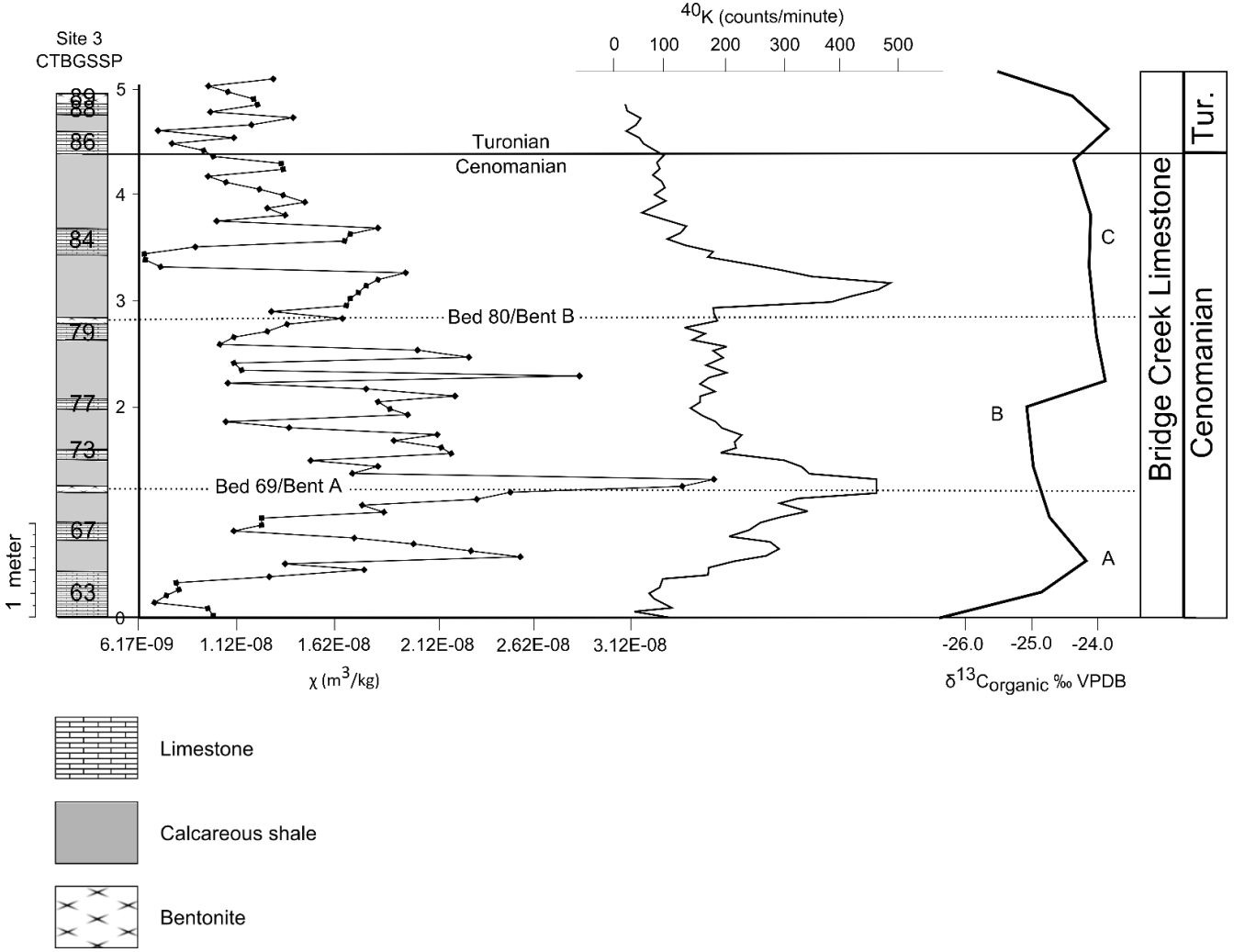

Figure 1.5b. CTB GSSP/Site 3 data. Left to right: CTB GSSP/Site 3 lithology; χ (magnetic susceptibility) and ^{40}K GRS curves (modified from Ellwood et al., 2008); $\delta^{13}C_{organic}$ curve (modified from Kennedy et al., 2005) for this interval. Dotted lines represent the correlation of datasets to the CTB GSSP using bentonite Beds 69 and 80.

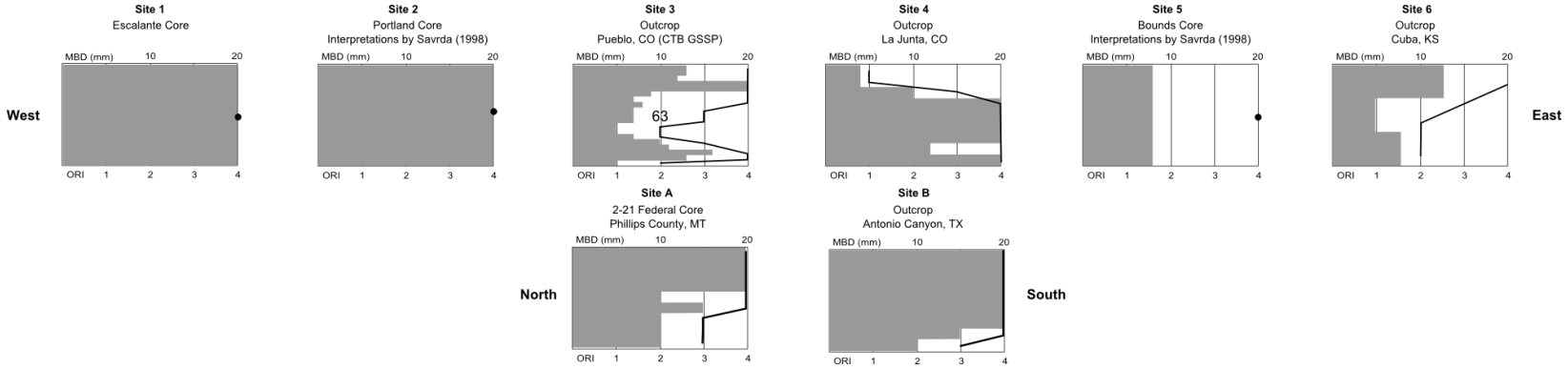

Figure 1.5c Oxygen interpretations from basal Bridge Creek Limestone Bed 63 trace fossil fabrics along the West–East and North–South transects. Bars represent MBD in the bed (top axis). Line represents ORI interpretation (bottom axis); a dot is used if a single observation interval represents an entire bed. Sites 1, 3, 4, 6, A, and B MBD and ORI interpretations were taken every 0.02 m. Sites 2 and 5 (Portland and Bounds Cores, respectively) maximum burrow data and ORI interpretations are every 0.05 m and taken directly from Savrda (1998).

detecting amount of ^{40}K in rocks and extrapolating for U and Th using decay proxies. ^{40}K is a major component in clays, which are the weathered products of crustal rocks that are deposited in marine depositional settings as shales (Ellwood et al., 2006). Thus, in the CWIS, both χ and GRS datasets show similar trends, indicating Bed 63 formed during sediment-starved conditions. This is observed in each of the limestone beds (Figure 1.5b).

In order to effectively trace trends in χ and GRS across the CWIS, a fine sampling interval must be used. Where possible, samples for χ were collected every 0.05 m and GRS readings were taken every 0.10 m. Well-log GRS (presented in API units) was substituted for field GRS data when correlating to core.

RESULTS AND DISCUSSION

Correlation of Bed 63 along each transect

Bed 63 is the boundary bed between deposition of calcareous shale below, and initiation of deposition of limestone and calcareous shale bed couplets above. This abrupt contact, represented by the base of Bed 63, can be traced throughout the CWIS (Figure 1.2). Tools for correlation, other than lithostratigraphy, were used to trace Bed 63 throughout the CWIS (e.g. Site 6). These tools include χ, and field GRS and well-log GRS curves derived from field and core samples, as well as public domain core data from the Western Interior Seaway Drilling Project (Dean and Arthur, 1998), all aiding in correlation (Figure 1.5b).

The CTB GSSP outcrop at Site 3, Bed 63, and other beds from the Bridge Creek Limestone Member, are directly correlatable across large distances. Also, several of the lower limestone beds and each bentonite bed can be traced through core and outcrop from sites 2 to 5 (Hattin, 1975; Elder, 1988). Because of the strong correlation and its importance to global

stratigraphy, data from the outcrop at the CTB GSSP were chosen to be representative of the entire transect.

Along the West–East transect, Bed 63 thins eastward, with easternmost Site 6 being the most condensed (Figure 1.5d). Variability in thickness, in contrast with the thinning trend of Bed 63 from west to east, is likely the result of differences in sediment supply, accommodation, and the bathymetric setting among each site (Elder et al., 1994). Along the North–South transect, Bed 63 thickens from 0.20 m at Site A, across the West–East transect to 0.76 m Site B in the south (Figure 1.5d).

The correlation of Bed 63 along the North–South transect is more complicated than that along the West–East transect. In order to include Bed 63 at Sites A and B in this study, Bed 63 must be an isochronous horizon throughout the basin. Bed 63 is a horizon that represents a short-lived period of time in the CWIS, for which absolute and relative age dating proxies are too coarse to yield good age control. Thus, establishing an interpretation of Bed 63's synchronicity among all sites should be difficult due to variability in bathymetric and depositional regimes over long distances. However, Bed 63 was deposited during the first major pulse of Tethys waters into the CWIS (Eicher and Diner, 1989; Gale et al., 2002), which caused the facies change between calcareous shale beds below and limestone and calcareous shale couplets above. While regional flooding surfaces may be diachronous considering the duration of time for Tethys waters to advance into the CWIS northern portions of the CWIS (Slingerland et al., 1996; Cattaneo and Steel, 2003), the base of Bed 63 represents a synchronous horizon. Work by Elder (1994) and Hattin (1971) traced this burrow-mottled flooding surface, from the deep central axis of the basin towards the clastic margin to the west (at Site 1), and biozone boundaries, either evidenced by ammonoid index taxa (e.g. *Sciponoceras gracile/Neocardioceras juddii* Zone boundary) or

	Sites	Bed 63 Thickness	Bed 63 Description
West–East Transect	**Site 1**	1.38 m	Bioturbated fossiliferous limestone; grades into lime-rich sandstone at base; abrupt contact at top
	Site 2	0.60 m	Bioturbated massive limestone
	Site 3	0.50 m	Bioturbated massive limestone
	Site 4	0.25	Bioturbated massive limestone
	Site 5	0.10 m	Bioturbated limestone; grades into calcareous shale at base and top
	Site 6	0.10 m	Moderately bioturbated limestone; grades into calcareous shale at base
North–South Transect	**Site A**	0.20 m (?)	Fine lenticular nodules at top; grades into calcareous shale at base
	Site B	0.76 m	Bioturbated massive limestones with pyrite replaced burrow fills

Figure 1.5d Thickness and lithologic descriptions for Bed 63 at each site.

recognizable shifts in paleocommunities (e.g. *Depanochilus* gastropods), coincided with the base of Bed 63 in both western and central portions of the seaway. The compatibility of these litho– and biostratigraphic conditions indicate that the base of Bed 63 is a synchronous stratal horizon throughout the CWIS.

Site A synchronicity with CTB GSSP

Bed 63 at Site A was correlated by comparing lithologic descriptions for the Cone Member of the Marias River Formation from the Cobban et al. (1976) survey of the formation at the Sweetgrass Arch in western Montana, to the 2-21 "Federal Core" drilled in Phillips County, Montana (Gautier, 1986). Two marker beds, a thick bentonite bed and an overlying blue-gray limestone bed with crushed bivalves and an amalgam of fish scales, were correlated from outcrop (Cobban et al., 1976) to the Federal Core. Bed 63 was identified in the core by correlating the two marker beds from Sweetgrass Arch outcrop to the Federal Core. Then, fossil data from outcrop were referenced to the ammonite and inoceramid zones present at the CTB GSSP. This correlation is shown in Figure 1.6. *Sciponoceras gracile* was found in the Sweetgrass Arch outcrop below the two marker beds. That zone is shown at the CTB GSSP (Kennedy, 2005) to extend from the Hartland Shale up through Bed 63 to just below the base of Bed 79, putting it within the OAE II interval.

The top of Bed 63 was determined to be located at 355.8 m in the Federal Core and is described as a > 2.0 m thick calcareous shale bed whose top is interbedded with fine (~0.01 m thick) limestone laminae. The fine limestone laminae horizon at the top of Bed 63 in the Federal Core is equivalent to Bed 63 elsewhere in the basin. In outcrop, this bed is at the very base of the relation between nodular limestones and limestone layers to early diagenesis of localized concentrations of bioclastic carbonate and carbonate cement below the sediment–water interface.

High CO_2 levels in reducing conditions below the sediment–water interface shifts carbonate equilibrium to favor dissolution of carbonate content, until reaching higher pH where$CaCO_3$ will precipitate as a cement, lithifying components. Moller and Kvingan (1988) indicate that nodular layers thin in such a way that they transition from nodules to small lenses

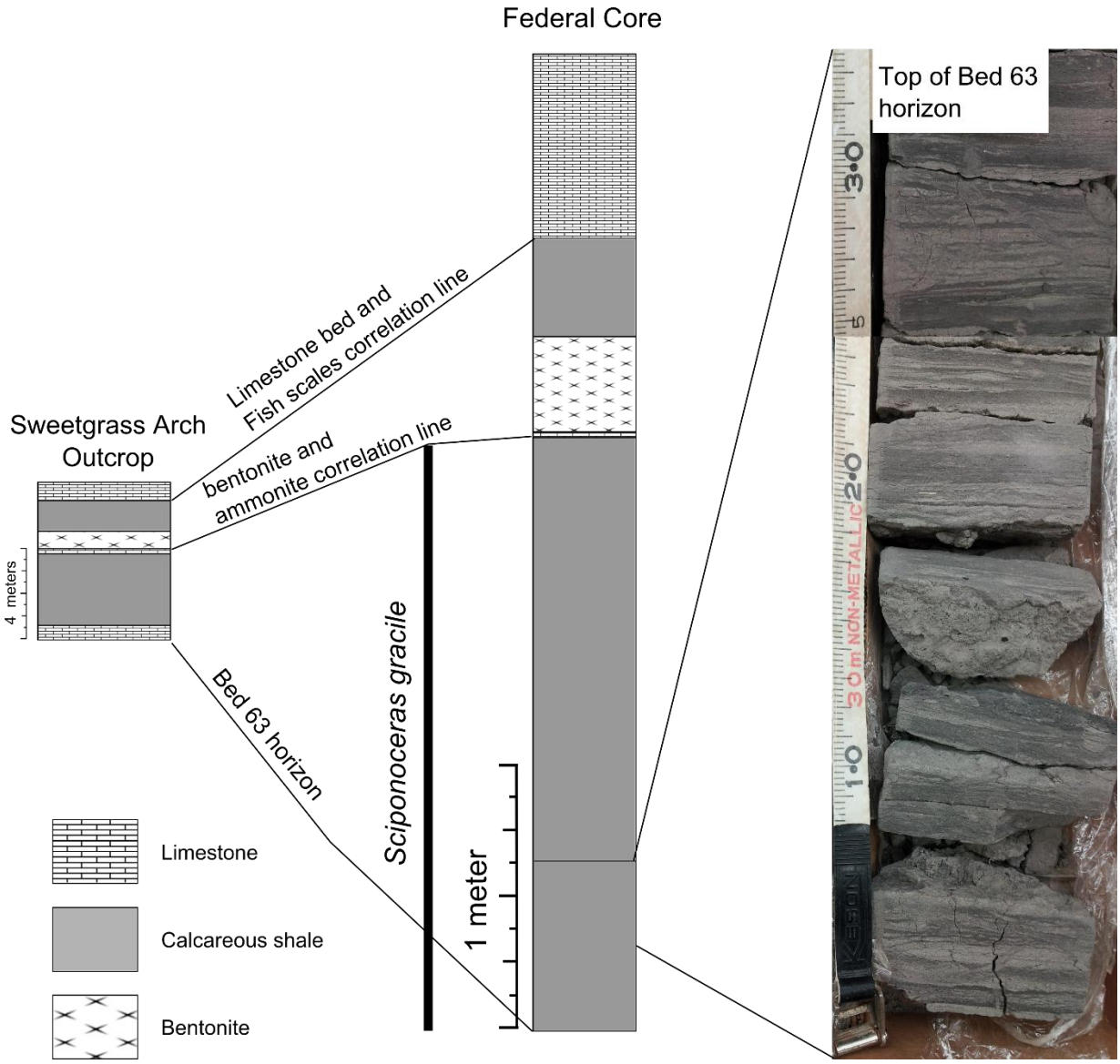

Figure 1.6 Sweetgrass Arch to 2-21 Federal Core correlation using traceable horizons. Tie-lines show correlation between base of Bed 63 horizon, the ammonite zone for *Sciponoceras gracile* among both locations, and the corresponding lithology represented by matching bentonite and limestone beds containing crushed fish scales. The Federal Core is more condensed than the outcrop of the same interval at the Sweetgrass Arch to the east, and this reflected in the scales used to correlate the two. Sweetgrass outcrop lithologic column is modified from Cobban et al., (1976). Photographs of the core were taken by J. Grosskopf at the USGS Core Research Center in Denver, CO.

$CaCO_3$ will precipitate as a cement, lithifying components. Moller and Kvingan (1988) indicate that nodular layers thin in such a way that they transition from nodules to small lenses set in

shale across the basin. They show that limestone layers, nodular limestone layers, and limestone lenses (best described as Flaser-type bedding) form at different depths under a set combination of depositional, biological, and chemical interactions.

In the Ordivician and Silurian rocks studied by Moller and Kvingan (1988) they observed a correlation between water depth and siliciclastic input to the resultant limestone bedding type. They concluded as water depth decreases and more mixing and siliciclastic sediment are involved, nodules become finer and more lenticular. These thin, lenticular limestone beds are representative of the limestone component in the Federal Core. This thinning trend as a result of decreasing water depth and increased sediment mixing is also reflective of the thinning trend of Bed 63 from west to east along the West–East transect, where the north-central Montana section represented in the Federal Core, is far more condensed than the Sweetgrass Arch outcrop in western Montana.

To summarize, marker beds correlate from the Sweetgrass Arch outcrop to the 2-21 Federal Core, ammonite zones match from the Sweetgrass Arch outcrop to the CTB GSSP in Pueblo, CO. Similar thinning and matching lithology of the basal bed of the Cone Member, between the Sweetgrass Arch outcrops and the 2-21 Federal Core, corroborate the correlation of Bed 63, indicating that it is of the same age as that along the West–East transect.

Site B synchronicity with CTB GSSP

Deposits in the section exposed at Site B are interpreted by Goldhammer and Johnson (2001) to be from a restricted platform set higher than the surrounding seafloor of the CWIS, and very proximal to the open ocean setting of the Tethys Sea (Fig 1.1). In as much as a restricted basin would present a different depositional setting, a restricted basin could also present a

sedimentary environment disparate from the broad-scale depositional environment of the CWIS. Under these conditions, the resultant strata could be difficult to correlate to other sites. Whether there is a horizon at Site B that represents benthic oxygen conditions during OAE II-time must be established. Using patterns in the $\delta^{13}C$ curve, planktonic foraminifera, and stratigraphic consistency throughout the CWIS, it is obvious that Bed 63 is present at Site B and that it is isochronous to other CWIS sites. The CTB GSSP stage and lithology are shown in Figure 1.7 under part a. Part b of Figure 1.7 shows the relation between ammonoid zones, OAE II duration, and relation of distinctive parts A, B, and C of the $\delta^{13}C_{organic}$ curve at the CTB GSSP as reported in Kennedy et al. (2005). Figure 1.7 part c is the correlation of distinctive $\delta^{13}C_{organic}$ peaks that correlate to the $\delta^{13}C_{carbonate}$ curve, as well as ammonoid zones and nannofossil ranges (reported in Kennedy et al., 2005), each of which are used by Corbett and Watkins (2013) for correlation from southern Texas, to the CTB GSSP.

The Fasken "A" #1-H Core, reported in Corbett and Watkins (2013) is in the southern portion of the CWIS proximal Site B (Fasken Core; Figure 1.1).The Fasken Core was taken ~250 km west of Corpus Christi, Texas, ~450 km southeast of Site B. The section studied by Donovan et al. (2012) is in Lozier Canyon, ~30 km east of Langtry, TX. The Site B outcrop is an offshoot of Lozier Canyon, situated a few kilometers the main outcrop.

Corbett and Watkins (2013) correlate the $\delta^{13}C_{carbonate}$ curve and its distinctive excursions (A, B, and C; Figure 1.7 part d) to the CTB GSSP (Figure 1.7 part c). The Fasken Core $\delta^{13}C_{carbonate}$ closely matches the $\delta^{13}C_{carbonate}$ curve at the CTB GSSP (reported by Kennedy et al., 2005). It is important to note that the interval the $\delta^{13}C_{carbonate}$ curve represents varies between each of these

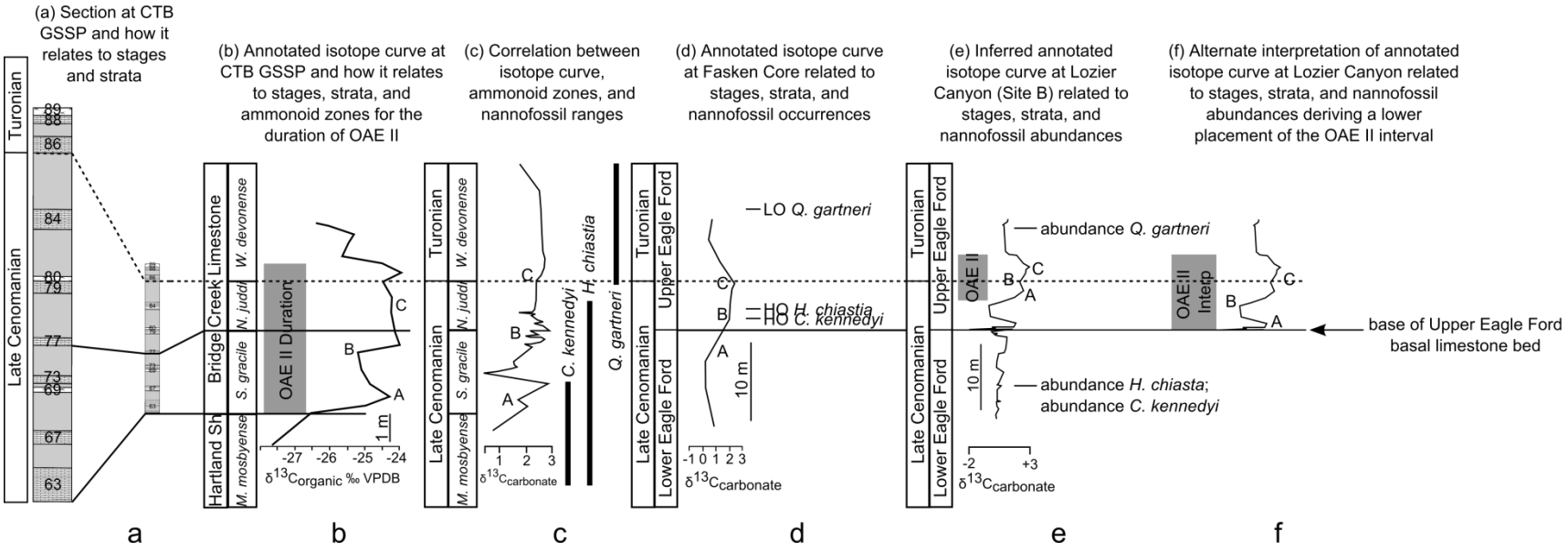

Figure 1.7 Diagram depicting correlation from CTB GSSP/Site 3 to Fasken Core and Site B to visually explain an alternate interpretation of OAE II duration at Site B. Curves modified from Kennedy et al. (2005), Donovan and Staerker (2010), Donovan et al., (2012), and Corbett and Watkins (2013).

sites. The expression of the $\delta^{13}C_{carbonate}$ curves from the Fasken Core and Lozier Canyon outcrop (Figure 1.7 part e) are both expanded (10.00 m and 7.50 m, respectively), compared to sections to the north along the West–East transect, where the same curve is condensed to ~5 m at the CTB GSSP (Figure 1.7 part c).

The correlations of Corbett and Watkins (2013) place the start of the $\delta^{13}C_{carbonate}$ curve, representing OAE II, at or just below the base of Bed 63, which marks the start of OAE II in other parts of the seaway. Their biostratigraphic correlation matched the nannofossils and $\delta^{13}C_{carbonate}$ excursions from Fasken Core to the same excursions and ammonoid zones at the CTB GSSP (parts c and d of Figure 1.7).

Donovan et al. (2012) correlate the Lozier Canyon section to the CTB GSSP using the peaks of the $\delta^{13}C_{carbonate}$ curve from the Lozier Canyon outcrop. The duration of OAE II that is expressed as the $\delta^{13}C_{carbonate}$ curve for Lozier Canyon is longer than what is interpreted by Donovan et al. (2012). They indicate that evidence for the OAE II begins ~3.5 m higher in the section than the first positive spike in $\delta^{13}C_{carbonate}$ (part e of Figure 1.7). The bed at the height of the first positive spike height matches the lithology and broad-scale stratal pattern for the CWIS, in that it represents the contact between a thick section of calcareous shale (Lower Eagle Ford in Texas; Hartland Shale at the CTB GSSP; Figures 1.2, 1.7 part a) and the limestone and calcareous shale bed couplets (Upper Eagle Ford in Texas; Bridge Creek Limestone at the CTB GSSP; Figures 1.2, 1.7 part a).

Nannofossil zones from Corbett and Watkins (2013) and Donovan et al. (2012) relatively date this basal bed to be in the same time as Bed 63. The last occurrence of *Corollithion kennedyi* and *Helenia chiastia*, along with the first occurrence of *Quadrum gartneri*, offer coarse biostratigraphic control that correlates the Fasken Core to Lozier Canyon (Figure 1.7 parts d–e).

If the expression of $\delta^{13}C_{carbonate}$ at the Lozier Canyon locality is interpreted to be the first signal peak in the basal bed at Lozier Canyon (Figure 1.7 part f), then the biostratigraphic correlation is still valid. This would extend the duration of the curve at Lozier Canyon, and in turn OAE II-time, from 7.5 m to 11 m. This interpretation better matches thicknesses expressed in the expanded section at Site B, relative to OAE II sections along the West–East transect. It also matches the interpreted duration of OAE II expressed in the Fasken Core by Corbett and Watkins (2013).

In summary, Bed 63 along the West–East transect is synchronous with the basal bed dividing the Lower and Upper Eagle Ford Formations in Texas (Donovan et al., 2012). interpretation that the first peak in the $\delta^{13}C_{carbonate}$ curve is located ~5 m below where it is interpreted to occur in the Lozier Canyon section (Figure 1.7 part f) does not interfere with biostratigraphic age control, and matches the lithologic character of this section. This increase in duration for OAE II, as expressed by the $\delta^{13}C_{carbonate}$ curve, is close to the duration interpreted by Corbett and Watkins (2013) for the nearby Fasken Core. A recently published correlation of $\delta^{13}C_{organic}$ and $\delta^{13}C_{carbonate}$ curves for the Lozier Canyon site by Lowery et al. (2014) matches this interpretation.

Spatial variation in benthic oxygen concentrations

Figure 1.5c represents the trace fossil fabrics in Bed 63, among different sites on both the West–East transect and North–South transect, and illustrates maximum burrow diameter and ORI. Here, ORI is categorized by a combination of observations including traces present, trace density per every 0.02 m^2 [except for sites 2 and 5, observed and reported by Savrda (1998)], and maximum burrow diameter. The resulting ORI was used to the estimate oxygen variation for that bed. High ORIs in Bed 63 indicate that well-oxygenated bottom waters were prevalent

throughout all parts of the seaway, regardless of proximity to the margins or deeper areas. Bed 63 is representative of high benthic oxygen conditions because of the occurrence of *Thalassinoides* and *Teichichnus*, and an abundance of other traces found in environments in high benthic oxygen concentrations (Savrda, 1998; 1998b). Additionally, these traces exhibit large burrow diameters ranging from 4–20 mm, and most sites have a high burrow concentration ranging from 1–5 traces/0.02 m^2.

West–East Transect

The drop in ORI from loss of burrow diversity, density, and burrow diameter from Site 1 near the western margin of the CWIS to Site 6 near the eastern margin (Figure 1.5c) may be due to the change in sedimentation and associated dilution effects and different water mass chemistry at the eastern margin relative to the rest of the basin (Slingerland et al., 1996; Corbett and Watkins, 2013). In the Slingerland et al. (1996) model, paleocurrents in the CWIS are driven by prevailing winds and Coriolis effects on two distinct water masses from the northern and southern openings of the seaway. Warm saline-rich waters ran northward from the Tethys Sea along the eastern margin of the CWIS. Relatively cooler and fresher waters, sourced from the Boreal Sea, ran along the western margin southward. Slingerland et al. (1996) hypothesizes that there was a broad gyre in the center of the seaway that resulted from the interaction of these two water masses.

Site 1, along the western margin of the CWIS represents the paleoenvironment with the highest flux of terrigenous input. The dilution model predicts this setting would have lower benthic oxygen levels due to oxygen-limiting conditions from water stratification. This is not the case in that ORI 4 is maintained throughout the duration of the Bed 63 at Site 6. This indicates that limestone produced on the western margin of the CWIS is the result of sediment starvation

and productivity caused by sea level rise and carbonate productivity by Tethyan water mass incursion. This is not the case for the eastern margin in that ORIs 2–4 are maintained through the duration of Bed 63 at Site 6. This corresponds to interpretations from ORIs from interpreted oxygen curves by Savrda (1998), and CWIS circulation models by Slingerland et al. (1996) and Kump and Slingerland (1999). The compared to Site 1/western margin, the dilution model predicts opposite carbonate deposition conditions near the easternmost margin, as the site is far removed from main terrigenous flux in the western portions of the basin, and more mixing should occur in the relatively shallower waters of the basin, and this is not the case.

Warm saline-rich waters comprising the Tethyan water mass are linked to global perturbations associated with OAE II (Bowman and Bralower, 2005) and they would impact CWIS benthic environment during water mass mixing. Snow et al. (2005) attribute the Caribbean Large Igneous Province, the subaqueous eruptions at southern reaches of the CWIS, to be responsible for major drop in oxygen in global waters. In addition to the water mass low in oxygen from effects of OAE II, the Tethys waters travelling northward along the eastern margin may have had been further depleted in oxygen from the dissolved load of metals and oxygen-absorbing compounds sourced from the submarine magmatic eruptions. Either one, or these combined effects may have made this warm Tethyan water mass have slightly reducing conditions as it traveled northward along the eastern margin of the CWIS that contributed to the slightly lower benthic oxygen concentrations observed in the Bed 63 horizon at Site 6 (Slingerland et al., 1996; Pancost et al., 1998).

Corbett and Watkins (2013) report that rich planktonic microfossil assemblages found at Site 6 indicates high surface fertility near the eastern margin of the CWIS. Benthic waters from the Tethys moving northward along the eastern margin could be responsible for this productivity

increase, as suggested in the Slingerland et al. (1996) model. Perhaps less surface water mixing occurred at Site 6 than is suggested by their model and the warm, saline-rich Tethys water mass may have contributed to the loss of overall benthic oxygen to the eastern portion of the basin by adding water that, relative to CWIS water, was less able to take oxygen into solution. Additionally, water stratification due to increased freshwater input (dilutional effects) from the eastern margin of the CWIS is an unexplored cause for the drop in benthic oxygen in this portion of the seaway, but may provide a viable explanation. Lack of mixing of freshwater, and CWIS and Tethys water masses may have caused the slight decline in benthic oxygen that is evident at Site 6. Neither the individual effects from dilution or productivity models, nor the effects from combined dilution–productivity model are sufficient to understand the benthic paleoenvironmental conditions along the eastern margin of the CWIS. Further research along this margin will provide insight on the interaction of differing water masses at this region in the CWIS.

North–South Transect

Sites A and B, are very similar in estimated oxygen content, even though located at the opposite ends of the CWIS, in close proximity to Boreal and Tethys seas, respectively (Figure 1.1). Lithologic and ORI interpretations from Site A reveal combined dilution and productivity model effects played a role in the carbonate depositions. Dilution effects were evident in fine lenses of limestone layered between darker calcareous shale layers. Productivity effects were evident in the presence of limestone in conditions that clearly favored calcareous shale deposition, while bioturbation is present.

The models that invoke low oxygen Tethys waters to account for differences in benthic oxygen along the West–East transect as a response of low oxygen in the Tethys waters do not

explain ORI results along the southern portion of North–South transect. Bed 63 at Site B represents the benthic oxygen conditions of the Tethys Sea because the site is proximal to the inlet of Tethyan waters. The ORI from Site B indicates high benthic oxygen conditions. Site B does not fall within the CWIS water-mixing model proposed by Slingerland et al. (1996). Site B has been interpreted by Goldhammer and Johnson (2001) to be located in a restricted part of the basin, set at a higher bathymetry than the Tethys, and separated from CWIS and Tethys bottom waters and their interchange. This shallower platform (~60 m deep, compared to ~120 m for the CWIS, as estimated by Donovan et al, 2012) would also make this depositional setting more susceptible to being mixed by wind and wave action. Site B favors productivity models for CWIS stratigraphy, but represents a more complicated relationship between shallow water processes, and the mixing of CWIS and Tethys water masses. The observed benthic oxygen conditions could have prevailed at Site B, but not at Site 6, due to the lack of terrigenous input in a silled basin set on a higher platform than the rest of the seaway. As previously stated, the controls on terrigenous input and associated water stratification effects, as well as the state of the CWIS water mass after mixing with Tethyan water mass along the eastern margin of the CWIS is enigmatic (Watkins, 1989; Corbett and Watkins, 2013).

Temporal variation in benthic oxygen concentrations

Variable ORIs through Bed 63 at the CTB GSSP (Site 3) indicate variable oxygen conditions during the deposition of this bed, but never do the conditions register as anoxic. Bed 63 ichnofabrics at Site 3 exhibit burrow diameters that range from 0.05 – 0.20 m, and trace types and burrow concentrations that represent oxygen concentrations from dysoxic to oxic. The interpreted oxygen curve from varying ORIs in Bed 63 at Site 3 is derived from an ichnofabric that transitions from ORI 4 to ORI 2 and back to ORI 4, from base to top of Bed 63 (Figure

1.5a). This establishes an interpreted oxygen curve that varies from oxic to dysoxic and back to oxic again. While sites 2 and 5 were sampled at a frequency that may have been too coarse to capture this trend, Sites 3 and 4 do capture this small-scale variation from base to top of the bed (Fig 1.5c). This fluctuation in ORIs within a bed is important in understanding how oxygen characteristics changed through time throughout the basin.

In the dilution model, limestone beds form when there is a lack of terrigenous input, and high oxygen concentration in the CWIS. ORIs from Bed 63 indicating changes from well-oxygenated levels to lower oxygen levels along the deep central axis of the CWIS must be from a combination of dilution and productivity models, with the dilution model and the productivity model occurring concomitantly, and the productivity phase having stronger effects (Leithold and Dean, 1998; Pancost et al., 1998; Sageman et al., 1997, 1998).

Orbitally-forced changes in CWIS oxygen

As explained earlier, changes in CWIS benthic oxygen concentrations during OAE II are attributed to changes in climate due to precessional, obliquity, and eccentricity-scale orbitally-forced climatic cycles, which result in the recognizable limestone and calcareous shale bed couplets. Sageman et al. (1997, 1998) argue the dilution model suggests limestone and shale couplets represent obliquity-scale influences to runoff, and, in turn, CWIS oxygen variability. Fine-scale, short-term variation in trace fossil fabrics found in Bed 63 at sites 3 and 4 may be the result of precessional-scale forcing brought about by effects from productivity cycles (P1 = 18.5 kyr and P2 = 22.5 kyr [calculated from data presented by Berger et al. (1992)] at ~93.9 Ma). Sageman et al. (1997) attribute Bed 63 to represent carbonate productivity by Tethyan waters moving into the CWIS marking the onset of marine transgression, with the maximum highstand farther up-section into the Turonian-age Upper Bridge Creek Limestone. The small-scale

changes in ORI observed for Bed 63 at sites 3 and 4 could be attributed to precessional-forced Tethyan productivity cycles imprinted on the obliquity-forced CWIS dilution effects (in the limestone phase) during the deposition of the Bed 63 limestone. Eicher and Diner (1989) and Sageman et al. (1997, 1998) interpret the deposition of each limestone bed in the Lower Bridge Creek Limestone to be related to Tethyan waters' influence in the basin. If this is the case, Bed 63 at site 3 and 4 then may represent two precessional cycles (P1 = 18.5, P2 = 22.5 at ~93.9 Ma) that may indicate two pulses of carbonate production brought about by Tethyan calcareous microorganism productivity pulses resulting in Bed 63 deposition.

CONCLUSIONS

Oxygen-related ichnofabrics (ORI) along a West–East and North–South transects of basal Bridge Creek Limestone, Bed 63, indicate that benthic waters were well-oxygenated across the entire Cretaceous Western Interior Seaway (CWIS) during Oceanic Anoxic Event II (OAE II), which matches previous work from cores in the central portions of the CWIS. Two models explain the occurrence of calcareous shale and limestone beds in Bridge Creek Limestone strata. Bed 63 was formed during lack of terrigenous input into the basin during sediment-starved and well-oxygenated conditions. Bed 63 was deposited during conditions that produced large concentrations of skeletal carbonate from microfossils, due to Tethys and CWIS water mass mixing. Both carbonate depositional processes resulted in oxygenated conditions for the base of Bed 63. Four sites, each representing extreme differences in controls on limestone deposition, all represent well-oxygenated benthic conditions, evidenced by ORIs exhibiting high trace diversity, high density, and large burrow diameters. Only in the easternmost site along the West–East transect is there a slight drop in benthic oxygen conditions, but these conditions are only dysoxic.

Benthic oxygen concentrations, therefore, were controlled by lack of sediment delivery into the basin and the Tethyan waters that were influenced by global conditions during OAE II. Precessional-scale benthic oxygen variations that are noticeable in the trace fossil fabric from Bed 63 at some locations across the CWIS West–East transect through the basin, and thereby, under the productivity model, track pulses carbonate production in Tethyan waters.

REFERENCES

Arthur, M.A. and Schlanger, S.O. 1979. Cretaceous "oceanic anoxic events" as causal factors in development of reef-reservoired giant oil fields. *The American Association of Petroleum Geologists Bulletin*, **63**, 870-885.

Berger, A., Loutre, M.F., and Laskar, J. 1992. Stability of the astronomical frequencies over the Earth's history for paleoclimate studies. *Science*, **255**, 560-566.

Bowman, A.R. and Bralower, T.J. 2005. Paleoceanographic significance of high-resolution carbon isotope records across the Cenomanian-Turonian boundary in the Western Interior and New Jersey coastal plain, USA. *Marine Geology*, **217**, 305-321.

Cattaneo, A. and Steele, R.J. 2003. Transgressive deposits: a review of their variability. *Earth Science Reviews*, **62**, 187-228.

Cobban, W.A., Erdman, C.E., Lemke, R.W. and Maughan, E.K. 1976. Type sections and stratigraphy of the members of the Blacklead and Marias River Formations (Cretaceous) of the Sweetgrass Arch, Montana. U.S. Geological Survey, Professional Paper 974.

Cobban, W.A., Merewether, E.A., Fouch, T.D., and Obradovich, J.D. 1994. Some Cretaceous shorelines in the Western Interior of the United States, *in* Caputo, M.V., Peterson, J.A., and Franczyk, K.J. eds., Mesozoic Systems of the Rocky Mountain Region, USA: Rocky Mountain Section SEPM – Society for Sedimentary Geology, 393-414.

Corbett, M.J. and Watkins, D.K. 2013. Calcareous nannofossil paleoecology of the mid-Cretaceous Western Interior Seaway evidence of oligotrophic surface waters during OAE2. *Palaeogeography, Palaeoclimatology, Palaeoecology*, **392**, 510-523.

Dean, W.E. and Arthur, M.A. 1998. Cretaceous Interior Seaway Drilling Project: an overview. Stratigraphy and Paleoenvironments of the Cretaceous Western Interior Seaway, USA, SEPM Concepts in Sedimentology and Paleontology, **6**, 1-10.

Demaison, G.J. and Moore, G.T. 1980. Anoxic environments and oil source bed genesis. *The American Association of Petroleum Geologists Bulletin*, **64**, 1179-1209.

Donovan, A.D. and Staerker, T.S. 2010. Sequence stratigraphy of the Eagle Ford (Boquillas) Formation in the subsurface of South Texas and outcrops of West Texas. *Gulf Coast Association of Geological Societies Transactions*, **60**, 861-899.

Donovan, A.D., Staerker, T.S., Pramudito, A., Li, W., Corbett, M.J., Lowery, C.M., Romero, A.M. and Gardner, R.D. 2012. The Eagle Ford outcrops of West Texas: a laboratory for understanding heterogeneities within unconventional mudstone reservoirs. *Gulf Coast Association of Geological Societies Journal*, **1**, 162-185.

Eicher, D.L. and Diner, R. 1989. Origin of the Cretaceous Bridge Creek cycles in the Western Interior, United States. *Palaeogeography, Palaeoclimatology, Palaeoecology*, **74**, 127-146.

Ekdale, A.A. 1985. Trace fossils and mid-Cretaceous anoxic events in the Atlantic Ocean. Society of Economic Paleontologists and Mineralogists, Special Publication, **35**, 333-342.

Ekdale, A.A., and Mason, T.R. 1988. Characteristic trace-fossil associations in oxygen-poor sedimentary environments. *Geology*, **16**, 720-723.

Elder, W.P. 1988. Geometry of Upper Cretaceous bentonite beds: Implications about volcanic source areas and paleowind patterns, western interior, United States. *Geology*, **16**, 835-838.

Elder, W.P., Gustason, E.R., and Sageman, B.B. 1994. Correlation of basinal carbonate cycles to nearshore parasequences in the Late Cretaceous Greenhorn Seaway, Western Interior U.S.A. *Geological Society of America Bulletin*, **106**, 892-902.

Ellwood, B.B., Balsam, W.L., and Roberts, H.H. 2006. Gulf of Mexico sediment sources and sediment transport trends from magnetic susceptibility measurements of surface samples. *Marine Geology*, **230**, 237-248.

Ellwood, B.B., Tomkin, J.H., Ratcliffe, K.T., Wright, M., and Kafafy, A.M. 2008. High-resolution magnetic susceptibility and geochemistry for the Cenomanian/Turonian boundary GSSP with correlation to time equivalent core. *Palaeogeography, Palaeoclimatology, Palaeoecology*, **261**, 105-126.

Ellwood, B.B., Wang, W., Tomkin, J.H., Ratcliffe, K.T., hassani, A.E., and Wright, A.M. 2013. Testing high resolution magnetic susceptibility and gamma radiation methods in the Cenomanian-Turonian (Upper Cretaceous) GSSP and near-by coeval section. *Palaeogeography, Palaeoclimatology, Palaeoecology*,**378**, 75-90.

Fischer, A.G., 1980. Gilbert-bedding rhythms and geochronology. *Geological Society of America Special Papers*, **183**, 93-104.

Fischer, A.G., Herbert, T.D., and Premoli Silva, I. 1985. Carbonate bedding cycles in Cretaceous pelagic and hemipelagic sequences, *in* Pratt, L.M., Kauffman, E.G., and Zelt, F.B. eds., Fine-grained deposits and biofacies of the Cretaceous Western Interior Seaway: evidence of cyclic sedimentary processes, SEPM – Field Trip Guidebook 4, 1-10.

Fisher, C.G. and Arthur, M.A. 2002. Water mass characteristics in the Cenomanian US Western Interior Seaway as indicated by stable isotopes of calcareous organisms. *Palaeogeography, Palaeoclimatology, Palaeoecology*, **188**, 189-213.

Friedrich, O., Erbacher, J., Wilson, P.A., Moriya, K. and Mutterlose, J. 2009. Paleoenvironmental changes across the Mid Cenomanian Event in the tropical Atlantic Ocean (Demera Rise ODP Leg 207) inferred from benthic foraminiferal assemblages. *Marine Micropaleontology*, **71**, 28-40.

Gale, A.S., Hardenbol, J., Hathaway, B., Kennedy, W.J., Young, J.R., and Phansalkar, V. 2002.Global correlation of Cenomanian (Upper Cretaceous) sequences: Evidence for Milankovitch control on sea level. *Geology*, **30**, 291-294.

Gautier, D. L. 1986. Cretaceous shales from the western interior of North America: Sulfur/carbon ratios and sulfur-isotope composition. *Geology*, **14**, 225-228.

Gilbert, G.K. 1895. Sedimentary measurement of geologic time. *Journal of Geology*, **3**, 121-127.

Goldhammer, R.K. and Johnson, C.A. 2001. Middle Jurassic-Upper Cretaceous paleogeographic evolution and sequence-stratigraphic framework of the northwest Gulf of Mexico rim, *in* C. Bartolini, R.T. and Cantu-Chapa, eds., The western Gulf of Mexico Basin: Tectonics, sedimentary basins, and petroleum systems: AAPG Memoir 75, 45-81.

Grosskopf, J. F. 2015. Litho- and chemostratigraphic correlation from Upper Eagle Ford Formation outcropping at Lozier and Antonio Canyons, near Langtry, Texas, to the Cenomanian–Turonian Boundary GSSP, Pueblo, CO. Diss. Louisiana State University, 2015. Baton Rouge: LSU, 2015. Electronic.

Hattin, D.E. 1971. Widespread, synchronously deposited, burrow-mottled limestone beds in Greenhorn Limestone (Upper Cretaceous) of Kansas and Central Colorado. *American Association of Petroleum Geologists Bulletin*, **55**,412-431.

Hattin, D.E. 1975. Stratigraphy and depositional environment of Greenhorn Limestone (Upper Cretaceous) of Kansas. Kansas Geological Survey Bulletin 209, University of Kansas.

Karlin, R., and Levi, S. 1983. Diagenesis of magnetic minerals in Recent haemipelagic sediments. *Nature*, **303**, 327-330.

Karlin, R., and Levi, S. 1985. Geochemical and sedimentological control of magnetic properties of hemipelagic sediments. *Journal of Geophysical Research*, **90**, 10373-10392.

Keller, G., Berner, Z., Adatte, T., and Stueben, D. 2004. Cenomanian-Turonian and $\delta^{13}C$, and $\delta^{18}O$, sea level and salinity variations at Pueblo, Colorado. *Palaeogeography, Palaeoclimatology, Palaeoecology*, **211**, 19-43.

Kennedy, W.J., Walaszczyk, I., and Cobban, W.A. 2005. The Global Boundary Stratotype Section and Point for the base of the Turonian Stage of the Cretaceous: Pueblo, Colorado, U.S.A. Episodes: Journal of International *Geoscience*, **28**, 93-104.

Kolonic, S., Wagner, T., Forster, A., Sinninghe Damste, J.S., Walsworth-Bell, B., Erba, E., Turgeon, S., Brumsack, H., Chellai, E., Tsikos, H., Kuhnt, W., and Kuypers, M. M. 2005. Black shale deposition on the northwest African Shelf during the Cenomanian/Turonian oceanic even: Climate coupling and global organic carbon burial. *Paleoceanography*, **20**, PA1006. doi:10.1029/2003PA000950.

Kump, L. R. and Arthur, M.A. 1999. Interpreting carbon-isotope excursions: carbonates and organic matter. *Chemical Geology*, **161**, 181-198.

Kump, L.R. and Slingerland, R.L. 1999. Circulation and stratification of the early Turonian Western Interior Seaway: Sensitivity to a variety of forcings. *Evolution of the Cretaceous Ocean-Climate System*, Geological Society of America, Boulder: Special Paper #332, 445 p.

Leithold, E.L. and Dean, W.E. 1998. Depositional processes and carbon burial on a Turonian prodelta at the margin of the Western Interior Seaway. Stratigraphy and paleoenvironments of the Cretaceous Western Interior Seaway, USA, SEPM: Concepts in Sedimentology and Paleontology, **6**, 189-200.

Lowery, C.M., Corbett, M.J., Leckie, R.M., Watkins, D., Romero, A.M., and Pramudiot, A. 2014. Foraminiferal and nannofossil paleoecology and paleoceanography of the Cenomanian–Turonian Eagle Ford Shale of southern Texas. *Palaeogeography, Palaeoclimatology, Palaeoecology*, **413**, 49-65.

Meyers, S.R., Sageman, B.B., and Lyons, T.W. 2005. Organic carbon burial rate and the molybdenum proxy: Theoretical framework and application to Cenomanian-Turonian oceanic anoxic event 2. *Paleoceanography*, **20**, PA2002. doi:10.1029/2004PA001068.

Meyers, S.R., Siewert, S.E., Singer, B.S., Sageman, B.B., Condon, D.J., Obradovich, J.D., Jicha, B.R., and Sawyer, D.A. 2012. Intercalibration of radioisotopic and astrochronologic time scales for the Cenomanian-Turonian boundary interval, Western Interior Basin, USA. *Geology*, **40**, 7-10.

Moller N.K. and Kvingan, K. 1988. The genesis of nodular limestones in the Ordivician and Silurian of the Oslo Region (Norway). *Seidmentology*, **35**, 405-420.

Pancost, R.D., Freeman, K.H., and Arthur, M.A. 1998. Organic geochemistry of the Cretaceous Western Interior Seaway: a trans-basinal evaluation. Stratigraphy and paleoenvironments of the Cretaceous Western Interior Seaway, USA, SEPM: Concepts in Sedimentology and Paleontology, **6**, 173-188.

Pedersen, T.F. and Calver, S.E. 1990. Anoxia vs. productivity: what controls the formation of organic-carbon-rich sediments and sedimentary rocks? *The American Association of Petroleum Geologists Bulletin*, **74**, 454-466.

Pratt, L.M. 1984. Influence of paleoenvironmental factors on preservation of organic matter in Middle Cretaceous Greenhorn Formation, Pueblo, Colorado. *The American Association of Petroleum Geologists Bulletin*, **9**, 1146-1159.

Sageman, B.B., Meyers, S.R., and Arthur, M.A. 2006. Orbital time scale and new C-isotope record for Cenomanian-Turonian boundary stratotype. *Geology*, **34**, 125-128.

Sageman, B.B., Rich, J., Arthur, M.A., Birchfield, G.E., and Dean, W.E. 1997. Evidence for Milankovitch periodicities in Cenomanian-Turonian lithologic and geochemical cycles, Western Interior U.S.A.. *Journal of Sedimentary Research*, **67**, 286-302.

Sageman, B.B., Rich, J., Arthur, M.A., Dean, W.E., Savrda, C.E., and Bralower, T.J. 1998. Multiple Milankovitch Cycles in the Bridge Creek Limestone (Cenomanian-Turonian), Western Interior Basin. Stratigraphy and paleoenvironments of the Cretaceous Western Interior Seaway, USA, SEPM: Concepts in Sedimentology and Paleontology, **6**,153-171.

Savrda, C.E. 1998. Ichnology of the Bridge Creek Limestone: Evidence for temporal and spatial variations in paleo-oxygenation in the western interior seaway. Stratigraphy and paleoenvironments of the Cretaceous Western Interior Seaway, USA, SEPM: Concepts in Sedimentology and Paleontology, **6**, 127-136.

Savrda, C.E. 1998. Ichnocoenoses in the Niobrara Formaion: Implications for the benthic oxygen histories. Stratigraphy and paleoenvironments of the Cretaceous Western Interior Seaway, USA, SEPM: Concepts in Sedimentology and Paleontology, **6**, SEPM: Concepts in Sedimentology and Paleontology, **6**, 137-151.

Savrda, C.E., and Bottjer, D.J. 1994. Ichnofossils and Ichnofabrics in rhythmically bedded pelagic/hemi-pelagic carbonates: recognition and evaluation of benthic redox and scour cycles. *Special Publications of the International Association of Sedimentologists*, **19**, 195-210.

Schlanger, S.O., and Jenkyns, H.C. 1976. Cretaceous oceanic anoxic events: causes and consequences. *Geologie en Mijnbouw*, **55**, 179-184.

Slingerland , R.L., Kump, L.R, Arthur, M.A., Fawcett, P.J., Sageman, B.B., and Barron, E.J. 1996. Estuarine circulation in the Turonian Western Interior Seaway of North America. *Geological Society of America Bulletin*, **108**, 941-952.

Snow, L.J., Duncan, R.A., and Bralower, T.J. 2005. Trace element abundances in the Rock Canyon Anticline, Pueblo, Colorado, marine sedimentary section and their relationship to Caribbean plateau construction and ocean anoxic event 2. *Paleoceanography*, **20**, PA3005. doi:10.1029/2004PA001093.

Tribovillard, N., Algeo, T.J., Lyons, T., and Riboulleau, A. 2006. Trace metals as paleoredox and paleoproductivity proxies: an update. *Chemical Geology*, **232**, 12-32.

Tyson, R.V. and Pearson, T.H. 1991. Modern and ancient continental shelf anoxia: an overview. *Geological Society, London, Special Publications*, **58**, 1-24. doi:10.1144/GSL.SP.1991.058.01.01.

Watkins, D.K. 1989. Nannoplankton productivity fluctuations and rhythmically-bedded pelagic carbonates of the Greenhorn Limestone (Upper Cretaceous). *Palaeogeography, Palaeoclimatology, Palaeoecology*, **74,** 75-86.

CHAPTER 2: TRACE FOSSILS AND SEDIMENT ACCUMULATION RATES FROM CRETACEOUS WESTERN INTERIOR SEAWAY OUTCROPS EVIDENCE VARIABLE BENTHIC OXYGEN CONDITIONS FOR THE DURATION OF THE OAE II INTERVAL

ABSTRACT

Efforts to understanding the character of benthic oxygen conditions in the Cretaceous Western Interior Seaway (CWIS) during, but dissociated from Oceanic Anoxic Event II (OAE II), has a long, rich history in published literature among stratigraphers, paleontologists, geochemists, and petroleum geologists. These studies have mainly focused on two cores from the deep central axis of the CWIS, leaving paleoenvironmental interpretations for other portions of the seaway not thoroughly explored. The purpose of this study was to address the question concerning special and temporal variation of paleoenvironmental conditions for sites in the CWIS at different depths and proximities to nutrient sources for the duration of OAE II. For this study, the oxygen content of the benthic environment was interpreted using oxygen-related ichnofabrics (ORI) built on the principle that tracemakers have varying oxygen tolerances. Trace fossil data were collected from limestone beds spanning the OAE II interval from 3 cores and 4 outcrops along a West–East transect that stretched from near the western margin into the deep central axis, and towards the eastern margin of the CWIS. Trace fossil interpretations were corroborated by redox-sensitive trace elements.

Limestone and calcareous shale beds comprise the lithology in the CWIS during OAE II-time. These alternating strata represent variations in carbonate deposition controlled by orbitally-forced long-term changes to climate. Variations in benthic oxygen conditions interpreted from ORIs coincide with variations in lithology, which can be explained by differences in detrital

influx from fluviodeltaic sources, or from changes in carbonate productivity in the CWIS as influenced by Tethyan waters and global OAE II conditions.

Overall, ORIs from the limestone beds indicated well-oxygenated benthic conditions throughout the CWIS, with only minor drops in oxygen towards the east, and in the latter portion of the OAE II interval. Some thicker limestone beds also showed that benthic oxygen conditions varied on, perhaps, a precessional scale (P1 = 18.5 ky and P2 = 22.5 ky at ~93.9 Ma). However, detectable cycles in time-series analyses are known to be rather coarse (eccentricity) for the OAE II interval in the CWIS due to competing phases of carbonate dilution and productivity. This lack of resolution adds to the difficulty in determining the role that fine-scale orbitally-forced climatic effects had on the benthic oxygen conditions in the CWIS.

INTRODUCTION AND PREVIOUS WORK

Cretaceous Interior Seaway Paleoenvironment

The Cretaceous Western Interior Seaway (CWIS) may be one of the most studied paleogeographic settings in North America. High levels of organic carbon content, orbitally-forced intercalated packages of calcareous shale and limestone beds, and strata that correlate well over a broad region make the CWIS the prime target for petrological, geochemical, biostratigraphic, cyclostratigraphic, and paleontologic studies (Arthur and Schlanger, 1979; Schlanger and Jenkyns, 1976; Elder, 1988; Elder et al., 1994; Sageman et al., 1997; Meyers et al., 2005; Sageman et al., 2006; Savrda and Bottjer, 1994; Savrda, 1998; Grosskopf, 2015a, this dissertation; and others).

The high concentration of total organic carbon, particularly in the Middle Cretaceous strata of the CWIS, results from a series of globally-expressed Oceanic Anoxic Events (OAE).

OAEs are interpreted as times with no benthic oxygen, leading to excellent preservation of organic carbon (Schlanger and Jenkyns, 1976; Arthur and Schlanger, 1979; Demaison and Moore, 1980; Tyson and Pearson, 1991; Kump and Arthur, 1999). These events are recognized in strata as positive $\delta^{13}C_{organic}$ excursions. $+\delta^{13}C_{organic}$ values preserved in the rock record are due to the global drawdown of atmospheric CO_2 (Kump and Arthur, 1999).

The best-expressed and largest $+\delta^{13}C_{organic}$ excursion found in CWIS strata is from OAE II, spanning the Cenomanian-Turonian Boundary (CTB, 93.9±0.15 Ma [reported by Meyers et al., 2012]), and lasting ~600 ky (Sageman, 2006). OAE II is thought to be the strongest episode of anoxia that ever existed in the Cretaceous, the trigger for which was brought about by an increase in primary productivity due to nutrient input from submarine fissure eruptions from the subaqueous Caribbean Large Igneous Province (CLIP) to the south (Snow et al., 2005; Turgeon and Creaser, 2008). The submarine CLIP, active from 95 to 87 Ma, produced hydrothermal fluids containing trace metals and sulfides. Increased sourcing of the trace metals increased primary production of microorganisms, which used up much of the oxygen during metabolism of organic detritus (Bralower, 2008). Also, dissolved oxygen bound to metals and sulfides further depleting the oxygen in the water column (Pancost et al., 2008). In addition to the CLIP, the High Arctic Large Igneous Province, situated in the Arctic to the east of the northern opening of the CWIS, was active during OAE II-time and may have had similar effects on the CWIS as did the CLIP (Eldrett et al., 2014).

While CWIS strata do preserve the $+\delta^{13}C_{organic}$ excursion, studies indicate that the bottom-waters were not anoxic but dysoxic (2.0 – 0.2 ml of O_2/l of H_2O) conditions in the CWIS (Tyson and Pearson, 1991) during OAE II (Sageman et al., 1997; Pedersen and Calvert, 1990; Keller et al., 2004; Meyers et al., 2005; Grosskopf, 2015a). Fossil inoceramid bivalves are present in every

layer throughout the CWIS where the $+\delta^{13}C_{organic}$ excursion is found. These bivalves would not have been able to live in an environment without any oxygen (Elder, 1989; Sageman and Bina, 1997; Henderson, 2004). Using trace fossils across the CWIS, Savrda and Bottjer (1994), Savrda (1998), and Grosskopf (2015a) showed these benthic environments were oxygenated through the duration of OAE II.

Paleogeography and Stratigraphy

Formation of the CWIS was brought about by one of the greatest sea level highstands of the Cretaceous, combined with a low-lying area to accommodate the additional seawater. Continent–continent convergence of the Farallon and Kula plates with the North American plate caused the Sevier Orogeny, which formed a large retro-arc foreland basin known as the Western Interior Basin (Shurr et al., 1994). Contemporaneous high global temperatures caused climate-driven eustasy and thermal expansion of seawater that led to inundation of the basin (Gale et al., 2002). At maximum transgression of the CWIS, the seaway ran from the Boreal (proto-Arctic Sea) to the Tethys Sea (proto-Gulf of Mexico) making the basin 6,000 km long and 2,000 km wide (Slingerland, 1996; Bowman and Bralower, 2005). The deepest portions were 200–500 m deep (Bowman and Bralower, 2005). The CWIS at maximum transgression is depicted in Figure 2.1 based off Late Cenomanian shorelines reported from Cobban et al. (1994).

The strata composing the Cenomanian–Turonian Global boundary Stratotype Section and Point (CTB GSSP; Site 3 in Figure 2.1), represents the paleogeographic center of the CWIS during OAE II-time (Kennedy et al., 2005). The OAE II interval is in the uppermost Hartland Shale and Bridge Creek Limestone members of the Greenhorn Formation. The base of Bed 63, at the boundary between the Hartland Shale and Bridge Creek Limestone, marks initiation of maximum transgression of the Greenhorn Cyclothem in the CWIS, and the onset of highest

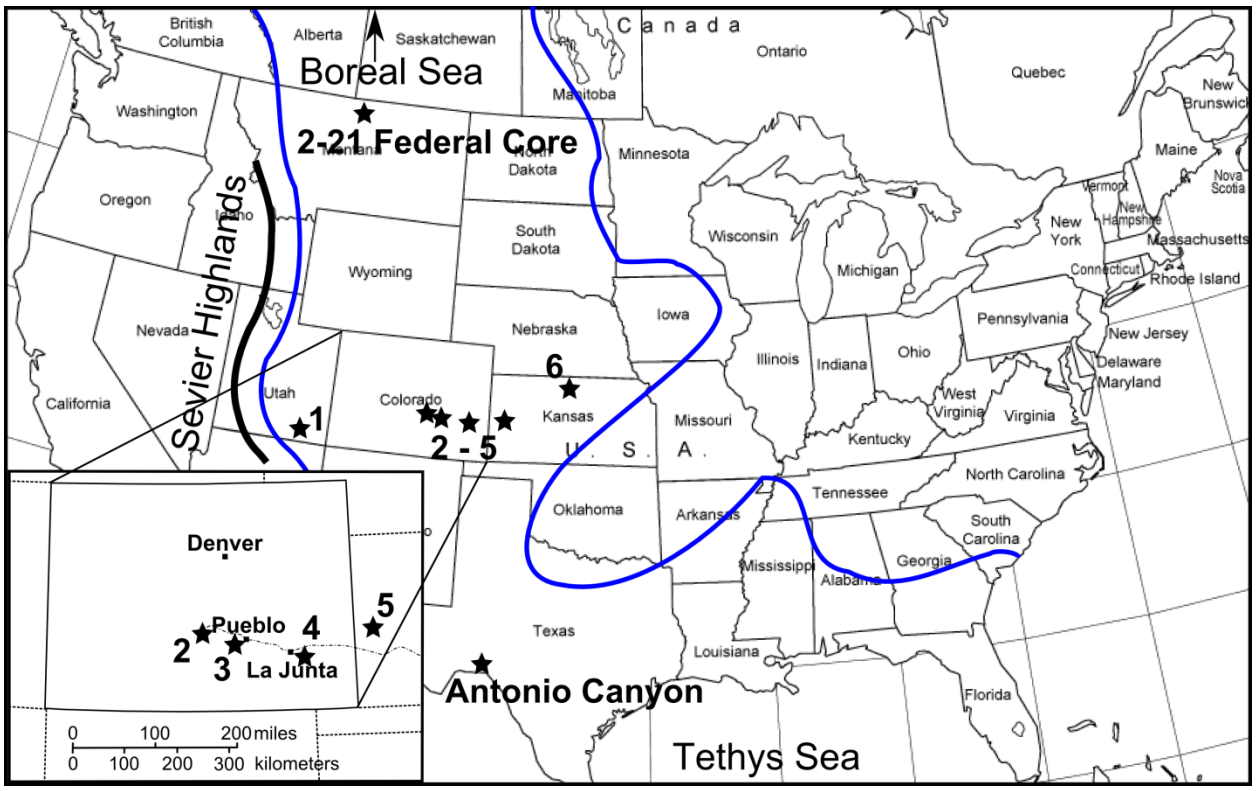

Figure 2.1 Location of field sites and cores along a West–East transect and North–South transect across the Cretaceous Western Interior Seaway (CWIS). Bold blue lines represent the CWIS shoreline at maximum transgression at ~94 Ma; modeled after Cobban et al. (1994) and Slingerland et al. (1996). Stars indicate field or core localities where: 1 – Waheap Wash outcrop outside of Big Water, UT and nearby USGS Escalante core from Garfield County, UT; 2 – USGS Portland core from Florence, CO; 3 – CTB GSSP railroad cut south of Pueblo, CO; 4 – outcrop on Comanche National Grassland southwest of La Junta, CO; 5 – Amoco Bounds core from Greeley County, KS; 6 – US Highway 36 roadcut outside of Cuba, KS; Federal Core, Phillips County, MT; Antonio Canyon – offshoot of Lozier Canyon, near Langtry, TX. Figure modified from Grosskopf (2015a).

$+\delta^{13}C_{organic}$ levels, which is argued by many authors to be the start of OAE II in CWIS strata (Keller et al., 1994; Sageman et al., 1997). These authors maintain that strata representing conditions during OAE II in the CWIS are contained within the Lower Bridge Creek limestone.

This project focuses on the Lower Bridge Creek Limestone and equivalent intervals that represent OAE II-time throughout different portions of the CWIS. Figure 2.2 shows the simplified stratigraphic framework across the basin. The CTB at the GSSP is located at the base

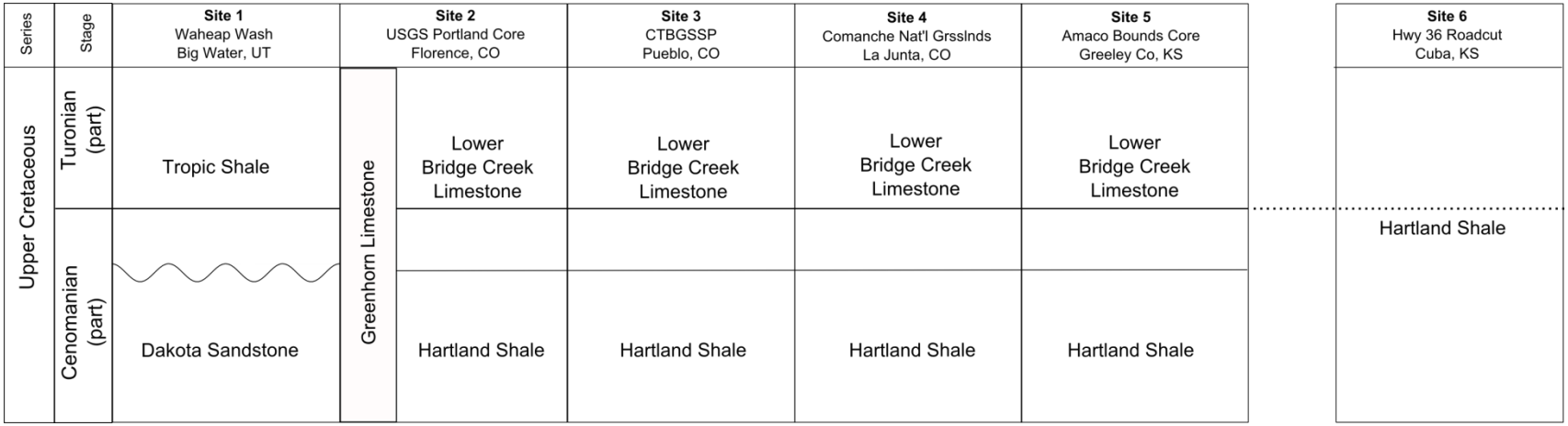

Figure 2.2 Simplified stratigraphic framework for CWIS strata spanning OAE II along West–East transect. Solid line represents where the CTB is known, and dotted line represents in what stratigraphic unit it is found when the exact placement is unknown. Note at Site 1 the Dakota Sandstone is time-equivalent to the Hartland Shale. At Site 6, the name "Hartland Shale" in Central and East Kansas comprises Hartland Shale and Bridge Creek Limestone members due to a facies shift west to east (Hattin, 1975).

of limestone Bed 86. Beds comprising the Bridge Creek Limestone include intercalated dark grey–grey calcareous shales, light grey–white limestones, and thick bentonite marker beds. Calcareous shale and limestone bed intercalations are interpreted as having a decimeter-scale frequency due to long-term orbitally-forced climatic effects (Hattin, 1971, and later, in Fischer, 1980). Sageman et al. (1997) and Sageman et al. (1998) determined that the obliquity cycle (O1 = 39 kyr and O2 = 50.5 kyr, calculated from data presented by Berger et al., [1992] at ~93.9 Ma) is the major cycle responsible for the limestone and calcareous shale bed intercalations in the Bridge Creek Limestone, while other Milankovitch Cycles are detected. Fischer (1980) postulated that the bed intercalations must have been effects from carbonate dilution or productivity that were controlled by long-term cyclic changes to atmospheric and oceanic conditions. The dilution model maintains that deposition of calcareous shale beds coincide with wetter periods. Wetter periods in the CWIS would increase terrigenous flux into the basin from the Sevier Highlands to the west (Figure 2.1). The sediment- and nutrient-rich freshwater would form a capping layer on top of the denser, more saline CWIS seawater, and water stratification would be established in the CWIS. Pratt (1984) explains that the stratified water column would drop benthic oxygen concentrations into dysoxic–anoxic state, which would allow for organic matter to be preserved in the oxygen-limiting conditions. For drier periods, lack of terrigenous input into the basin allowed for vertical mixing in the water column, which increase carbonate deposition, and little organic carbon to be preservedThe productivity model maintains that Tethyan seawater is responsible for limestone and shale bed couplets in the CWIS. Eicher and Diner (1989) explain that the Tethys Sea is susceptible to global effects on in sea level, and atmospheric and ocean chemistry, and these fluctuations manifest as the intercalated Bridge Creek Limestone beds. Carbonate production occurs when there are incursions of carbonate-rich

Tethyan waters into the CWIS causing vertical mixing in the water column, which also contributes large quantities of biogenic carbonate as a consequence of primary productivity due to water mixing.

Bioturbation: Trace fossils as benthic oxygen indicators

Trace fossils are remnants of ancient organisms' behavior, making those that are sensitive to changing benthic oxygen conditions good indicators of bottom-water conditions (Bromley and Ekdale, 1984). Characteristics of trace maker assemblages that vary due to changes in oxygen levels include burrow diameter, burrow depth, diversity of traces, and concentration of traces (Savrda and Bottjer, 1994; Savrda, 2007). Categorizing and comparing these parameters in trace fossil fabrics in order to track changes to the benthic environments is the concept behind oxygen-related ichnofabrics (ORIs) (Savrda and Bottjer, 1994; Savrda, 1998; Savrda, 1998b, Savrda, 2007).

Trace fossils observed in rocks are concentrated in what is referred to as the "historical layer", which later becomes preserved in the rock record. Above the historical layer lies a "mixed layer" where all surface-dwelling and shallowly-burrowing organisms reside and rework sediment (Savrda, 2007). The larger the trace and the higher the concentration of traces, the more the historical layer is bioturbated. The "transition layer" describes the bioturbation of the historical layer from trace makers living in the mixed layer, and is often tiered due to oxygen being the limiting factor as burrow depth into the substrate increases. Overall, thickness of the transition layer decreases as oxygen decreases, and this is evidenced in strata as a transition from more complex to simpler ORIs (Savrda, 2007).

Composition of the strata in the CWIS indicates that the substrate was limey mud with alternating amounts of mud or lime in each bed. For the most part, trace makers do not prefer one type of sediment over the other (Savrda, 2007). Therefore, traces span both calcareous shale and limestone beds, and very little bias in ORIs is brought about by substrate variation. However, type of substrate can control interstitial (pore-water) oxygen concentrations, which may affect ORIs (Savrda, 2007).

Chondrites, *Planolites*, *Taenidium*, *Zoophycus*, *Thalassinoides*, and *Teichichnus* trace fossils are found throughout the CWIS in strata spanning OAE II time. Each of the trace makers responsible for these traces has a varying level of oxygen tolerance (Figure 2.3). Figure 2.3 outlines the parameters used to categorize a bed containing these trace fossils, including burrow diameter and diversity. From ORI 1 to ORI 4, benthic oxygen increases as evidenced by increasing burrow diameter and diversity (Savrda and Bottjer, 1994; Savrda, 1998). Data that depict temporal variations in sediment accumulation rates (SAR), identified using time-series analyses, when used in conjunction with ORI data, allows rates of change in benthic oxygen conditions to be traced through time (Sageman et al., 1997; Sageman et al., 1998; Sageman et al., 2006).

Purpose and approach

The purpose of this work was to better understand benthic oxygen conditions during OAE II throughout the CWIS by analyzing trace fossil fabrics, whose presence already indicates that benthic oxygen was present in CWIS strata during OAE II time. Additionally, understanding

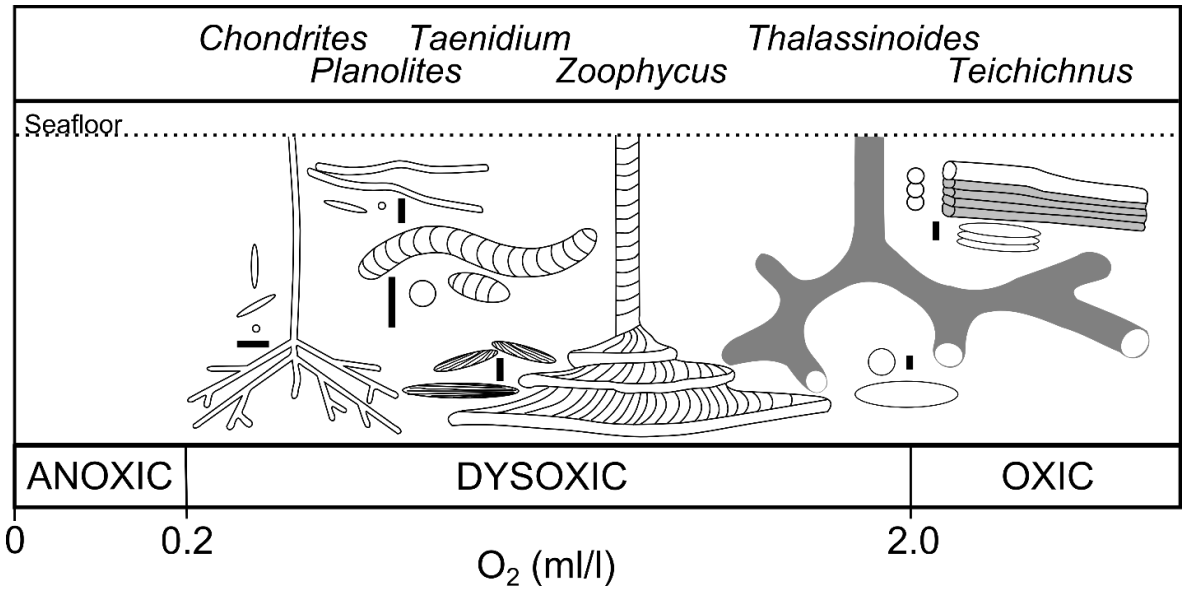

ORI Zone	Traces Present	Diversity (relative)	Burrow Diameter (mm)	Oxygen Content
ORI Zone 1	*Chondrites* *Planolites*	Lowest	2 – 6 range; 3 – 4 average	**Lowest**
ORI Zone 2	*Chondrites* *Planolites* *Taenidium* *Zoophycus*	Medium	3 – 8 range; 4 – 5 average	**Low**
ORI Zone 3	Same as ORI Zone 2	Medium	6 – 10 range; 8 average	**Medium**
ORI Zone 4	Same as ORI zone 3 *Thalassonoides* *Teichichnus*	High	8 – 20 range; 12 average	**High**

Figure 2.3 Trace fossils and how they appear in cuttings and their corresponding oxygen-related ichnofabric (ORI) ranks. Black scale bars represent 1 cm for each trace fossil type. Descriptions: *Chondrites* – feeding/dwelling behavior; a complex system of small branching tunnels with uniform diameter; positioned vertically in substrate. *Planolites* – deposit-feeding trace; unbranched, straight, or curved cylindrical burrows; positioned horizontally to sub-horizontally in substrate. *Taenidium* – deposit-feeding trace; cylindrical burrows with marked miniscate backfill; positioned horizontally or vertically in the substrate. *Zoophycus* – complex feeding/dwelling spreiten structure (corkscrew) with shallowly inclined horizontal structures that have chevron-shaped surfaces on and meniscate lamination within the trace. *Thalassonoides* – feeding/dwelling structure of crustaceans; relatively large unlined burrows linked in a 3D branching network. *Teichichnus* – feeding/dwelling structure; series of stacked longitudinally-nested tubes that are spreiten in shape; positioned vertically or horizontally in substrate (Savrda, 1998). Oxygen Related Ichnofabrics (ORIs) 1 – 4 and how they indicate benthic oxygen content in relation to the trace fossils present, diversity of traces present, burrow diameter, and burrow depth.

how these fabrics change due to changing oxygen conditions through time in different parts of the basin is explored. It is argued here that changes to ORIs during OAE II track bimodal variations in benthic oxygen between moderate-to-low oxygen and oxic (>2.0 ml of O_2/l of H_2O) conditions on an obliquity and precessional time-scales. This is because the changes in ORIs are related to long-term changes in climate, and therefore related to fluviodeltaic nutrient input into the basin from the margins of the CWIS (dilution model) with some aspects of carbonate productivity in other parts of the basin, at least in the early stages of the OAE II interval.

Another aspect of this work is focused on an outcrop-derived means of paleoenvironmental data collection. This is important to CWIS research in that it adds localities to the key reference cores from the Cretaceous Western Interior Seaway Drilling Project from Dean and Arthur (1998), increasing resolution of sites and data, which can firmly establish predictions on CWIS paleoenvironmental characteristics throughout more of the basin.

With the incorporation of two cores (Portland Core and Bounds Core) from a previous study by Savrda (1998), the Escalante Core, and four outcrops along a West–East transect spanning from Waheap Wash, UT, to Cuba, KS, bottom-water conditions eclipsing OAE II in the CWIS were interpreted using oxygen-related trace fossil fabrics as oxygen indicators.

METHODS

Tracking benthic oxygen conditions temporally and spatially from outcrop and core in CWIS strata representing OAE II-time requires a variety of stratigraphic, geophysical, ichnologic, and geochemical techniques. The main focus of this study covers correlatable limestone beds from six sites: four outcrops (Sites 1, 3, 4, 6) and three cores (Site 1, 2, 5) along a West–East transect across the CWIS (Figure 2.1). The West–East transect stretches from near the

western paleoshoreline at Site 1, through the deep central axis of the basin at Site 3, to near the eastern paleoshoreline at Site 6 (Figure 2.1). All correlations are tied to the CTB GSSP, where the limestone beds are well-defined. Bed names at each site are referred by their correlated equivalent at the CTB GSSP.

Magnetic Susceptibility

Low-field, bulk mass-specific magnetic susceptibility (χ) is a geophysical technique where a magnetic field is induced in a rock sample, and the resulting induced magnetism of the sample (χ) corresponds to the concentration of paramagnetic, diamagnetic, and ferrimagnetic materials in that sample. Paramagnetic materials, such as clays, acquire a low, positive induced magnetism in the presence of an applied magnetic field, which returns to zero once the inducing field is removed. Diamagnetic materials, such as quartz and calcite, acquire a very low, negative induced magnetism in the presence of an inducing magnetic field. Ferrimagnetic materials, such as magnetite, can overpower the weaker paramagnetic and diamagnetic materials, but in marine sediments, these are usually destroyed by sulfate-reducers (Karlin and Levi, 1983; Karlin and Levi, 1985; Ellwood et al., 2000; Ellwood et al., 2006; Ellwood et al., 2008). In the very low alternating magnetic fields of the Williams Magnetic Susceptibility Bridge at Louisiana State University, single-domain and pseudo-single domain ferrimagnetic grains will not acquire a magnetization and therefore do not affect the induced magnetization of a sample where there is a high concentration of such grains (Ellwood et al., 2006). An excessive amount of multi-domain ferrimagnetic components, beyond natural concentrations, would need to be present in a sample for χ levels to be beyond those for marine rocks, which range from $1x10^{-09}$–$1x10^{-07}$ (Ellwood et al., 2000).

Typically, strata or rocks derived from a terrigenous source have higher χ levels than pelagic crystalline rocks, like limestones, due to the higher concentration of paramagnetic and ferrimagnetic minerals present. This basic principle makes χ a useful parameter in correlation, cyclostratigraphy, and reconstructing past depositional environments (Ellwood et al., 2006; Ellwood et al., 2008; Ellwood et al., 2013).

Using χ for correlation and cyclostratigraphy requires that samples are taken at short, regular intervals in order to have high enough resolution to detect small-scale changes in terrigenous input due to orbitally-forced long-term climatic effects. Regarding deposition, changes in χ at one location over time can lead to interpretation of small-scale changes in proximity to source or source flux over time (Ellwood et al., 2006). It is thought that precessional, obliquity, and eccentricity Milankovitch Cycles mainly influence the processes that cause changes in source proximity (via sea-level change) and flux (via climate change) in the CWIS (Sageman et al., 1997; Sageman et al., 2006). For correlation, unique patterns in χ variation among sections, along with well-known marker beds and the geological and geochemical interpretation, aids in matching coeval climate-driven depositional events between separate sections, even from unrelated facies.

Additionally, χ aids in calculating SAR for sampled sections with a known thickness and detectable periodicity (Ellwood, 2008). χ sampled at fixed intervals combined with time-series analyses, such as the multitaper method (MTM), leads to detection of statistically-significant recurring patterns, which, using the known thickness for the measured section, can be extrapolated to cycles per meter. This, combined with the estimated Milankovitch periodicity at the time, allows for calculation of the SAR for a section.

Site 1 (outcrop; Figure 2.1) χ samples were collected from near the base of the Tropic Shale to the Bed 80 bentonite at 0.10 m intervals. Site 2 (Figure 2.1) samples were collected from core (Ellwood et al., 2008), at ~0.05 m intervals; only measurements from the base of Bed 63 through the Bed 89 bentonite are reported here. Site 3 (Figure 2.1) χ values were reported by Ellwood et al. (2008) and only those from the base of Bed 63 through the top of Bed 86 at 0.05 m intervals were used. Site 4 (Figure 2.1) χ values span from the base of Bed 63 to the Bed 89 bentonite at a 0.05 m sampling frequency. Site 5 (Figure 2.1) χ values were derived using a portable Bartington Magnetic Susceptibility Probe on site in the USGS Core Research Center in Denver, CO, where the core was measured every 0.05 m from the base of Bed 63 to the top of the Bed 89 bentonite. Site 6 (Figure 2.1) χ was sampled every 0.05 m starting at the base of the Bed 63 limestone bed up through the top of the Hartland Shale [coeval with the Bridge Creek Limestone in Eastern Kansas stratigraphy (see Figure 2.2); Hattin (1975)].

All samples for which χ was measured were crushed, to remove magnetic anisotropic effects, and 0.01 kg was placed in small plastic sample bags for measurement. All χ readings were taken using the mass-dependent Williams Magnetic Susceptibility Bridge at Louisiana State University. χ was calculated using mass and the average of three χ readings. For Site 5, non-invasive χ sampling had to be performed in order to keep the core intact. This was accomplished using the Bartington Probe. Unfortunately, values produced by the Bartington Probe were too low for adequate time-series analysis of the core. For the Site 1 Escalante Core, χ sampling was attempted at regular intervals using a Dremel tool on the back, rounded side of the working half of the core. The powder that was collected at semi-regular intervals was placed in a metal container that was passed over a magnet in order to remove any metal contaminants from

the Dremel tool or drill bit when the core was drilled. This was repeated three times per each sample. Poor data resulted from this technique as well.

Gamma-ray readings

Field gamma ray spectroscopy (GRS) data were acquired using a portable gamma ray spectrometer (RS-125 Super Gamma-Ray Spectrometer). The instrument detects the amount of ^{40}K in a sample and uses daughter proxies to determine U and Th isotope concentrations. Similar to interpretations using χ, high concentrations of ^{40}K, U, and Th, indicate higher levels of terrigenous material, mainly because of the high amounts of ^{40}K in detrital components from continents. (Keller, 1994; Ellwood, 2008).

The RS-125 Gamma-Ray Spectrometer uses a NaI crystal to detect ^{40}K levels across a volume of about 1 m^3 (Radiation Solutions Inc., 2010). There is significant overlap when sampling is taken at short intervals using this device, and any curve constructed from these data is dampened due to averaging of the signal. Even so, this is a good tool for correlation, because it captures peaks and troughs that can be correlated to other sections and datasets. It was determined that sampling every 0.10 m was the best collection method for gathering these data from the decimeter-scale strata.

For this study, sampling interval at Sites 3, 4, and 6 was every 0.10 m over the same measured section used for sampling for χ. The instrument measurement time was 120 s. Reported GRS readings for core are public domain well-log GRS data (in API units) from the Western Interior Seaway Drilling Project and project website (Dean and Arthur, 1998). These were used in place of the field GRS readings from the field instrument.

Site 1 well-log GRS data span from the base of the Tropic Shale (lower Bridge Creek Limestone equivalent) to Bed 80 bentonite, Bentonite B, and were sampled at ~0.06 m intervals. Site 2 well-log GRS values were derived from core at every ~0.06 m from the base of Bed 63 through Bed 89 bentonite, Bentonite C. Site 3 field GRS values were measured from the base of Bed 63 through the top of Bed 86 and were sampled at ~0.10 m intervals; Bed 89 bentonite values were not recorded (Ellwood et al., 2008). Site 4 field GRS values reported span from the base of Bed 63 to Bed 89 bentonite at a 0.10 m sampling frequency. Site 5 well-log GRS spans from the base of Bed 63 to Bed 89 bentonite, and is sampled every ~ 0.06 m. Site 6 field GRS values were sampled every 0.10 m starting at the base of Bed 63 through the top of the Hartland Shale.

Time-series Analysis

Time-series analysis is used in cyclostratigraphy to determine SARs in the rock record. MTM and Fourier transform (FT) are useful tools for finding trends in continuous datasets where cycles are assumed to occur. MTM and FT use χ datasets, where Milankovitch Cyclicity is assumed to be the major influence on trends in concentrations of paramagnetic or ferrimagnetic versus diamagnetic materials. These cycles can be detected if the section represents relatively continuous marine sedimentation and the section is sampled at regular intervals in order to track time (Ellwood, 2012).

The kSpectra Toolkit software (spectraworks.com) was used for the MTM analyses, producing significant recurring trends in detrended χ data as peaks reaching above 90, 95, and 99% confidence levels. The frequency of these trends is reported in cycles/meter on the x-axis. These results can be crosschecked with FT results (calculated using Matlab), and with real

variations observed in strata and χ data to determine a strong match between MTM, FT, and obvious trends in the dataset from the lithology.

Trace Fossil Data

For trace fossil observations at each outcrop, blocks 0.10 m^3 or larger were cut, using a portable cement saw, from limestone beds representing OAE II-time (beds 63, 67, 79, 84, 86, and 88). Blocks were extracted, labeled, oriented, and securely wrapped for transport. Later, in the lab, blocks were cut with an oil or water-saw and photographed. Identification of traces present and measurements of maximum diameter and trace density were taken every 0.02 m on the flat, slabbed surface of each limestone block. For Portland and Bounds cores (Sites 2 and 5, respectively), Savrda's (1998) trace fossil data were used (collected every 0.05 m). Trace fossil data from the Escalante Core were collected in place of incomplete field collections from Waheap Wash at Site 1.

Geochemistry Data

Redox-sensitive trace elements act as a proxy for determining benthic oxygen levels in that they track the oxygen availability in the water column and below the sediment–water interface whereby measured enrichments of these elements indicate oxygen-limiting conditions (Tribovillard, 2006). Uranium is a useful trace element for determining if benthic oxygen changes were detritally-derived or derived through organic matter production under anoxic or euxinic conditions (Tribollivard, 2006). If U is in low abundance and there is weak correlation between U and organic carbon content then it can be assumed that U was derived from terrigenous sources and not authigenically. If, however U correlates well with organic carbon content, then it can be assumed U was enriched from organic matter accumulation under anoxic

conditions (Tribovillard, 2006). U concentrations are used in this manner to corroborate trace fossil interpretations.

The U concentration data used as a proxy for benthic oxygen conditions are from geochemical analyses reported in Ellwood et al. (2008) for the CTB GSSP. Those samples were analyzed by Chemostrat Ltd. They were ground to a powder in a ball mill and, following Li-metaborate fusion, analyzed using inductively-coupled plasma optical emission spectrometry (ICP-OES) and mass spectrometry (ICP-MS). The analytical methods resulted in U abundance readings from the samples reported as parts per million by weight (ppm). Precision errors for the U concentrations were around 3% for the ICP-OES (Ba, Cr, Sc, Sr, Zn and Zr). The U abundances determined from the ICP-MS were generally less precise, with precision error in the order of ± 3 to 7 ppm for the trace element, depending on abundance. Expanded uncertainty values (95% confidence) which incorporate all likely errors within a statistical framework were derived from 11 batches of 5 certified reference materials (CRMs), each prepared in duplicate, are typically 7-12% (relative) for trace elements.

U concentrations can be compared to concentrations found in limestone and marine shale rocks deposited in oxic settings. Enrichments of U in limestone and shales reported from previous work were plotted with U data and calcium carbonate ($CaCO_3$) content in rocks sampled from the CTB GSSP. $CaCO_3$ concentrations were measured for selected samples from the CTB GSSP section that corresponded with a U reading (n=50). The vacuum-gasometric technique of Jones and Kaiteris (1983) was performed in the LSU Rock Magnetism Laboratory. A ~0.5 g rock sample was ground to a fine powder, and then dried for 1.5 hours on a hotplate at 40°C. A 0.25 g sub-sample was then reacted with phosphoric acid for 1.5 hours under a vacuum in a glass reaction vessel. After complete reaction, the pressure difference was then read from a

digital pressure gauge and used to calculate the sample carbonate concentration from a calibration equation.

RESULTS AND DISCUSSION

χ, field, and well-log GRS curves correlate well at the CTB GSSP (first reported in Ellwood et al., 2008). Bentonites register strong positive shifts in both datasets, while thick limestone beds represent smoother negative shifts. Calcareous shales register as positive signal plateaus. Figure 2.4a shows the correlation between χ and field GRS values and two bentonite marker beds, Beds 69 (Bentonite A) and 80, at the CTB GSSP (Site 3). % $CaCO_3$ is reported alongside the CTB GSSP lith-log in Figure 2.4b. Both limestone and calcareous shale beds had high $CaCO_3$ content, ranging from 50–90% $CaCO_3$. Large deviations from this range were consistent with bentonite beds (little-to-no $CaCO_3$). These values are reported every ~0.1 m. The % $CaCO_3$ coincides well with χ and field GRS data curves regarding terrigenous input, where a greater % $CaCO_3$ correlates with less clay input, and in turn, lower χ and field GRS values.

Figure 2.5 represents the correlation of signal peaks of χ values for each site across the West–East transect from Utah to Kansas. As with Site 3 χ values, sites along the West–East transect display abrupt positive shifts due to bentonite beds. The same trends from the CTB GSSP χ values exist in other sites along the West–East transect with thick limestone beds and calcareous shales being represented by shifts to low levels and variable plateaus, respectively.

Figure 2.6 represents the correlation of field and well-log GRS signal peaks from outcrop and core among sites 1 – 6 along the West–East transect. Well-log GRS readings from sites 1, 2, and 5 are from public domain data from the Western Interior Seaway Drilling Project and USGS Core Research Center websites (Dean and Arthur, 1998). χ, and field and well-log GRS curves

exhibit the same trends for bentonite, limestone, and calcareous shale beds among sites across the West–East transect. One notable trend in field and well log GRS values at each site is that the

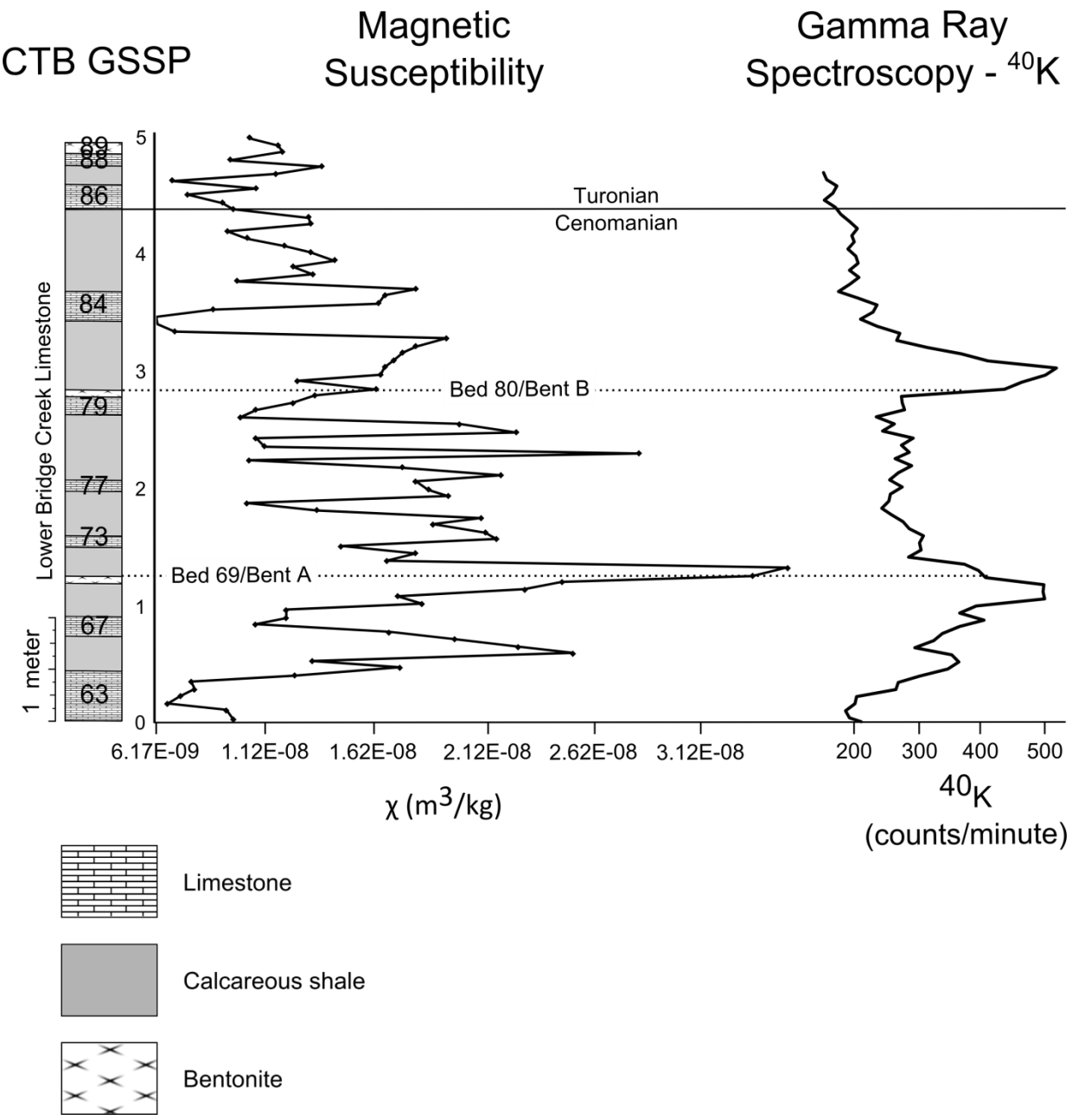

Figure 2.4a Correlation between χ and GRS datasets along with lithology at the CTB GSSP (Site 3, Figure 2.1).

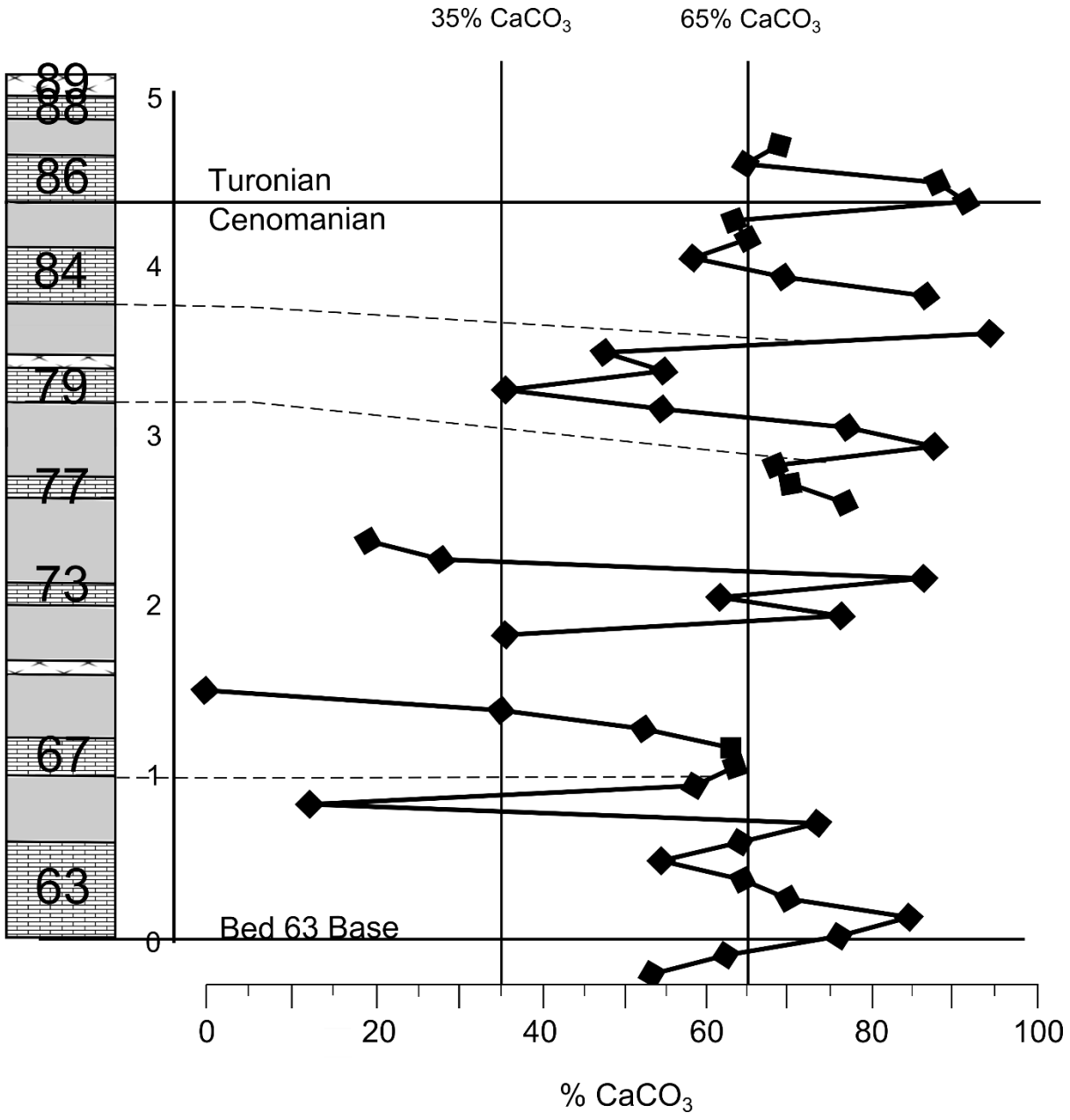

Figure 2.4b Correlation between lithology at the CTB and corresponding % calcium carbonate ($CaCO_3$) levels. With vertical lines at 35% $CaCO_3$ and 65% $CaCO_3$ representing the range of values for $CaCO_3$ versus clay content for marls. Dashed horizontal lines show correlations between limestone beds and $CaCO_3$ content. Lith-log is slightly modified to better match measurements from Ellwood et al. (2008).

highest values lie between Bed 69 – Bed 80 bentonites. There is a weak trend in these values, increasing toward the east along the transect.

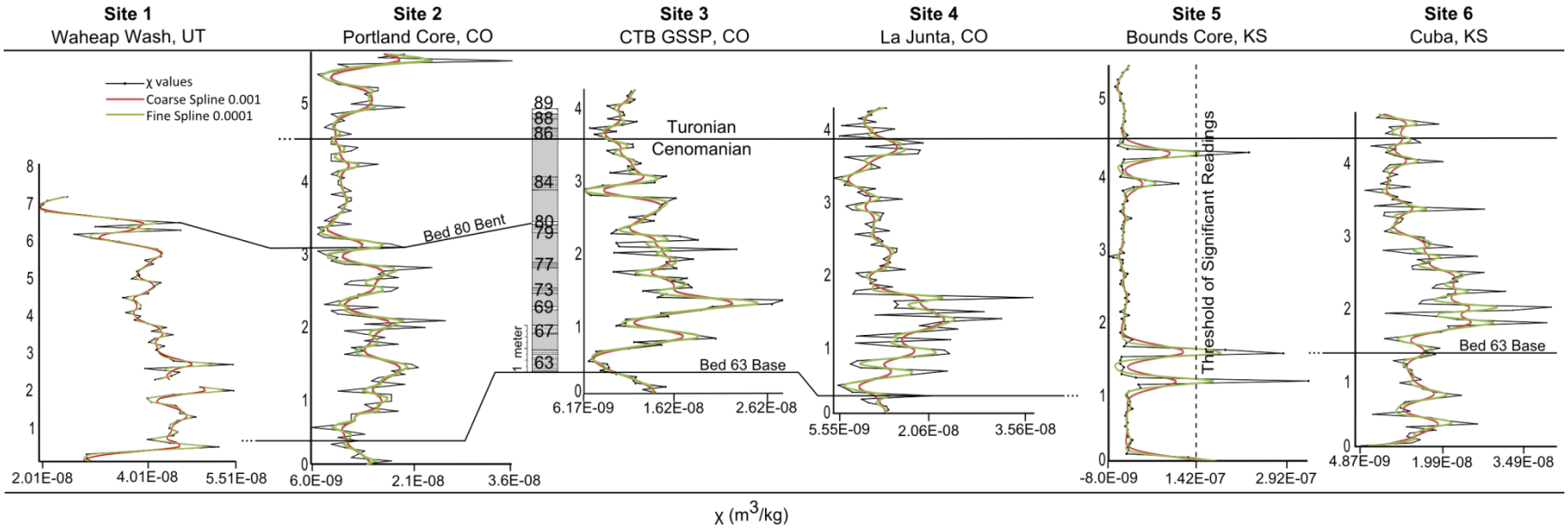

Figure 2.5 Correlation of χ data for sites 1 – 6 relative to the CTB. Curves are lengths of sections scaled to the CTB GSSP (Site 3), with 1 m being the same for each section, with the exception that Site 1 is plotted at 0.5 m scale. The base of Bed 63 for each section is represented by the correlation line. Site 1 is tied to the Portland Core and CTB GSSP sections by the bentonite Bed 80 (Bentonite B, reported in Elder, 1988). Sampling intervals for each section are listed in the methods.

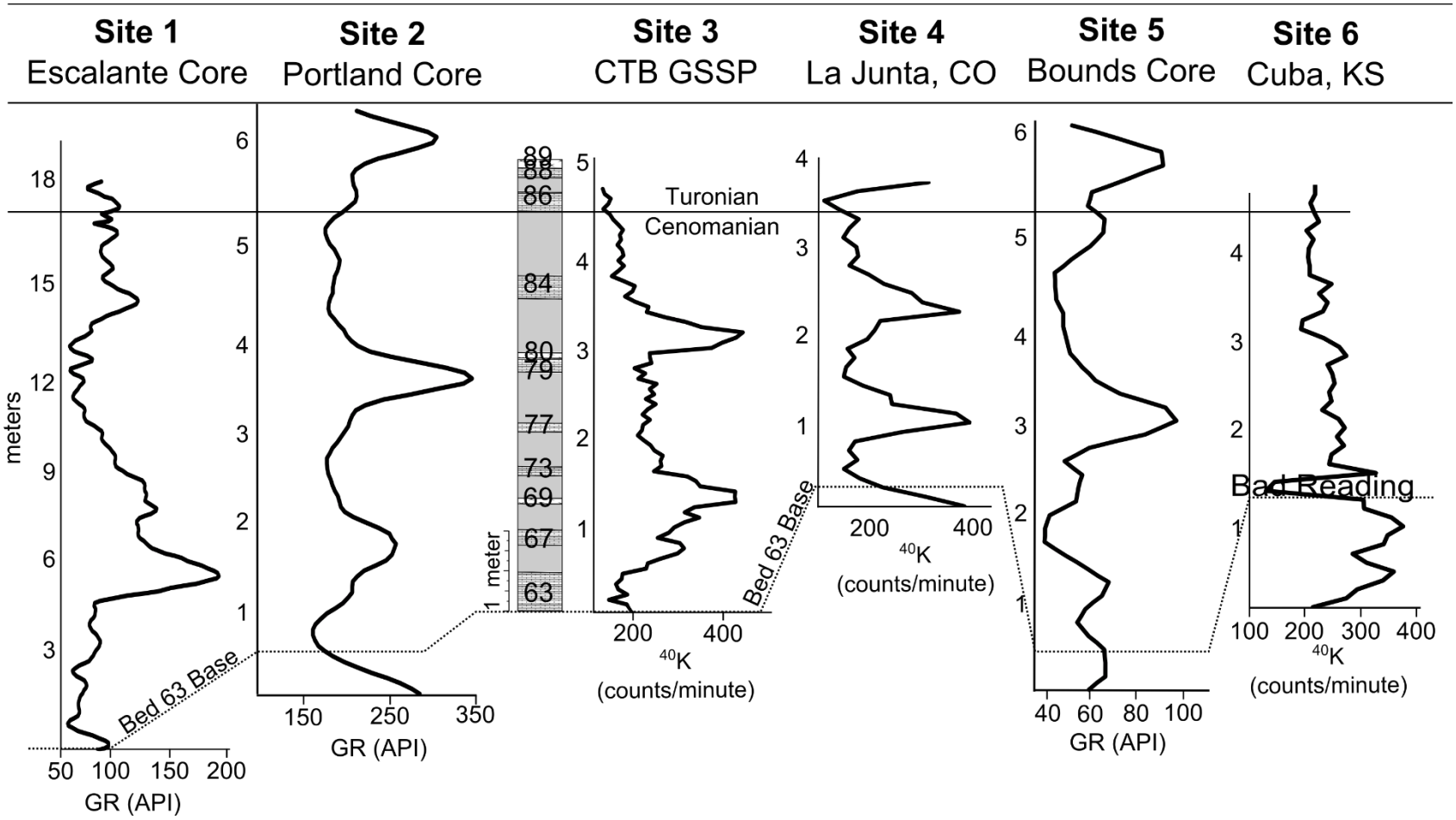

Figure 2.6 Correlation of field and well-log GRS data for sites 1 – 6, relative to the CTB. Curves are actual lengths of sections when scaled to the CTB GSSP (Site 3), with 1 m being the same for each section, with the exception of Site 1 at 0.5 m scale. The base of Bed 63 for each section is represented by the dotted correlation line. Sampling intervals for each section are listed in the methods.

The well-defined, easily-correlatable χ, field and well-log GRS signal peaks allow for the correlation of key limestone beds in CWIS strata among the six sites (Figures 2.5–2.6). In Figure 2.7, the Site 1 column is expressed at half the scale of the other sites due to extended thickness of the section. Beds at the CTB GSSP (Site 3) are labeled and the correlation lines bounding each bed represent the spatial tracing of that bed across the CWIS West–East transect. Thickness of the section representing OAE II across the West–East transect decreases eastward, with easternmost Site 6 being the most condensed section. Photographs highlighting some of these correlatable horizons among outcrops are shown in Figure 2.8.

Figure 2.9 represents the relationship between correlative limestone beds with respect to maximum burrow diameter and ORI, where ORI (represented by a line or dot; Figure 2.9) is the combination of traces present, trace density count per 0.02 m^2, and maximum burrow diameter. ORI categorization establishes an interpreted oxygen curve for that bed. While the beds may actually have different thicknesses, they are represented here as having the same thickness in order to easily depict changes in benthic oxygen through the section and across the basin. Maximum burrow diameter data for sites 1, 3, 4, and 6, as well as ORI interpretations were taken every 0.02 m. For sites 2 and 5 (Portland and Bounds Cores, respectively), maximum burrow diameter data and ORI interpretations were given at 0.05 m intervals by Savrda (1998). Bed numbers are listed on all Site 3 beds, and those at the same level at the other sites represent the same bed (Figure 2.9) These data demonstrate that most of the thick limestone beds from each site have variable ORIs on a 0.02 m scale. Sites 1, 2, 5, and 6 show a strong trend, where maximum burrow diameter and ORI drop moving up-section, while Sites 3 and 4 show no trend among limestone bed ORIs throughout the section. The thick limestone beds, especially Bed 63,

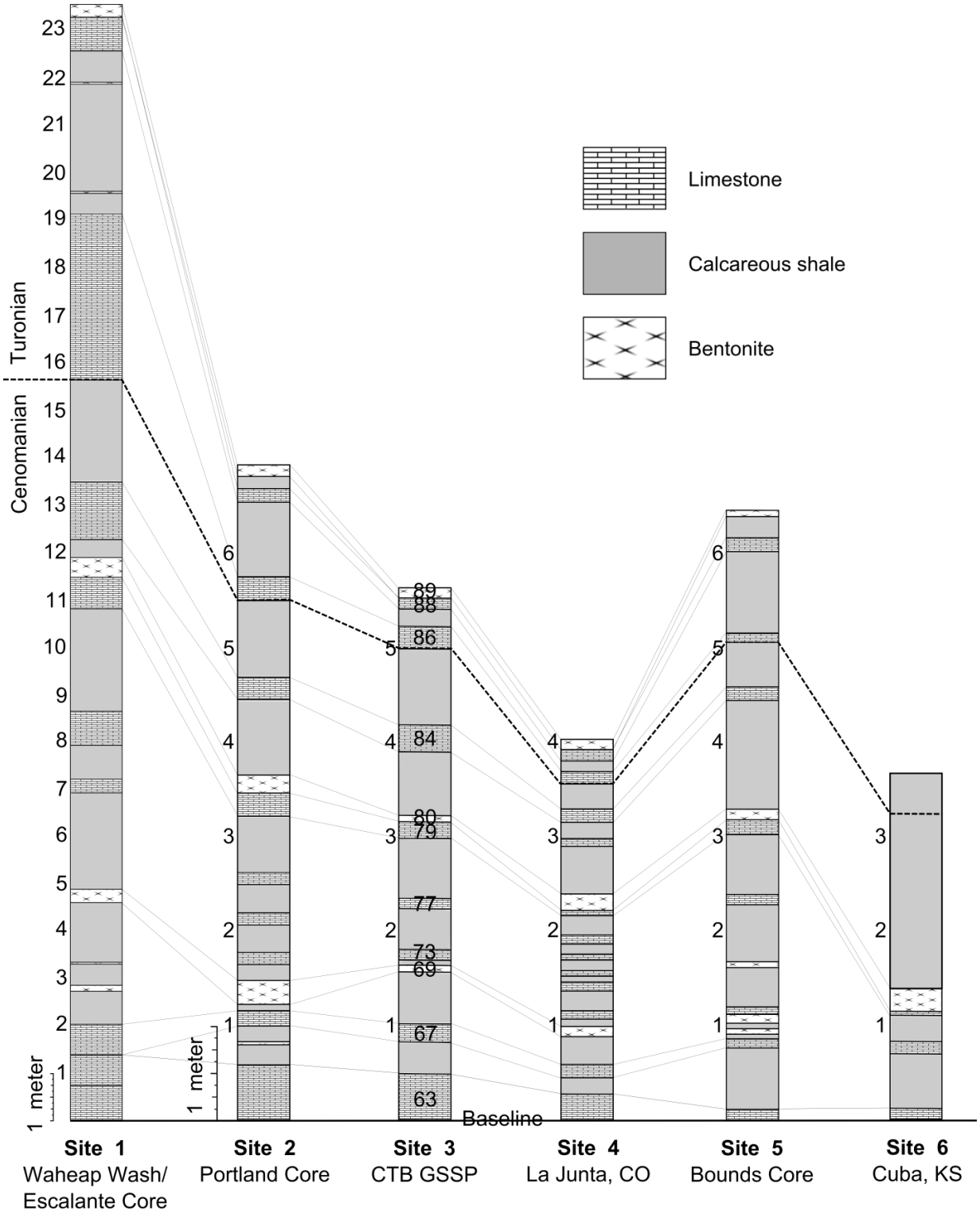

Figure 2.7 Lithologic correlation of sites 1 – 6. Escalante Core descriptions from the USGS Core Research Center in Denver, CO, are used to complete the Site 1 (Waheap Wash, Big Water, UT) outcrop lithology. The CTB at Site 6 was placed using results from graphic comparison, discussed later in the text.

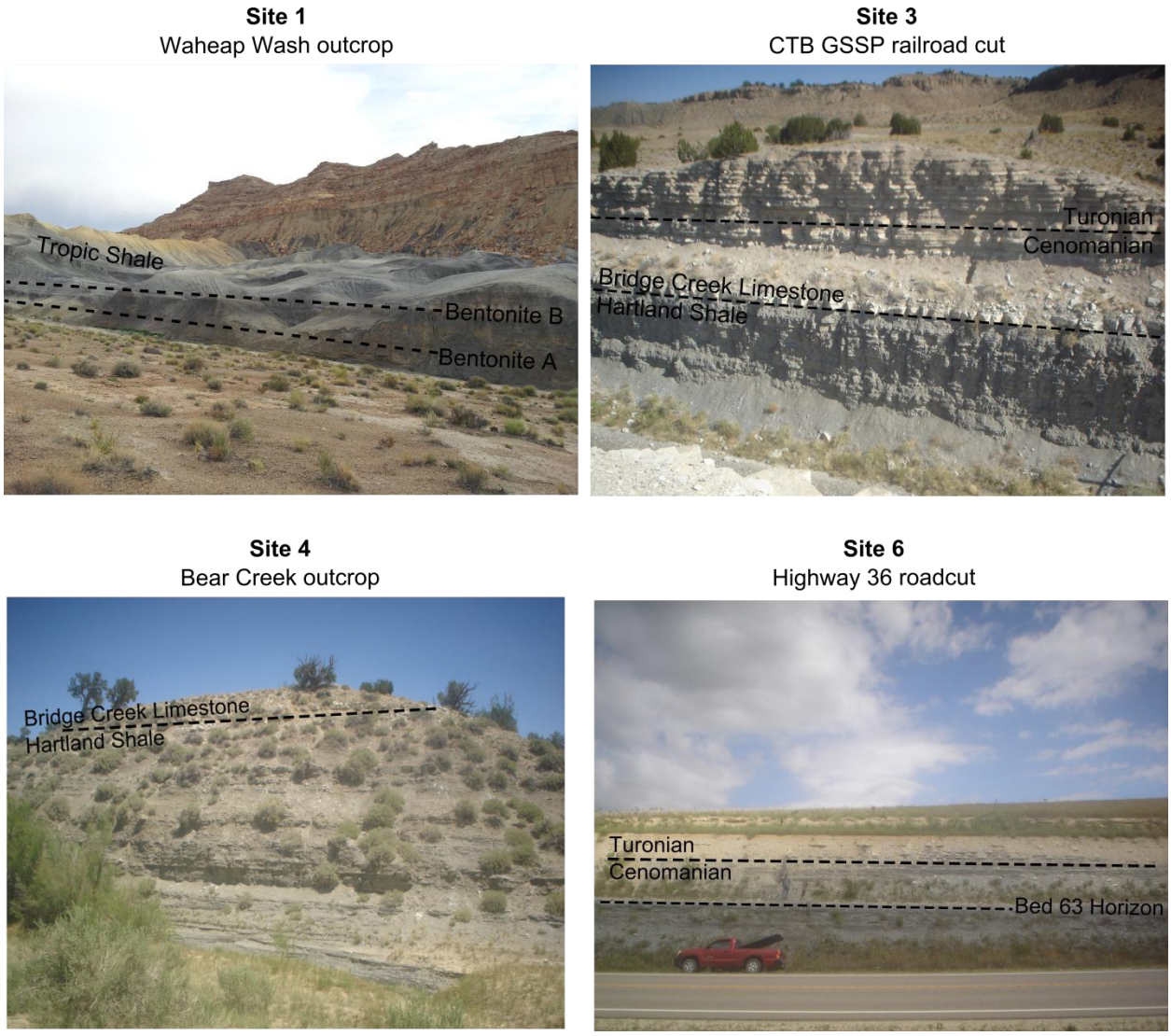

Figure 2.8 Annotated field photographs showing correlative horizons. Photographs by J. Grosskopf.

exhibit variability in the ORI spanning the entire thickness of the bed. The basal limestone bed, Bed 63, shows little-to- no change in ORI between Site 1 in the west and Site 6 in the east. However, beds near the top of the section, such as beds 79, 84, and 86 drop in ORI values, west to east, from ORI 4 to ORI 1, but values never drop to anoxic levels, as traces are still present.

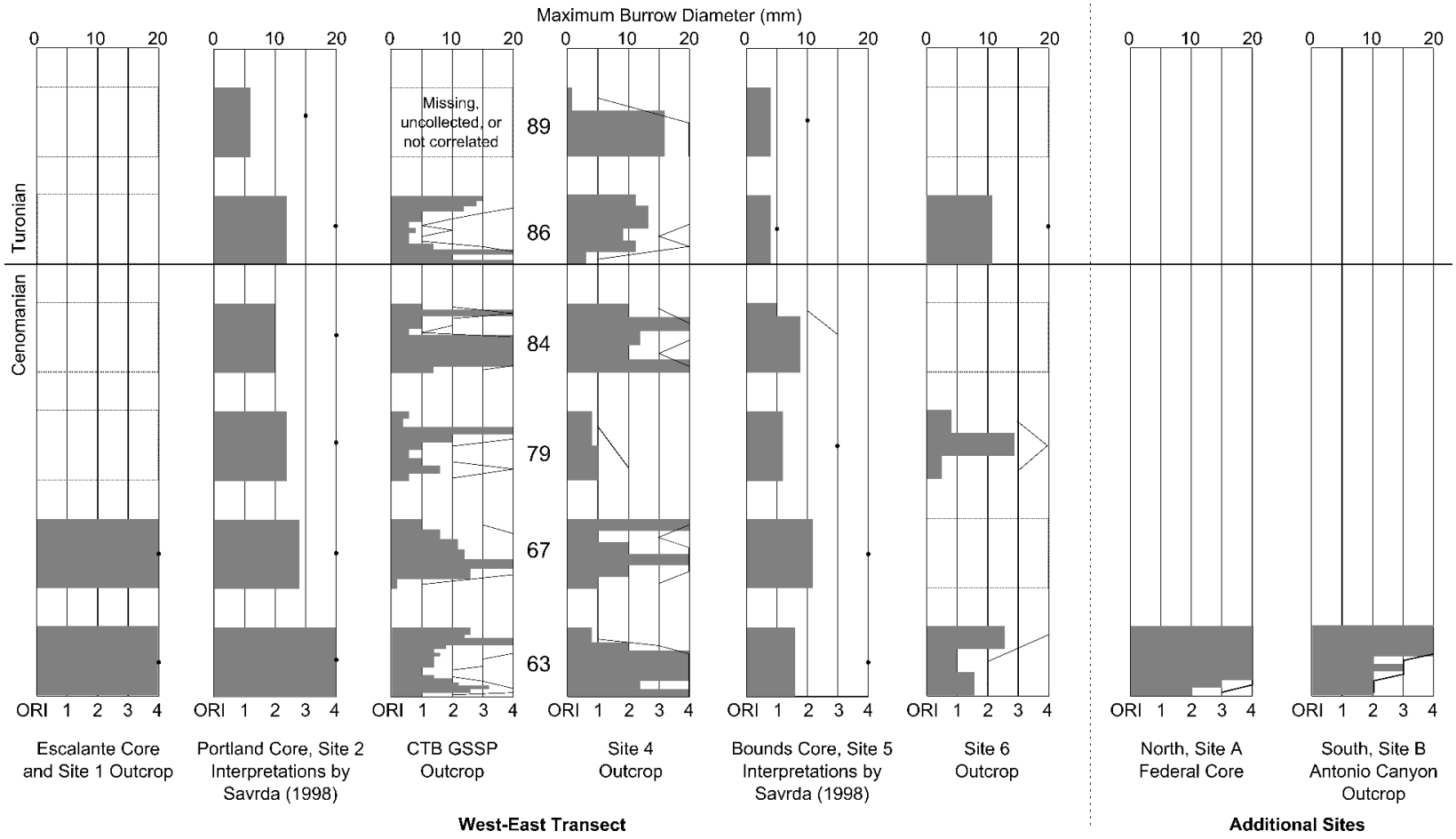

Figure 2.9 Oxygen interpretations from Lower Bridge Creek Limestone limestone bed trace fossil fabrics along the CWIS West–East transect. Bars represents maximum burrow diameter in the bed (top axis). Line represents ORI interpretation (bottom axis); a dot is used if a single observation interval represents an entire bed. Sites 1, 3, 4, 6, and additional northern and southern sites (Sites A and B, respectively), the maximum burrow and ORI interpretations were taken every 0.02 m. Sites 2 and 5 (Portland and Bounds Cores, respectively), maximum burrow data and ORI interpretations are every 0.05 m and reported by Savrda (1998). Bed numbers are placed beside graphs for Site 3. Boxed in areas without graphs indicate that data are missing, bed was not collected, or a correlation could not be confidently made to include in the study.

Time-series data

MTM and FT analyses of χ values reveal high-confidence recurring trends in the data, but only for Site 1 indicating the Milankovitch Cycles that may have controlled sedimentation characteristics in that portion of the basin. In Late Cretaceous time at the ~93.9 Ma CTB horizon, the period duration of Milankovitch Cycles was 18.5 and 22.5 kyr precessional cyclicity (P1 and P2, respectively), and 39 and 50.5 kyr obliquity cyclicity (O1 and O2 cycles, respectively) [calculated from data presented by Berger et al. (1992)]. Figure 2.10 shows juxtaposed MTM and FT plots produced from χ values for Site 1, and the positions of peaks that represent O1, O2, P1, P2 cycles. Those peaks that show high MTM confidence that corresponds to a FT peak are indicated by shaded areas.

Trends in limestone beds

Bed 63 limestone

Bed 63 is the only bed that can be correlated to each site in this study. At each of the sites, Bed 63 is indicative of high benthic oxygen conditions because of the presence of *Thalassinoides* and other traces found in higher benthic oxygen concentrations, as well as large burrow diameters and high burrow concentrations. This is also true for Bed 63 at the northern and southern termini of the seaway (Grosskopf 2015a). The ORI categorization from Bed 63 representing the benthic oxygen concentrations from the northern portion of the seaway is from 2-21 Federal Core from Phillips County, MT (Figure 2.1). Representing the southern portion of the seaway is an outcrop in Lozier Canyon, near Langtry, Texas (Figure 2.1). Both sites show the same trend as along the West–East transect (Grosskopf, 2015a; this dissertation). The Bed 63 ORI plots from these sites are depicted in Figure 2.9 alongside the West–East limestone bed ORI plots.

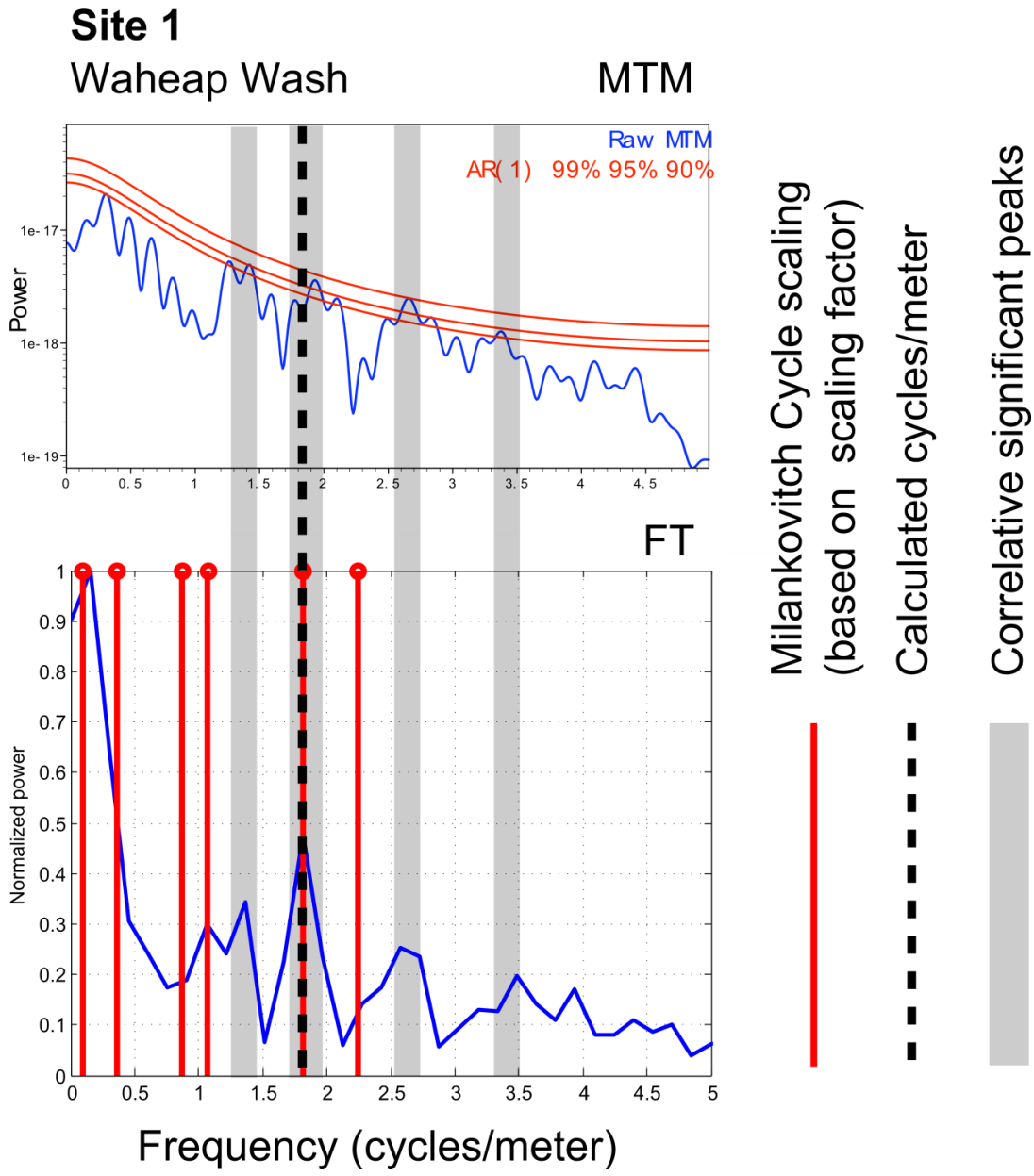

Figure 2.10 Multi-taper (MTM) and Fourier transform (FT) time series results for Site 1. Red vertical lines represent peaks that are spaced on a Milankovitch frequency in reference to the ~100 kyr eccentricity band and corresponding harmonic number, where, right-to-left the red lines correspond to P1, P2, O1, O2, E1, and E2. Dashed black lines represent cycles/meter calculated from data smoothed using splines (data presented later in the discussion. Grayed zones represent peaks that correlate between MTM and FT results. Red lines in MTM plots represent confidence intervals of 90, 95, and 99%, bottom to top. Data are reported in half of the cycles/meter because the sampling interval for χ was 0.10 m rather than 0.05 m.

Bed 63 ichnofabrics at Site 3 (the CTB GSSP) exhibit burrow diameters ranging from 5 – 20 mm, with trace types and concentration ranging from dysoxic to oxic. ORIs from these data range from ORI 2 to ORI 4, and from base to top of the bed are interpreted to indicate that oxygen levels varied from oxic to dysoxic, and then back to oxic again (Figure 2.9). This fluctuation in ORIs within a single bed is important in understanding how oxygen characteristics changed through time throughout the CWIS.

Variable ORIs throughout Bed 63 indicate variable oxygen levels during the deposition of this interval, but never does an ORI within the bed indicate anoxic conditions. High ORIs in Bed 63 indicate that well-oxygenated bottom waters are prevalent throughout all parts of the seaway, regardless of proximity to the margins or deeper areas, which directly contradicts the notion that OAE II conditions exhibit widespread stagnation from the Late Cenomanian (Bed 63 time) into the Turonian.

Other traceable limestone beds

For sites along the West–East transect from base to top of the transect that represents OAE II-time, regionally correlatable beds 67, 79, 84, 86, and 88 (Figure 2.9) each exhibit high benthic oxygen conditions from the high ORIs throughout. Although these beds are thinner, and less extensive than Bed 63, they still show the same response to OAE II benthic oxygen changes over time and across the basin. Due to the type of traces present, large burrow diameters, and high burrow concentrations, beds range from ORI 1 to 4, establishing an interpreted oxygen curve ranging from moderate to high oxygen conditions. Similar to Bed 63, in each particular bed there is variation in ORIs from base to top, due to short-lived changes in benthic oxygen. Likewise, as in Bed 63, benthic oxygen drops towards the east along the West–East transect, with Site 6 registering the lowest oxygen levels along the transect (Figure 2.9).

This observation is supported by the high ORIs in beds through the CTB and matches the dilution model from Fischer (1980) and Eicher and Diner (1985). In Savrda (1998), two different signals were noted in an interpreted oxygen curve derived from ORIs observed in beds representing OAE II-time from the Portland and Bounds Cores; 1) high-frequency low-amplitude, and 2) high-amplitude low-frequency benthic oxygen signals. The former signal represents changing ORIs in calcareous shale beds, while the latter represents limestone beds. The highest benthic oxygen levels in the section coincide with thick limestone beds, matching the combined dilution–productivity models for the CWIS.

Geochemistry

At outcrop-scale, geochemical evidence corroborates higher oxygen conditions in limestone beds during OAE II (Figure 2.11). For the CTB GSSP section, U concentrations were at or below average marine carbonate-rich sedimentary rocks. In the OAE II succession, limestones and calcareous shales both register high $CaCO_3$ percentages. The calcareous shale portions of the interval contain a high amount of $CaCO_3$, sometimes only 10–15% less than that of the limestones. Considering the high $CaCO_3$ content of these beds, when U concentrations are compared to levels of that of average marine shale (2.7 ppm and 3.0 ppm, reported by Evans and Goodman [1941] and Wedephol [1971], respectively), they mainly fall between average limestone (1.3 ppm; reported byTribovillard et al. [2006]) and marine shale levels. The sharp spikes in U concentration are associated with the weathered ash particles that compose the bentonite beds.

U concentrations for the OAE II interval occur at lower levels than in the strata bracketing the section representing OAE II-time. This is depicted in Figure 2.11 by higher values

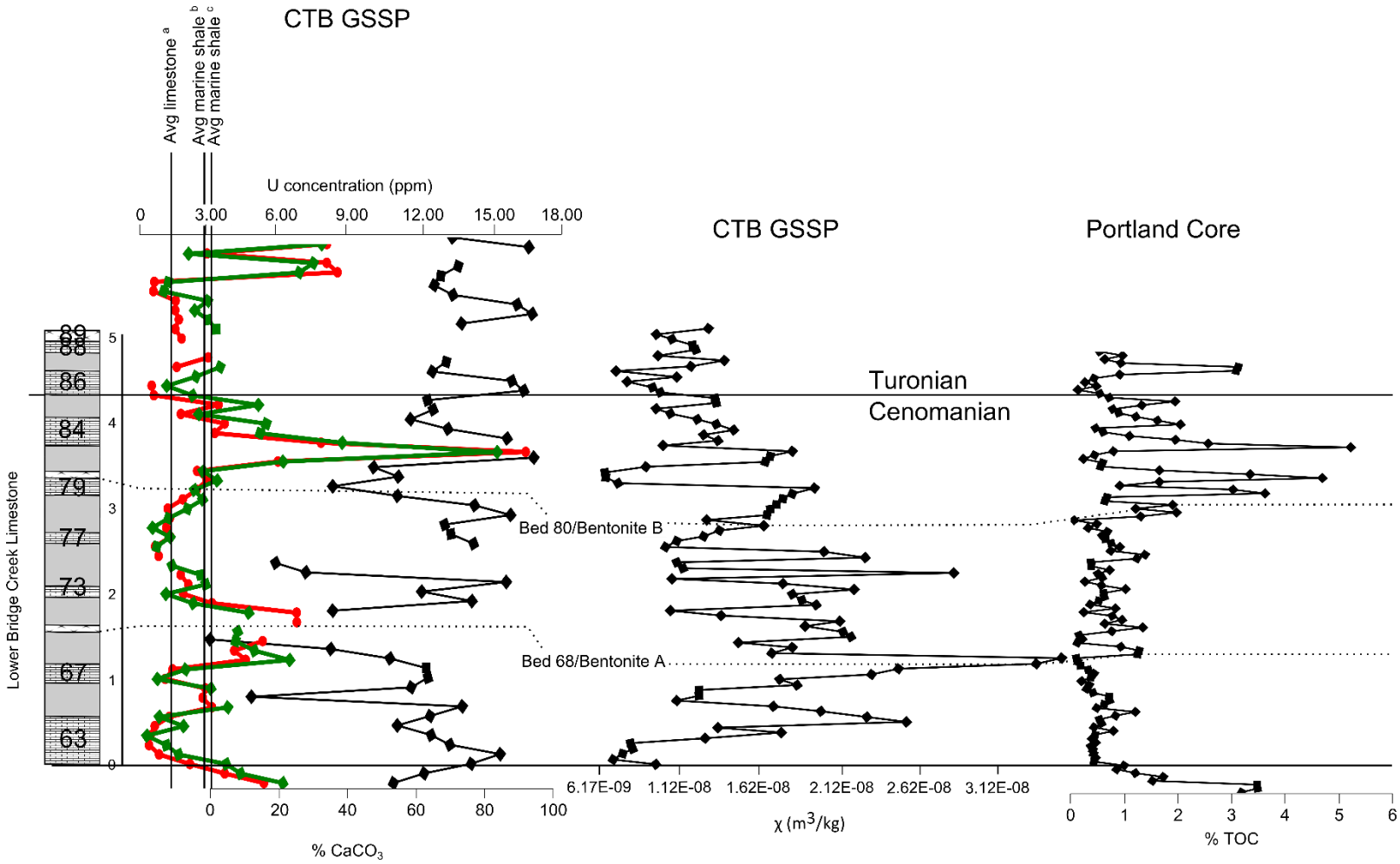

Figure 2.11 U concentration curves from ICP-OES (red) and ICP-MS (green) along with TOC (% organic carbon) curve from Portland Core spanning OAE II tied to the Site 3 lithology. TOC curve from data reported by Sageman et al. (1997), and geochemistry and χ data reported in Ellwood et al. (2008). Sources for U levels from average marine sedimentary rocks (represented by vertical lines intersecting axis for U concentrations) are Evans and Goodman (1941), Wedephol (1971), and Tribovillard (2006) for a, b, c, respectively. Lith-log is slightly modified here to better match measurements from Ellwood et al. (2008).

in U concentration below the base of Bed 63, and above Bed 89 bentonite, which represents the extent of OAE II in CWIS strata (Sageman et al., 1997). These data further match ORI results indicating benthic conditions were not anoxic. Additionally, total organic carbon (TOC) data from the strata representing OAE II-time in the Portland Core (Site 2) are at lower levels than beds above or below the OAE II portion of the section (Sageman et al., 1997; Dean and Arthur, 1998; Figure 2.11).

U concentrations register low values in each limestone bed. Evidence for rise in U concentrations eastward along the West–East transect would corroborate the ichnofabric interpretations from those sites, and potentially strengthen the Slingerland et al. (1996) paleoceanographic model predictions of less oxygen along the eastern margin of the CWIS due to warmer saline-rich waters there. Furthermore, similar to Bed 63, the drop U eastward would match results from the Savrda (1998) Portland and Bounds Core interpreted oxygen curves.

Periodicity in ORIs indicates oxic conditions during OAE II in the CWIS

In Earth's history, there may only be a few instances of shallow basins that exhibit such obvious changes to benthic oxygen through time as a response to effects of obliquity or precessional- scale climate forcing. This is a very unique setting because, one, there is a latitudinally-extensive, large open epicontinental seaway, where at the northern terminus there is cool, fresher seawater running southward, and at the southern terminus, there is warm saline-rich water flowing northward (Slingerland, et al., 1996). Two, these distinctive water masses converge forming a broad gyre with the cool water flowing along the westward flank, and warm water along the eastern flank (Slingerland et al., 1996; Pancost et al., 1998). Three, at the northern terminus lies the subaqueous, High Artic Large Igneous Province (Eldrett et al., 2014), while at the southern terminus is the subaqueous CLIP, both of which source oxygen-sorbing

trace metals and other compounds that stress the whole seas in their respective regions (Snow et al., 2005). Four, there are active subaerial volcanoes dumping voluminous amounts of ash across the shallow seaway, thus stressing plankton and benthos, while contributing oxygen-sorbing compounds to the water chemistry (Barclay et al., 2010; Brumsack, 2006). Five, there is a large amount of sediment supplied from the Sevier Orogeny proximal to and paralleling the western margin of the CWIS that constantly, via rivers, provides nutrients into the basin driving carbon production in an already oxygen-imbalanced system (Bowman and Bralower, 2005; Corbett and Watkins, 2013). And six, this is occurring in the Middle-Late Cretaceous during record high global temperatures, record atmospheric CO_2 concentrations, and record sea level highs (Gale et al., 2002).

If each of these six factors were looked at individually, the only parameter that has any type of periodicity is terrigenous input into the basin, which is controlled by a recurring change in Earth's insolation as an effect of orbitally-forced erosional pulses related to climate cycling between wet and dry periods. This explains how there are ordered fluctuations through the OAE II interval between dysoxic-to-oxic calcareous shale beds and oxygen-rich limestone beds. It also explains how small-scale changes in ichnofabrics, which are more apparent in the thicker beds, may be on the order of precessional-scale variations. Conditions during OAE II may have been oxygen-stressed, but a benthic fauna still prevailed throughout the duration of OAE II, as there are ichnofossils from oxygenated environments preserved in each of the limestones. Starving the CWIS of sediment-laden nutrients relieved at least one of the stresses, allowing benthic life to thrive. This is evidenced in thick limestones from Beds 63 up through Bed 88 and the calcareous shale beds in between, throughout the OAE II interval.

But Sageman et al. (1997, 1998) argue this dilution model interpretation can only work for the Upper Bridge Creek Limestone. They claim that obliquity-forced climate effects forcing wetter and drier conditions resulting in dilution effects would have a stronger influence on higher latitudes only, thereby controlling the freshwater and terrigenous flux into the CWIS. Precessional-scale climate cycles, they claim, match with carbonate productivity cycles as a response of seawater moving in from the Tethyan realm. The combined dilution–productivity model assigns obliquity responsible for the calcareous shale component due to effects in high northern hemisphere latitudes, and precession responsible for the limestone component due to effects of production during higher levels of insolation at low latitudes. These two competing, but sometimes in sync depositional cycles have adverse effects on time-series analysis.

This explains the infrequent MTM and FT peak correspondence among sites, except for results shown in Figure 2.10. Due to the two controls of sediment deposition occurring in the basin correspondence between analyses only occurred at Site 1 (Figure 2.10), which is the most expanded succession of OAE II strata due to proximity to the western margin, which represents the dilution component of the combined carbonate dilution–productivity model.

Sageman et al. (1997) and Sageman et al. (1998) explain that time-series for the Lower Bridge Creek Limestone is complex because orbital frequencies are out of phase. This is evidenced by the complex bedding in the Lower Bridge Creek Limestone succession consisting of variable bed thicknesses, thin or missing limestone beds, and presence of thick bentonite beds. They corrected for this by plotting E2, E1, O, and P Milankovitch Cyclicities calculated for the Upper Bridge Creek Limestone, onto the Lower Bridge Creek Limestone to assign sediment accumulation rates (SARs) for the Lower Bridge Creek.

Resolving small-scale variation in oxygen concentrations

Graphic comparison is a method used to establish SAR that is independent of MTM and FT. It is useful in corroborating MTM and FT results and comparing SAR between sites (Ellwood et al., 2008). In essence, graphic comparison matches the positive "peaks" and negative "valleys" from one high-resolution cyclic dataset to another and the difference between each is apparent on a constructed line-of-correlation, assuming that sites are correlated independently. A χ bar-log must first be constructed, where a positive shift is represented by a black bar and a negative shift is represented by a white bar. One cycle consists of two bars, each singly representing a half cycle. Figures 2.12–2.16 show the bar-log constructed for each site along the West–East transect. A line-of-correlation is the resulting qualitative comparison among correlated sections based on the duration of each correlatable half cycle, using the bar-logs.

Graphic comparison is robust in that two different sections can be compared using the same data set. Marker beds, independent of SAR, such as bentonite beds, represent an instantaneous horizon. Because it is instantaneous, bentonite thicknesses can throw off interpretations of duration due to changing the slope of line of correlation. Therefore, sample readings of bentonite are removed from the dataset, but the position is still noted and can be plotted as well. Furthermore, a section can be compared to a uniform bar-log model that represents a fixed SAR, in order to examine deviations from a uniform SAR or check hypotheses concerning the SAR at a given level in the section. This has been successfully applied to the CTB GSSP (Site 3) and Portland Core (Site 2) e.g. Ellwood et al. (2008), and some of those plots are used here. Lastly, graphic comparison is a useful tool in comparing two different high-resolution datasets. For instance, χ, field and well-log GRS data, or redox-sensitive trace element data (Ellwood et al., 2008).

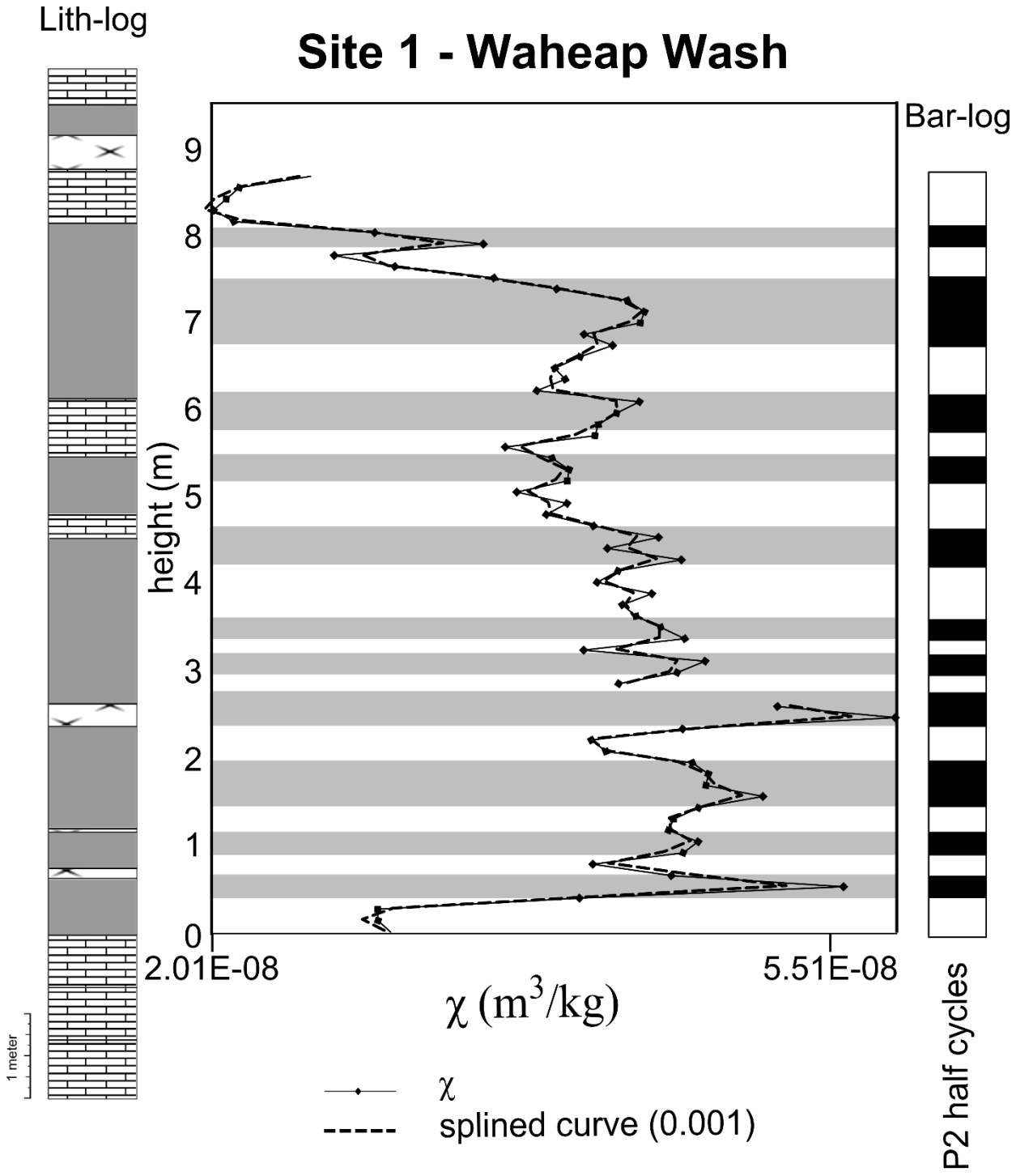

Figure 2.12 Bar-log derivation for Site 1 and corresponding lith-log. Shaded horizontal bars represent a positive shift in χ values, where the upper and lower boundaries of each bar are placed at the midpoint of a shift on the splined χ data curve (represented by a dashed line).

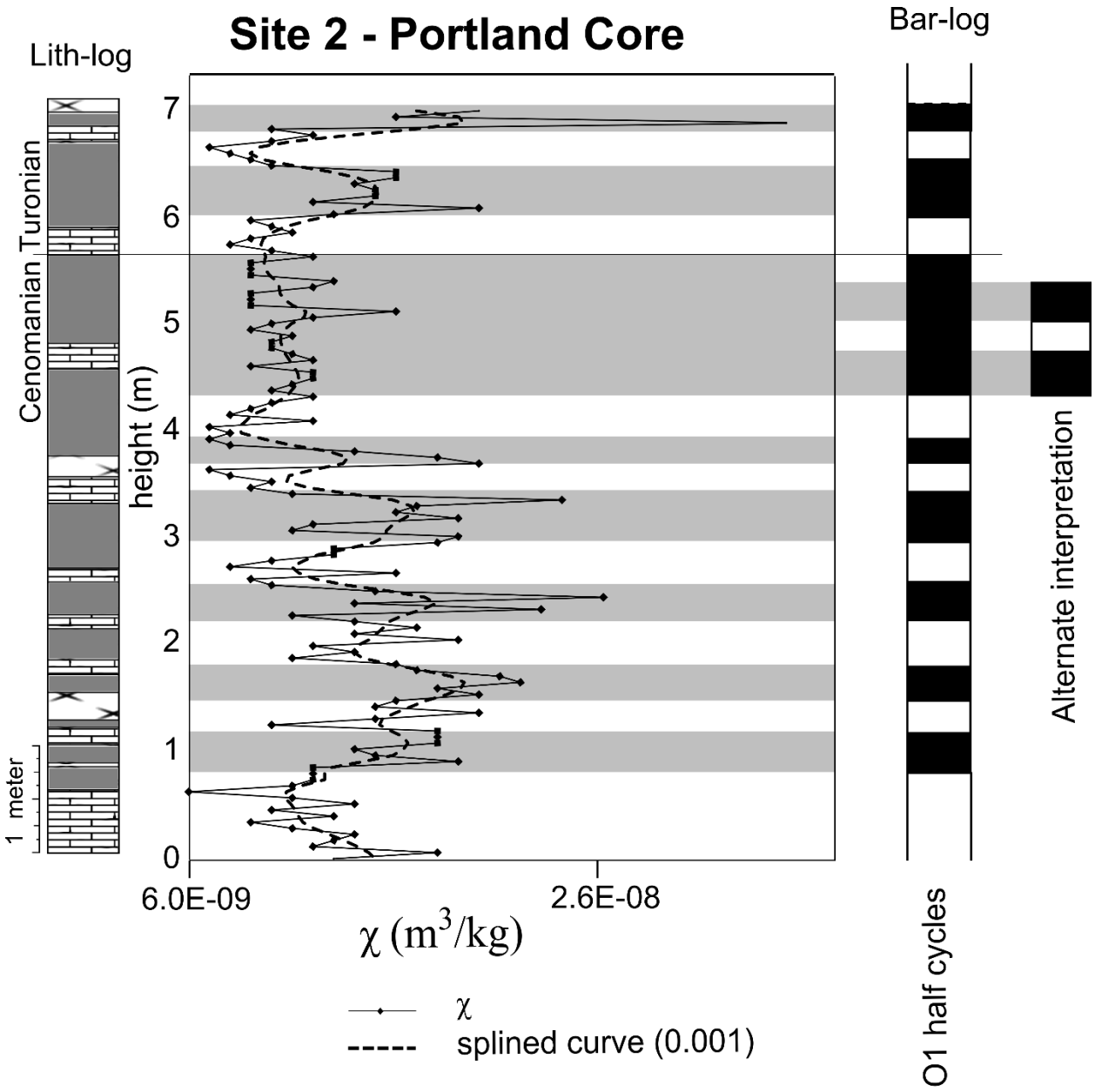

Figure 2.13 Bar-log derivation for Site 2. Alternate interpretation of the splined curve are given to the side of the bar-log. Refer to Figure 2.12 for further explanation of figure details.

Figure 2.17 shows the utilization of graphic comparison, where three sections, sites 2, 4, and 6 (on the x-axis) are compared with Site 3 (on the y-axis). Other sites could not be compared

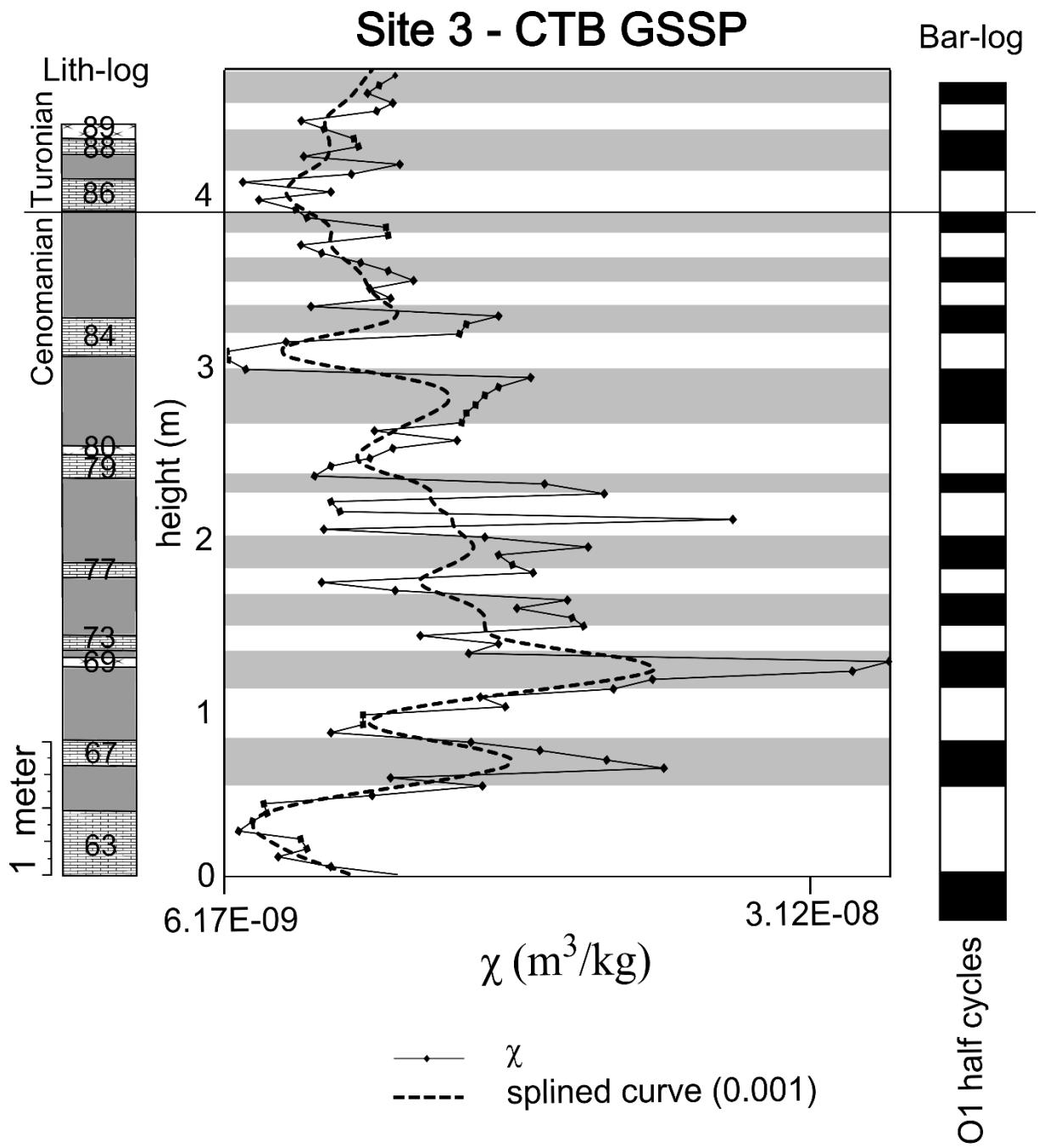

Figure 2.14 Bar- log derivation for Site 3. Refer to Figure 2.12 for further explanation of figure details.

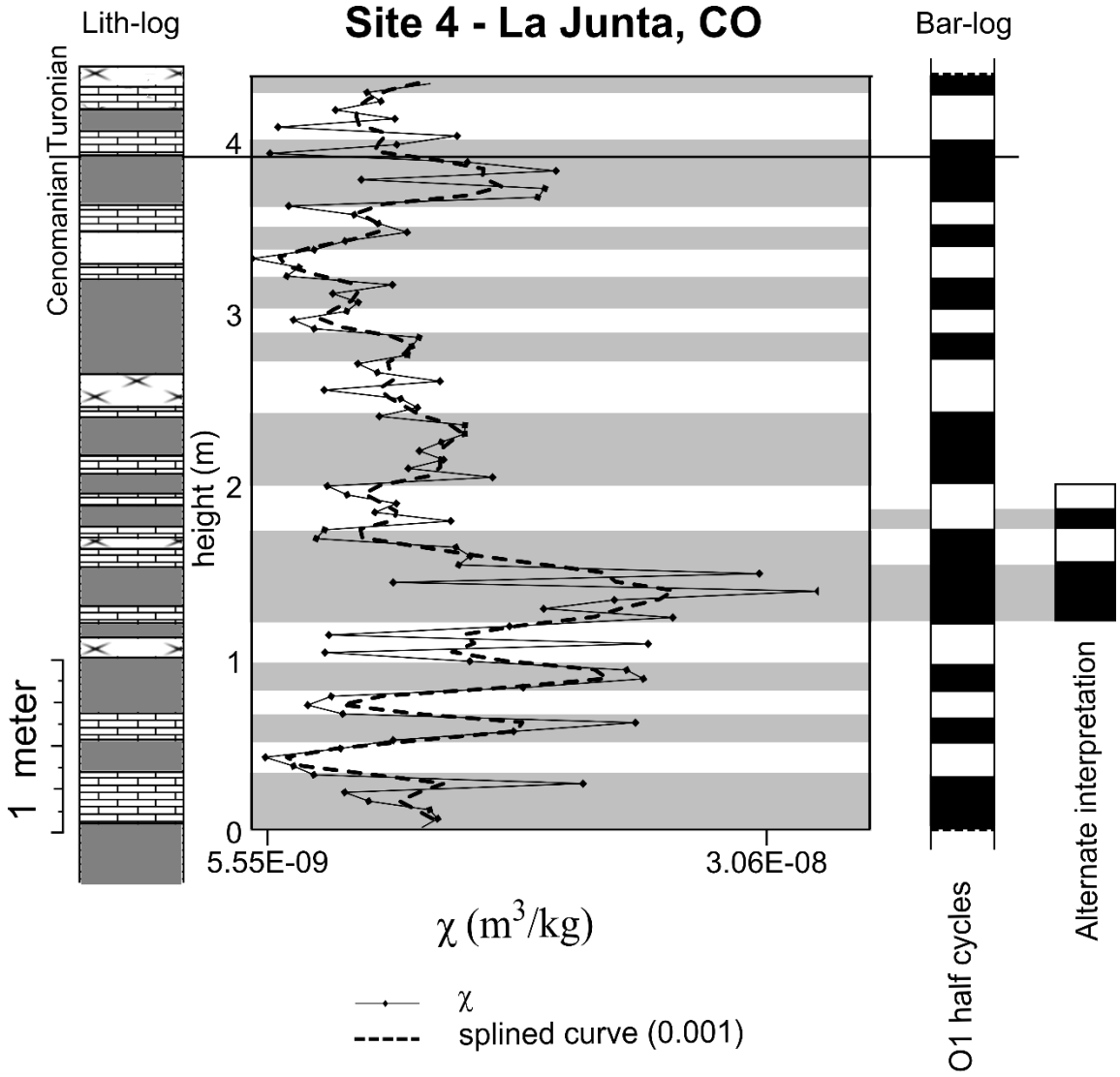

Figure 2.15 Bar- log derivation for Site 4. Alternate interpretation of the splined curve are given to the side of the bar-log. Refer to Figure 2.12 for further explanation of figure details.

because they were either lacking usable χ data (Site 5), or as in the case of Site 1, it represents only a portion of the section (Bed 63 to Bentonite B; Elder, 1988).

In Figure 2.17, graphic comparison was used to place the CTB at Site 6 by tracing the CTB from Site 3 through the line of correlation between Sites 3 and 6, and at that intersection, projecting this point into the Site 6 bar log. The height of the CTB at Site 6 is determined to be

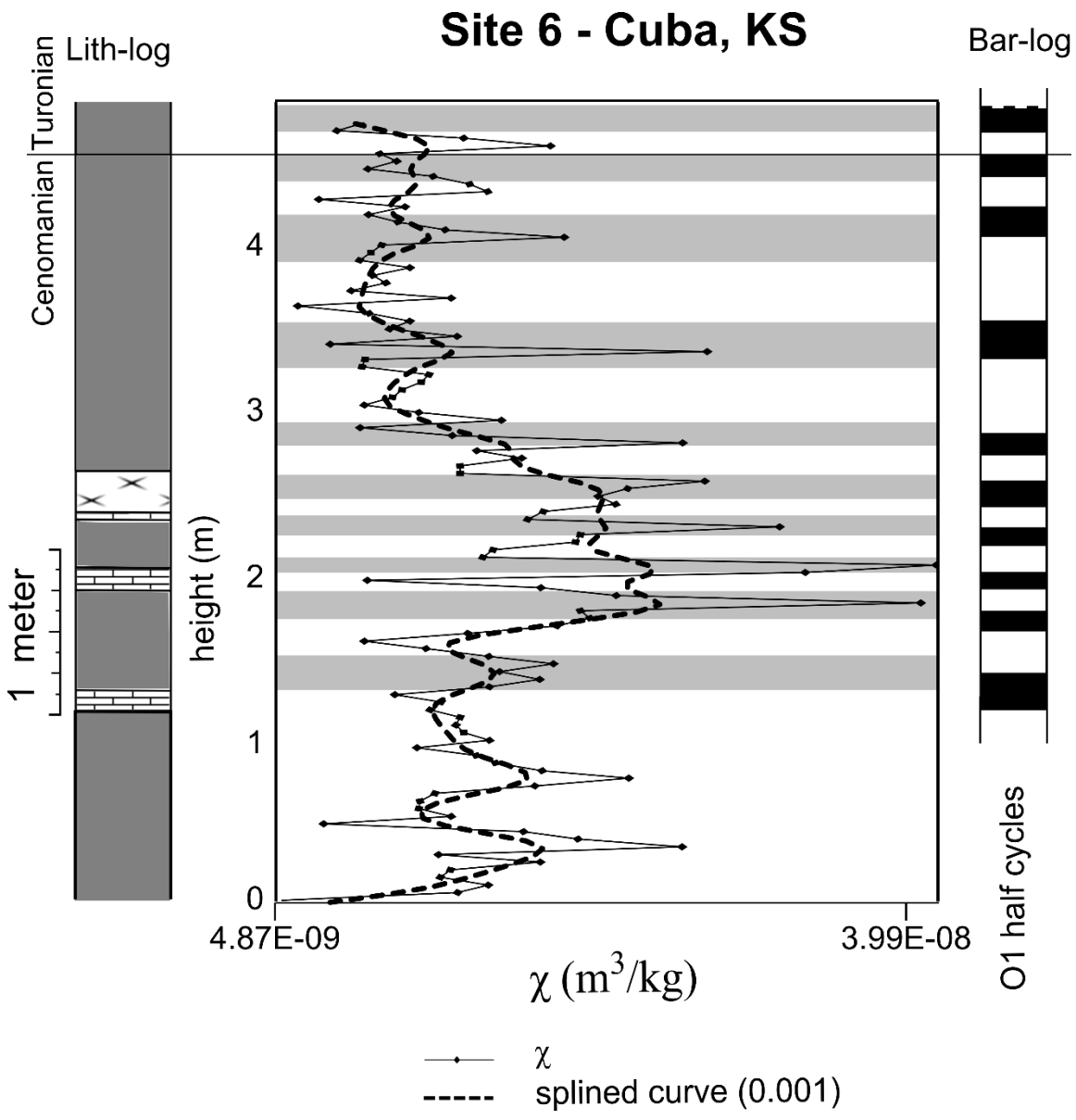

Figure 2.16 Bar-log derivation for Site 6. Refer to Figure 2.12 for further explanation of figure details.

3.12 m above the top of Bed 63. Top of bed is used here because the limestone bed bench on the outcrop is very discernable, while the base of that limestone grades into calcareous shale and the contact is not well-defined. The height of the CTB here is close to the interpreted base of the Jetmore Member by Hattin (1975).

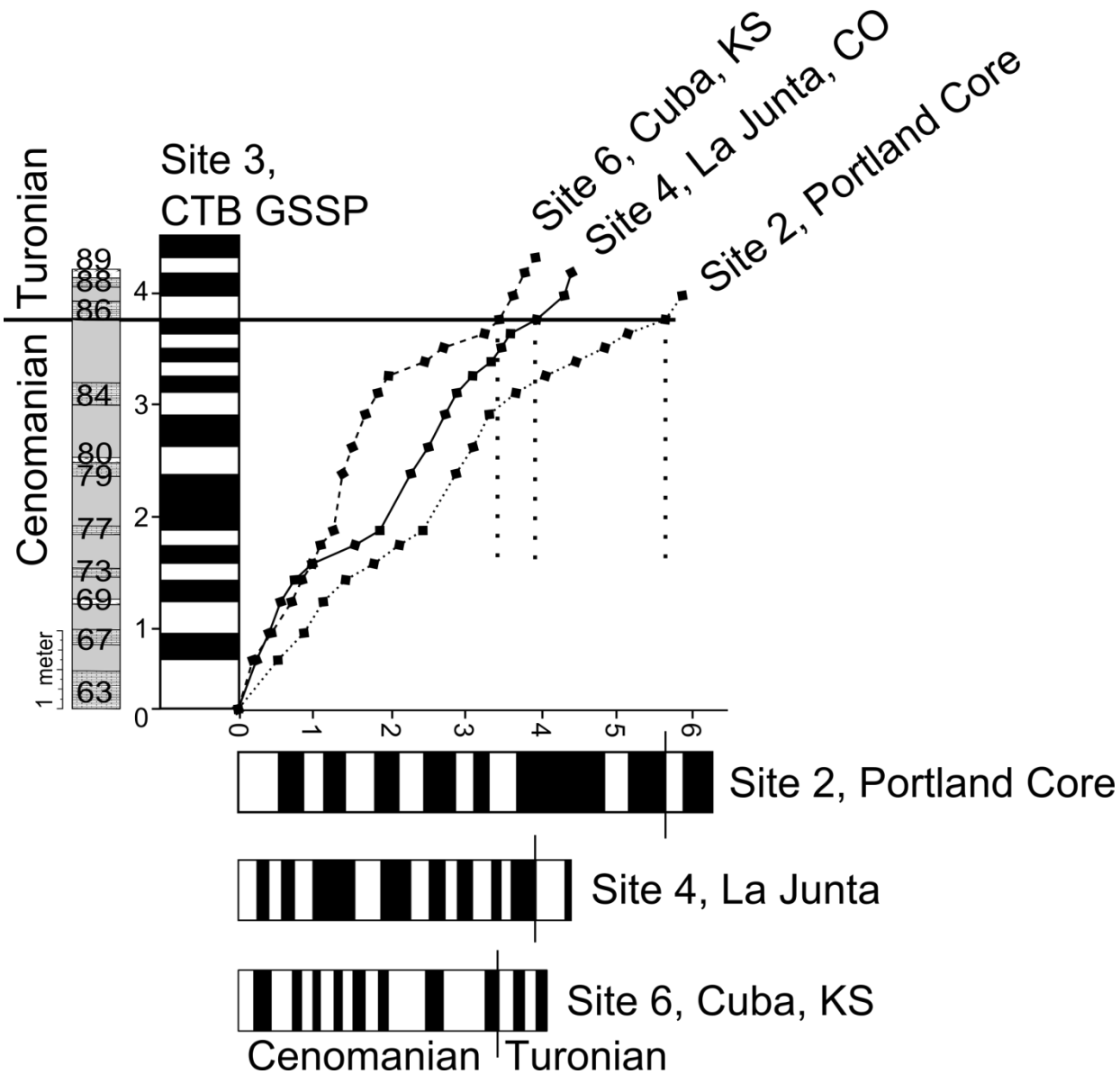

Figure 2.17 Graphic comparison between Site 3/CTB GSSP and other sections that have correlatable cycles. Each line of correlation intersects the CTB line, placing the horizon at the known height of the CTB in the scaled sections on the x-axis. The line-of-correlation places the CTB at Site 6 at 3.12 m above the base of Bed 63.

Normally, to derive real SARs for these sites, MTM or FT cycles are used as a guide to best match cycle frequency observed in outcrop or core to a specific Milankovitch Cyle, and then calculate cycle duration using the appropriate Milankovitch Cycle frequency, at ~93.9 Ma. Yet,

no cycle per meter from the splined χ data directly matched any statistically significant peak in MTM or FT data, except Site 1, sampled at 0.10 m.

It was shown in Sageman et al. (1997) that there is difficulty in discerning strong periodicity in Lower Bridge Creek Limestone strata from the obliquity- and precessional-forced components being out of phase and destructive to preserving a signal. This problem becomes clear from an examination of the line-of-correlation for each section compared to the CTB GSSP in Figure 2.17, and compared to a 39 kyr floating point time scale in Figure 2.18. SARs from cycle to cycle are too variable to produce good time-series results, but coarse stratal patterns depicted by the coarse transitions in the χ data curves are apparent enough for cyclostratigraphic application at Site 6, as explained earlier. This is more apparent when bar-logs are plotted against absolute dates using a floating-point time-scale.

It can be seen in Figures 2.17 and 2.18 that qualitative SARs trend along the West–East transect in the following ways: 1) SAR increases westward, and 2) there is an increase in SAR near the middle of most sections. This middle zone between beds 72–84, among most sites depicting high SARs only loosely matches the χ data for that section. χ values indicate the concentration of paramagnetic minerals from fluviodeltaic systems thereby tracking terrigenous flux. The carbonate content derived from the deposition of microfossil tests during productivity cycles in the CWIS effectively decreases the concentration of paramagnetic minerals while still adding to the SAR. Thus, whichever of the obliquity-scale dilution cycles or precessional-scale productivity cycles is in phase, they equally contribute to the overall SAR. This is indicated in the consistent slopes along portions of the line-of-correlations plotted against a floating-point time-scale model for O1. The line-of-correlations for the four sites have straight segments that represent equal SARs for carbonate-rich shale and limestone beds.

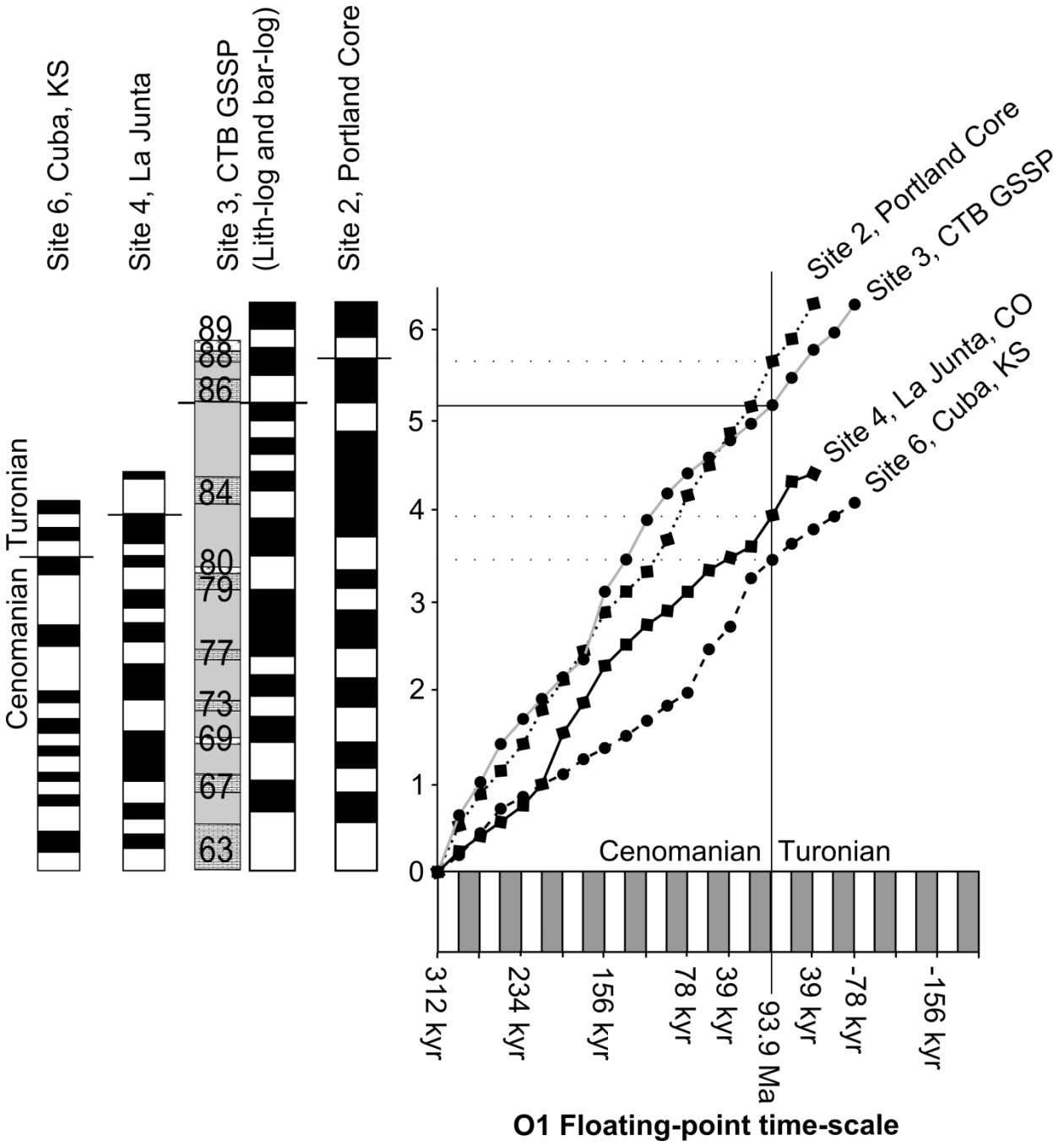

Figure 2.18 Graphic comparison of four sites with matching cycles plotted along a floating-point time-scale. Ages reflect the CTB (93.9 Ma) and the 39 kyr obliquity cycle(O1; calculated from data presented by Berger et al., 1992).

This matches the Ellwood et al. (2008b) graphic comparison across the Danian–Selandian Boundary at the Danian–Selandian Boundary GSSP in Spain. There, a sharp contact divides Late Danian limestone and shale bed couplets (with thin calcareous shale beds and thick limestone beds) below the contact, and Selandian calcareous shale beds above. Bar logs constructed from χ levels through the section compared to a uniform floating-point time-scale established a line-of-correlation with no difference in slope through the transition between the major lithologies.

On a bed-by-bed or bedding couplet basis, it would take many orders of magnitude more diamagnetic minerals in a system to change the character of χ levels across bed transitions, and while there is a depositional change between limestone and calcareous shale beds, the χ levels do not shift too drastically as the signal is smoothed (Ellwood et al., 2008). This affect is responsible for the smooth, curved line-of-correlation compared to what would be a step-like line-of-correlation if one component of depositional system, either limestone or calcareous shale, was responsible for a majority of the SAR. Only when viewed on depositional-scales of the highest frequency, on the millennial-scale in a single bed, would a step-like line-of-correlation be observable. In fact, this would be the case in all beds, in that the major depositional component represents the resulting bed type, while the other depositional component was present and contributing a near-equal amount to SAR. This matches the relatively small variability in % $CaCO_3$between calcareous shales and limestones as depicted in Figures 2.4b and 2.11.

The high SAR zone between beds 72–84 is present in the floating-point time scale as well, with the SAR increase becoming more apparent in the sections farther from the western margin (sites 4 and 6). Perhaps the high SAR zone is more apparent in easternmost sites due to a relative drop in sea-level increasing sediment supply, where, under these conditions, calcareous

shale deposition would become the primary component of sediment supply. Evidence for this may be represented by trace element data where increased U concentrations coincide with a slight increase in TOC at that interval (Figure 2.11). Burial effects due to increased sediment supply can also play a role in the increased TOC preserved in this rock unit (Cowie and Hedges, 1992).

After the interpreted sea-level fall, SARs returned to lower levels, but represent a variation not as consistent as down-section. The latter varied portions of these lines-of-correlation represent the onset of dilution controlling the dominant source of deposition in the CWIS. This is consistent with trace element data through the succession, with high concentrations of U as well as TOC in that part of the OAE II interval. Eicher and Diner (1989) and Sageman et al. (1997) relate the cause of this trend to dilution and CWIS deepening. Approaching near-highstand times, effects of Tethys Sea productivity cycles became secondary to the prevailing dilution effects from obliquity-forcing in higher latitudes. The well-constrained orbital frequencies mentioned earlier in this paper are from the dominance of the obliquity signal found in CWIS beds in the Upper Bridge Creek Limestone. One interpretation for this final transition to strong orbitally-forced dilution during highstand is due to global climate change from organic carbon burial and the consequent CO_2 drawdown from effects of OAE II (Sageman et al., 1997). The CO_2 removed from the short-term carbon cycle caused global temperatures to drop, establishing stronger latitudinal climatic effects, one of which may have been polar ice. In this hypothesis, high latitudes had higher-amplitude obliquity-scale climate changes compared to earlier stages of the highstand represented by the lower portions of the OAE II succession. Cooler temperatures at higher latitudes made for stronger variation between wetter and drier portions of the obliquity-forced long-term climate cycle.

One other feature of the floating-point time-scale is the use of absolute ages. All SAR values were derived from relative differences in duration among cycles (two bars on the bar-log). If cycles from four sections in Figure 2.18 represent continuous deposition, then they only make up just over half of the time that OAE II represents. The duration of OAE II reported in Sageman et al. (2006) is 563–601 kyr, and duration derived from the O1 floating-point time-scale here is 390 kyr. The 192 kyr difference from the mean of age Sageman et al. (2006) can be lessened by considering the following. First, there is error in the 93.9±0.15 Ma (150 kyr) absolute age for the CTB. Second, placement of the start and end of OAE II using $\delta^{13}C$ curve data points that are not associated with marker beds or correlatable horizons (varies among authors' interpretations) presents inaccuracies in dating. Third, there is a major hiatus just prior to the increase in SARs in the zone between beds 72–84 due to a transgressive pulse (Elder, 1991; Meyers and Sageman, 2004). Fourth, other shorter hiatuses are present in these successions represented by the flooding surfaces and associated deposition some thicker limestone horizons (beds 63, 77, 79; Elder, 1994). Fifth, bed condensation from storm winnowing may be responsible for presence of the highly bioturbated bases and tops of limestone beds (Elder, 1991). Lastly, there is inherent error using a consistent time-scale derived from the Upper Bridge Creek Limestone to account for the phase-shifting in orbitally-forced bedding couplets that is known to occur in the Lower Bridge Creek Limestone (Meyers et al., 2014; this paper).

Precessional-scale variation in thick limestone beds?

Short-term variations in the trace fossil fabrics observed in thicker limestone beds in the Lower Bridge Creek Limestone may be due to precessional-scale productivity cycles from the mixing of the CWIS and Tethys waters (Sageman et al., 1997). This is the same trend of high-frequency variation observed in calcareous shales in the Portland and Bounds cores by Savrda

(1998). For example, there is a *Chondrites*-rich zone that is very noticeable in Bed 86 at Site3 (Figure 2.19). This 6 cm thick zone contains a dense arrangement of *Chondrites* for that interval. The calculated SAR at that height in the section (Figure 2.14) is 0.6 cm/kyr. Therefore, the *Chondrites*-rich zone represents 3.6 kyr. While limestone beds represent higher benthic oxygen conditions, compared to the calcareous shales from the same section, this zone represents the lowest benthic oxygen concentration of this limestone layer. This relates to the presence of the single trace type, *Chondrites*. Bromley and Ekdale (1984) and Ekdale (1985) claim that the sole presence of *Chondrites* indicates very low oxygen conditions. The low benthic oxygen conditions (2.0 – 0.2 ml of O_2/l of H_2O), represented by the presence of only *Chondrites* over a duration of 3.6 kyr, indicates that benthic oxygen concentrations varied on a few thousand year time scale, and possibly even more frequently in that region of the globe that the CWIS covered.

Due to the control of detrital input on benthic oxygen concentrations, oxygen conditions could fluctuate on the order of seasons. For instance, the CWIS could have had areas that drained nutrients from the Sevier Highlands and contributed to a hypoxic zone like the present Mississippi River delta hypoxic zone that lasts 30 to 60 days in the summer months (Rabalais et al., 2002). No known geologic technique, when applied to Mesozoic strata, has high enough resolution to capture this signal, unless an area underwent very high sedimentation. Decreasing the sampling interval from 0.10 m to 0.02 m in the Escalante Core and Waheap Wash (Site 1), where calculated SARs are highest, may capture a signal at higher frequency than P2.

For variations in benthic oxygen concentrations at seasonal and longer durations (> 1 kyr) bioturbation would remove any evidence of anoxic bottom waters at 0.6 cm/yr SAR in the upper portion of the OAE II interval. Burrow depths from ORI 1–ORI 4 range from < 0.03 cm to 8 cm

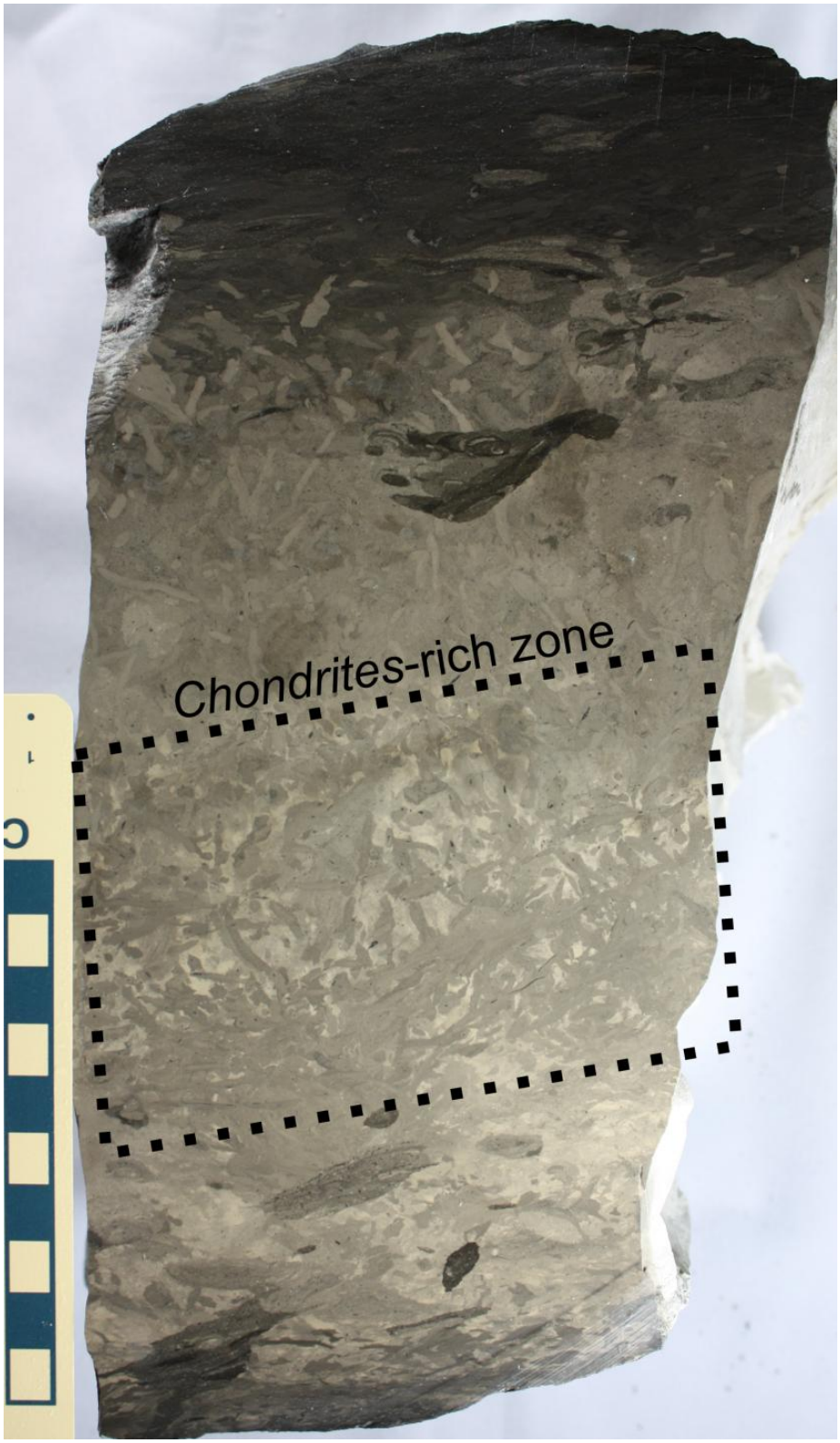

Figure 2.19 *Chondrites*-rich zone in Bed 86 at the CTB GSSP. Scale to the left is 10 cm. Photograph by J. Grosskopf.

(Savrda, 1998). Therefore, the shortest interval of benthic oxygen concentrations that could be preserved from not being reworked at a 0.6 cm/kyr SAR is ~4.8 kyr.

Did the CWIS have steady states of benthic oxygen that lasted this long? Did OAE II actually had an effect on CWIS waters, but the evidence could not preserved in the rock record because it is erased by burrowers? Even if some technique could derive results that better represents short-order benthic oxygen conditions during OAE II-time, it may still trend towards being oxic. The prevalence of macrofauna, as evidenced by bioturbation and body fossils for the duration of the OAE II interval, indicates that substrates had to have been habitable, even for the organisms with little-to-no tolerance under low oxygen conditions. There is good correlation between these data and the ORI data, which indicates that there was active oxidation of detritus because there were oxygenated bottom waters, which led to low TOC values due to organics being actively degraded, metabolized, and reworked from activity in the benthic environment.

The evidence for the OAE II interval being oxic this lies in intervals outside of OAE II where conditions appear to have had less benthic oxygen than the OAE II interval. The redox-sensitive trace element concentrations and TOC levels from the OAE II interval are much lower than those lower (Hartland Shale Member), or higher (Upper Bridge Creek Limestone) in the succession (Dean and Arthur, 1998; Sageman et al., 1997). While bioturbation destroys high-resolution component to tracking these benthic oxygen conditions, the fact that states of benthic oxygen expected for OAE II are preserved in successions outside of the OAE II interval signifies that the CWIS was unaffected by OAE II.

CONCLUSIONS

Oxygen-related trace fossil fabrics from correlatable limestone beds across the Cretaceous Western Interior Seaway (CWIS) representing conditions during the Oceanic Anoxic Event II (OAE II) interval, indicate well-oxygenated benthic oxygen conditions for the duration of OAE II. U levels corroborate these trace fossil interpretations. There is a slight drop in benthic oxygen towards the east in the CWIS and up-section through the OAE II interval, with no single time representing anoxic conditions.

Short-term changes to benthic oxygen conditions were brought about by orbitally-forced climatic effects. Limestone beds in the Lower Bridge Creek may be the result of combined effects of lack of terrigenous input and diminished water stratification effects, as well as increased calcareous microorganism productivity from vertical mixing of CWIS and Tethys water masses. Magnetic susceptibility (χ) datasets are useful in determining the correlation and timing of these short-term climate-forced events. χ datasets track the complicated depositional history of the CWIS during OAE II-time.

This paper establishes χ and trace fossil data as useful research tools for an outcrop-approach to paleoenvironmental investigations in the CWIS.

REFERENCES

Arthur, M.A. and Schlanger, S.O. 1979. Cretaceous "oceanic anoxic events" as causal factors in development of reef-reservoired giant oil fields. *The American Association of Petroleum Geologists Bulletin*, **63**, 870-885.

Barclay, R.S., McElwain, J.C., Sageman, B.B. 2010. Carbon sequestration activated by volcanic CO_2 pulse during Oceanic Anoxic Event 2. *Nature Geoscience: Letters*, **3**, 205-208.

Berger, A., Loutre, M.F., and Laskar, J. 1992. Stability of the astronomical frequencies over the Earth's history for paleoclimate studies. *Science*, **255**, 560-566.

Bowman, A.R. and Bralower, T.J. 2005. Paleoceanographic significance of high-resolution carbon isotope records across the Cenomanian-Turonian boundary in the Western Interior and New Jersey coastal plain, USA. *Marine Geology*, **217**, 305-321.

Bralower, T.J. 2008. Volcanic cause of catastrophe. *Nature*, **454**, 285-287.

Bromley, R. G. and Ekdale, A.A. 1984. Chondrites: A trace fossil indicator of anoxia in sediments. *Science*, **224**, 872-884.

Brumsack, H. 2006. The trace metal content of recent organic carbon-rich sediments: Implications for Cretaceous black shale formation. *Palaeogeography, Palaeoclimatology, Palaeoecology*, **232**, 344-361.

Cobban, W.A., Merewether, E.A., Fouch, T.D., and Obradovich, J.D. 1994. Some Cretaceous shorelines in the Western Interior of the United States, *in* Caputo, M.V., Peterson, J.A., and Franczyk, K.J. eds., Mesozoic Systems of the Rocky Mountain Region, USA: Rocky Mountain Section SEPM – Society for Sedimentary Geology, 393-414.

Corbett, M.J. and Watkins, D.K. 2013. Calcareous nannofossil paleoecology of the mid-Cretaceous Western Interior Seaway evidence of oligotrophic surface waters during OAE2. *Palaeogeography, Palaeoclimatology, Palaeoecology*, **392**, 510-523.

Cowie, G.L. and Hedges, J.I. 1992. The role of anoxia in organic matter preservation in coastal sediments: relative stabilities of the major biochemical under oxic and anoxic depositional settings. *Organic Geochemistry*, **19**, 229-234.

Dean, W.E. and Arthur, M.A. 1998. Cretaceous Interior Seaway Drilling Project: an overview. Stratigraphy and Paleoenvironments of the Cretaceous Western Interior Seaway, USA, SEPM Concepts in Sedimentology and Paleontology, **6**, 1-10.

Demaison, G.J. and Moore, G.T. 1980. Anoxic environments and oil source bed genesis. *The American Association of Petroleum Geologists Bulletin*, **64**, 1179-1209.

Eicher, D.L. and Diner, R. 1989. Origin of the Cretaceous Bridge Creek cycles in the Western Interior, United States. *Palaeogeography, Palaeoclimatology, Palaeoecology*, **74**, 127-146.

Ekdale, A.A. 1985. Trace fossils and mid-Cretaceous anoxic events in the Atlantic Ocean. Society of Economic Paleontologists and Mineralogists, Special Publication, **35**, 333-342.

Elder, W.P. 1988. Geometry of Upper Cretaceous bentonite beds: Implications about volcanic source areas and paleowind patterns, western interior, United States. *Geology*, **16**, 835-838.

Elder, W.P. 1989. Molluscan extinction patterns across the Cenomanian-Turonian Stage boundary in western interior of the United States. *Paleobiology*, **15**, 299-320.

Elder, W.P. 1991. Environmental factors controlling Cretaceous limestone-marlstone rhythms, *in* Einsele, G., Ricken, W., and Seilacher, A., eds., Cycles and events in stratigraphy: Berlin, Springer-Verlag, 79-93.

Elder, W.P., Gustason, E.R., and Sageman, B.B. 1994. Correlation of basinal carbonate cycels to nearshore parasequences in the Late Cretaceous Greenhorn seaway, Western Interior U.S.A. *Geological Society of America Bulletin*, **106**, 892-902.

Eldrett, J.S., Minisini, D., and Bergman, S.C. 2014. Decoupling of the carbon cycle during Oceanic Anoxic Event 2. *Geology*, **42**, 567-570.

Ellwood, B.B., Balsam, W.L., and Roberts, H.H. 2006. Gulf of Mexico sediment sources and sediment transport trends from magnetic susceptibility measurements of surface samples. *Marine Geology*, **230**, 237-248.

Ellwood, B.B, Brett, C.E., Tomkin, J.H., and Macdonald, W.D. 2012. Visual identification and quantification of Milankovitch climate cycles in outcrop: an example from the Upper Ordivician Kope Formation, Northern Kentucky. *Geological Society, London, Special Publications*, **373**, 341-353. doi: 10.1144/SP373.2.

Ellwood, B.B., Crick, R.E., Hassani, A.E., Benoist, S.L., and Young, R.H. 2000. Magnetosusceptibility event and cyclostratigraphy method applied to marine rocks: Detrital input versus carbonate productivity. *Geology*, **28**, 1135-1138.

Ellwood, B.B., Tomkin, J.H., Ratcliffe, K.T., Wright, M., and Kafafy, A.M. 2008. High-resolution magnetic susceptibility and geochemistry for the Cenomanian/Turonian boundary GSSP with correlation to time equivalent core. *Palaeogeography, Palaeoclimatology, Palaeoecology*, **261**, 105-126.

Ellwood, B.B., Tomkin, J.H., Febo, L.A., and Stuart Jr., C.N. 2008. Time series analysis of magnetic susceptibility variations in deep marine sedimentary rocks: A test using the upper Danian–Lower Selandian proposed GSSP, Spain. *Palaeogeography, Palaeoclimatology, Palaeoecology*, **261**, 270-279.

Ellwood, B.B., Wang, W., Tomkin, J.H., Ratcliffe, K.T., Hassani, A.E., and Wright, A.M. 2013. Testing high resolution magnetic susceptibility and gamma radiation methods in the Cenomanian-Turonian (Upper Cretaceous) GSSP and near-by coeval section. *Palaeogeography, Palaeoclimatology, Palaeoecology*,**378**, 75-90.

Evans, R.D. and Goodman, C . 1941. Radioactivity of rocks. *Geological Society of America Bulletin*, **52**, 459-490.

Fischer, A.G., 1980. Gilbert-bedding rhythms and geochronology. *Geological Society of America Special Papers*, **183**, 93-104.

Gale, A.S., Hardenbol, J., Hathaway, B., Kennedy, W.J., Young, J.R., and Phansalkar, V. 2002.Global correlation of Cenomanian (Upper Cretaceous) sequences: Evidence for Milankovitch control on sea level. *Geology*, **30**, 291-294.

Grosskopf, J. F. 2015. Basal Bridge Creek Limestone bed (Bed 63) trace fossils indicate oxygenated bottom-waters throughout the Cretaceous Western Interior Seaway During Oceanic Anoxic Event II. Diss. Louisiana State University, 2015. Baton Rouge: LSU, 2015. Electronic.

Hattin, D.E. 1971. Widespread, synchronously deposited, burrow-mottled limestone beds in Greenhorn Limestone (Upper Cretaceous) of Kansas and Central Colorado. *American Association of Petroleum Geologists Bulletin*, **55**,412-431.

Hattin, D.E. 1975. Stratigraphy and depositional environment of Greenhorn Limestone (Upper Cretaceous) of Kansas. Kansas Geological Survey Bulletin 209, University of Kansas.

Henderson, R.A. 2004. A Mid-Cretaceous association of shell beds and organic-rich shale: Bivalve exploitation of a nutrient-rich, anoxic sea-floor environment. *Palaios*, **19**, 156-169.

Jones, G.A. and Kaiteris, P. 1983. A vacuum-gasometric technique for rapid and precise analysis of calcium carbonate in sediments and soils. *Journal of Sedimentary Petrology*, **53**, 655-660.

Karlin, R., and Levi, S. 1983. Diagenesis of magnetic minerals in Recent haemipelagic sediments. *Nature*, **303**, 327-330.

Karlin, R., and Levi, S. 1985. Geochemical and sedimentological control of magnetic properties of hemipelagic sediments. *Journal of Geophysical Research*, **90**, 10373-10392.

Keller, G., Berner, Z., Adatte, T., and Stueben, D. 2004. Cenomanian-Turonian and $\delta^{13}C$, and $\delta^{18}O$, sea level and salinity variations at Pueblo, Colorado. *Palaeogeography, Palaeoclimatology, Palaeoecology*, **211**, 19-43.

Kennedy, W.J., Walaszczyk, I., and Cobban, W.A. 2005. The Global Boundary Stratotype Section and Point for the base of the Turonian Stage of the Cretaceous: Pueblo, Colorado, U.S.A. Episodes: Journal of International *Geoscience*, **28**, 93-104.

Kump, L. R. and Arthur, M.A. 1999. Interpreting carbon-isotope excursions: carbonates and organic matter. *Chemical Geology*, **161**, 181-198.

Leithold, E.L. and Dean, W.E. 1998. Depositional processes and carbon burial on a Turonian prodelta at the margin of the Western Interior Seaway. Stratigraphy and paleoenvironments of the Cretaceous Western Interior Seaway, USA, SEPM: Concepts in Sedimentology and Paleontology, **6**, 189-200.

Meyers, S.R., and Sageman, B.B. 2004. Detection, quantification, and significance of hiatuses in pelagic and hemipelagic strata. *Earth and Planetary Science Letters*, **224**, 55-72.

Meyers, S.R., Sageman, B.B., and Lyons, T.W. 2005. Organic carbon burial rate and the molybdenum proxy: Theoretical framework and application to Cenomanian-Turonian oceanic anoxic event 2. *Paleoceanography*, **20**, PA2002. doi:10.1029/2004PA001068.

Meyers, S.R., Siewert, S.E., Singer, B.S., Sageman, B.B., Condon, D.J., Obradovich, J.D., Jicha, B.R., and Sawyer, D.A. 2012. Intercalibration of radioisotopic and astrochronologic time scales for the Cenomanian-Turonian boundary interval, Western Interior Basin, USA. *Geology*, **40**, 7-10.

Pancost, R.D., Freeman, K.H., and Arthur, M.A. 1998. Organic geochemistry of the Cretaceous Western Interior Seaway: a trans-basinal evaluation. Stratigraphy and paleoenvironments of the Cretaceous Western Interior Seaway, USA, SEPM: Concepts in Sedimentology and Paleontology, **6**, 173-188.

Pedersen, T.F. and Calvert, S.E. 1990. Anoxia vs. productivity: what controls the formation of organic-carbon-rich sediments and sedimentary rocks? *The American Association of Petroleum Geologists Bulletin*, **74**, 454-466.

Pratt, L.M. 1984. Influence of paleoenvironmental factors on preservation of organic matter in Middle Cretaceous Greenhorn Formation, Pueblo, Colorado. *The American Association of Petroleum Geologists Bulletin*, **9**, 1146-1159.

Rabalais, N.N., Turner, R.E., and Wiseman, W.J. 2002. Gulf of Mexico Hypoxia, A.K.A. "The Dead Zone". *Annual Review of Ecology, Evolution, and Systematics*, **33**, 235-263. doi: 10.1146/annurev.ecolsys.33.010802.150513.

Radiation Solutions Inc. 2010. RS-220GN Super-IDENT gamma_neutron handheld gamma-ray spectrometer: system description manual. Mississauga, Ontario, Canada. www.radiaitonsolutions.ca.

Sageman, B.B. and Bina, C.R. 1997. Diversity and species abundance patterns in Late Cenomanian black shale biofacies, Western Interior, US. *Palaios*, 449-466.

Sageman, B.B., Rich, J., Arthur, M.A., Birchfield, G.E., and Dean, W.E. 1997. Evidence for Milankovitch periodicities in Cenomanian-Turonian lithologic and geochemical cycles, Western Interior U.S.A.. *Journal of Sedimentary Research*, **67**, 286-302.

Sageman, B.B., Meyers, S.R., and Arthur, M.A. 2006. Orbital time scale and new C-isotope record for Cenomanian-Turonian boundary stratotype. *Geology*, **34**, 125-128.

Sageman, B.B., Rich, J., Arthur, M.A., Dean, W.E., Savrda, C.E., and Bralower, T.J. 1998. Multiple Milankovitch Cycles in the Bridge Creek Limestone (Cenomanian-Turonian), Western Interior Basin. Stratigraphy and paleoenvironments of the Cretaceous Western Interior Seaway, USA, SEPM: Concepts in Sedimentology and Paleontology, **6**,153-171.

Savrda, C.E. 1998. Ichnology of the Bridge Creek Limestone: Evidence for temporal and spatial variations in paleo-oxygenation in the western interior seaway. Stratigraphy and paleoenvironments of the Cretaceous Western Interior Seaway, USA, SEPM: Concepts in Sedimentology and Paleontology, **6**, 127-136.

Savrda, C.E. 1998. Ichnocoenoses in the Niobrara Formation: implications for benthic oxygenation histories. Stratigraphy and paleoenvironments of the Cretaceous Western Interior Seaway, USA, SEPM: Concepts in Sedimentology and Paleontology, **6**, 137-151.

Savrda, C.E. 2007. Trace fossils and marine benthic oxygenation. Trace fossils: *Concepts, Problems, Prospects*. Miller ed. Elsevier, Oxford.

Savrda, C.E., and Bottjer, D.J. 1994. Ichnofossils and Ichnofabrics in rhythmically bedded pelagic/hemi-pelagic carbonates: recognition and evaluation of benthic redox and scour cycles. *Special Publications of the International Association of Sedimentologists*, **19**, 195-210.

Schlanger, S.O., and Jenkyns, H.C. 1976. Cretaceous oceanic anoxic events: causes and consequences. *Geologie en Mijnbouw*, **55**, 179-184.

Shurr, G.W., Ludvigson, G.A., Hammond, R.H. 1994. Perspectives on the Eastern Margin of the Cretaceous Western Interior Basin. Geological Society of America, Boulder: Special Paper#287, 264 p.

Slingerland , R.L., Kump, L.R, Arthur, M.A., Fawcett, P.J., Sageman, B.B., and Barron, E.J. 1996. Estuarine circulation in the Turonian western interior seaway of North America. *Geological Society of America Bulletin*, **108**, 941-952.

Snow, L.J., Duncan, R.A., and Bralower, T.J. 2005. Trace element abundances in the Rock Canyon Anticline, Pueblo, Colorado, marine sedimentary section and their relationship to Caribbean plateau construction and ocean anoxic event 2. *Paleoceanography*, **20**, PA3005. doi:10.1029/2004PA001093.

Tribovillard, N., Algeo, T.J., Lyons, T., and Riboulleau, A. 2006. Trace metals as paleoredox and paleoproductivity proxies: an update. *Chemical Geology*, **232**, 12-32.

Turgeon, S.C. and Creaser, R.A. 2008. Cretaceous anoxic event 2 triggered by a massive magmatic episode. *Nature*: *Letters*, **454**, 323-326.

Tyson, R.V. and Pearson, T.H. 1991. Modern and ancient continental shelf anoxia: an overview. *Geological Society, London, Special Publications*, **58**, 1-24. doi:10.1144/GSL.SP.1991.058.01.01.

Wedepohl, K.H., 1971. Environmental influences on the chemical composition of shales and clays. In: Ahrens, L.H., Press, F.,Runcorn, S.K., Urey, H.C. (Eds.), Physics and Chemistry of the Earth. Pergamon, Oxford, pp. 305–333.

CHAPTER 3: LITHO- AND CHEMOSTRATIGRAPHIC CORRELATION FROM UPPER EAGLE FORD FORMATION OUTCROPPING AT LOZIER AND ANTONIO CANYONS, NEAR LANGTRY, TEXAS, TO THE CENOMANIAN–TURONIAN BOUNDARY GSSP, PUEBLO, COLORADO

ABSTRACT

The question concerning spatial and temporal variation in benthic oxygen conditions throughout the Cretaceous Western Interior Seaway (CWIS) is further studied here by focusing on a site proximal to the Tethys Sea. The paleoenvironmental data for the interval that represents Oceanic Anoxic Event II (OAE II) could not be collected due to lack of correlating synchronous horizons among other parts of the CWIS. This correlation is made here with a series of new interpretations for the Upper Eagle Ford Formation succession that outcrops along Antonio Canyon and Lozier Canyons , near Langtry, TX, which places the start of OAE II, as recognized by distinctive positive excursions in $\delta^{13}C_{organic}$ and $\delta^{13}C_{carbonate}$ signals, ~5 m below the current placement. Lithology that matches the Cenomanian–Turonian Global Boundary Stratotype Section and Point (CTB GSSP) outcrop and USGS Portland Core, both in Colorado, to the Lozier Canyon and Antonio Canyon outcrops, substantiates this new interpretation by identifying the base of the basal Bridge Creek Limestone, Bed 63, and the base of the basal Upper Eagle Ford bed as a synchronous horizon. These correlations are corroborated by field, lab, and well-log GRS data, where a strong shift to low GRS values occurs at this horizon, and the lithology changes from calcareous shale to intercalated calcareous shale and limestone beds, the same lithologic pattern as the CTB GSSP and Portland Core.

Extending the OAE II interval to the base of the Upper Eagle Ford Formation does not interfere with current biostratigraphic interpretations for the Lozier and Antonio Canyon outcrops. Further, beds sampled spanning the initial position OAE II succession at Antonio and

Lozier Canyon sites show organic carbon concentrations and trace fossil fabrics that depict low benthic oxygen conditions, which only match the paleoenvironmental conditions of the CTB GSSP and Portland Core in strata post-OAE II.

The CTB and end of OAE II cannot be identified in the Lozier and Antonio Canyon outcrops until more research is performed on the interval between the Lower Eagle Ford–Upper Eagle Ford contact and up-section through the OAE II interval.

INTRODUCTION

The Middle–Late Cretaceous Eagle Ford Formation is exposed near Langtry, TX, in the well-known Lozier Canyon and connected Antonio Canyon outcrops (Figure 3.1; Donovan and Staerker, 2010; Donovan et al., 2012). The current placement of the Cenomanian–Turonian Boundary (~93.9 Ma) in these successions occurs in Facies C2, approximately 20 m above the K65 transgressive surface (TS), which divides Facies C1 and C2 (Figure 3.2; Donovan et al., 2012). The Cenomanian–Turonian Global Boundary Stratotype Section and Point (CTB GSSP), situated just outside Pueblo, CO (Site 3, Figure 3.1), is the global standard stratotype designated to represent global ocean and atmospheric conditions at that time (Kennedy et al., 2005). The CTB is located within the Bridge Creek Limestone Member of the Greenhorn Formation at the base of Bed 86 (Figures 3.2, 3.3). This is ~4.5 m above the base of Bed 63, which marks the contact between Hartland Shale and Bridge Creek Limestone Members (Fig 3.2; Kennedy et al., 2005). The K65TS horizon in the Eagle Ford Formation, between Facies C1 and C2, is interpreted by Donovan et al. (2012) to be synchronous with the contact between Hartland Shale and Bridge Creek Limestone Members of the Greenhorn Formation in the Cretaceous Western Interior Seaway (CWIS; Figures 3.2, 3.3)

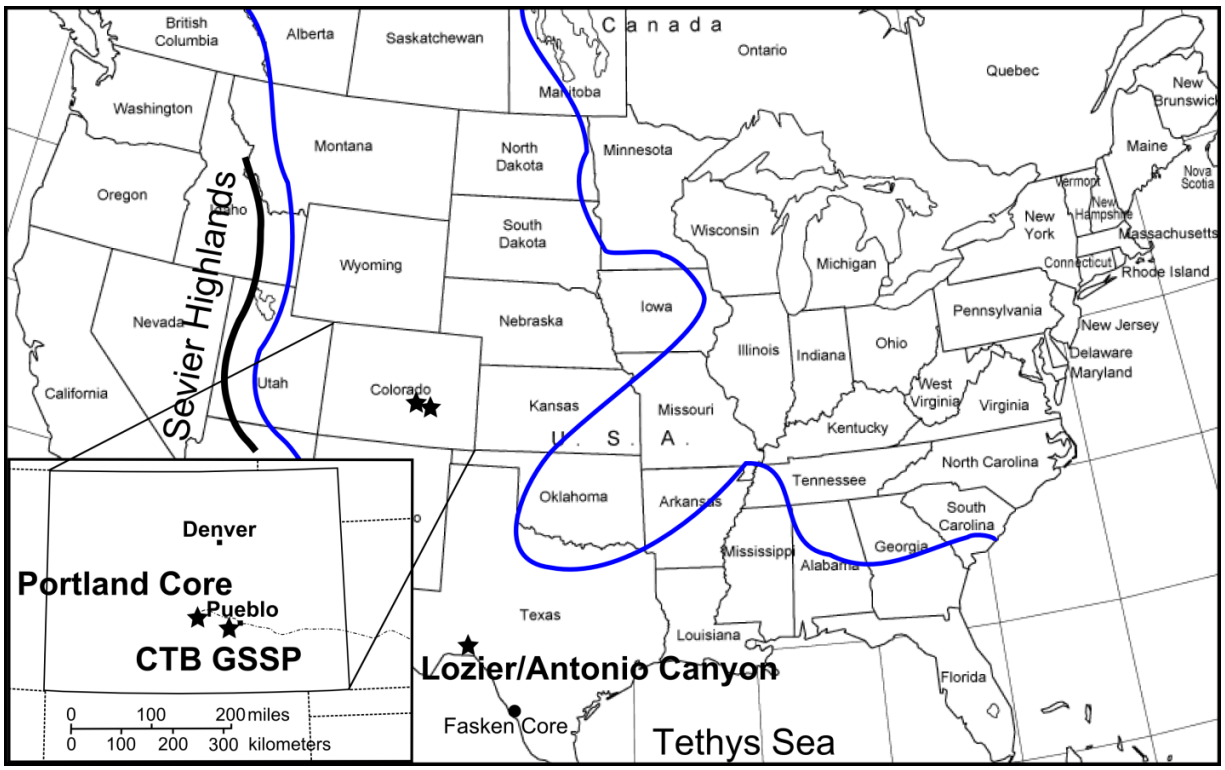

Figure 3.1 Location of field sites and cores in the Cretaceous Western Interior Seaway (CWIS). Bold blue lines represent the CWIS shoreline at maximum transgression at ~94 Ma; modeled after Cobban et al. (1994) and Slingerland et al. (1996). In the central portions of the CWIS, stars indicate USGS Portland core from Florence, CO and Cenomanian–Turonian Boundary GSSP (CTB GSSP) railroad cut south of Pueblo, CO. To the south, Antonio Canyon and Lozier Canyon outcrops, near Langtry, TX. The point represents Fasken Core from Webb County, TX, reported in Corbett and Watkins (2013). Modified from Grosskopf (2015a).

Corresponding $\delta^{13}C_{organic}$ and $\delta^{13}C_{carbonate}$ data between the Antonio Canyon outcrop and CTB GSSP are used by Donovan et al. (2012) to make this correlation, determining the height of the CTB and duration of Oceanic Anoxic Event II (OAE II) in the Eagle Ford Formation at Lozier and Antonio Canyon outcrops. OAE II is recognized as a global positive shift in $\delta^{13}C_{organic}$ and $\delta^{13}C_{carbonate}$ values (Figure 3.2). The heavily-studied CTB GSSP has carbon isotope data, among others, as well as direct correlation to the USGS Portland Core (Site 2, Fig 3.1), drilled in Fremont County, CO, ~100 km to the west of Pueblo, CO. The abundance of data collected from

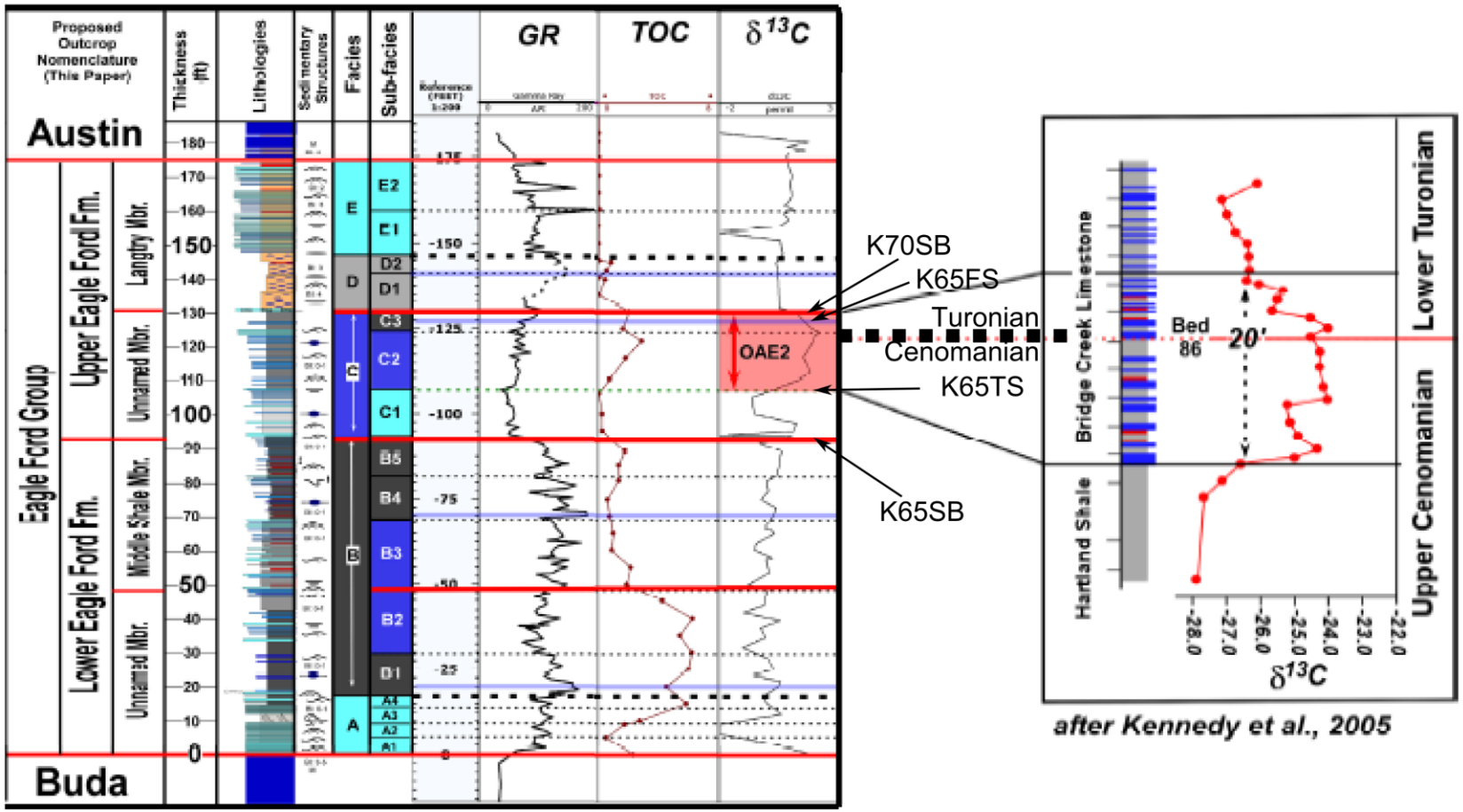

Figure 3.2 The Eagle Ford Formation nomenclature and well-log GRS (in API), TOC, and $\delta^{13}C$ curves for Lozier Canyon outcrop with Donovan et al. (2012) correlation to the CTB GSSP (right). Modified from Donovan et al. (2012).

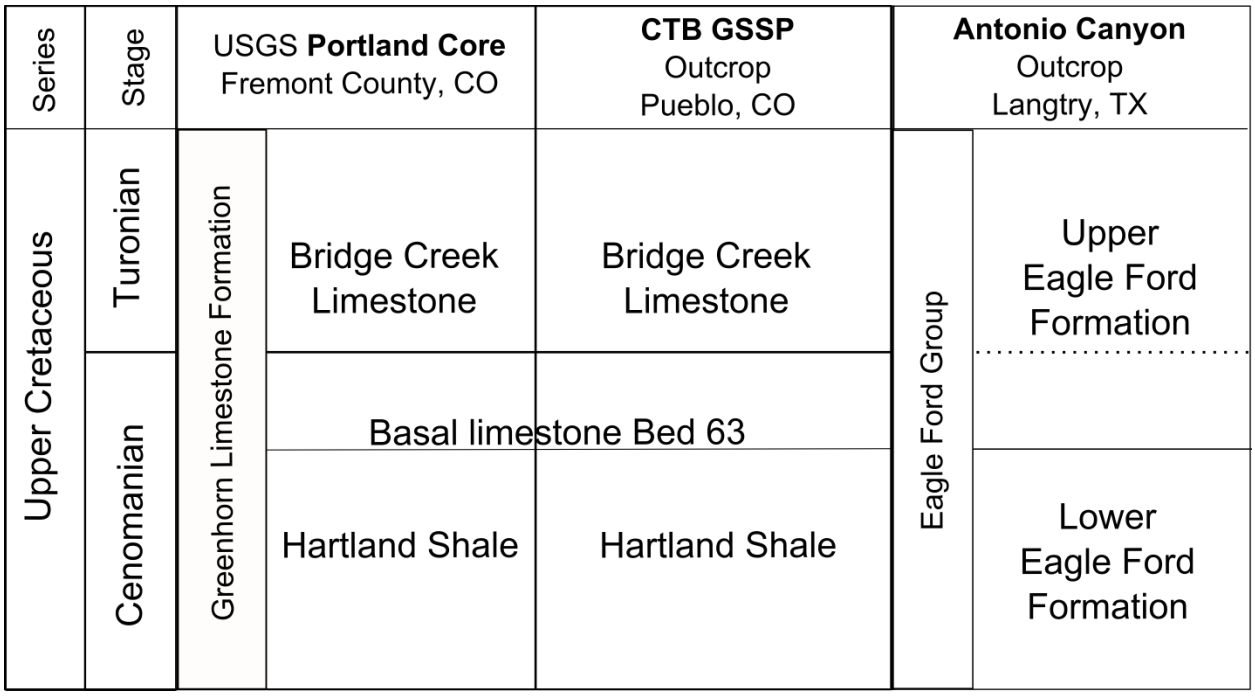

Figure 3.3 Simplified stratigraphic framework for CWIS strata spanning OAE II among the three sites in the CWIS. Solid line represents where the CTB is known, and dotted line represents in what stratigraphic unit it is found when the exact placement is unknown.

these two sites as well as the amount of geologic time they represent, make correlation of these sections to the Eagle Ford Formation outcrops possible on short and long time-scales.

In this paper, data from CTB GSSP outcrop and Portland Core are used in deriving an alternate interpretation to that of Donovan et al. (2012). The alternate interpretation establishes a correlative horizon between the Hartland Shale–Bridge Creek Limestone contact at the CTB GSSP, into the Eagle Ford Formation outcrops. An alternate interpretation of the $\delta^{13}C$ signal that corresponds with OAE II is determined as well.

METHODS

Magnetic Susceptibility (χ)

Low-field bulk magnetic susceptibility (χ) is a geophysical tool used in stratigraphy to track changes in sediment flux driven by orbitally-forced, long-term climate changes (Ellwood et al., 2000). χ is the acquired magnetization of a rock sample placed in an inducing magnetic field. The concentration of paramagnetic, diamagnetic, and ferrimagnetic minerals in a rock sample dictates the χ value. Paramagnetic minerals, such as biotite and illite, are derived from terrigenous sources. Calcite and quartz are examples of diamagnetic minerals, which are usually found in marine depositional settings. Paramagnetic materials acquire a small, but positive induced magnetism in the presence of an applied magnetic field. Diamagnetic materials have very low negative susceptibility values. Magnetite is an example of a ferrimagnetic mineral. Ferrimagnetic materials exhibit strong χ values, but in marine sediments magnetite is destroyed by sulfate-reducing bacteria (Karlin and Levi, 1983; Karlin and Levi, 1985) limiting their impact in many marine rocks. In addition, due to the extremely low alternating magnetic fields in which χ is measured, single domain and pseudo-single domain magnetite grains generally do not acquire an induced magnetization (χ), and will not contribute to χ unless concentrations of these grains are high (Ellwood et al., 2000; Ellwood et al., 2006).

χ values for marine rocks generally range from $1x10^{-09}$ – $1x10^{-07}$ (Ellwood et al., 2000). In a facies sense, higher χ values tend to support those depositional environments that are proximal to terrigenous sources, as weathered continental rocks tend to have a higher concentration of paramagnetic and ferrimagnetic minerals than marine facies that are mainly composed of diamagnetic materials (Ellwood, 2006). Both Eagle Ford and Greenhorn Formation sections that represent OAE II-time, are similar in lithology. Each are composed of intercalated

beds of limestone and calcareous shales. The χ values for these rocks range between 1.0 x 10^{-09} – 1.0 x10^{-08}, well within expected values for rocks where χ results dominantly from paramagnetic minerals. Limestone beds represent times of sediment starvation and carbonate productivity, and are consequently recognized by lower χ values, while calcareous shales represent slightly higher values (Sageman et al., 1997; Ellwood et al., 2008; Grosskopf, 2015b). Strong positive spikes in χ values from these locations indicate bentonite beds, mainly because χ in these beds are dominated by ferrimagnetic constituents.

χ samples were collected at 0.05 m intervals at the Antonio Canyon outcrop along an 8 m section spanning from the base of the 115 Foot limestone bed in Facies C2, up through Facies D (Figure 3.2). χ samples reported by Ellwood et al. (2008) for the CTB GSSP and Portland Core were collected at the same 0.05 sampling interval, although some portions of the Portland Core were sampled at 0.10 m intervals. In preparing the samples, ~0.01 kg of sample was crushed before measurement in the mass-dependent Williams Magnetic Susceptibility Bridge at Louisiana State University. χ is calculated relative to mass of the sample and the mean of three χ readings are used as the reported χ values.

Gamma-ray spectroscopy

Gamma-ray spectroscopy (GRS) using a portable gamma-ray spectrometer is a useful tool for correlation in the field. The RS-125 Super Gamma-Ray handheld Spectrometer used in this research detects the amount of ^{40}K directly, and extrapolates for U and Th using decay proxies. These data have the same trends as do χ data [e.g. (Ellwood et al., 2013; Grosskopf, 2015a; Grosskopf, 2015b)] in that ^{40}K is detritally-derived, where higher concentrations are expected in facies proximal to terrigenous sources.

The NaI crystal in the spectrometer detects radiation levels in a $1m^3$ cone-shaped field of influence from the front of the detector (Radiation Solutions Inc., 2010). This large area will, in effect, smooth stratigraphic readings through the section by collecting gamma radiation readings from strata around the targeted sampling spot. Therefore, sampling interval was adjusted based on what is being detected.

For the case of the strata spanning the OAE II interval in the Greenhorn and Eagle Ford Formations, decimeter-scale variation in bed types is the prevalent lithology. A test was conducted at the CTB GSSP determining the best sampling interval for these types of strata using the handheld spectrometer. A sampling interval of 0.10, 0.20, 0.30, and 0.40 m was tested (Figure 3.4). It was determined that 0.10 m spacing is the best for finer lithologic changes in the strata. Data were collected for 120 seconds at each sample location.

Field GRS data from Antonio Canyon contributed by Donovan (personal communication) for this research were collected at ~0.30 m intervals for a time interval less than of 60 seconds. This resulted in the dataset having values for ^{40}K, U, and Th, that do not correlate well to other sites. In order to derive meaningful GRS data for Antonio Canyon section, the samples collected for χ were placed in a germanium gamma-ray detector in the nuclear physics laboratory at Louisiana State University and run for 1 hour each. Mass for laboratory GRS samples ranged from 0.02–0.05 kg. K, U, and Th counts were calculated from detection of their isotopes: ^{40}K, ^{214}Bi (daughter isotope proxy for U), and ^{218}Ac (daughter isotope proxy for Th).Well-log GRS values are reported for the Portland Core in API units and were measured at ~0.06 m intervals. These are public domain core data from the Western Interior Seaway Drilling Project (Dean and Arthur, 1998). The core is stored at the USGS Core Research Center in Denver, CO.

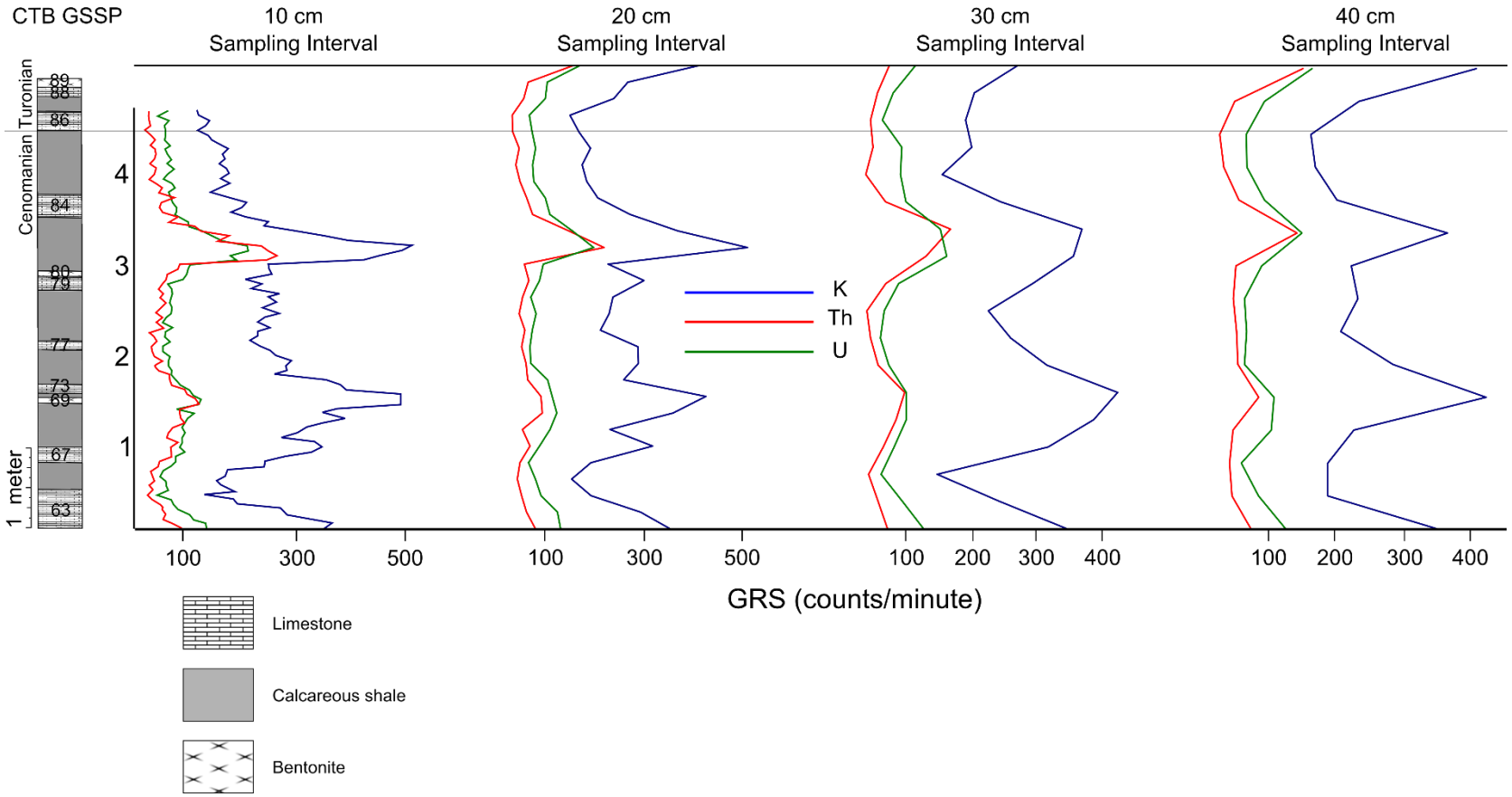

Figure 3.4 Field GRS sampling measurement at the CTB GSSSP at 0.1, 0.2, 0.3, and 0.4 m intervals at the CTB GSSP.

RESULTS

χ as well as field, laboratory, and well-log GRS datasets correlate well at the CTB GSSP and Portland Core (Figure 3.5). These datasets correlate well with lithology where every shift to low levels in χ and GRS curves represents a limestone bed and every shift to higher values represents a calcareous shale bed. Sharp shifts to hight levels represent bentonite marker beds. These data also correlate well with each other in the Antonio Canyon outcrop, and closely match the lithology (Figure 3.6). Lab GRS data reported in Figure 3.6 are in total counts, or sum of ^{40}K, Th, and U, in counts $gram^{-1}$ hr^{-1}. Figure 3.7 shows these data for each individual element.

Figure 3.8 shows an expanded dataset of χ and well-log GRS values from the Portland Core, spanning OAE II-time, for much of the Greenhorn Formation, including the Hartland Shale and Bridge Creek Limestone contact. Scaled alongside it is the well-log GRS curve for Antonio Canyon, modified from Donovan et al. (2012).

DISCUSSION

Correlation between Antonio and CTB GSSP Sections

There is a unique transition in lithology in all sections sampled from continuous strata of calcareous shale, followed by an abrupt contact at the base of a thick limestone bed, and then the onset of intercalated limestone and calcareous shale beds above the contact. This indicates that the Bridge Creek Limestone and Hartland Shale contact is synchronous with the Lower Eagle Ford and Upper Eagle Ford Formation contacts at the K65 sequence boundary (SB), rather than the Facies C1–C2 contact (K65TS) as indicated by Donovan et al. (2012). At the CTB GSSP and Portland Core this sequence is represented by the Hartland Shale, the Hartland Shale–Bridge Creek Limestone contact, and Bridge Creek Limestone above (Figures 3.2, 3.3). At the Antonio

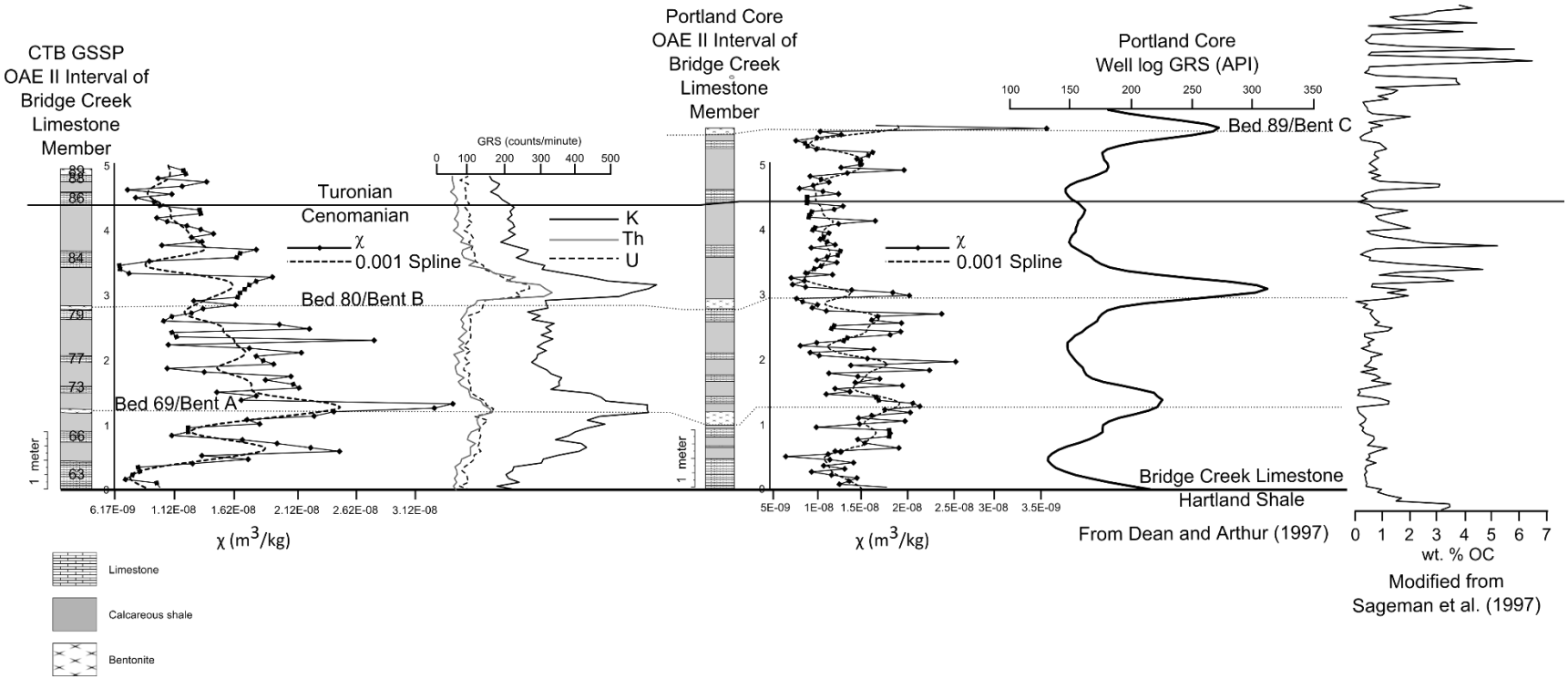

Figure 3.5 χ, field GRS, and well log GRS (API) dataset correlation for the CTB GSSP and Portland Core. χ and field GRS data for CTB GSSP and the Portland Core data are from Ellwood et al. (2008). Portland Core API data are reported by Dean and Arthur, (1998). Also presented here is the weight percent organic carbon curve modified from Sageman et al., (1997).

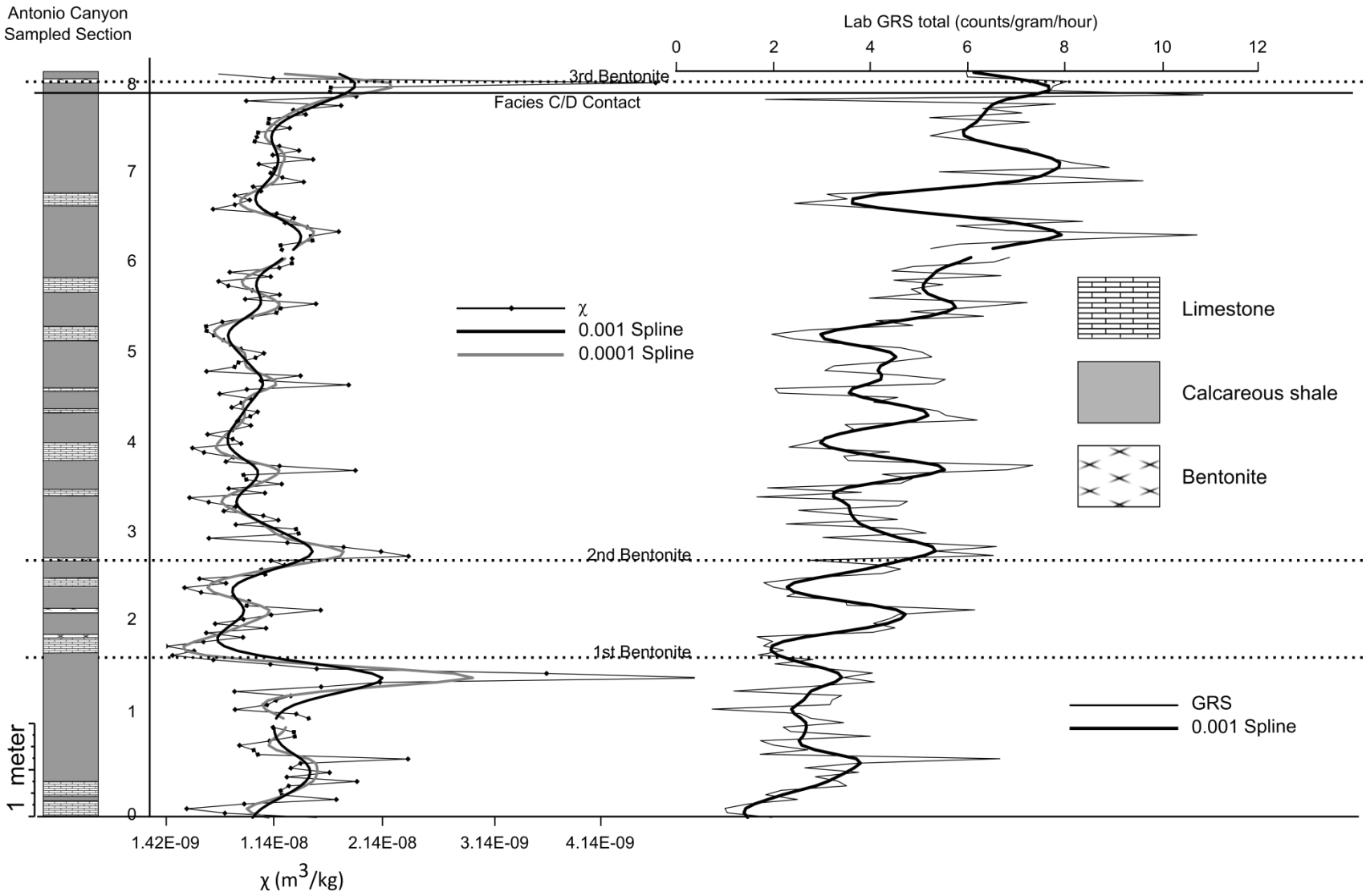

Figure 3.6 χ and total measured GRS counts for the collected Antonio Canyon section. Bentonite layers used in the bentonite correlation tests, discussed later are labeled with dotted lines. Individual counts are shown in Figure 3.7 (next page).

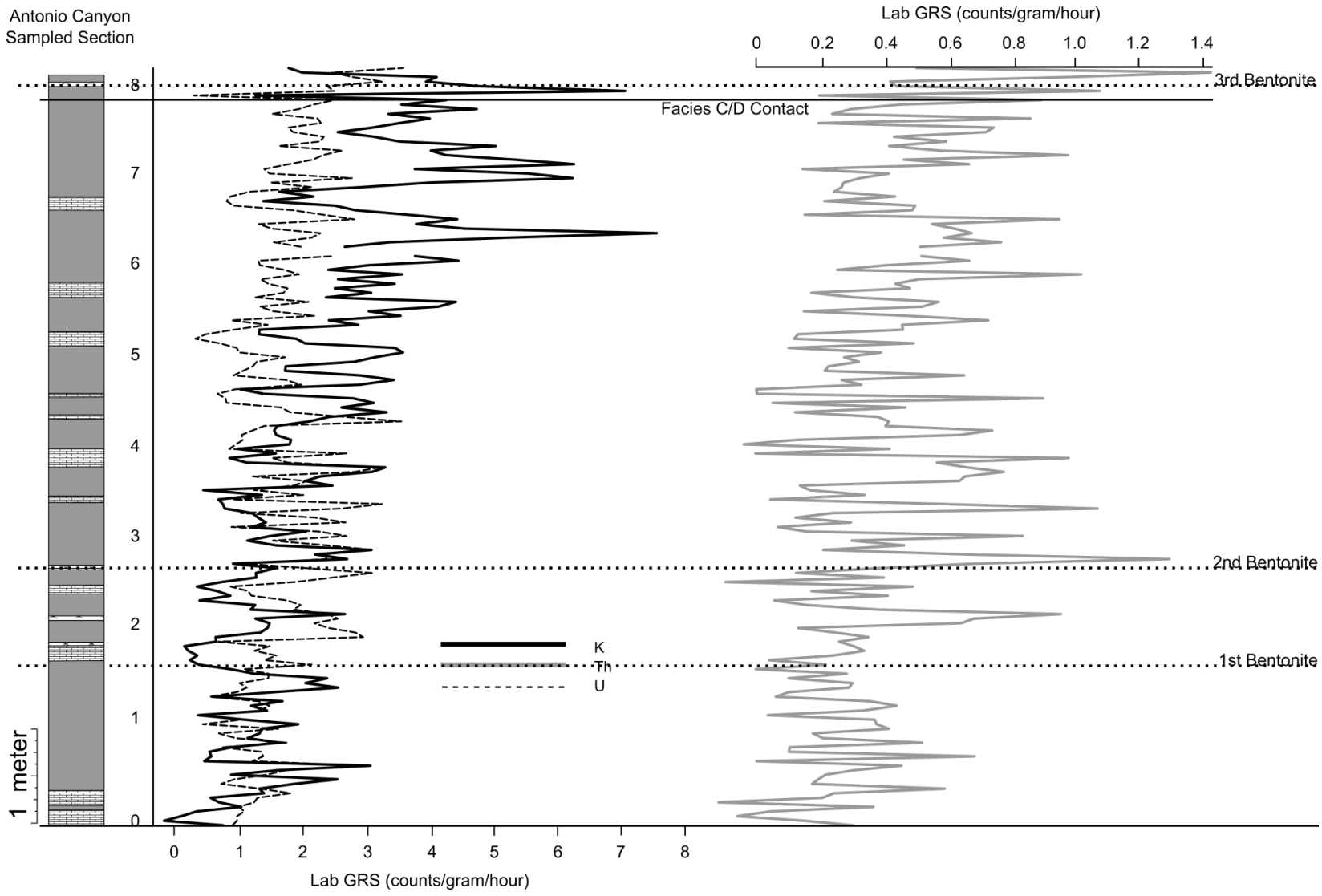

Figure 3.7 ^{40}K, Th, and U measured lab GRS values for the collected Antonio Canyon section. Bentonite layers used in the bentonite correlation tests dotted lines are labeled.

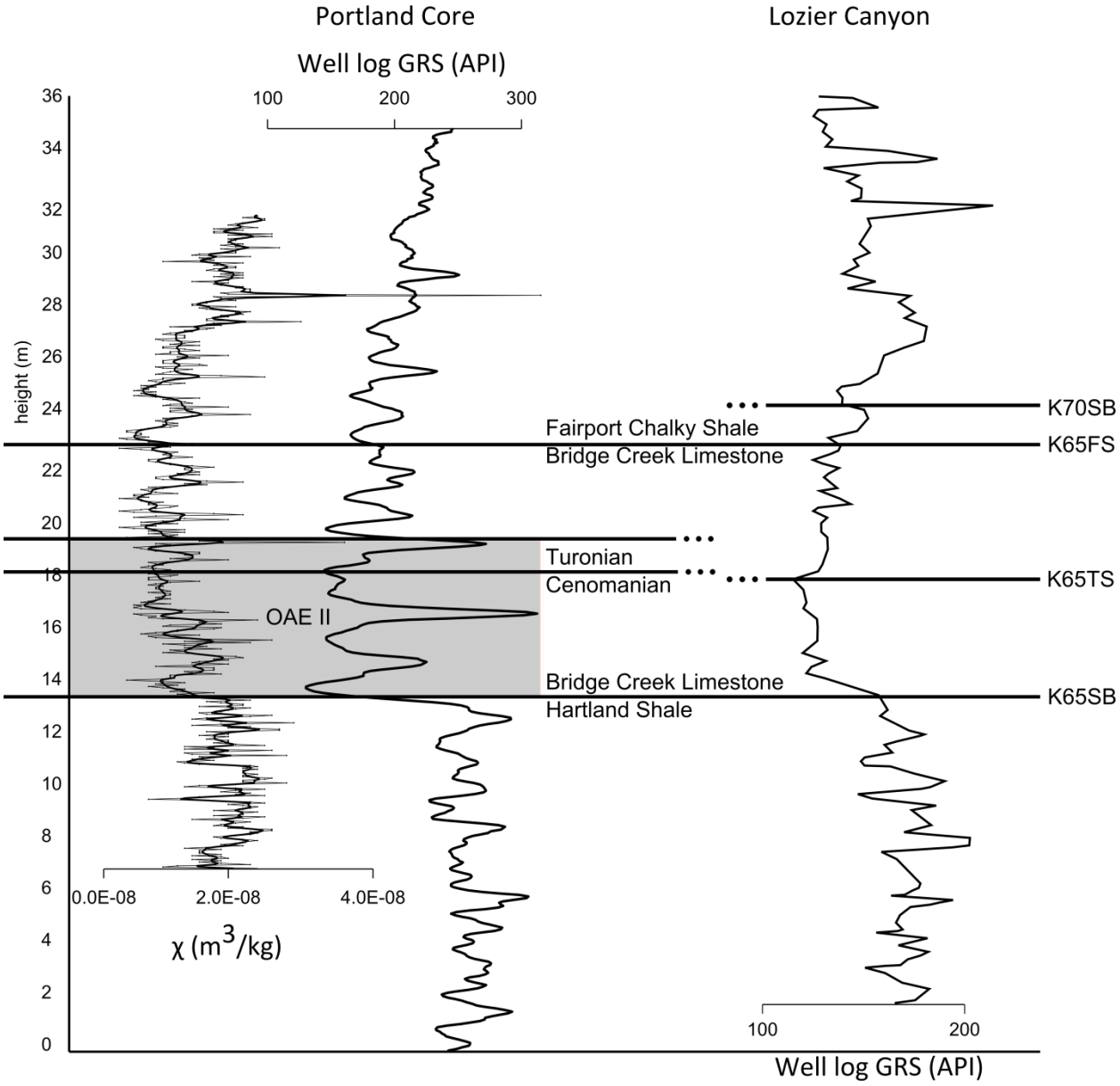

Figure 3.8 χ and well log GRS (API) values from expanded Portland Core section plotted beside Lozier Canyon API GRS data. χ values are from Ellwood et al. (2008). Portland Core API values are from Dean and Arthur (1998). Antonio Canyon API curve is modified from Donovan et al. (2012).

Canyon section, this same sequence is represented by the Lower Eagle Ford Facies B (Middle Shale Member), followed by the Lower Eagle Ford–Upper Eagle Ford contact, and the Upper Eagle Ford Facies C (Unnamed Member) above the contact (Figure 3.2).

The abrupt contact between lithologies, calcareous shale to interbedded limestone and calcareous shale beds is interpreted as the K65 sequence boundary (K65SB) in Donovan and Staerker (2010) and Donovan et al. (2012), and a flooding surface by Elder et al. (1994). The horizon is very apparent throughout CWIS strata. It is traced from the near the western margin, across the deep central axis and to the shallow eastern margin of the seaway (Figure 3.1; Elder et al, 1994; Grosskopf, 2015a; Grosskopf, 2015b), and to northern portions of the seaway in Montana and Canada (Cobban et al., 1976; Grosskopf, 2015a). This horizon represents the same time throughout the seaway. Consequently, the basal limestone, Bed 63 at the CTB GSSP, is the same limestone bed as the base of Upper Eagle Ford Formation (base of Facies C1) at Antonio Canyon. χ and well-log GRS data show these facies changes through the contact. Below the contact, Portland Core χ and well-log GRS values are high, indicating higher concentration of detrital materials (Figure 3.8) represented by calcareous shales, followed by a marked drop in χ and well-log GRS values at the correlative K65SB horizon at Antonio Canyon, which relates to the limestone beds, and then a gradual increase of well-log GRS values up-section after the K65SB horizon.

The relationship of the K65SB horizon between Portland Core strata to Antonio Canyon strata becomes even more apparent when the shift in well-log GRS data is correlated (Figure 3.8). Again, the K65SB is the point at which the Antonio Canyon well-log GRS curve shows a marked decrease, and this directly correlates to the sharp decrease in the Portland Core GRS curve.

CTB GSSP and Portland Core successions are interpreted to be from a deep depositional environment, while deposits in the Antonio Canyon section are interpreted by Goldhammer and Johnson (2001) to represent a shallow (~60 m deep; from Donovan et al., 2012) restricted

platform set higher than the deeper portions (~120 m; from Donovan et al., 2012) of the CWIS. The restricted platform at such a southerly position in the CWIS is exposed to open ocean conditions, and should represent a depositional environment different from the depositional environment in the geographic center of the CWIS. Yet, due to interaction of Tethyan and CWIS waters driving carbonate productivity here as well as other parts of the CWIS (Fischer, 1980; Grosskopf, 2015a; Grosskopf, 2015b), there is a strong correlation in lithology and GRS curves, particularly at the basal limestone Bed 63 between these sections (Figures 3.6–3.8)

Identifying the start of OAE II at Antonio Canyon

Further correlation using the $\delta^{13}C$ curves present in datasets from these sections, as well as biostratigraphy, implies that the Lower Eagle Ford–Upper Eagle Ford contact is synchronous with base of Bed 63 (Hartland Shale–Bridge Creek Limestone contact), and therefore synchronous with the start of OAE II. Corbett and Watkins (2013) use positive excursions from series of cores proximal to the CTB GSSP and Lozier Canyon to show correlation among sites and how these relate to nannofossil ranges and abundances. Grosskopf (2015a) used data from the Fasken "A" #1-H Core (~450 km southeast of the Lozier Canyon section; Figure 3.1) to correlate from the CTB GSSP and Lozier Canyon to the Fasken Core. Figure 3.9 shows the correlation from the Corbett and Watkins (2013) $\delta^{13}C_{carbonate}$ curve and its distinctive parts, A, B, and C compared to the other sections. The expression of OAE II in the $\delta^{13}C_{carbonate}$ curves from the Fasken Core and Lozier Canyon curves spans 10.00 m and 7.50 m, respectively, while the interval is 7 m thick at the CTB GSSP (Figure 3.9). The correlation by Corbett and Watkins (2013) places the start of the positive shift in the $\delta^{13}C_{carbonate}$ curve, representing the start of OAE II, at or just below the base of Bed 63 (Figure 3.9). Their ideal biostratigraphic correlation

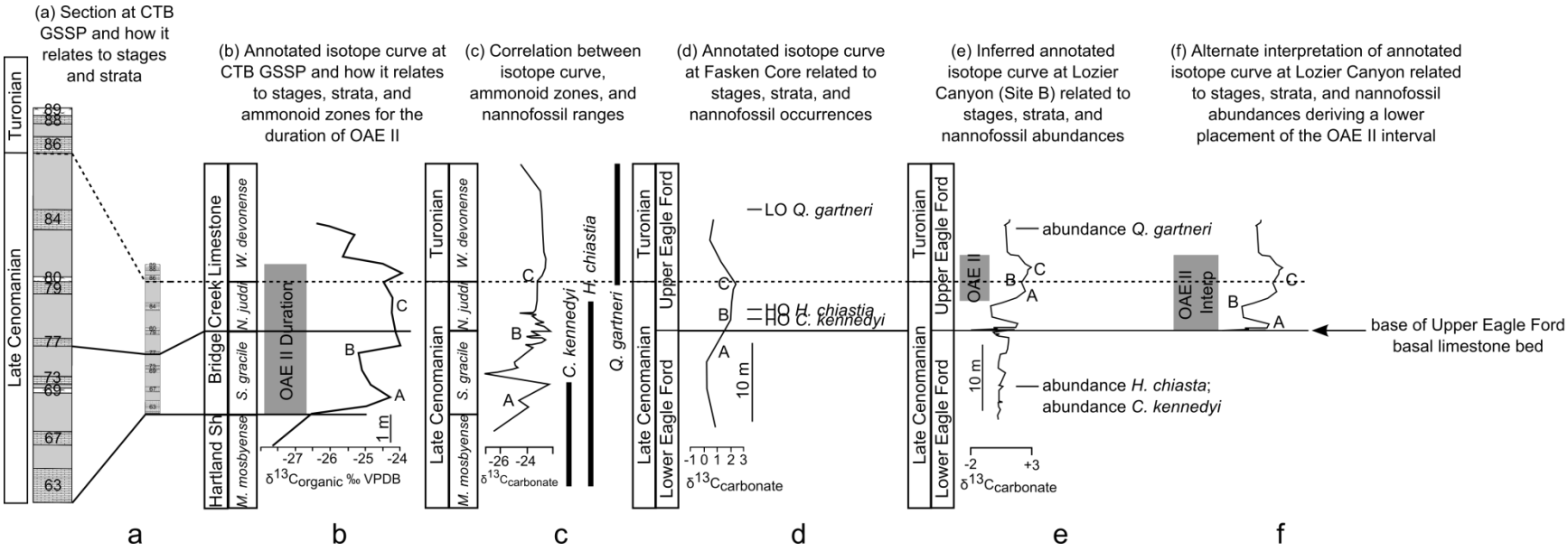

Figure 3.9 Diagram depicting correlation from CTB GSSP/Site 3 to Fasken Core and Antonio Canyon to visually explain an alternate interpretation of OAE II duration at Antonio Canyon. Curves modified from Kennedy et al. (2005), Donovan and Staerker (2010), Donovan et al., (2012), and Corbett and Watkins (2013). Figure taken from Grosskopf (2015a).

matches the nannofossil ranges for three successions and +$\delta^{13}C_{carbonate}$ excursions from Fasken Core. Figure 3.9 also shows the correlation between $\delta^{13}C_{carbonate}$ and $\delta^{13}C_{organic}$ curves, as well as the ammonoid zones for the CTB GSSP. Figures 3.2 and 3.9 depict the Donovan (2012) correlation for the Lozier Canyon section to the CTB GSSP, and using peaks in the $\delta^{13}C_{carbonate}$ curve.

The synchronous horizon represented by well-log GRS data discussed earlier (Figure 3.8), matches the onset of OAE II expressed by the $\delta^{13}C_{carbonate}$ curve for Lozier Canyon, starts farther down-section than the level interpreted by Donovan et al. (2012). The first positive spike in $\delta^{13}C_{carbonate}$ (Figure 3.9) is evidence for the start of OAE II in those strata; ~5 m lower in the section than what is interpreted (Figures 3.2, 3.9). This positive spike in $\delta^{13}C_{carbonate}$ falls at the Lower Eagle Ford–Upper Eagle Ford contact, synchronous with the positive spikes in $\delta^{13}C_{carbonate}$ and $\delta^{13}C_{organic}$ curves at the Hartland Shale–Bridge Creek Limestone contact at the CTB GSSP (Figure 3.9).

This interpretation does not interfere with nannofossil zone interpretations of the last occurrence of *Corollithion kennedyi* and *Helenia chiastia* and the first occurrence of *Quadrum gartneri* from Corbett and Watkins (2013), or the nannofossil abundances from Donovan et al., (2012). The last curve in Figure 3.9 represents the alternate hypothesis of the initial $\delta^{13}C_{carbonate}$ excursion occurring lower at the Lower Eagle Ford–Upper Eagle Ford boundary in the Lozier Canyon section. Note that this may extend the duration of OAE II-time, from 7.5 m to 11 m, which is closer in thickness to the 10 m that is expressed in the Fasken Core (Corbett and Watkins, 2013). This interpretation matches a recently published interpretation by Lowery et al. (2014) for the Lozier and Antonio Canyon outcrops.

Correlation of Antonio Canyon succession to the Central US successions

The evidence presented here suggests that the section sampled for χ and field and lab GRS, as well as readings from well log GRS at the base of the 115 Foot Limestone Bed in Facies C2 at Antonio Canyon, does not represent strata deposited during OAE II-time. This bed is ~5 m above the Lower Eagle Ford–Upper Eagle Ford contact (Figure 3.8).

Testing bentonite marker bed correlations

In the field, bentonite marker beds in the interpreted OAE II portion of the Antonio Canyon section showed poor correlation to bentonite beds from the OAE II sections at the CTB GSSP and Portland Core. In order to determine any correlation of bentonite beds in the Antonio Canyon section to the CTB GSSP and Portland Core sections, the concentration of trace elements was measured for these thick bentonite marker beds that can be traced throughout the CWIS, and strata that represent OAE II-time (Elder, 1988). The ash composing Bed 69, 80, and89 bentonites (also referred to as Bentonites A, B, and C, respectively in CWIS literature) was sourced from subaerial volcanoes in the Sevier Highlands along the western margin of the seaway (Elder, 1988). Paleowind currents carried large quantities of ash eastward into the CWIS where the particles could accumulate and be preserved in the rock record as aerially-extensive bentonite beds. Thickness and broad continuity of these bentonite marker beds make them great tools for correlation to distant sites in the CWIS (Elder, 1988).

Hahn et al. (1979) illustrate the utility of element concentrations in determining if ash beds were derived from a similar source using ratios of certain trace elements. David (2009) used this technique to compare trace element ratios among ash beds from different locations sourced from the same volcano. The two trace element ratio tests, Ba/Rb vs Sr/Rb and Zr/Rb vs Sr/Rb, show similarity in trace element concentrations among related ash beds. Figures 3.10a and 3.10b

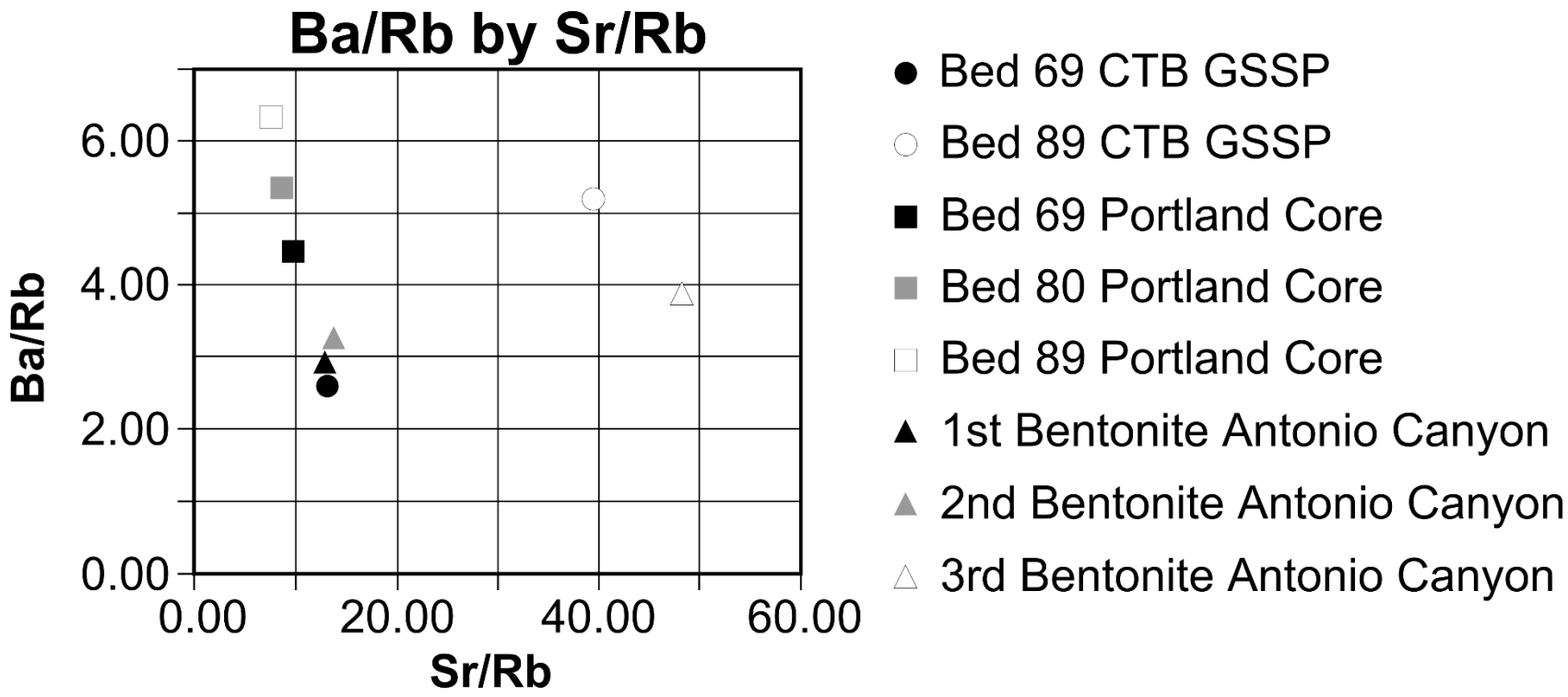

Figure 3.10a Ba/Rb by Sr/Rb trace element ratios for testing bentonite correlations from the CTB GSSP and Portland Core to the collected Antonio Canyon section.

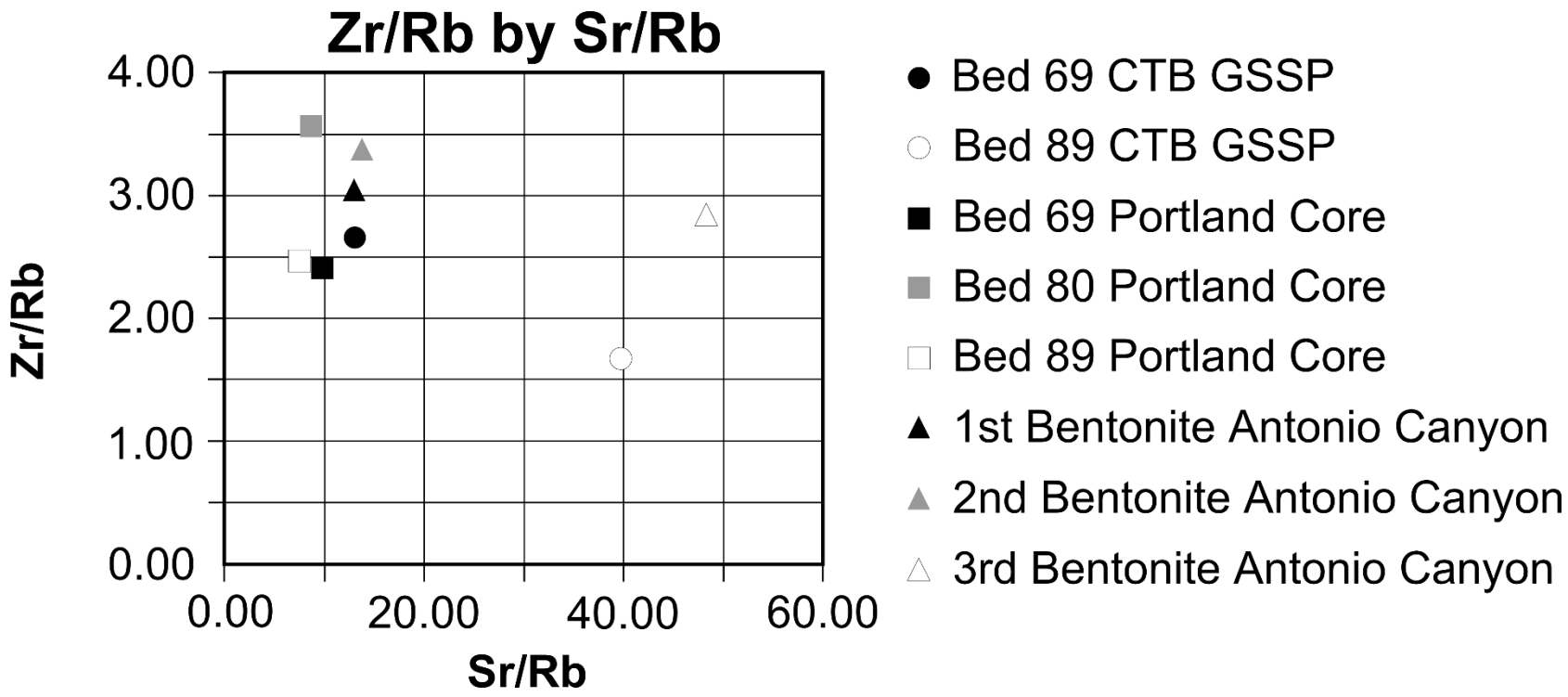

Figure 3.10b Zr/Rb by Sr/Rb trace element ratios for testing bentonite correlations from the CTB GSSP and Portland Core to the collected Antonio Canyon section.

shows the two tests used here to determine the similarity between bentonite beds at the Antonio Canyon section (referred to as the 1st, 2nd, and 3rd Antonio Canyon bentonite beds; heights shown in Figure 3.6) and the CTB GSSP and Portland Core sections. Data used in Figures 3.10a and 3.10b are from bentonite samples collected by Ellwood et al. (2008) and Grosskopf (2015) that were processed by Chemostrat Inc. The trace element ratios from both tests should match if bentonites from the Antonio Canyon section are the strata equivalent to bentonite beds at the Portland Core and CTB GSSP, assuming the specific bentonite bed was derived from the same volcanic source. While there is similarity between the 1st Antonio Canyon bentonite and Bed 69 bentonite at the CTB GSSP, the bentonite beds for the CTB GSSP and Portland Core have poor trace element correlations. The direct lithologic correlation from the CTB GSSP bentonite beds to the Portland Core bentonite beds, and proximity of the two, should result in close values for each individual bentonite bed between the sites for both trace element ratio tests. While there is definite correlation between the CTB GSSP and Portland Core, this is not the case. Outcomes for each correlation test of Antonio Canyon bentonite to those at the CTB GSSP and Portland Core must be rejected.

Sediment accumulation rates and cyclicity

Detrital flux from terrigenous sources affects organic matter production, accumulation, and preservation (Pratt, 1984; Cowie and Hedges, 1992). An increase in detrital material into the basin, develops a sediment-rich freshwater surface layer that increases primary production due to sourcing of nutrients while developing a stratified water column. The production component contributes to the total organic content that could be preserved in the rock record. It also allows for better organic matter preservation potential, under oxygen-poor benthic conditions due to effects of water column stratification, and burial under higher sediment accumulation rates

(SAR). An obvious sign of an increase in preserved organic matter are high total organic carbon (TOC) values (Cowie and Hedges, 1992).

There is a strong relationship between strata type and TOC in CWIS strata (Sageman et al., 1997) in the Upper Bridge Creek Limestone. Underlying the alternating limestone and calcareous shale beds at each site are continuous deposits of calcareous shale: Hartland Shale at CTB GSSP and Portland Cores, and Lower Eagle Ford at Lozier and Antonio Canyons. There is a marked decrease in TOC crossing the contact at the top of these members [Figures 3.2 and 3.5 (reported by Sageman et al.,1997 as weight percent organic carbon)]. TOC levels are relatively low in the lower portions of intercalating limestone and calcareous shale beds, and TOC increases gradually up-section. This increase up-section follows trends in χ, and field and well-log GRS, and suggests the TOC increase is related to SAR.

Multitaper (MTM) and Fourier transform (FT) methods are independent statistical approaches to identify cycles in datasets. MTM and FT for χ data for Antonio Canyon, CTB GSSP, and the Portland Core successions are reported in Figures 3.11a and 3.11b. Robust results for MTM and FT come from sections that represent continuous sedimentation, undisrupted by hiatuses or sediment reworking, and a short, regular, sampling interval to capture any signal in the time that is expressed in that section. MTM and FT methods allow determination of which Milankovitch Cycle best relates to the frequency of cycles exhibited by cyclicity in the successions. Milankovitch frequencies that are represented by the alternating strata found at each section, are precessional, P1 = 18.5 kyr, P2 = 22.5 kyr, and obliquity, O1 = 39 kyr, and O2 = 50.5 kyr [ages calculated for ~93.9 Ma from data reported by Berger et al., (1992)]. The orbital cycle responsible for decimeter-scale bed alternation in these sections is shown to be O1

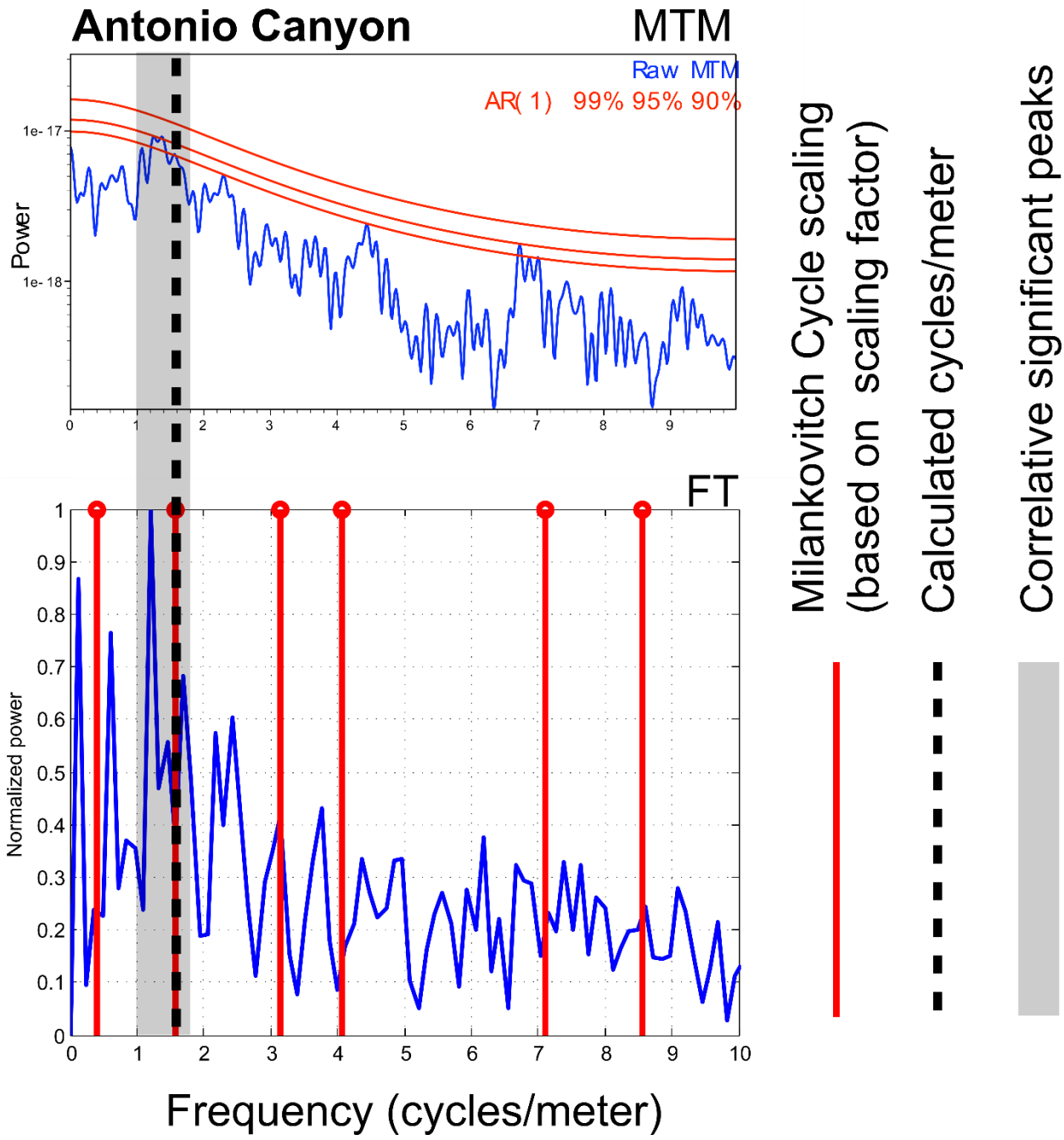

Figure 3.11a Multi-taper (MTM) and Fourier transform (FT) results for CTB GSSP, Portland Core, and Antonio Canyon. Red vertical lines represent peaks that are spaced on a Milankovitch frequency in reference to E1 (~100 kyr eccentricity band) and harmonic number. Dashed black lines represent cycles/meter calculated from splined data (reported later in Figure 3.12a). Grayed zones represent peaks that correlate between MTM and FT results. Red lines in MTM plots represent confidence intervals of 90, 95, and 99%, bottom to top. Portland Core plots half the cycles/meter than that of the other sites due to 0.10 m sampling interval.

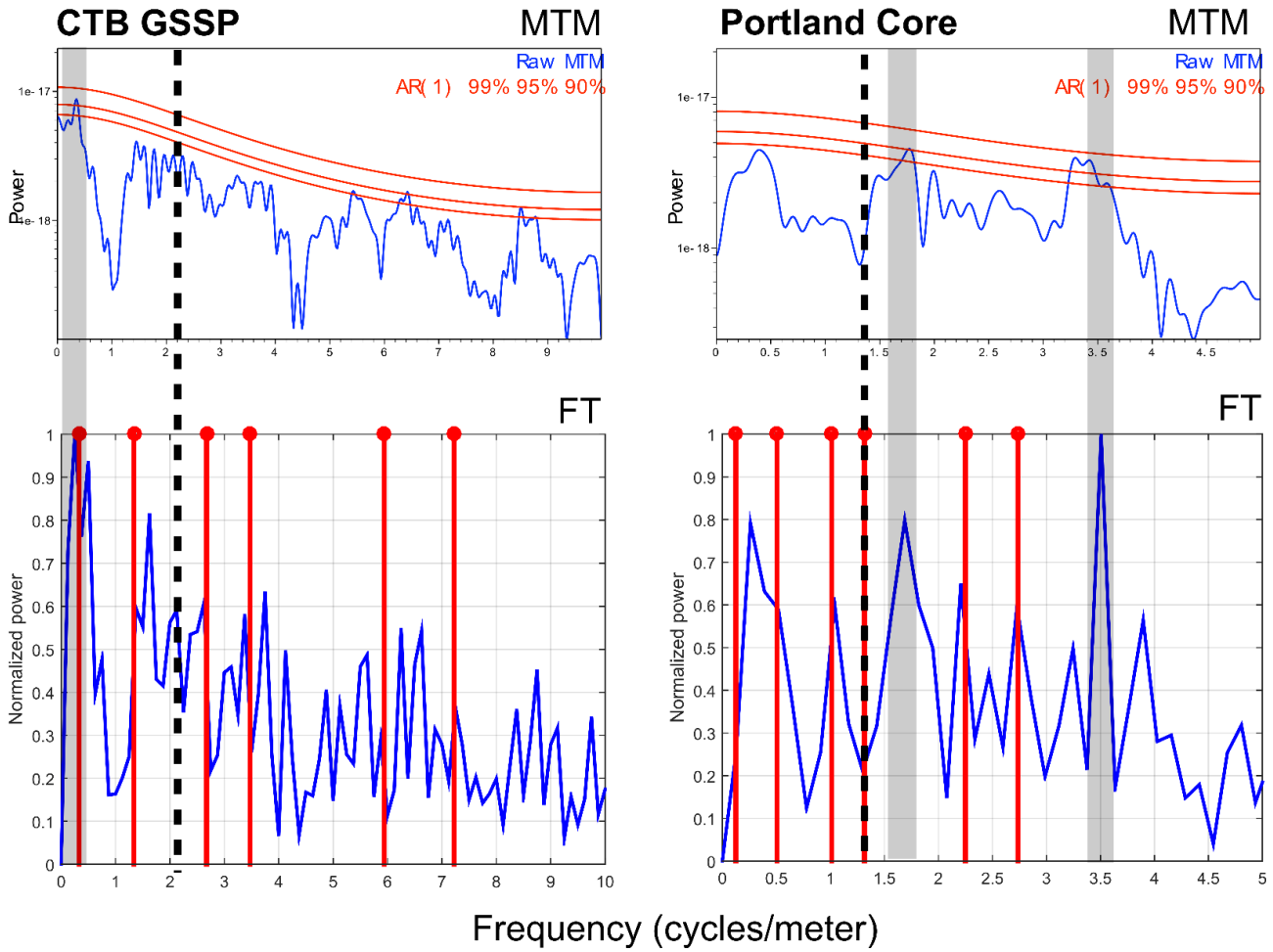

Figure 3.11b Multi-taper (MTM) and Fourier transform (FT) results for CTB GSSP, Portland Core, and Antonio Canyon. Red vertical lines represent peaks that are spaced on a Milankovitch frequency in reference to E1 (~100 kyr eccentricity band) and harmonic number. Dashed black lines represent cycles/meter calculated from splined data (reported later in Figure 3.12b). Grayed zones represent peaks that correlate between MTM and FT results. Red lines in MTM plots represent confidence intervals of 90, 95, and 99%, bottom to top. Portland Core plots half the cycles/meter than that of the other sites due to 0.10 m sampling interval.

(Sageman et al., 1997; Sageman et al., 1998; Sageman et al., 2006; Ellwood et al., 2008; Ellwood et al., 2013). While O1 may be responsible for the decimeter-scaled bedding, Sageman et al. (2006) and Ellwood et al. (2013) show it is the E1 (~100 kyr) eccentricity band that is best expressed in these strata. This is due to inconsistencies in SAR as seen in voluminous ash accumulation represented by thick bentonite beds, and other hiatuses or non-deposition, at least in the Lower Bridge Creek Limestone (Sageman et al., 1997).

Figures 3.12a and 3.12b show the SARs for Antonio Canyon (Fig 3.12a), and CTB GSSP and Portland Core sites (Fig 3.12b). These are derived from smoothed χ data (using splines), from which bar-logs are built. Any shift in the negative or positive direction along the smoothed χ curve represents a change in terrigenous sediment flux, altered by long-term changes to climate. Cyclic shifts in values allude to the role of orbital-forcing on these long-term climate changes. Each bar represents a half cycle, and a whole cycle consists of a set of white and black bars. The amount of cycles present in the section is found and reported in cycles per meter. High TOC levels from the collected section at Antonio Canyon may indicate anoxia due to a paucity of trace fossils. The basal Bridge Creek Limestone, Bed 63, and other laterally-extensive limestone beds, and their correlatable equivalents among different sites throughout the seaway, including the Lozier and Antonio Canyons, show signs of well-oxygenated bottom waters (e.g. Grosskopf, 2015a Figs 1.4, 1.5; Grosskopf, 2015b Figure 2.9) evidenced by the presence of trace fossils. There is a paucity of trace fossils in the limestone beds from the sampled Antonio Canyon section (Figure 3.13). Only limestone beds lower than the collected section show the same level of bioturbation observed at other sites throughout the CWIS (Figure 3.13).

Another point of dissimilarity between the section collected at Antonio Canyon, and those successions representing OAE II, the CTB GSSP and Portland Core, is the level of

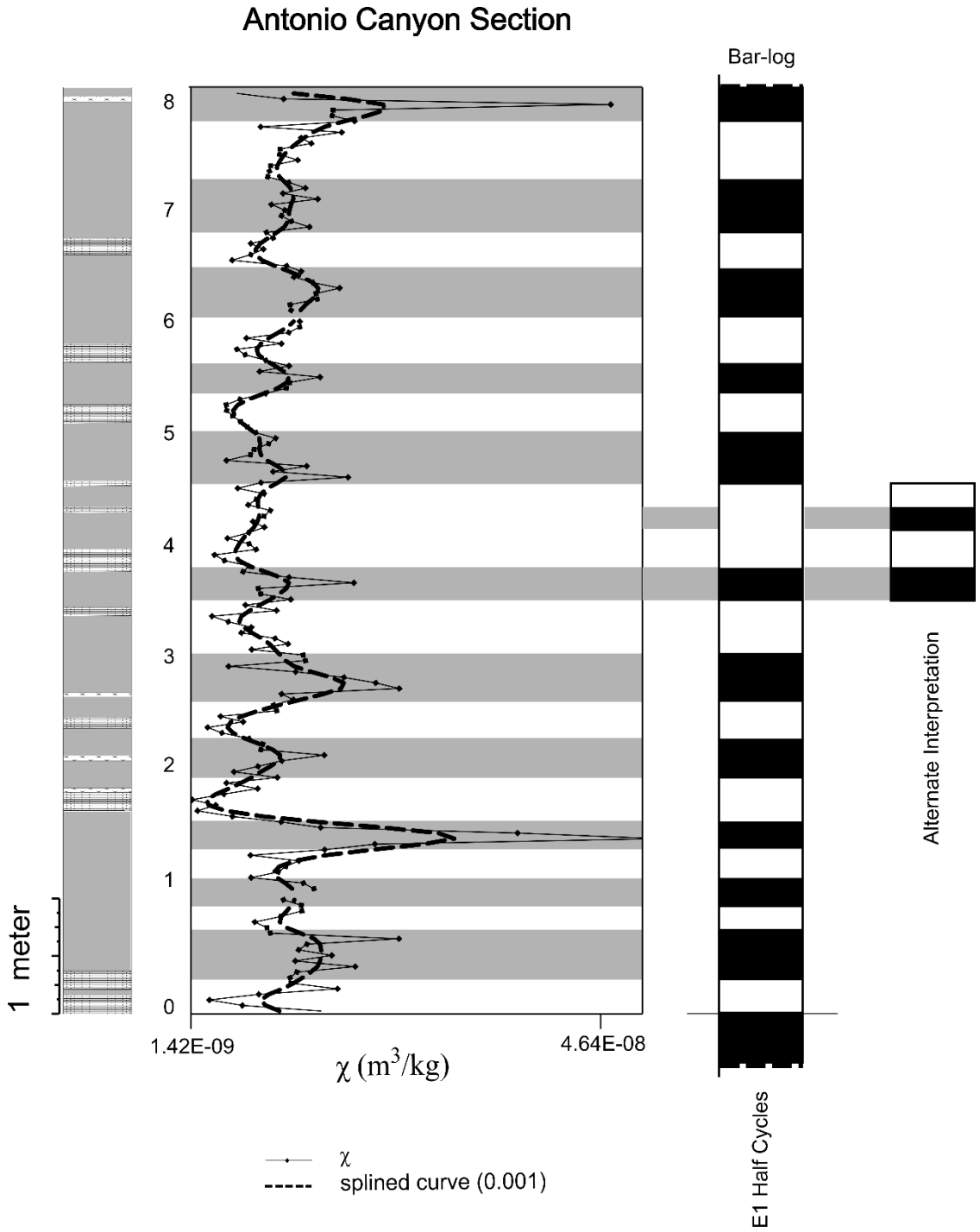

Figure 3.12a Bar-log derivation from χ data for Antonio Canyon section. Shaded areas on the splined χ curve indicate bar-log divisions. Bar logs show half cycles for the section.

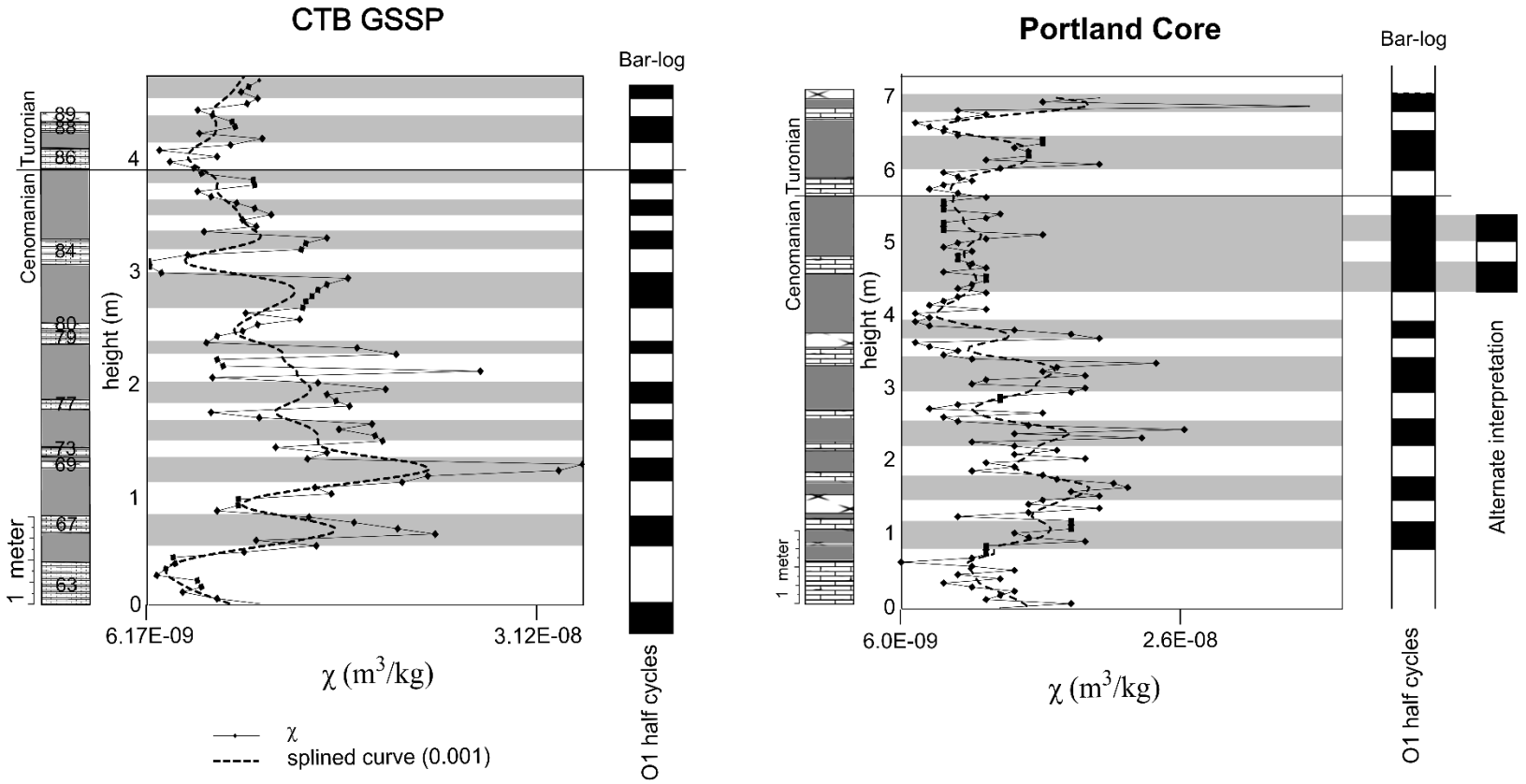

Figure 3.12b Bar-log derivation from χ data for CTB GSSP and Portland Core sections. Shaded areas on the splined χ curve indicate bar-log divisions. Bar logs show half cycles for the section

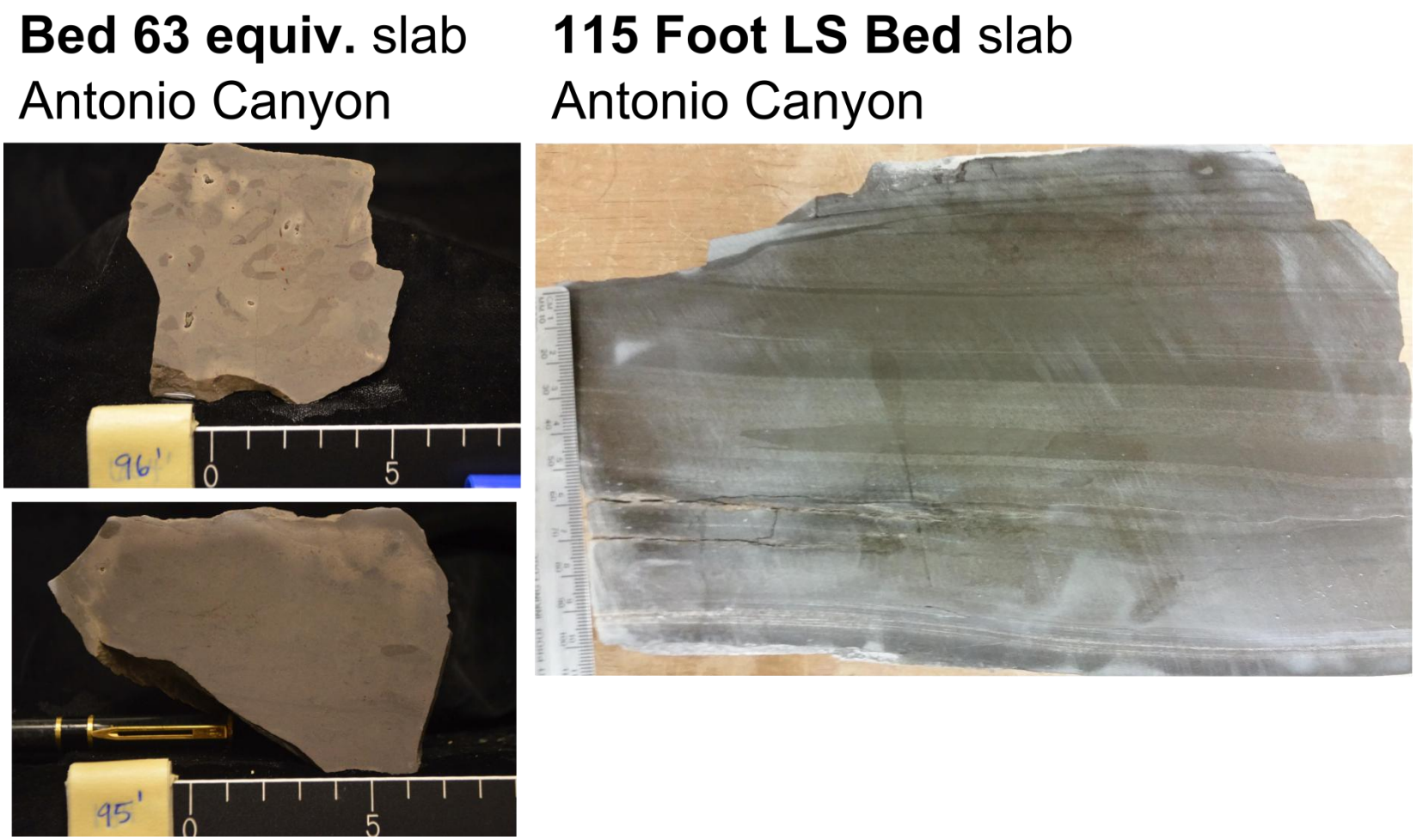

Figure 3.13 Photographs comparing trace fossils from slabbed Bed 63 at CTB GSSP, Bed 63 equivalent from La Junta, CO (~100 km away), and the time-equivalent limestone bed at Antonio Canyon, as well as the 115 Foot Limestone Bed. Scale is 0.05 m. Photographs of slabbed Antonio Canyon beds by R. Gardner. Bed 63 photographs taken by J. Grosskopf.

Table 3.1 Cycle duration calculations and calculated SARs for CTB GSSP, Portland Core, and Antonio Canyon sections. Shaded areas show significant match between calculated and statistically-significant cycles calculated using the MTM.

location	measured section length (m)	measured section length (cm)	half cycles (from splined x data)	whole cycles (from splined x data)	calculated cycles/m	corresponding significant MTM peak
CTB GSSP	4.761	476.125	18	10	2.100	-
Portland Core	6.000	600.000	15	8	1.333	-
Antonio Canyon	8.45	845.313	23	12	1.69	1.7

location	MTM confidence (%)	interpreted Milankovitch Cycle	frequency of cycle @ ~93.5 Ma (ky)	half cycle average SAR (cm/kyr)
CTB GSSP	-	O1	39	0.687
Portland Core	-	O1	39	1.039
Antonio Canyon	90	E1	100	0.368

confidence of measured cycles that match MTM and FT results (Figures 3.11a and 3.11b; Table 3.1). The section collected at Antonio Canyon differs from the other two sections in that the observed cycles (indicated by bar-logs) closely match what is observed in the MTM and FT results for the χ dataset (Table 3.1). This is important because the Lower Bridge Creek Limestone is known to be difficult to establish frequencies that correlate between observed lithologic variations, and MTM or FT results. This is noted in Sageman et al. (1997), where they could only establish powerful frequencies from FT tests farther up-section in the Bridge Creek Limestone, and in fact, used those frequencies to establish a time-scale for the Lower Bridge Creek Limestone. CTB GSSP and Portland Sections MTM or FT results (Table 3.1; Figures 3.11a and 3.11b), do not match for the reasons outlined above.

Antonio Canyon sampled section correlation to Portland Core

The section collected at Antonio Canyon, from the base of the 115 Foot Limestone Bed up through the Facies C–Facies D contact (Figures 3.14a and 3.14b), may correlate to the Portland Core. Figure 3.8 shows an extended correlation between χ and well-log GRS curves. These data span the Hartland Shale, Bridge Creek Limestone, and Fairport Chalky Shale Members of the Greenhorn Formation.

The Lozier Canyon well-log GRS curve is correlated to the Portland Core by the sharp negative excursion at the K65SB horizon present at both sites (K65SB at Lozier Canyon, and the Hartland Shale–Bridge Creek Limestone contact at the CTB GSSP and Portland Core localities). Apart from the obvious GRS excursion, little can be correlated between the sites beyond loosely curve-matching the GRS datasets. These data clearly show the beginning of the start of OAE II at the base of the basal limestone bed of the Upper Eagle Ford. Additional research is needed to

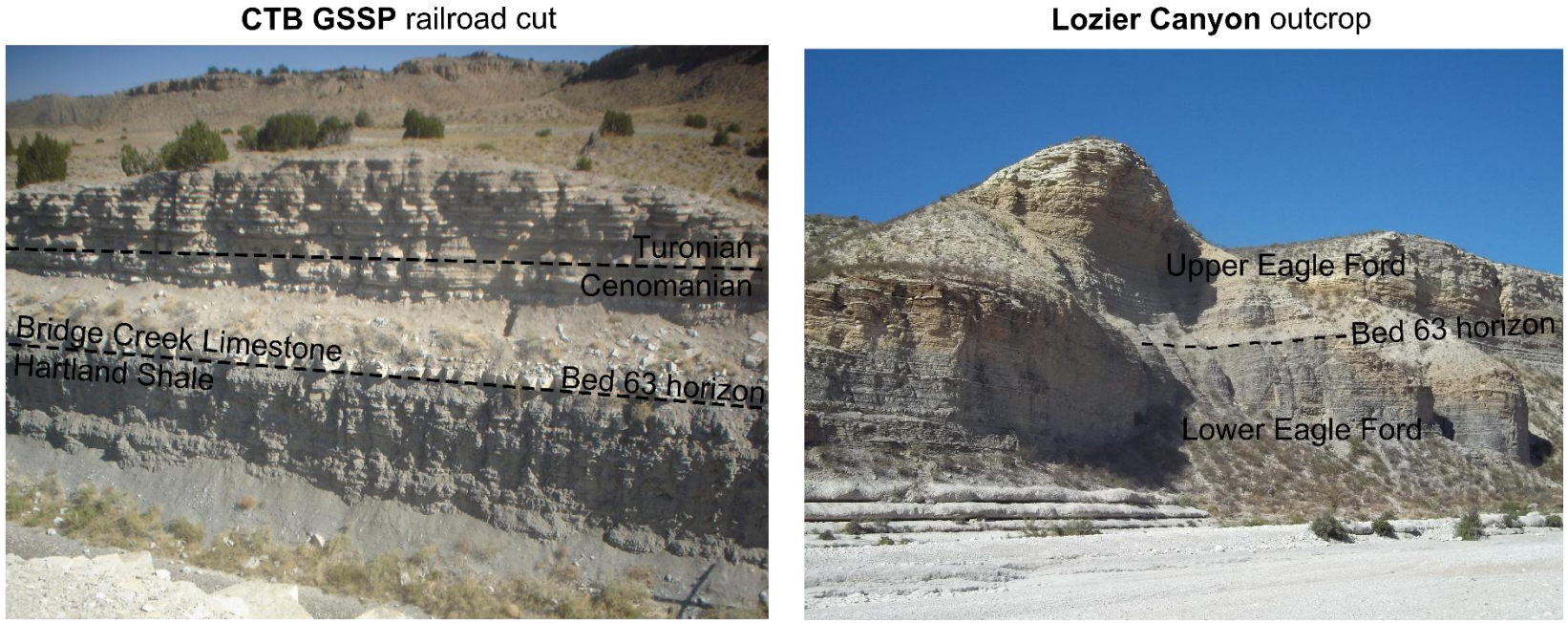

Figure 3.14a Annotated photographs of correlative horizons between CTB GSSP and Lozier Canyon outcrops. Lozier Canyon photograph by R. Ellis. CTB GSSP photograph by J. Grosskopf.

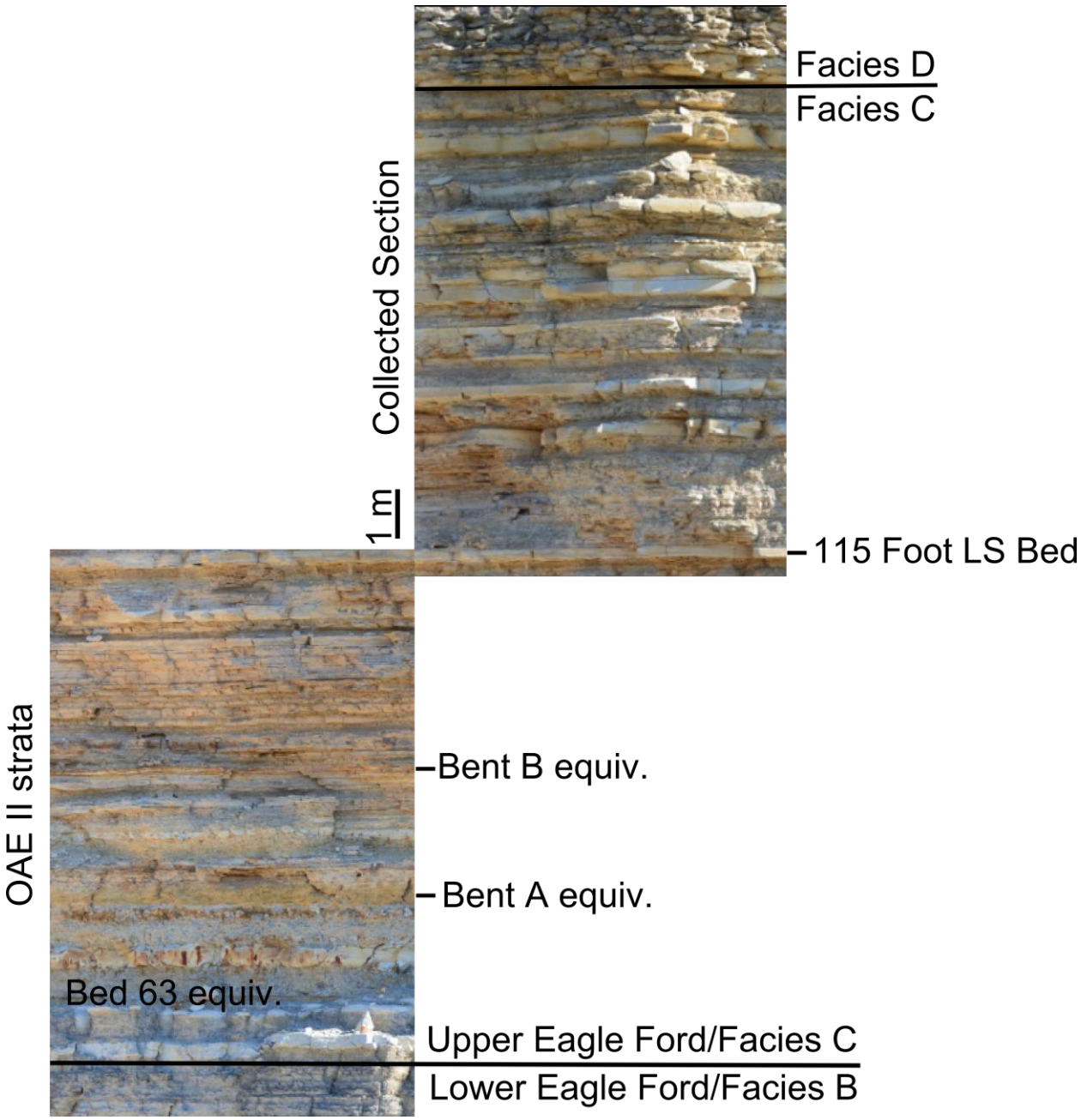

Figure 3.14b Annotated photographs of Antonio Canyon outcrop succession collected and uncollected. Photograph by J. Grosskopf.

confidently place the height of the CTB (Figure 3.14b). In the same sense, more work is needed to place the end of OAE II in the Antonio Canyon section.

CONCLUSIONS

An alternate interpretation of correlation from Lozier and Antonio Canyon outcrops in Texas, to the Cenomanian–Turonian Global boundary Stratotype Section and Point (CTB GSSP) outcrop and Portland Core in Colorado, pins the base of basal limestone bed of the Upper Eagle Ford Formation to be isochronous to the base of the basal Bridge Creek Limestone, Bed 63. These contacts represent a synchronous horizon that can be traced throughout CWIS strata.

The following evidence supports this alternate interpretation. One, a sharp drop and gradual rise in GRS data from the Antonio Canyon section better match the GRS and χ data higher in CTB GSSP and Portland Core successions. Inferences on relation of χ, and field, lab, and well-log GRS values to sediment accumulation rate and related effects, such as loss of oxygen to the benthic environment and subsequent organic carbon preservation, show that the section collected at Antonio Canyon must have occurred after OAE II time. Two, correlating to the OAE II interval at Lozier Canyon/Antonio Canyon is possible if the recognizable portions A, B, and C, shown in Figure 3.9, of the $\delta^{13}C$ curve are matched among the CTB GSSP outcrop, auxiliary Fasken Core, and the $\delta^{13}C_{organic}$ $\delta^{13}C_{carbonate}$ curves at the Lozier Canyon outcrop. This interpretation places the start of OAE II at Lozier Canyon at the base of the basal limestone bed of the Upper Eagle Ford Formation, which represents the Lower Eagle Ford–Upper Eagle Ford contact. The amount of time represented in this new interpretation better matches the OAE II duration that the $\delta^{13}C$ curve represents in this portion of the CWIS, compared to CTB GSSP and Portland Core $\delta^{13}C$ curves. This new interpretation does not interfere with any biostratigraphic correlations.

Geochemical analyses, using Sr, Rb, Zr, and Ba elemental ratios show no similarity between bentonite beds that show clear correlation between CTB GSSP and Portland Core. Therefore, such analyses could not be used to correlate in to the Antonio Canyon Section. The section collected at the Antonio Canyon outcrop, starting at the base of the 115 Foot Limestone Bed in Facies C2, is positioned above strata that represent OAE II-time. More work is needed to determine the height of the CTB and end of OAE II in Lozier and Antonio Canyon outcrops.

REFERENCES

Berger, A., Loutre, M.F., and Laskar, J. 1992. Stability of the astronomical frequencies over the Earth's history for paleoclimate studies. *Science*, **255**, 560-566.

Cobban, W. A., Erdman, C.E., Lemke, R.W. and Maughan, E. K. 1976. Type sections and stratigraphy of the members of the Blacklead and Marias River Formations (Cretaceous) of the Sweetgrass Arch, Montana. U.S. Geological Survey, Professional Paper 974.

Cobban, W.A., Merewether, E.A., Fouch, T.D., and Obradovich, J.D. 1994. Some Cretaceous shorelines in the Western Interior of the United States, *in* Caputo, M.V., Peterson, J.A., and Franczyk, K.J. eds., Mesozoic Systems of the Rocky Mountain Region, USA: Rocky Mountain Section SEPM – Society for Sedimentary Geology, 393-414.

Corbett, M.J. and Watkins, D.K. 2013. Calcareous nannofossil paleoecology of the mid-Cretaceous Western Interior Seaway evidence of oligotrophic surface waters during OAE2. *Palaeogeography, Palaeoclimatology, Palaeoecology*, **392**, 510-523.

Cowie, G.L. and Hedges, J.I. 1992. The role of anoxia in organic matter preservation in coastal sediments: relative stabilities of the major biochemical under oxic and anoxic depositional settings. *Organic Geochemistry*, **19**, 229-234.

David, B.T. 2009. "Chemical fingerprinting" of volcanic tephra found in Kansas using trace elements. [M.S. thesis]: Kansas State University, Manhattan, KS.

Dean, W.E. and Arthur, M.A. 1998. Cretaceous Interior Seaway Drilling Project: an overview. Stratigraphy and Paleoenvironments of the Cretaceous Western Interior Seaway, USA, SEPM Concepts in Sedimentology and Paleontology, **6**, 1-10.

Donovan, A.D. and Staerker, T.S. 2010. Sequence stratigraphy of the Eagle Ford (Boquillas) Formation in the subsurface of South Texas and outcrops of West Texas. *Gulf Coast Association of Geological Societies Transactions*, **60**, 861-899.

Donovan, A.D., Staerker, T.S., Pramudito, A., Li, W., Corbett, M.J., Lowery, C.M., Romero, A.M. and Gardner, R.D. 2012. The Eagle Ford outcrops of West Texas: a laboratory for understanding heterogeneities within unconventional mudstone reservoirs. *Gulf Coast Association of Geological Societies Journal*, **1**, 162-185.

Elder, W.P. 1998. Geometry of Upper Cretaceous bentonite beds: implications about volcanic source areas and paleowind patterns, western interior, United States. *Geology*, **16**, 835-838.

Elder, W.P., Gustason, E.R., and Sageman, B.B. 1994. Correlation of basinal carbonate cycles to nearshore parasequences in the late Cretaceous Greenhorn seaway, Western Interior U.S.A. *Geological Society of America Bulletin*, **7**, 892-902.

Ellwood, B.B., Balsam, W.L., and Roberts, H.H. 2006. Gulf of Mexico sediment sources and sediment transport trends from magnetic susceptibility measurements of surface samples. *Marine Geology*, **230**, 237-248.

Ellwood, B.B., Crick, R.E., Hassani, A.E., Benoist, S.L., and Young, R.H. 2000. Magnetosusceptibility event and cyclostratigraphy method applied to marine rocks: Detrital input versus carbonate productivity. *Geology*, **28**, 1135-1138.

Ellwood, B.B., Tomkin, J.H., Ratcliffe, K.T., Wright, M., and Kafafy, A.M. 2008. High-resolution magnetic susceptibility and geochemistry for the Cenomanian/Turonian boundary GSSP with correlation to time equivalent core. *Palaeogeography, Palaeoclimatology, Palaeoecology*, **261**, 105-126.

Ellwood, B.B., Wang, W., Tomkin, J.H., Ratcliffe, K.T., Hassani, A.E., and Wright, A.M. 2013. Testing high resolution magnetic susceptibility and gamma radiation methods in the Cenomanian-Turonian (Upper Cretaceous) GSSP and near-by coeval section. *Palaeogeography, Palaeoclimatology, Palaeoecology*,**378**, 75-90.

Goldhammer, R.K. and Johnson, C.A. 2001. Middle Jurassic-Upper Cretaceous paleogeographic evolution and sequence-stratigraphic framework of the northwest Gulf of Mexico rim, *in* C. Bartolini, R.T. and Cantu-Chapa, eds., The western Gulf og Mexico Basin: Tectonics, sedimentary basins, and petroleum systems: AAPG Memoir 75, 45-81.

Grosskopf, J. F. 2015. Basal Bridge Creek Limestone bed (Bed 63) trace fossils indicate oxygenated bottom-waters throughout the Cretaceous Western Interior Seaway During Oceanic Anoxic Event II. Diss. Louisiana State University, 2015. Baton Rouge: LSU, 2015. Electronic.

Grosskopf, J. F. 2015. Trace fossils and sediment accumulation rates: Tools for understanding the nature of benthic oxygen conditions for the duration of OAE II from Cretaceous Western Interior Seaway outcrops. Diss. Louisiana State University, 2015. Baton Rouge: LSU, 2015. Electronic.

Hahn, G.A., Rose, W.R., and Meyers, T. 1979. Geochemical correlation of genetically related rhyolitic ash-flow air-fall ashes, central and western Guatemala and the equatorial Pacific. *Geological Society of America Special Special Papers*, **180**, 101-112.

Karlin, R., and Levi, S. 1983. Diagenesis of magnetic minerals in Recent haemipelagic sediments. *Nature*, **303**, 327-330.

Karlin, R., and Levi, S. 1985. Geochemical and sedimentological control of magnetic properties of hemipelagic sediments. *Journal of Geophysical Research*, **90**, 10373-10392.

Kennedy, W.J., Walaszczyk, I., and Cobban, W.A. 2005. The Global Boundary Stratotype Section and Point for the base of the Turonian Stage of the Cretaceous: Pueblo, Colorado, U.S.A. Episodes: Journal of International *Geoscience*, **28**, 93-104.

Meyers, S.R., and Sageman, B.B. 2007. Quantification of deep-time orbital forcing by average spectral misfit. *American Journal of Science*, **307**, 773-792. doi: 10.2475/05.2007.01.

Pratt, L.M. 1984. Influence of paleoenvironmental factors on preservation of organic matter in Middle Cretaceous Greenhorn Formation, Pueblo, Colorado. *The American Association of Petroleum Geologists Bulletin*, **9**, 1146-1159.

Radiation Solutions Inc. 2010. RS-220GN Super-IDENT gamma_neutron handheld gamma-ray spectrometer: system description manual. Mississauga, Ontario, Canada. www.radiaitonsolutions.ca.

Sageman, B.B., and Bina, C.G. 1997. Diversity and species abundance patterns in Late Cenomanian Black Shale Biofacies, Western Interior, U.S.. *Palaios*, **12**, 449-466.

Sageman, B.B., Rich, J., Arthur, M.A., Birchfield, G.E., and Dean, W.E. 1997. Evidence for Milankovitch periodicities in Cenomanian-Turonian lithologic and geochemical cycles, Western Interior U.S.A.. *Journal of Sedimentary Research*, **67**, 286-302.

Sageman, B.B., Rich, J., Arthur, M.A., Dean, W.E., Savrda, C.E., and Bralower, T.J. 1998. Multiple Milankovitch Cycles in the Bridge Creek Limestone (Cenomanian-Turonian), Western Interior Basin. Stratigraphy and paleoenvironments of the Cretaceous Western Interior Seaway, USA, SEPM: Concepts in Sedimentology and Paleontology, **6**,153-171.

Sageman, B.B., Meyers, S.R., and Arthur, M.A. 2006. Orbital time scale and new C-isotope record for Cenomanian-Turonian boundary stratotype. *Geology*, **34**, 125-128.

Slingerland , R.L., Kump, L.R, Arthur, M.A., Fawcett, P.J., Sageman, B.B., and Barron, E.J. 1996. Estuarine circulation in the Turonian western interior seaway of North America. *Geological Society of America Bulletin*, **108**, 941-952.

DISSERTATION CONCLUSIONS

Oxygen-related trace fossil fabrics composing the laterally-extensive Bed 63 indicate well-oxygenated bottom-waters throughout the Cretaceous Western Interior Seaway (CWIS) for the duration of Oceanic Anoxic Event II (OAE II, 93.9±0.15 Ma). Bed 63 is the basal layer in the Lower Bridge Creek Limestone, whose strata represent OAE II-time. Bridge Creek Limestone strata are composed of interbedded limestone and calcareous shale beds that alternate due to orbitally-forced climatic effects that impact depositional characteristics in the CWIS. Deposition of the bedding couplets in the Lower Bridge Creek Limestone is the result of carbonate dilution and production process driven by competing obliquity- and precessional-scale orbital-forcing, respectively. Limestone beds in the Upper Bridge Creek Limestone represent times of extended sediment starvation, and consequent well-oxygenated benthic conditions, while the interbeds of calcareous shale represent times when there is more terrigenous input and carbon preservation. Calcareous shale bed trace fossil fabrics indicate less benthic oxygen, relative to limestone beds, due to the flux of freshwater and nutrients from the continent, and consequent water stratification.

There are short-term changes in trace fossil fabrics from the thicker limestone beds that might be tied to shorter orbital cycles. Magnetic susceptibility (χ) and gamma-ray spectroscopy (GRS) data are used to track changes in detrital components in the Bridge Creek Limestone strata to detect these short-term changes. Lower Bridge Creek Limestone strata are problematic in attaining good correspondence between cycles derived from splined χ data, and those calculated from MTM and FT analyses. Relationships between assumptions about depositional characteristics in the CWIS can be made using graphic comparison techniques, matching bar-logs (derived from smoothed χ data) from different sections along a line-of-correlation. These

also help correlate cycles between sites. The sediment accumulation rates calculated from the χ data detected among sites could not be used in determining the timing of high-frequency than precessional-scale variations.

Correlation from the Antonio Canyon section collected along the North–South transect to the Cenomanian–Turonian Boundary GSSP outcrop and Portland Core indicates the 8-meter-long section was collected from an interval representing time after OAE II. However, a correlation can be made using lithologic trends in strata among CWIS, a strong negative excursion in well log GRS data, and strong positive spike in $\delta^{13}C_{carbonate}$ values between the Antonio Canyon outcrop and the Portland Core. These correlations indicate that the basal limestone bed of the Upper Eagle Ford Formation is synchronous with Bed 63 in CWIS strata, which marks the Hartland Shale–Bridge Creek Limestone contact in the Greenhorn Formation.

REFERENCE SUMMARY

Arthur, M.A. and Schlanger, S.O. 1979. Cretaceous "oceanic anoxic events" as causal factors in development of reef-reservoired giant oil fields. *The American Association of Petroleum Geologists Bulletin*, **63**, 870-885.

Barclay, R.S., McElwain, J.C., Sageman, B.B. 2010. Carbon sequestration activated by volcanic CO_2 pulse during Oceanic Anoxic Event 2. *Nature Geoscience: Letters*, **3**, 205-208.

Berger, A., Loutre, M.F., and Laskar, J. 1992. Stability of the astronomical frequencies over the Earth's history for paleoclimate studies. *Science*, **255**, 560-566.

Bowman, A.R. and Bralower, T.J. 2005. Paleoceanographic significance of high-resolutioncarbon isotope records across the Cenomanian-Turonian boundary in the Western Interior and New Jersey coastal plain, USA. *Marine Geology*, **217**, 305-321.

Bralower, T.J. 2008. Volcanic cause of catastrophe. *Nature*, **454**, 285-287.

Bromley, R. G. and Ekdale, A.A. 1984. Chondrites: A trace fossil indicator of anoxia in sediments. *Science*, **224**, 872-884.

Brumsack, H. 2006. The trace metal content of recent organic carbon-rich sediments: Implications for Cretaceous black shale formation. *Palaeogeography, Palaeoclimatology, Palaeoecology*, **232**, 344-361.

Cattaneo, A. and Steele, R.J. 2003. Transgressive deposits: a review of their variability. *Earth Science Reviews*, **62**, 187-228.

Cobban, W.A., Erdman, C.E., Lemke, R.W. and Maughan, E. K. 1976. Type sections and stratigraphy of the members of the Blacklead and Marias River Formations (Cretaceous) of the Sweetgrass Arch, Montana. U.S. Geological Survey, Professional Paper 974.

Cobban, W.A., Merewether, E.A., Fouch, T.D., and Obradovich, J.D. 1994. Some Cretaceous shorelines in the Western Interior of the United States, *in* Caputo, M.V., Peterson, J.A., and Franczyk, K.J. eds., Mesozoic Systems of the Rocky Mountain Region, USA: Rocky Mountain Section SEPM – Society for Sedimentary Geology, 393-414.

Corbett, M.J. and Watkins, D.K. 2013. Calcareous nannofossil paleoecology of the mid-Cretaceous Western Interior Seaway evidence of oligotrophic surface waters during OAE2. *Palaeogeography, Palaeoclimatology, Palaeoecology*, **392**, 510-523.

Cowie, G.L. and Hedges, J.I. 1992. The role of anoxia in organic matter preservation in coastal sediments: relative stabilities of the major biochemical under oxic and anoxic depositional settings. *Organic Geochemistry*, **19**, 229-234.

David, B.T. 2009. "Chemical fingerprinting" of volcanic tephra found in Kansas using trace elements. [M.S. thesis]: Kansas State University, Manhattan, KS.

Dean, W.E. and Arthur, M.A. 1998. Cretaceous Interior Seaway Drilling Project: an overview. Stratigraphy and Paleoenvironments of the Cretaceous Western Interior Seaway, USA, SEPM Concepts in Sedimentology and Paleontology, **6**, 1-10.

Demaison, G.J. and Moore, G.T. 1980. Anoxic environments and oil source bed genesis. *The American Association of Petroleum Geologists Bulletin*, **64**, 1179-1209.

Donovan, A.D. and Staerker, T.S. 2010. Sequence stratigraphy of the Eagle Ford (Boquillas) Formation in the subsurface of South Texas and outcrops of West Texas. *Gulf Coast Association of Geological Societies Transactions*, **60**, 861-899.

Donovan, A.D., Staerker, T.S., Pramudito, A., Li, W., Corbett, M.J., Lowery, C.M., Romero, A.M. and Gardner, R.D. 2012. The Eagle Ford outcrops of West Texas: a laboratory for understanding heterogeneities within unconventional mudstone reservoirs. *Gulf Coast Association of Geological Societies Journal*, **1**, 162-185.

Eicher, D.L. and Diner, R. 1989. Origin of the Cretaceous Bridge Creek cycles in the Western Interior, United States. *Palaeogeography, Palaeoclimatology, Palaeoecology*, **74**, 127-146.

Ekdale, A.A. 1985. Trace fossils and mid-Cretaceous anoxic events in the Atlantic Ocean. Society of Economic Paleontologists and Mineralogists, Special Publication, **35**, 333-342.

Ekdale, A.A., and Mason, T.R. 1988. Characteristic trace-fossil associations in oxygen-poor sedimentary environments. *Geology*, **16**, 720-723.

Elder, W.P. 1998. Geometry of Upper Cretaceous bentonite beds: implications about volcanic source areas and paleowind patterns, western interior, United States. *Geology*, **16**, 835-838.

Elder, W.P. 1989. Molluscan extinction patterns across the Cenomanian-Turonian Stage boundary in western interior of the United States. *Paleobiology*, **15**, 299-320.

Elder, W.P., Gustason, E.R., and Sageman, B.B. 1994. Correlation of basinal carbonate cycles to nearshore parasequences in the Late Cretaceous Greenhorn Seaway, Western Interior U.S.A. *Geological Society of America Bulletin*, **106**, 892-902.

Eldrett, J.S., Minisini, D., and Bergman, S.C. 2014. Decoupling of the carbon cycle during Oceanic Anoxic Event 2. *Geology*, **42**, 567-570.

Ellwood, B.B., Crick, R.E., Hassani, A.E., Benoist, S.L., and Young, R.H. 2000. Magnetosusceptibility event and cyclostratigraphy method applied to marine rocks: Detrital input versus carbonate productivity. *Geology*, **28**, 1135-1138.

Ellwood, B.B., Balsam, W.L., and Roberts, H.H. 2006. Gulf of Mexico sediment sources and sediment transport trends from magnetic susceptibility measurements of surface samples. *Marine Geology*, **230**, 237-248.

Ellwood, B.B, Brett, C.E., Tomkin, J.H., and Macdonald, W.D. 2012. Visual identification and quantification of Milankovitch climate cycles in outcrop: an example from the Upper Ordivician Kope Formation, Northern Kentucky. *Geological Society, London, Special Publications*, **373**, 341-353. doi: 10.1144/SP373.2.

Ellwood, B.B., Tomkin, J.H., Ratcliffe, K.T., Wright, M., and Kafafy, A.M. 2008. High-resolution magnetic susceptibility and geochemistry for the Cenomanian/Turonian boundary GSSP with correlation to time equivalent core. *Palaeogeography, Palaeoclimatology, Palaeoecology*, **261**, 105-126.

Ellwood, B.B., Tomkin, J.H., Febo, L.A., and Stuart Jr., C.N. 2008. Time series analysis of magnetic susceptibility variations in deep marine sedimentary rocks: A test using the upper Danian–Lower Selandian proposed GSSP, Spain. *Palaeogeography, Palaeoclimatology, Palaeoecology*, **261**, 270-279.

Ellwood, B.B., Wang, W., Tomkin, J.H., Ratcliffe, K.T., Hassani, A.E., and Wright, A.M. 2013. Testing high resolution magnetic susceptibility and gamma radiation methods in the Cenomanian-Turonian (Upper Cretaceous) GSSP and near-by coeval section. *Palaeogeography, Palaeoclimatology, Palaeoecology*,**378**, 75-90.

Evans, R.D. and Goodman, C . 1941. Radioactivity of rocks. *Geological Society of America Bulletin*, **52**, 459-490.

Fischer, A.G., 1980. Gilbert-bedding rhythms and geochronology. *Geological Society of America Special Papers*, **183**, 93-104.

Fischer, A.G., Herbert, T.D., and Premoli Silva, I. 1985. Carbonate bedding cycles in Cretaceous pelagic and hemipelagic sequences, *in* Pratt, L.M., Kauffman, E.G., and Zelt, F.B. eds., Fine-grained deposits and biofacies of the Cretaceous Western Interior Seaway: evidence of cyclic sedimentary processes, SEPM – Field Trip Guidebook 4, 1-10.

Fisher, C.G. and Arthur, M.A. 2002. Water mass characteristics in the Cenomanian US Western Interior Seaway as indicated by stable isotopes of calcareous organisms. *Palaeogeography, Palaeoclimatology, Palaeoecology*, **188**, 189-213.

Friedrich, O., Erbacher, J., Wilson, P.A., Moriya, K. and Mutterlose, J. 2009. Paleoenvironmental changes across the Mid Cenomanian Event in the tropical Atlantic Ocean (Demera Rise ODP Leg 207) inferred from benthic foraminiferal assemblages. *Marine Micropaleontology*, **71**, 28-40.

Gale, A.S., Hardenbol, J., Hathaway, B., Kennedy, W.J., Young, J.R., and Phansalkar, V. 2002.Global correlation of Cenomanian (Upper Cretaceous) sequences: Evidence for Milankovitch control on sea level. *Geology*, **30**, 291-294.

Gautier, D. L. 1986. Cretaceous shales from the western interior of North America: Sulfur/carbon ratios and sulfur-isotope composition. *Geology*, **14**, 225-228.

Gilbert, G.K. 1895. Sedimentary measurement of geologic time. *Journal of Geology*, **3**, 121-127.

Goldhammer, R.K. and Johnson, C.A. 2001. Middle Jurassic-Upper Cretaceous paleogeographic evolution and sequence-stratigraphic framework of the northwest Gulf of Mexico rim, *in* C. Bartolini, R.T. and Cantu-Chapa, eds., The western Gulf og Mexico Basin: Tectonics, sedimentary basins, and petroleum systems: AAPG Memoir 75, 45-81.

Grosskopf, J. F. 2015. Basal Bridge Creek Limestone bed (Bed 63) trace fossils indicate oxygenated bottom-waters throughout the Cretaceous Western Interior Seaway During Oceanic Anoxic Event II. Diss. Louisiana State University, 2015. Baton Rouge: LSU, 2015. Electronic.

Grosskopf, J. F. 2015. Trace fossils and sediment accumulation rates: Tools for understanding the nature of benthic oxygen conditions for the duration of OAE II from Cretaceous Western Interior Seaway outcrops. Diss. Louisiana State University, 2015. Baton Rouge: LSU, 2015. Electronic.

Grosskopf, J. F. 2015. Litho- and chemostratigraphic correlation from Upper Eagle Ford Formation outcropping at Lozier and Antonio Canyons, near Langtry, Texas, to the Cenomanian–Turonian Boundary GSSP, Pueblo, CO. Diss. Louisiana State University, 2015. Baton Rouge: LSU, 2015. Electronic.

Hattin, D.E. 1971. Widespread, synchronously deposited, burrow-mottled limestone beds in Greenhorn Limestone (Upper Cretaceous) of Kansas and Central Colorado. *American Association of Petroleum Geologists Bulletin*, **55**,412-431.

Hattin, D.E. 1975. Stratigraphy and depositional environment of Greenhorn Limestone (Upper Cretaceous) of Kansas. Kansas Geological Survey Bulletin 209, University of Kansas.

Henderson, R.A. 2004. A Mid-Cretaceous association of shell beds and organic-rich shale: Bivalve exploitation of a nutrient-rich, anoxic sea-floor environment. *Palaios*, **19**, 156-169.

Jones, G.A. and Kaiteris, P. 1983. A vacuum-gasometric technique for rapid and precise analysis of calcium carbonate in sediments and soils. *Journal of Sedimentary Petrology*, **53**, 655-660.

Karlin, R., and Levi, S. 1983. Diagenesis of magnetic minerals in Recent haemipelagic sediments. *Nature*, **303**, 327-330.

Karlin, R., and Levi, S. 1985. Geochemical and sedimentological control of magnetic properties of hemipelagic sediments. *Journal of Geophysical Research*, **90**, 10373-10392.

Keller, G., Berner, Z., Adatte, T., and Stueben, D. 2004. Cenomanian-Turonian and $\delta^{13}C$, and $\delta^{18}O$, sea level and salinity variations at Pueblo, Colorado. *Palaeogeography, Palaeoclimatology, Palaeoecology*, **211**, 19-43.

Kennedy, W.J., Walaszczyk, I., and Cobban, W.A. 2005. The Global Boundary Stratotype Section and Point for the base of the Turonian Stage of the Cretaceous: Pueblo, Colorado, U.S.A. Episodes: Journal of International *Geoscience*, **28**, 93-104.

Kolonic, S., Wagner, T., Forster, A., Sinninghe Damste, J.S., Walsworth-Bell, B., Erba, E., Turgeon, S., Brumsack, H., Chellai, E., Tsikos, H., Kuhnt, W., and Kuypers, M. M. 2005. Black shale deposition on the northwest African Shelf during the Cenomanian/Turonian oceanic even: Climate coupling and global organic carbon burial. *Paleoceanography*, **20**, PA1006. doi:10.1029/2003PA000950.

Kump, L. R. and Arthur, M.A. 1999. Interpreting carbon-isotope excursions: carbonates and organic matter. *Chemical Geology*, **161**, 181-198.

Kump, L.R. and Slingerland, R.L. 1999. Circulation and stratification of the early Turonian Western Interior Seaway: Sensitivity to a variety of forcings. *Evolution of the Cretaceous Ocean-Climate System*, Geological Society of America, Boulder: Special Paper #332, 445 p.

Lowery, C.M., Corbett, M.J., Leckie, R.M., Watkins, D., Romero, A.M., and Pramudiot, A. 2014. Foraminiferal and nannofossil paleoecology and paleoceanography of the Cenomanian–Turonian Eagle Ford Shale of southern Texas. *Palaeogeography, Palaeoclimatology, Palaeoecology*, **413**, 49-65.

Leithold, E.L. and Dean, W.E. 1998. Depositional processes and carbon burial on a Turonian prodelta at the margin of the Western Interior Seaway. Stratigraphy and paleoenvironments of the Cretaceous Western Interior Seaway, USA, SEPM: Concepts in Sedimentology and Paleontology, **6**, 189-200.

Meyers, S.R., and Sageman, B.B. 2004. Detection, quantification, and significance of hiatuses in pelagic and hemipelagic strata. *Earth and Planetary Science Letters*, **224**, 55-72.

.

Meyers, S.R., and Sageman, B.B. 2007. Quantification of deep-time orbital forcing by average spectral misfit. *American Journal of Science*, **307**, 773-792. doi: 10.2475/05.2007.01.

Meyers, S.R., Sageman, B.B., and Lyons, T.W. 2005. Organic carbon burial rate and the molybdenum proxy: Theoretical framework and application to Cenomanian-Turonian oceanic anoxic event 2. *Paleoceanography*, **20**, PA2002. doi:10.1029/2004PA001068

Meyers, S.R., Siewert, S.E., Singer, B.S., Sageman, B.B., Condon, D.J., Obradovich, J.D., Jicha, B.R., and Sawyer, D.A. 2012. Intercalibration of radioisotopic and astrochronologic time scales for the Cenomanian-Turonian boundary interval, Western Interior Basin, USA. *Geology*, **40**, 7-10.

Moller N.K. and Kvingan, K. 1988. The genesis of nodular limestones in the Ordivician and Silurian of the Oslo Region (Norway). *Seidmentology*, **35**, 405-420.

Pancost, R.D., Freeman, K.H., and Arthur, M.A. 1998. Organic geochemistry of the Cretaceous Western Interior Seaway: a trans-basinal evaluation. Stratigraphy and paleoenvironments of the Cretaceous Western Interior Seaway, USA, SEPM: Concepts in Sedimentology and Paleontology, **6**, 173-188.

Pedersen, T.F. and Calver, S.E. 1990. Anoxia vs. productivity: what controls the formation of organic-carbon-rich sediments and sedimentary rocks? *The American Association of Petroleum Geologists Bulletin*, **74**, 454-466.

Pratt, L.M. 1984. Influence of paleoenvironmental factors on preservation of organic matter in Middle Cretaceous Greenhorn Formation, Pueblo, Colorado. *The American Association of Petroleum Geologists Bulletin*, **9**, 1146-1159.

Rabalais, N.N., Turner, R.E., and Wiseman, W.J. 2002. Gulf of Mexico Hypoxia, A.K.A. "The Dead Zone". *Annual Review of Ecology, Evolution, and Systematics*, **33**, 235-263. doi: 10.1146/annurev.ecolsys.33.010802.150513.

Radiation Solutions Inc. 2010. RS-220GN Super-IDENT gamma_neutron handheld gamma-ray spectrometer: system description manual. Mississauga, Ontario, Canada. www.radiaitonsolutions.ca.

Sageman, B.B., and Bina, C.G. 1997. Diversity and species abundance patterns in Late Cenomanian Black Shale Biofacies, Western Interior, U.S.. *Palaios*, **12**, 449-466.

Sageman, B.B., Meyers, S.R., and Arthur, M.A. 2006. Orbital time scale and new C-isotope record for Cenomanian-Turonian boundary stratotype. *Geology*, **34**, 125-128.

Sageman, B.B., Rich, J., Arthur, M.A., Birchfield, G.E., and Dean, W.E. 1997. Evidence for Milankovitch periodicities in Cenomanian-Turonian lithologic and geochemical cycles, Western Interior U.S.A.. *Journal of Sedimentary Research*, **67**, 286-302.

Sageman, B.B., Rich, J., Arthur, M.A., Dean, W.E., Savrda, C.E., and Bralower, T.J. 1998. Multiple Milankovitch Cycles in the Bridge Creek Limestone (Cenomanian-Turonian), Western Interior Basin. Stratigraphy and paleoenvironments of the Cretaceous Western Interior Seaway, USA, SEPM: Concepts in Sedimentology and Paleontology, **6**,153-171.

Savrda, C.E. 1998. Ichnology of the Bridge Creek Limestone: Evidence for temporal and spatial variations in paleo-oxygenation in the western interior seaway. Stratigraphy and paleoenvironments of the Cretaceous Western Interior Seaway, USA, SEPM: Concepts in Sedimentology and Paleontology, **6**, 127-136.

Savrda, C.E. 1998. Ichnocoenoses in the Niobrara Formaion: Implications for the benthic oxygen histories. Stratigraphy and paleoenvironments of the Cretaceous Western Interior Seaway, USA, SEPM: Concepts in Sedimentology and Paleontology, **6**, SEPM: Concepts in Sedimentology and Paleontology, **6**, 137-151.

Savrda, C.E. 2007. Trace fossils and marine benthic oxygenation. Trace fossils: *Concepts, Problems, Prospects*. Miller ed. Elsevier, Oxford.

Savrda, C.E., and Bottjer, D.J. 1994. Ichnofossils and Ichnofabrics in rhythmically bedded pelagic/hemi-pelagic carbonates: recognition and evaluation of benthic redox and scour

cycles. *Special Publications of the International Association of Sedimentologists*, **19**, 195-210.

Schlanger, S.O., and Jenkyns, H.C. 1976. Cretaceous oceanic anoxic events: causes and consequences. *Geologie en Mijnbouw*, **55**, 179-184.

Slingerland, R.L., Kump, L.R, Arthur, M.A., Fawcett, P.J., Sageman, B.B., and Barron, E.J. 1996. Estuarine circulation in the Turonian Western Interior Seaway of North America. *Geological Society of America Bulletin*, **108**, 941-952.

Snow, L.J., Duncan, R.A., and Bralower, T.J. 2005. Trace element abundances in the Rock Canyon Anticline, Pueblo, Colorado, marine sedimentary section and their relationship to Caribbean plateau construction and ocean anoxic event 2. *Paleoceanography*, **20**, PA3005. doi:10.1029/2004PA001093.

Tribovillard, N., Algeo, T.J., Lyons, T., and Riboulleau, A. 2006. Trace metals as paleoredox and paleoproductivity proxies: an update. *Chemical Geology*, **232**, 12-32.

Turgeon, S.C. and Creaser, R.A. 2008. Cretaceous anoxic event 2 triggered by a massive magmatic episode. *Nature*: *Letters*, **454**, 323-326.

Tyson, R.V. and Pearson, T.H. 1991. Modern and ancient continental shelf anoxia: an overview. *Geological Society, London, Special Publications*, **58**, 1-24. doi:10.1144/GSL.SP.1991.058.01.01.

Watkins, D.K. 1989. Nannoplankton productivity fluctuations and rhythmically-bedded pelagic carbonates of the Greenhorn Limestone (Upper Cretaceous). *Palaeogeography, Palaeoclimatology, Palaeoecology*, **74,** 75-86.

Wedepohl, K.H., 1971. Environmental influences on the chemical composition of shales and clays. In: Ahrens, L.H., Press, F.,Runcorn, S.K., Urey, H.C. (Eds.), Physics and Chemistry of the Earth. Pergamon, Oxford, pp. 305–333.

APPENDIX A: MAGNETIC SUSCEPTIBILITY DATA

Site 1 – Waheap Wash, Big Water, UT

sample #	ht (m)	χ (m^3/kg)
-1	-0.1	3.00E-08
1	0	2.93E-08
2	0.1	2.93E-08
3	0.2	4.06E-08
4	0.3	5.53E-08
5	0.4	4.57E-08
6	0.5	4.13E-08
7	0.6	4.64E-08
8	0.7	4.72E-08
9B	0.8	4.56E-08
10	0.9	4.58E-08
11	1	4.72E-08
12	1.1	5.08E-08
13	1.2	4.76E-08
14	1.3	4.78E-08
15	1.4	4.69E-08
16	1.5	4.20E-08
17	1.6	4.12E-08
18	1.7	4.63E-08
19	1.8	5.82E-08
20	1.9	5.16E-08
	0	
22B	2.1	4.28E-08
23	2.2	4.60E-08
24	2.3	4.76E-08
25	2.4	4.08E-08
26	2.5	5.80E-08
27	2.6	4.65E-08
28	2.7	4.51E-08
29	2.8	4.37E-08
30	2.9	4.30E-08
31	3	4.46E-08
32	3.1	4.16E-08
33	3.2	4.27E-08
34	3.3	4.63E-08
35	3.4	4.21E-08
36	3.5	4.50E-08
37	3.6	4.14E-08
38	3.7	3.87E-08
39	3.8	3.99E-08
40	3.9	3.71E-08
41	4	3.99E-08

42	4.1	4.00E-08
43	4.2	3.90E-08
44	4.3	3.64E-08
45	4.4	4.14E-08
46	4.5	4.16E-08
47	4.6	4.26E-08
48	4.7	4.39E-08
49	4.8	3.82E-08
50	4.9	3.98E-08
51	5	3.92E-08
52	5.1	4.06E-08
53	5.2	4.24E-08
54	5.3	4.08E-08
55	5.4	4.40E-08
56	5.5	4.42E-08
57	5.6	4.32E-08
58	5.7	3.93E-08
59	5.8	3.58E-08
60	5.9	3.03E-08
61	6	2.69E-08
62	6.1	4.78E-08
63	6.2	3.10E-08
64	6.3	4.76E-08
65	6.4	3.52E-08
66	6.5	2.91E-08
67	6.6	2.13E-08
68	6.7	2.01E-08
69	6.8	2.08E-08
70	6.9	2.16E-08
71	7	2.56E-08

Site 1 – Escalante Core, UT

Sample #	depth (m)	depth (ft)	χ (m^3/kg)
1	254.45	837.00	7.25E-08
2	254.35	836.67	1.38E-06
3	254.25	836.33	1.49E-07
4	254.14	836.00	6.87E-08
5	254.04	835.67	1.61E-07
6	253.94	835.33	1.95E-07
7	253.84	835.00	3.93E-07
8	253.74	834.67	2.62E-07
9	253.64	834.33	7.52E-07
10	253.54	834.00	1.99E-07
11	253.43	833.67	4.21E-08
12	253.33	833.33	1.03E-07
13	253.23	833.00	1.07E-07
14	253.13	832.67	1.33E-07
15	253.03	832.33	5.60E-08
16	252.93	832.00	1.46E-07
17	252.83	831.67	1.33E-07
18	252.73	831.33	1.09E-07
19	252.62	831.00	3.06E-07
20	252.52	830.67	2.88E-07
21	252.42	830.33	2.35E-07
22	252.32	830.00	
23	252.22	829.67	6.99E-08
24	252.12	829.33	8.45E-08
25	252.02	829.00	2.05E-07
26	251.91	828.67	1.42E-07
27	251.81	828.33	9.24E-08
28	251.71	828.00	6.89E-08
29	251.61	827.67	1.81E-07
30	251.51	827.33	4.40E-07
31	251.41	827.00	4.60E-07
32	251.31	826.67	2.87E-07
33	251.21	826.33	3.96E-07
34	251.10	826.00	3.58E-07
35	251.00	825.67	4.11E-07
36	250.90	825.33	3.96E-07
37	250.80	825.00	1.90E-07
38	250.70	824.67	1.02E-07
39	250.60	824.33	9.53E-08
40	250.50	824.00	1.36E-07
41	250.39	823.67	1.64E-07
42	250.29	823.33	1.46E-07
43	250.19	823.00	1.26E-07
44	250.09	822.67	9.44E-08

45	249.99	822.33	1.00E-07
46	249.89	822.00	1.29E-07
47	249.79	821.67	2.10E-07
48	249.69	821.33	1.41E-07
49	249.58	821.00	9.79E-08
50	249.48	820.67	1.21E-07
51	249.38	820.33	1.22E-07
52	249.28	820.00	4.10E-07
53	249.18	819.67	3.98E-07
54	249.08	819.33	3.92E-07
55	248.98	819.00	1.50E-07
56	248.57	817.67	1.43E-07
57	238.64	785.00	5.76E-08
58	238.54	784.67	5.76E-08
59	238.44	784.33	5.31E-08
60	238.34	784.00	6.46E-08
61	238.23	783.67	5.70E-08
62	238.13	783.33	9.71E-08
63	238.03	783.00	2.93E-07
64	237.93	782.67	4.75E-07
65	237.83	782.33	2.99E-07
66	237.73	782.00	1.19E-07
67	237.63	781.67	7.37E-08
68	237.53	781.33	5.76E-08
69	237.42	781.00	6.22E-08
70	237.02	779.67	6.70E-08
71	236.92	779.33	6.55E-08
72	236.82	779.00	5.97E-08
73	236.71	778.67	6.76E-08
74	236.61	778.33	6.35E-08
75	236.51	778.00	6.01E-08
76	236.41	777.67	7.00E-08
77	236.31	777.33	6.28E-08

Site 2 – Portland Core, CO

Sample #	depth (m)	depth (ft)	χ (m^3/kg)	
26A	138.98	456	9.31E-09	------Top of Bridge Creek Limestone
25A	139.03	456.1	1.17E-08	
24A	139.08	456.3	5.18E-09	
23A	139.13	456.5	8.02E-09	
22A	139.18	456.6	1.02E-08	
21A	139.23	456.8	1.32E-08	
20A	139.28	457	1.24E-08	
19A	139.33	457.1	1.1E-08	
18A	139.37	457.3	1.16E-08	
17A	139.42	457.4	1.5E-08	
16A	139.47	457.6	1.21E-08	
15A	139.52	457.7	9.06E-09	
14A	139.57	457.9	8.68E-09	
13A	139.62	458.1	9.67E-09	
12A	139.67	458.2	1.18E-08	
11A	139.72	458.4	1.17E-08	
10A	139.76	458.5	1.45E-08	
9A	139.81	458.7	1.77E-08	
8A	139.86	458.9	1.41E-08	
7A	139.91	459	1.35E-08	
6A	139.96	459.2	1.46E-08	
5A	140.01	459.4	1.62E-08	
4A	140.06	459.5	1.34E-08	
3A	140.11	459.7	1.6E-08	
2A	140.15	459.8	1.2E-08	
1A	140.2	460	9.95E-09	
1	140.25	460.1	9.67E-09	
2	140.31	460.3	1.08E-08	
3	140.36	460.5	1.72E-08	
4	140.4	460.6	2.24E-08	
5	140.45	460.8	1.37E-08	
6	140.5	461	1.67E-08	
7	140.55	461.1	1.37E-08	
8	140.6	461.3	8.81E-09	
9	140.65	461.5	1.11E-08	
10	140.7	461.6	8.19E-09	
11	140.75	461.8	8.66E-09	
12	140.8	461.9	9.89E-09	
13	140.85	462.1	1.32E-08	
14	140.91	462.3	6.92E-09	

15	140.94	462.4	6.7E-09
16	140.98	462.5	9.45E-09
17	141.03	462.7	5.31E-09
18	141.08	462.9	7.55E-09
19	141.13	463	7.87E-09
20	141.18	463.2	1.11E-08
21	141.23	463.4	8.7E-09
22	141.3	463.6	8.68E-09
23	141.33	463.7	1.27E-08
24	141.38	463.8	1.15E-08
25	141.43	464	9.88E-09
26	141.48	464.2	8.14E-09
27	141.52	464.3	5.24E-09
28	141.57	464.5	6.51E-09
29	141.63	464.7	1.84E-08
30	141.67	464.8	2.17E-08
31	141.73	465	1.03E-08
32	141.77	465.1	6.85E-09
33	141.82	465.3	1.37E-08
34	141.87	465.5	2.03E-08
35	141.92	465.6	1.06E-08
36	141.97	465.8	8.46E-09
37	142.02	465.9	1.28E-08
38	142.06	466.1	8.49E-09
39	142.11	466.2	9.65E-09
40	142.16	466.4	4.98E-09
41	142.19	466.5	7.15E-09
42	142.24	466.7	1.37E-08
43	142.3	466.9	9.34E-09
44	142.35	467	1.4E-08
45	142.39	467.2	8.67E-09
46	142.45	467.4	1.28E-08
47	142.5	467.5	1.21E-08
48	142.55	467.7	6.26E-09
49	142.59	467.8	1.08E-08
50	142.64	468	2.02E-08
51	142.69	468.1	1.65E-08
52	142.74	468.3	3.6E-08
53	142.79	468.5	1.01E-08
54	142.84	468.6	1.25E-08
55	142.89	468.8	9.73E-09
56	142.94	469	7.32E-09
57	142.98	469.1	8.35E-09

58	143.03	469.3	8.65E-09
59	143.08	469.4	9.67E-09
60	143.13	469.6	1.61E-08
61	143.18	469.8	1.56E-08
62	143.24	469.9	1.43E-08
63	143.28	470.1	1.47E-08
64	143.33	470.2	1.47E-08
65	143.38	470.4	1.25E-08
66	143.42	470.5	1.97E-08
67	143.47	470.7	1.32E-08
68	143.52	470.9	8.96E-09
69	143.57	471	1.02E-08
70	143.62	471.2	1.11E-08
71	143.67	471.4	9.31E-09
72	143.72	471.5	7.73E-09
73	143.77	471.7	1.04E-08
74	143.81	471.8	1.22E-08
75	143.86	472	8.6E-09
76	143.92	472.2	8.62E-09
77	143.96	472.3	8.58E-09
78	144.01	472.5	1.27E-08
79	144.06	472.6	1.17E-08
80	144.1	472.8	9.13E-09
81	144.15	472.9	8.9E-09
82	144.19	473.1	8.79E-09
83	144.25	473.3	1.64E-08
84	144.3	473.4	1.22E-08
85	144.36	473.6	9.51E-09
86	144.4	473.8	9.24E-09
87	144.45	473.9	1.11E-08
88	144.51	474.1	1.05E-08
89	144.55	474.2	1.01E-08
90	144.59	474.4	1.09E-08
91	144.64	474.5	1.18E-08
92	144.69	474.7	9.08E-09
93	144.74	474.9	1.24E-08
94	144.81	475.1	1.21E-08
95	144.84	475.2	1.09E-08
96	144.89	475.4	9.72E-09
97	144.93	475.5	1.2E-08
98	144.99	475.7	1.02E-08
99	145.03	475.8	9.43E-09
100	145.1	476	8.44E-09

101	145.13	476.1	1.15E-08
102	145.18	476.3	6.78E-09
103	145.23	476.5	8.3E-09
104	145.29	476.7	6.93E-09
105	145.33	476.8	8.42E-09
106	145.38	477	1.37E-08
107	145.42	477.1	1.84E-08
108	145.47	477.3	2.03E-08
109	145.52	477.4	7.38E-09
110	145.57	477.6	8.08E-09
111	145.62	477.8	9.78E-09
112	145.67	477.9	9.19E-09
113	145.72	478.1	1.08E-08
114	145.77	478.2	2.4E-08
115	145.81	478.4	1.67E-08
116	145.87	478.6	1.6E-08
117	145.92	478.7	1.94E-08
118	145.96	478.9	1.17E-08
119	146.01	479	1.14E-08
120	146.06	479.2	1.93E-08
121	146.11	479.4	1.81E-08
122	146.16	479.5	1.32E-08
123	146.21	479.7	1.28E-08
124	146.24	479.8	9.69E-09
125	146.29	480	7.83E-09
126	146.35	480.2	1.62E-08
127	146.4	480.3	8.96E-09
128	146.45	480.5	9.98E-09
129	146.5	480.6	1.55E-08
130	146.55	480.8	2.56E-08
131	146.61	481	1.36E-08
132	146.69	481.3	2.26E-08
133	146.74	481.4	1.11E-08
134	146.79	481.6	1.44E-08
135	146.83	481.7	1.69E-08
136	146.89	481.9	1.41E-08
137	146.94	482.1	1.95E-08
138	146.99	482.3	1.18E-08
139	147.04	482.4	1.35E-08
140	147.08	482.5	1.08E-08
141	147.13	482.7	1.65E-08
142	147.18	482.9	1.68E-08
143	147.23	483	2.07E-08

144	147.28	483.2	2.15E-08
145	147.33	483.4	1.75E-08
146	147.38	483.5	2.04E-08
147	147.43	483.7	1.6E-08
148	147.47	483.8	1.45E-08
149	147.52	484	1.98E-08
150	147.57	484.2	1.46E-08
151	147.62	484.3	9.66E-09
152	147.67	484.5	1.8E-08
153	147.72	484.6	1.81E-08
154	147.77	484.8	1.8E-08
155	147.82	485	1.44E-08
156	147.88	485.2	1.52E-08
157	147.96	485.4	1.91E-08
158	148.01	485.6	1.18E-08
159	148.02	485.6	1.24E-08
160	148.02	485.6	1.25E-08
161	148.06	485.8	1.1E-08
162	148.1	485.9	6.15E-09
163	148.15	486.1	1.12E-08
164	148.2	486.2	1.39E-08
165	148.25	486.4	1.05E-08
166	148.3	486.5	1.29E-08
167	148.35	486.7	9.12E-09
168	148.4	486.9	1.14E-08
169	148.45	487	1.43E-08
170	148.5	487.2	1.34E-08
171	148.55	487.4	1.23E-08
172	148.6	487.5	1.77E-08
173	148.74	488	1.34E-08
174	148.79	488.2	1.5E-08
175	148.84	488.3	1.7E-08
176	148.84	488.3	1.6E-08
177	149.03	488.9	1.93E-08
178	149.13	489.3	2.28E-08
179	149.22	489.6	1.74E-08
180	149.32	489.9	1.87E-08
181	149.41	490.2	2.21E-08
182	149.51	490.5	2.21E-08
183	149.6	490.8	1.57E-08
184	149.7	491.1	2.31E-08
185	149.8	491.5	2.08E-08
186	149.89	491.8	1.97E-08

Bridge Creek Limestone

Hartland Shale

187	149.99	492.1	1.88E-08
188	150.08	492.4	1.58E-08
189	150.18	492.7	1.7E-08
190	150.27	493	2.59E-08
191	150.37	493.3	2.33E-08
192	150.46	493.6	1.74E-08
193	150.56	494	1.5E-08
194	150.65	494.3	1.77E-08
195	150.75	494.6	1.92E-08
196	150.85	494.9	2.85E-08
197	150.94	495.2	1.93E-08
198	151.04	495.5	1.51E-08
199	151.13	495.8	2.28E-08
200	151.23	496.2	1.96E-08
201	151.32	496.5	2.69E-08
202	151.42	496.8	2.67E-08
203	151.51	497.1	1.73E-08
204	151.61	497.4	2.02E-08
205	151.71	497.7	1.99E-08
206	151.8	498	1.57E-08
207	151.9	498.4	2E-08
208	151.99	498.7	1.81E-08
209	152.09	499	1.67E-08
210	152.18	499.3	1.96E-08
211	152.28	499.6	2.03E-08
212	152.37	499.9	1.75E-08
213	152.47	500.2	2.08E-08
214	152.56	500.5	2.51E-08
215	152.66	500.9	1.37E-08
216	152.76	501.2	1.8E-08
217	152.85	501.5	1.44E-08
218	152.95	501.8	2.56E-08
219	153.04	502.1	1.94E-08
220	153.14	502.4	1.41E-08
221	153.23	502.7	1.54E-08
222	153.33	503.1	2.76E-08
223	153.42	503.3	1.6E-08
224	153.52	503.7	1.67E-08
225	153.62	504	1.48E-08
226	153.71	504.3	1.75E-08
227	153.81	504.6	1.3E-08
228	153.9	504.9	1.44E-08
229	154	505.2	1.6E-08

230	154.09	505.5	2.35E-08
231	154.19	505.9	2.39E-08
232	154.28	506.2	2.15E-08
233	154.38	506.5	2.41E-08
234	154.48	506.8	2.16E-08
235	154.57	507.1	2.2E-08
236	154.67	507.4	2.16E-08
237	154.76	507.7	2.39E-08
238	154.86	508.1	2.15E-08
239	154.95	508.4	2.16E-08
240	155.05	508.7	2.58E-08
241	155.14	509	2.53E-08
242	155.24	509.3	2.17E-08
243	155.33	509.6	2.18E-08
244	155.43	509.9	2.77E-08
245	155.53	510.3	2.1E-08
246	155.62	510.6	1.6E-08
247	155.72	510.9	1.41E-08
248	155.81	511.2	2.08E-08
249	155.91	511.5	2.51E-08
250	156	511.8	2.07E-08
251	156.1	512.1	1.95E-08
252	156.19	512.4	2.28E-08
253	156.29	512.8	2.14E-08
254	156.39	513.1	2.45E-08
255	156.48	513.4	1.63E-08
256	156.58	513.7	1.42E-08
257	156.67	514	9.26E-09
258	156.77	514.3	1.79E-08
259	156.86	514.6	2.33E-08
260	156.96	515	2.51E-08
261	157.05	515.3	1.99E-08
262	157.15	515.6	2.25E-08
263	157.24	515.9	2.42E-08
264	157.34	516.2	2.28E-08
265	157.44	516.5	2.18E-08
266	157.53	516.8	1.82E-08
267	157.63	517.2	2.38E-08
268	157.72	517.5	2.23E-08
269	157.82	517.8	2.2E-08
270	157.91	518.1	1.81E-08
271	158.01	518.4	2.52E-08
272	158.1	518.7	2.19E-08

273	158.2	519	1.54E-08
274	158.3	519.4	1.97E-08
275	158.39	519.7	2.28E-08
276	158.49	520	2.09E-08
277	158.58	520.3	1.92E-08
278	158.68	520.6	1.78E-08
279	158.77	520.9	2.22E-08
280	158.87	521.2	1.96E-08
281	158.96	521.5	2.58E-08
282	159.06	521.9	2.55E-08
283	159.16	522.2	2.3E-08
284	159.25	522.5	2.37E-08
285	159.35	522.8	2.3E-08
286	159.44	523.1	2.05E-08
287	159.54	523.4	1.81E-08
288	159.63	523.7	1.9E-08
289	159.73	524	2.2E-08
290	159.82	524.3	2.43E-08
291	159.92	524.7	2.21E-08
292	160.01	525	2.08E-08
293	160.11	525.3	1.95E-08
294	160.21	525.6	2.24E-08
295	160.3	525.9	1.77E-08
296	160.4	526.2	1.43E-08
297	160.49	526.5	1.92E-08
298	160.59	526.9	1.61E-08
299	160.68	527.2	1.64E-08
300	160.78	527.5	1.56E-08
301	160.87	527.8	1.92E-08
302	160.97	528.1	1.49E-08
303	161.07	528.4	1.95E-08
304	161.16	528.7	2.01E-08
305	161.26	529.1	1.54E-08
306	161.35	529.4	1.92E-08
307	161.45	529.7	1.57E-08
308	161.54	530	1.91E-08
309	161.64	530.3	2.29E-08
310	161.73	530.6	1.34E-08
311	161.83	530.9	1.06E-08
312	161.92	531.2	2.44E-08

Site 3 – CTB GSSP, Pueblo, CO

sample #	height (m)	χ (m^3/kg)
1	0.01	1.64E-08
2	0.07	1.45E-08
3	0.12	1.79E-08
4	0.18	1.35E-08
5	0.23	1.32E-08
6	0.29	1.36E-08
7	0.34	1.07E-08
8	0.4	8.41E-09
9	0.45	9.66E-09
10	0.51	9.38E-09
11	0.56	6.69E-09
12	0.62	7.29E-09
13	0.67	7.92E-09
14	0.73	7.78E-09
15	0.78	1.25E-08
16	0.84	1.73E-08
17	0.89	1.33E-08
18	0.95	2.52E-08
19	1	2.27E-08
20	1.06	1.98E-08
21	1.11	1.68E-08
22	1.17	1.07E-08
23	1.22	1.21E-08
24	1.28	1.21E-08
25	1.33	1.83E-08
26	1.39	1.72E-08
27	1.44	2.30E-08
28	1.5	2.47E-08
29	1.55	3.34E-08
30	1.61	3.50E-08
31	1.66	1.67E-08
32	1.72	1.80E-08
33	1.77	1.46E-08
34	1.83	2.17E-08
35	1.88	2.12E-08
36	1.94	1.88E-08
37	1.99	2.10E-08
38	2.05	1.35E-08
39	2.1	1.03E-08
40	2.16	1.95E-08
41	2.21	1.86E-08
42	2.27	1.80E-08
43	2.32	2.19E-08
44	2.38	1.74E-08

45	2.43	1.04E-08
46	2.49	2.82E-08
47	2.54	1.11E-08
48	2.6	1.07E-08
49	2.65	2.26E-08
50	2.71	2.00E-08
51	2.76	1.00E-08
52	2.82	1.07E-08
53	2.87	1.24E-08
54	2.93	1.34E-08
55	2.98	1.62E-08
56	3.04	1.26E-08
57	3.09	1.64E-08
58	3.15	1.66E-08
59	3.2	1.70E-08
60	3.26	1.74E-08
61	3.31	1.80E-08
62	3.37	1.94E-08
63	3.42	7.00E-09
64	3.48	6.23E-09
65	3.53	6.17E-09
66	3.59	8.75E-09
67	3.64	1.63E-08
68	3.7	1.66E-08
69	3.75	1.80E-08
70	3.81	9.84E-09
71	3.86	1.33E-08
72	3.92	1.24E-08
73	3.97	1.43E-08
74	4.03	1.32E-08
75	4.08	1.20E-08
76	4.14	1.03E-08
77	4.19	9.40E-09
78	4.25	1.32E-08
79	4.3	1.31E-08
80	4.36	9.66E-09
81	4.41	9.17E-09
82	4.47	7.57E-09
83	4.52	1.07E-08
84	4.58	6.87E-09
85	4.63	1.16E-08
86	4.69	1.37E-08
87	4.74	9.52E-09
88	4.8	1.19E-08
89	4.85	1.17E-08
90	4.91	1.04E-08

91	4.96	9.42E-09
92	5.02	1.27E-08
93	5.07	1.34E-08
94	5.13	1.23E-08
95	5.18	1.28E-08
96	5.24	1.35E-08
97	5.29	1.27E-08
98	5.35	9.29E-09
99	5.4	7.22E-09
100	5.45	6.92E-09
101	5.51	1.03E-08
102	5.56	1.39E-08
103	5.62	1.72E-08
104	5.67	3.45E-08
105	5.73	9.07E-09
106	5.78	7.22E-09
107	5.84	8.05E-09
108	5.89	1.88E-08
109	5.95	1.50E-08
110	6	1.61E-08
111	6.06	1.67E-08
112	6.11	1.23E-08
113	6.17	1.29E-08
114	6.22	1.62E-08
115	6.27	1.26E-08
116	6.33	9.23E-09
117	6.38	1.15E-08
118	6.44	1.15E-08
119	6.49	1.67E-08
120	6.55	1.29E-08
121	6.6	1.22E-08
122	6.66	1.11E-08
123	6.71	7.83E-09
124	6.77	9.14E-09
125	6.82	1.31E-08
126	6.88	1.68E-08
127	6.93	8.21E-09
128	6.99	9.73E-09
129	7.04	1.76E-08
130	7.1	1.57E-08
131	7.15	1.55E-08
132	7.2	1.79E-08
133	7.26	2.10E-08
134	7.31	9.37E-09
135	7.37	6.27E-09
136	7.42	9.52E-09

137	7.48	1.45E-08
138	7.53	9.77E-09
139	7.59	1.26E-08
140	7.64	1.73E-08
141	7.7	1.84E-08
142	7.75	1.77E-08
143	7.81	1.89E-08
144	7.86	1.04E-08
145	7.92	1.20E-08
146	7.97	1.34E-08
147	8.02	1.10E-08
148	8.08	1.29E-08
149	8.13	1.65E-08
150	8.19	1.38E-08
151	8.24	1.43E-08
152	8.3	2.54E-08
153	8.35	1.18E-08
154	8.41	6.95E-09
155	8.46	1.91E-08
156	8.52	1.32E-08
157	8.57	1.98E-08
158	8.63	1.71E-08
159	8.68	1.21E-08
160	8.74	5.63E-09
161	8.79	8.96E-09

Site 4 – La Junta, CO

sample #	ht (m)	χ (m3/kg)
1	0	1.41E-08
2	0.05	1.49E-08
3	0.1	1.45E-08
4	0.15	1.14E-08
5	0.2	1.02E-08
6	0.25	2.22E-08
7	0.3	8.64E-09
8	0.35	7.63E-09
9	0.4	6.21E-09
10	0.45	9.98E-09
11	0.5	1.27E-08
12	0.55	1.87E-08
13	0.6	2.49E-08
14	0.65	1.01E-08
15	0.7	8.35E-09
16	0.75	9.52E-09
17	0.8	1.92E-08
18	0.85	2.53E-08
19	0.9	2.44E-08
20	0.95	1.65E-08
21	1	9.22E-09
22	1.05	2.55E-08
23	1.1	9.42E-09
24	1.15	1.85E-08
25	1.2	2.67E-08
26	1.25	2.02E-08
27	1.3	2.38E-08
28	1.35	3.41E-08
29	1.4	1.26E-08
30	1.45	3.11E-08
31	1.5	1.59E-08
32	1.55	1.65E-08
33	1.6	1.58E-08
34	1.65	3.94E-08
35	1.7	8.78E-09
36	1.75	9.19E-09
37	1.8	1.55E-08
38	1.85	1.17E-08
39	1.9	1.28E-08
40	1.95	1.03E-08

41	2	9.33E-09
42	2.05	1.77E-08
43	2.1	1.34E-08
44	2.15	1.52E-08
45	2.2	1.40E-08
46	2.25	1.51E-08
47	2.3	1.62E-08
48	2.35	1.63E-08
49	2.4	1.19E-08
50	2.45	1.39E-08
51	2.5	1.30E-08
52	2.55	9.17E-09
53	2.6	1.50E-08
54	2.65	1.19E-08
55	2.7	1.09E-08
56	2.75	1.34E-08
57	2.8	1.36E-08
58	2.85	1.40E-08
59	2.9	8.67E-09
60	2.95	7.63E-09
61	3	1.03E-08
62	3.05	1.72E-08
63	3.1	1.09E-08
64	3.15	9.60E-09
65	3.2	1.26E-08
66	3.25	7.29E-09
67	3.3	7.90E-09
68	3.35	5.55E-09
69	3.4	8.67E-09
70	3.45	1.02E-08
71	3.5	1.34E-08
72	3.55	1.19E-08
73	3.6	1.07E-08
74	3.65	7.38E-09
75	3.7	1.99E-08
76	3.75	2.03E-08
77	3.8	1.10E-08
78	3.85	2.08E-08
79	3.9	1.64E-08
80	3.95	6.46E-09
81	4	1.28E-08
82	4.05	1.59E-08
83	4.1	6.85E-09

84	4.15	1.27E-08
85	4.2	9.74E-09
86	4.25	1.20E-08
87	4.3	1.13E-08
88	4.35	1.45E-08

Site 5 – Bounds Core, KS

For Bartington Probe value conversion to Williams Magnetic Susceptibility Bridge at Louisiana State University. MS values are in counts. Conversion to Williams MS Bridge values by calculating for y using the

Line equation: $y = 5.478E^{-09}x + 1.12E^{-08}$

and

Polynomial equation: $y = -2.165E^{-11}x^2 + 6.103E^{-09}x + 8.24E^{-09}$

Where x = mean MS count for that sample

Sample 1 is located 0.5 m below the base of Bed 63 equivalent in the Bounds Core.

sample #	height (m)	MS1	MS2	MS3	Mean MS	χ conv, Line	χ conv, Poly
1	0	27	31	29	29	1.70062E-07	1.67019E-07
2	0.05	21	20	19	20	1.2076E-07	1.2164E-07
3	0.1	2	2	2	2	2.2156E-08	2.03594E-08
4	0.15	2	3	3	2.6667	2.5808E-08	2.43607E-08
5	0.2	2	2	3	2.3333	2.3982E-08	2.23625E-08
6	0.25	3	3	3	3	2.7634E-08	2.63542E-08
7	0.3	3	4	4	3.6667	3.1286E-08	3.03266E-08
8	0.35	2	3	2	2.3333	2.3982E-08	2.23625E-08
9	0.4	2	3	2	2.3333	2.3982E-08	2.23625E-08
10	0.45	3	2	2	2.3333	2.3982E-08	2.23625E-08
11	0.5	1	2	2	1.6667	2.033E-08	1.83515E-08
12	0.55	2	3	2	2.3333	2.3982E-08	2.23625E-08
13	0.6	2	2	2	2	2.2156E-08	2.03594E-08
14	0.65	2	1	2	1.6667	2.033E-08	1.83515E-08
15	0.7	2	2	2	2	2.2156E-08	2.03594E-08
16	0.75	3	4	4	3.6667	3.1286E-08	3.03266E-08
17	0.8	3	2	3	2.6667	2.5808E-08	2.43607E-08
18	0.85	3	3	3	3	2.7634E-08	2.63542E-08
19	0.9	3	3	2	2.6667	2.5808E-08	2.43607E-08
20	0.95	2	2	2	2	2.2156E-08	2.03594E-08
21	1	3	3	2	2.6667	2.5808E-08	2.43607E-08
22	1.05	5	6	7	6	4.4068E-08	4.40786E-08
23	1.1	5	5	6	5.3333	4.0416E-08	4.01735E-08
24	1.15	67	64	69	66.667	3.764E-07	3.18884E-07
25	1.2	4	6	4	4.6667	3.6764E-08	3.62492E-08
26	1.25	0	1	1	0.6667	1.4852E-08	1.2299E-08
27	1.3	1	0	1	0.6667	1.4852E-08	1.2299E-08
28	1.35	1	2	1	1.3333	1.8504E-08	1.63388E-08
29	1.4	0	0	1	0.3333	1.3026E-08	1.02719E-08
30	1.45	-	-	-		Missing Core	

31	1.5	-	-	-			
32	1.55	0	1	0	0.3333	1.3026E-08	1.02719E-08
33	1.6	1	1	0	0.6667	1.4852E-08	1.2299E-08
34	1.65	-	-	-			
35	1.7	-	-	-			
36	1.75	-	-	-		Missing Core	
37	1.8	-	-	-			
38	1.85	-	-	-			
39	1.9	57	51	57	55	3.1249E-07	2.78414E-07
40	1.95	33	33	31	32.333	1.88322E-07	1.82936E-07
41	2	1	2	1	1.3333	1.8504E-08	1.63388E-08
42	2.05	2	2	2	2	2.2156E-08	2.03594E-08
43	2.1	3	4	4	3.6667	3.1286E-08	3.03266E-08
44	2.15	1	1	1	1	1.6678E-08	1.43214E-08
45	2.2	0	0	1	0.3333	1.3026E-08	1.02719E-08
46	2.25	2	1	2	1.6667	2.033E-08	1.83515E-08
47	2.3	2	1	2	1.6667	2.033E-08	1.83515E-08
48	2.35	1	1	2	1.3333	1.8504E-08	1.63388E-08
49	2.4	1	1	0	0.6667	1.4852E-08	1.2299E-08
50	2.45	2	4	2	2.6667	2.5808E-08	2.43607E-08
51	2.5	0	0	1	0.3333	1.3026E-08	1.02719E-08
52	2.55	2	1	2	1.6667	2.033E-08	1.83515E-08
53	2.6	1	2	2	1.6667	2.033E-08	1.83515E-08
54	2.65	3	2	3	2.6667	2.5808E-08	2.43607E-08
55	2.7	2	1	2	1.6667	2.033E-08	1.83515E-08
56	2.75	3	2	3	2.6667	2.5808E-08	2.43607E-08
57	2.8	2	1	2	1.6667	2.033E-08	1.83515E-08
58	2.85	1	1	2	1.3333	1.8504E-08	1.63388E-08
59	2.9	0	0	1	0.3333	1.3026E-08	1.02719E-08
60	2.95	1	1	0	0.6667	1.4852E-08	1.2299E-08
61	3	2	2	1	1.6667	2.033E-08	1.83515E-08
62	3.05	3	2	2	2.3333	2.3982E-08	2.23625E-08
63	3.1	0	1	0	0.3333	1.3026E-08	1.02719E-08
64	3.15	1	1	0	0.6667	1.4852E-08	1.2299E-08
65	3.2	1	1	1	1	1.6678E-08	1.43214E-08
66	3.25	1	1	1	1	1.6678E-08	1.43214E-08
67	3.3	-9	0	1	-2.6667	-3.408E-09	-8.18862E-09
68	3.35	1	1	2	1.3333	1.8504E-08	1.63388E-08
69	3.4	0	0	1	0.3333	1.3026E-08	1.02719E-08
70	3.45	1	1	1	1	1.6678E-08	1.43214E-08
71	3.5	1	2	1	1.3333	1.8504E-08	1.63388E-08
72	3.55	1	1	1	1	1.6678E-08	1.43214E-08
73	3.6	1	1	1	1	1.6678E-08	1.43214E-08

74	3.65	1	1	2	1.3333	1.8504E-08	1.63388E-08
75	3.7	1	0	1	0.6667	1.4852E-08	1.2299E-08
76	3.75	1	1	1	1	1.6678E-08	1.43214E-08
77	3.8	1	2	1	1.3333	1.8504E-08	1.63388E-08
78	3.85	3	3	4	3.3333	2.946E-08	2.83428E-08
79	3.9	2	1	1	1.3333	1.8504E-08	1.63388E-08
80	3.95	0	0	1	0.3333	1.3026E-08	1.02719E-08
81	4	1	1	2	1.3333	1.8504E-08	1.63388E-08
82	4.05	0	1	2	1	1.6678E-08	1.43214E-08
83	4.1	3	2	2	2.3333	2.3982E-08	2.23625E-08
84	4.15	2	2	2	2	2.2156E-08	2.03594E-08
85	4.2	1	2	2	1.6667	2.033E-08	1.83515E-08
86	4.25	1	1	1	1	1.6678E-08	1.43214E-08
87	4.3	4	4	4	4	3.3112E-08	3.23056E-08
88	4.35	18	17	16	17	1.04326E-07	1.05734E-07
89	4.4	8	7	7	7.3333	5.1372E-08	5.1831E-08
90	4.45	0	1	0	0.3333	1.3026E-08	1.02719E-08
91	4.5	1	1	1	1	1.6678E-08	1.43214E-08
92	4.55	1	1	1	1	1.6678E-08	1.43214E-08
93	4.6	1	1	0	0.6667	1.4852E-08	1.2299E-08
94	4.65	1	1	1	1	1.6678E-08	1.43214E-08
95	4.7	2	1	1	1.3333	1.8504E-08	1.63388E-08
96	4.75	23	24	21	22.667	1.35368E-07	1.35451E-07
97	4.8	39	39	45	41	2.35798E-07	2.22069E-07
98	4.85	2	2	3	2.3333	2.3982E-08	2.23625E-08
99	4.9	-1	0	0	-0.3333	9.374E-09	6.20326E-09
100	4.95	1	1	1	1	1.6678E-08	1.43214E-08
101	5	1	1	2	1.3333	1.8504E-08	1.63388E-08
102	5.05	2	2	3	2.3333	2.3982E-08	2.23625E-08
103	5.1	2	1	1	1.3333	1.8504E-08	1.63388E-08
104	5.15	1	1	0	0.6667	1.4852E-08	1.2299E-08
105	5.2	1	1	1	1	1.6678E-08	1.43214E-08
106	5.25	2	1	2	1.6667	2.033E-08	1.83515E-08
107	5.3	1	2	1	1.3333	1.8504E-08	1.63388E-08
108	5.35	1	1	2	1.3333	1.8504E-08	1.63388E-08
109	5.4	1	2	2	1.6667	2.033E-08	1.83515E-08
110	5.45	2	1	1	1.3333	1.8504E-08	1.63388E-08
111	5.5	1	2	1	1.3333	1.8504E-08	1.63388E-08
112	5.55	0	1	0	0.3333	1.3026E-08	1.02719E-08
113	5.6	0	1	0	0.3333	1.3026E-08	1.02719E-08
114	5.65	1	0	1	0.6667	1.4852E-08	1.2299E-08
115	5.7	0	-1	0	-0.3333	9.374E-09	6.20326E-09
116	5.75	-1	-1	-1	-1	5.722E-09	2.11535E-09

117	5.8	0	1	-1	0	1.12E-08	8.24E-09
118	5.85	0	-1	0	-0.3333	9.374E-09	6.20326E-09
119	5.9	1	0	1	0.6667	1.4852E-08	1.2299E-08
120	5.95	2	0	1	1	1.6678E-08	1.43214E-08
121	6	2	3	2	2.3333	2.3982E-08	2.23625E-08
122	6.05	2	4	2	2.6667	2.5808E-08	2.43607E-08

Site 6 – Cuba, KS

sample #	height (m)	χ (m^3/kg)
1	0	4.87E-09
2	0.05	1.45E-08
3	0.1	1.62E-08
4	0.15	1.36E-08
5	0.2	1.41E-08
6	0.25	1.91E-08
7	0.3	1.35E-08
8	0.35	2.69E-08
9	0.4	2.11E-08
10	0.45	1.81E-08
11	0.5	7.17E-09
12	0.55	1.42E-08
13	0.6	1.24E-08
14	0.65	1.25E-08
15	0.7	1.33E-08
16	0.75	1.88E-08
17	0.8	2.39E-08
18	0.85	1.91E-08
19	0.9	1.66E-08
20	0.95	1.56E-08
21	1	1.23E-08
22	1.05	1.63E-08
23	1.1	1.49E-08
24	1.15	1.44E-08
25	1.2	1.46E-08
26	1.25	1.30E-08
27	1.3	1.36E-08
28	1.35	1.11E-08
29	1.4	1.63E-08
30	1.45	1.90E-08
31	1.5	1.68E-08
32	1.55	1.98E-08
33	1.6	1.62E-08
34	1.65	1.28E-08
35	1.7	9.42E-09
36	1.75	1.51E-08
37	1.8	2.00E-08
38	1.85	2.18E-08
39	1.9	2.13E-08
40	1.95	3.99E-08

41	2	2.32E-08
42	2.05	1.91E-08
43	2.1	9.58E-09
44	2.15	3.36E-08
45	2.2	4.08E-08
46	2.25	1.59E-08
47	2.3	1.65E-08
48	2.35	2.10E-08
49	2.4	2.13E-08
50	2.45	3.22E-08
51	2.5	1.84E-08
52	2.55	1.92E-08
53	2.6	2.32E-08
54	2.65	2.22E-08
55	2.7	2.39E-08
56	2.75	2.81E-08
57	2.8	1.47E-08
58	2.85	1.46E-08
59	2.9	1.80E-08
60	2.95	1.56E-08
61	3	2.69E-08
62	3.05	1.42E-08
63	3.1	9.18E-09
64	3.15	2.22E-08
65	3.2	1.78E-08
66	3.25	1.66E-08
67	3.3	1.69E-08
68	3.35	1.24E-08
69	3.4	9.40E-09
70	3.45	1.09E-08
71	3.5	1.15E-08
72	3.55	1.25E-08
73	3.6	1.29E-08
74	3.65	9.26E-09
75	3.7	9.43E-09
76	3.75	2.82E-08
77	3.8	7.53E-09
78	3.85	1.45E-08
79	3.9	1.08E-08
80	3.95	1.19E-08
81	4	9.66E-09
82	4.05	5.76E-09
83	4.1	1.42E-08

84	4.15	8.69E-09
85	4.2	1.06E-08
86	4.25	9.86E-09
87	4.3	1.19E-08
88	4.35	9.15E-09
89	4.4	9.76E-09
90	4.45	1.04E-08
91	4.5	2.04E-08
92	4.55	1.38E-08
93	4.6	1.13E-08
94	4.65	9.64E-09
95	4.7	1.16E-08
96	4.75	6.93E-09
97	4.8	1.62E-08
98	4.85	1.52E-08
99	4.9	1.32E-08
100	4.95	9.61E-09
101	5	1.12E-08
102	5.05	1.03E-08
103	5.1	1.96E-08
104	5.15	1.49E-08
105	5.2	7.91E-09
106	5.25	9.37E-09

Site B – Antonio Canyon, TX

sample #	height (m)	χ (m^3/kg)
A1	0	1.53E-08
A2	0.05	6.85E-09
A3	0.1	3.31E-09
A4	0.15	8.62E-09
A5	0.2	1.71E-08
A6	0.25	1.21E-08
A7	0.3	1.20E-08
A8	0.35	1.28E-08
A9	0.4	1.91E-08
A10	0.45	1.26E-08
A11	0.5	1.65E-08
A12	0.55	1.29E-08
A13	0.6	1.38E-08
A14	0.65	2.38E-08
A15	0.7	9.89E-09
A16	0.75	9.51E-09
A17	0.8	8.20E-09
A18	0.85	1.10E-08
A19	0.9	1.33E-08
A20	0.95	1.32E-08
A21	1	1.13E-08
A22	1.05	1.54E-07
A23	1.1	1.46E-08
A24	1.15	1.34E-08
A25	1.2	7.80E-09
A26	1.25	1.07E-08
A27	1.3	1.16E-08
A28	1.35	1.30E-08
A29	1.4	7.74E-09
A30	1.45	1.58E-08
A31	1.5	2.12E-08
A32	1.55	5.20E-08
1	1.6	3.66E-08
2	1.65	1.53E-08
3	1.7	1.11E-08
4	1.75	5.77E-09
5	1.8	1.99E-09
6	1.85	3.98E-09
7	1.9	1.42E-09
8	1.95	4.85E-09
9	2	8.52E-09
10	2.05	5.14E-09
11	2.1	1.06E-08
12	2.15	5.95E-09

13	2.2	8.55E-09
14	2.25	1.11E-08
15	2.3	1.57E-08
16	2.35	8.86E-09
17	2.4	9.07E-09
18	2.45	7.58E-09
19	2.5	4.65E-09
20	2.55	3.11E-09
21	2.6	6.94E-09
22	2.65	4.51E-09
23	2.7	1.06E-08
24	2.75	1.02E-08
25	2.8	1.24E-08
26	2.85	1.11E-08
27	2.9	2.38E-08
28	2.95	2.13E-08
29	3	1.78E-08
30	3.05	1.26E-08
31	3.1	5.37E-09
32B	3.15	1.37E-08
33	3.2	1.34E-08
34	3.25	7.87E-09
35	3.3	1.18E-08
36	3.35	1.04E-08
37B	3.4	6.74E-09
38	3.45	7.83E-09
39	3.5	5.34E-09
40	3.55	3.57E-09
41	3.6	1.06E-08
42	3.65	7.20E-09
43	3.7	1.21E-08
44	3.75	8.84E-09
45	3.8	8.57E-09
46	3.85	1.89E-08
47	3.9	1.19E-08
48	3.95	6.94E-09
49	4	7.63E-09
50	4.05	4.92E-09
51	4.1	3.84E-09
52	4.15	8.34E-09
53	4.2	7.57E-09
54	4.25	5.24E-09
55	4.3	7.54E-09
56	4.35	9.24E-09
57	4.4	8.00E-09
58	4.45	9.20E-09

59	4.5	9.88E-09
60	4.55	7.47E-09
61	4.6	8.36E-09
62	4.65	9.20E-09
63	4.7	6.35E-09
64	4.75	8.88E-09
65	4.8	1.83E-08
66	4.85	1.02E-08
67	4.9	1.38E-08
68	4.95	5.15E-09
69	5	7.73E-09
70	5.05	8.11E-09
71	5.1	9.68E-09
72.1	5.15	1.05E-08
72.2	5.2	8.31E-09
73	5.25	7.38E-09
74B	5.3	6.69E-09
75	5.35	5.82E-09
76	5.4	5.15E-09
77	5.45	5.11E-09
78	5.5	6.60E-09
79	5.55	9.35E-09
80	5.6	1.16E-08
81	5.65	1.20E-08
82	5.7	1.53E-08
83	5.75	8.73E-09
84	5.8	1.19E-08
85B	5.85	9.39E-09
86	5.9	7.16E-09
87	5.95	6.26E-09
88	6	1.11E-08
89	6.05	7.30E-09
9	6.1	1.19E-08
91	6.15	1.30E-08
92	6.2	1.31E-08
93		Missing
94	6.3	1.21E-08
95	6.35	1.20E-08
96	6.4	1.50E-08
97	6.45	1.48E-08
98	6.5	1.74E-08
99	6.55	1.45E-08
100	6.6	1.24E-08
101	6.65	1.32E-08
102	6.7	1.16E-08
103	6.75	5.74E-09

104	6.8	7.76E-09
105	6.85	9.14E-09
106	6.9	7.77E-09
107	6.95	1.02E-08
108	7	9.46E-09
109	7.05	1.41E-08
110	7.1	1.22E-08
111	7.15	1.11E-08
112	7.2	1.15E-08
13	7.25	1.00E-08
114	7.3	1.50E-08
115	7.35	1.13E-08
116	7.4	1.37E-08
117	7.45	1.19E-08
118	7.5	9.60E-09
119	7.55	9.79E-09
120	7.6	9.91E-09
121	7.65	1.28E-08
122	7.7	1.09E-08
123	7.75	1.09E-08
124	7.8	1.43E-08
125	7.85	1.32E-08
126	7.9	1.76E-08
127	7.95	8.82E-09
128	8	1.90E-08
129	8.05	1.66E-08
130B	8.1	1.67E-08
131	8.15	4.67E-08
132	8.2	1.13E-08
133	8.25	6.27E-09

APPENDIX B: GAMMA-RAY DATA

Site 1 – Escalante Core, UT

Well log GRS values are in American Petroleum Industry units (API).

depth (ft)	depth (m)	GRS (API)	
770.9	234.97	109.1	
771.1	235.03	107.5	--- Bentonite C
771.3	235.09	114.3	
771.5	235.15	118.6	
771.7	235.21	134.3	
771.9	235.28	137.1	
772.1	235.34	134.2	
772.3	235.4	135	
772.5	235.46	143.2	
772.7	235.52	129.3	
772.9	235.58	119.6	
773.1	235.64	103.7	
773.3	235.7	103.5	
773.5	235.76	99.4	
773.7	235.82	90.5	
773.9	235.88	91.7	
774.1	235.95	96.9	
774.3	236.01	101.9	
774.5	236.07	104.7	Turonian
774.7	236.13	114.6	----------
774.9	236.19	113.6	Cenomanian
775.1	236.25	118.5	
775.3	236.31	118.4	
775.5	236.37	119.7	
775.7	236.43	110.9	
776	236.52	103.1	
776.2	236.59	106.7	
776.4	236.65	112.9	
776.6	236.71	110.8	
776.8	236.77	96.5	
777	236.83	105.3	
777.2	236.89	112.4	
777.4	236.95	124.5	
777.6	237.01	115.8	
777.8	237.07	117.1	
778	237.13	108.1	
778.2	237.2	113.3	

778.4	237.26	103.4
778.6	237.32	98.7
778.8	237.38	109.7
779	237.44	101
779.2	237.5	102.9
779.4	237.56	103.7
779.6	237.62	108.2
779.8	237.68	107.1
780	237.74	107.6
780.2	237.8	115.3
780.4	237.87	119.9
780.6	237.93	113.1
780.8	237.99	105.8
781	238.05	103
781.2	238.11	97.8
781.4	238.17	108.6
781.6	238.23	116.3
781.8	238.29	112
782	238.35	116.1
782.2	238.41	121.9
782.4	238.48	126.4
782.6	238.54	133
782.8	238.6	134.8
783	238.66	137.6
783.2	238.72	133.8
783.4	238.78	129.8
783.6	238.84	125.6
783.8	238.9	118.8
784	238.96	109.1
784.2	239.02	108.3
784.4	239.09	106.4
784.6	239.15	102.1
784.8	239.21	90.7
785	239.27	87.1
785.2	239.33	95.7
785.4	239.39	102.6
785.6	239.45	95.6
785.8	239.51	88.9
786	239.57	83.7
786.2	239.63	77.6
786.4	239.69	83.6
786.6	239.76	71.9
786.8	239.82	78.1

787	239.88	77.5
787.2	239.94	79.2
787.4	240	93.2
787.6	240.06	101.3
787.8	240.12	104.7
788	240.18	92.5
788.2	240.24	78.4
788.4	240.3	69
788.6	240.37	72.4
788.8	240.43	79.6
789	240.49	88.4
789.2	240.55	91.7
789.4	240.61	92.5
789.6	240.67	84.2
789.8	240.73	82
790	240.79	83.1
790.2	240.85	83.8
790.4	240.91	82.8
790.6	240.97	75.6
790.8	241.04	76.9
791	241.1	80.3
791.2	241.16	86.5
791.4	241.22	89.4
791.6	241.28	87.4
791.8	241.34	94.7
792	241.4	86.1
792.2	241.46	86.7
792.4	241.52	89.4
792.6	241.58	90.1
792.8	241.65	92.4
793	241.71	96.5
793.2	241.77	101.3
793.4	241.83	104.1
793.6	241.89	112.9
793.8	241.95	100.2
794	242.01	98.5
794.2	242.07	104.1
794.4	242.13	109
794.6	242.19	110.6
794.8	242.26	108.3
795	242.32	112.8
795.2	242.38	115
795.4	242.44	119.2

795.6	242.5	112.6
795.8	242.56	119.7
796	242.62	113.9
796.1	242.65	109.4
796.3	242.71	122.1
796.5	242.77	121.9
796.7	242.83	128.9
796.9	242.9	124.2
797.1	242.96	130.3
797.3	243.02	151.2
797.5	243.08	135.1
797.7	243.14	146.5
797.9	243.2	137.7
798.1	243.26	134.7
798.3	243.32	144.8
798.5	243.38	151.9
798.7	243.44	139.2
798.9	243.5	136
799.1	243.57	134.6
799.3	243.63	153.5
799.5	243.69	154.4
799.7	243.75	159.3
799.9	243.81	145.8
800.1	243.87	136.6
800.3	243.93	135.3
800.5	243.99	129.2
800.7	244.05	134
800.9	244.11	139.7
801.1	244.18	135.9
801.3	244.24	134.9
801.5	244.3	139.4
801.7	244.36	130.5
801.9	244.42	134.4
802.1	244.48	141
802.3	244.54	148.9
802.5	244.6	147.4
802.7	244.66	141.1
802.9	244.72	145.6
803.1	244.78	161.5
803.3	244.85	174.4
803.5	244.91	169.7
803.7	244.97	176.9
803.9	245.03	182.7

--- Bentonite B

804.1	245.09	187.4
804.3	245.15	199.6
804.5	245.21	198.3
804.7	245.27	204.6
804.9	245.33	201.5
805.1	245.39	209.3
805.3	245.46	198.5
805.5	245.52	188.7
805.7	245.58	165.1
805.9	245.64	156.9
806.1	245.7	158.9
806.3	245.76	151.9
806.5	245.82	126.1
806.7	245.88	103.8
806.9	245.94	99.4
807.1	246	93.2
807.3	246.07	99.4
807.5	246.13	103.3
807.7	246.19	102.2
807.9	246.25	91
808.1	246.31	102.5
808.3	246.37	99
808.5	246.43	93.1
808.7	246.49	89.6
808.9	246.55	98
809.1	246.61	89.4
809.3	246.67	96.8
809.5	246.74	100.6
809.7	246.8	96.9
809.9	246.86	103.3
810.1	246.92	102.6
810.3	246.98	104
810.5	247.04	98.3
810.7	247.1	105.4
810.9	247.16	96.5
811.1	247.22	95.4
811.3	247.28	96.4
811.5	247.35	94.1
811.7	247.41	99.1
811.9	247.47	88.4
812.1	247.53	85.4
812.3	247.59	80.2
812.5	247.65	72.8

812.7	247.71	78.5
812.9	247.77	84.3
813.1	247.83	83.1
813.3	247.89	94.7
813.5	247.95	89.1
813.7	248.02	93.3
813.9	248.08	89.2
814.1	248.14	87.8
814.3	248.2	87.9
814.5	248.26	84.4
814.7	248.32	87.5
814.9	248.38	81.7
815.1	248.44	83.7
815.3	248.5	85.3
815.5	248.56	81.6
815.7	248.63	82.2
815.9	248.69	90
816	248.72	86.1
816.2	248.78	81.9
816.4	248.84	75.8
816.6	248.9	68.4
816.8	248.96	74.9
817	249.02	79.3
817.2	249.08	83
817.4	249.14	91
817.6	249.2	95.3
817.8	249.27	101
818	249.33	107.2
818.2	249.39	109.7
818.4	249.45	112.9
818.6	249.51	112.5
818.8	249.57	98.4
819	249.63	89.2
819.2	249.69	80.7
819.4	249.75	89.7
819.6	249.81	82.8
819.8	249.88	75.3
820	249.94	79.9
820.2	250	86.8
820.4	250.06	92.6
820.6	250.12	83.8
820.8	250.18	104.3
821	250.24	91.7

821.2	250.3	88.3	
821.4	250.36	90.3	
821.6	250.42	84.4	
821.8	250.48	88.8	
822	250.55	90.7	
822.2	250.61	95.9	
822.4	250.67	93.4	
822.6	250.73	97.1	
822.8	250.79	93.2	
823	250.85	93.8	
823.2	250.91	98.4	
823.4	250.97	92.9	
823.6	251.03	98.5	
823.8	251.09	110	
824	251.16	109.4	
824.2	251.22	112.6	
824.4	251.28	111.3	
824.6	251.34	113.3	
824.8	251.4	117.2	--- Bentonite A
825	251.46	127.1	
825.2	251.52	113.3	
825.4	251.58	119.7	
825.6	251.64	121.7	
825.8	251.7	115.7	
826	251.76	101.1	
826.2	251.83	100.6	
826.4	251.89	88.2	
826.6	251.95	71.2	
826.8	252.01	68.2	
827	252.07	63.2	
827.2	252.13	61.7	
827.4	252.19	57.1	
827.6	252.25	62.6	
827.8	252.31	60.4	
828	252.37	61.6	
828.2	252.44	72.6	
828.4	252.5	76.1	
828.6	252.56	87.2	
828.8	252.62	95.2	
829	252.68	103.3	
829.2	252.74	111.7	
829.4	252.8	125	
829.6	252.86	122.6	

829.8	252.92	132.8
830	252.98	128.4
830.2	253.04	122
830.4	253.11	117.5
830.6	253.17	113.3
830.8	253.23	120
831	253.29	128
831.2	253.35	111
831.4	253.41	115.5
831.6	253.47	104.4
831.8	253.53	84.8
832	253.59	62.7
832.2	253.65	61.2
832.4	253.72	58.1
832.6	253.78	62.2
832.8	253.84	62.4
833	253.9	64.1
833.2	253.96	59.4
833.4	254.02	61.8
833.6	254.08	65.3
833.8	254.14	58.4
834	254.2	60.9
834.2	254.26	58
834.4	254.33	49.5
834.6	254.39	54
834.8	254.45	46.3
835	254.51	46.5
835.2	254.57	41.1
835.4	254.63	41
835.6	254.69	37
835.8	254.75	34.7
835.9	254.78	36.9
836.1	254.84	42.7
836.3	254.9	44.5
836.5	254.97	39.4
836.7	255.03	45.9
836.9	255.09	56.7
837.1	255.15	65.3
837.3	255.21	62.8
837.5	255.27	65.3
837.7	255.33	71.9
837.9	255.39	65
838.1	255.45	53.2

838.3	255.51	51.2
838.5	255.57	45.3
838.7	255.64	49.5
838.9	255.7	49
839.1	255.76	46.3
839.3	255.82	49.3
839.5	255.88	48.3
839.7	255.94	44
839.9	256	40.2
840.1	256.06	44.4
840.3	256.12	37.8
840.5	256.18	29.9
840.7	256.25	32.1
840.9	256.31	36
841.1	256.37	33.4
841.3	256.43	38.5
841.5	256.49	40.6
841.7	256.55	36
841.9	256.61	38.1

Site 2 – Portland Core

Well log GRS values are in American Petroleum Industry units (API).

height (ft)	height (m)	GRS (API)
412.6	125.76	245.755
412.8	125.82	244.561
413	125.88	244.651
413.2	125.94	237.182
413.4	126	232.974
413.6	126.07	230.313
413.8	126.13	230.226
414	126.19	232.888
414.2	126.25	231.602
414.4	126.31	233.66
414.6	126.37	230.74
414.8	126.43	230.628
415	126.49	227.886
415.2	126.55	225.029
415.4	126.61	224.35
415.6	126.67	224.944
415.8	126.74	227.037
416	126.8	227.267
416.2	126.86	228.456
416.4	126.92	229.115
416.6	126.98	230.733
416.8	127.04	234.389
417	127.1	234.158
417.2	127.16	234.709
417.4	127.22	231.359
417.6	127.28	227.989
417.8	127.35	223.182
418	127.41	221.894
418.2	127.47	220.263
418.4	127.53	221.292
418.6	127.59	221.036
418.8	127.65	220.606
419	127.71	221.291
419.2	127.77	221.719
419.4	127.83	225.338
419.6	127.89	227.004
419.8	127.96	229.656
420	128.02	230.208
420.2	128.08	229.131

420.4	128.14	225.449
420.6	128.2	224.041
420.8	128.26	222.589
421	128.32	224.895
421.2	128.38	228.756
421.4	128.44	229.873
421.6	128.5	229.36
421.8	128.56	225.841
422	128.63	221.037
422.2	128.69	219.299
422.4	128.75	219.311
422.6	128.81	223.838
422.8	128.87	225.659
423	128.93	227.086
423.2	128.99	224.787
423.4	129.05	221.519
423.6	129.11	217.529
423.8	129.17	215.941
424	129.24	211.22
424.2	129.3	210.106
424.4	129.36	207.153
424.6	129.42	206.279
424.8	129.48	205.539
425	129.54	203.874
425.2	129.6	202.362
425.4	129.66	200.954
425.6	129.72	200.13
425.8	129.78	199.324
426	129.84	199.787
426.2	129.91	197.179
426.4	129.97	196.663
426.6	130.03	197.178
426.8	130.09	197.608
427	130.15	202.67
427.2	130.21	205.846
427.4	130.27	207.12
427.6	130.33	208.989
427.8	130.39	208.46
428	130.45	210.622
428.2	130.52	213.83
428.4	130.58	214.479
428.6	130.64	215.8
428.8	130.7	214.514

429	130.76	212.935
429.2	130.82	214.126
429.4	130.88	210.056
429.6	130.94	209.542
429.8	131	205.849
430	131.06	204.303
430.2	131.12	204.303
430.4	131.19	208.935
430.6	131.25	214.688
430.8	131.31	226.3
431	131.37	239.131
431.2	131.43	247.057
431.4	131.49	250.759
431.6	131.55	246.813
431.8	131.61	233.619
432	131.67	224.088
432.2	131.73	211.574
432.4	131.8	204.371
432.6	131.86	202.882
432.8	131.92	202.203
433	131.98	206.593
433.2	132.04	210.328
433.4	132.1	212.934
433.6	132.16	215.812
433.8	132.22	215.696
434	132.28	216.889
434.2	132.34	215.578
434.4	132.41	213.471
434.6	132.47	213.245
434.8	132.53	211.662
435	132.59	213.675
435.2	132.65	216.306
435.4	132.71	217.031
435.6	132.77	219.575
435.8	132.83	217.944
436	132.89	216.827
436.2	132.95	214.081
436.4	133.01	210.991
436.6	133.08	207.646
436.8	133.14	204.214
437	133.2	199.41
437.2	133.26	195.123
437.4	133.32	191.091

437.6	133.38	188.09
437.8	133.44	186.289
438	133.5	184.06
438.2	133.56	181.489
438.4	133.62	178.317
438.6	133.69	178.661
438.8	133.75	181.062
439	133.81	186.506
439.2	133.87	191.883
439.4	133.93	195.183
439.6	133.99	194.899
439.8	134.05	197.072
440	134.11	197.118
440.2	134.17	199.376
440.4	134.23	202.76
440.6	134.29	202.017
440.8	134.36	200.636
441	134.42	197.748
441.2	134.48	192.824
441.4	134.54	188.199
441.6	134.6	185.336
441.8	134.66	181.914
442	134.72	179.771
442.2	134.78	179.944
442.4	134.84	181.229
442.6	134.9	183.887
442.8	134.97	190.32
443	135.03	196.24
443.2	135.09	206.196
443.4	135.15	217.008
443.6	135.21	226.62
443.8	135.27	233.252
444	135.33	229.966
444.2	135.39	222.264
444.4	135.45	209.422
444.6	135.51	198.09
444.8	135.58	189.101
445	135.64	184.654
445.2	135.7	180.851
445.4	135.76	179.841
445.6	135.82	180.633
445.8	135.88	180.871
446	135.94	182.338

446.2	136	181.079	
446.4	136.06	176.398	
446.6	136.12	171.007	
446.8	136.18	166.011	
447	136.25	164.708	--- Top of Bridge Creek Limestone
447.2	136.31	167.398	
447.4	136.37	172.484	
447.6	136.43	176.937	
447.8	136.49	181.045	
448	136.55	183.699	
448.2	136.61	187.547	
448.4	136.67	191.272	
448.6	136.73	197.603	
448.8	136.79	200.951	
449	136.86	204.624	
449.2	136.92	205.916	
449.4	136.98	205.294	
449.6	137.04	206.519	
449.8	137.1	204.678	
450	137.16	202.932	
450.2	137.22	198.229	
450.4	137.28	191.78	
450.6	137.34	185.497	
450.8	137.4	180.828	
451	137.46	176.037	
451.2	137.53	174.02	
451.4	137.59	171.022	
451.6	137.65	167.798	
451.8	137.71	166.235	
452	137.77	165.217	
452.2	137.83	165.989	
452.4	137.89	167.719	
452.6	137.95	169.964	
452.8	138.01	172.375	
453	138.07	177.561	
453.2	138.14	183.447	
453.4	138.2	187.966	
453.6	138.26	191.104	
453.8	138.32	189.7	
454	138.38	187.92	
454.2	138.44	188.139	
454.4	138.5	187.823	
454.6	138.56	188.851	

454.8	138.62	188.322
455	138.68	184.994
455.2	138.74	182.466
455.4	138.81	180.509
455.6	138.87	180.243
455.8	138.93	183.903
456	138.99	190.546
456.2	139.05	198.748
456.4	139.11	208.211
456.6	139.17	214.42
456.8	139.23	215.566
457	139.29	213.735
457.2	139.35	207.373
457.4	139.42	200.435
457.6	139.48	195.851
457.8	139.54	194.113
458	139.6	197.16
458.2	139.66	202.944
458.4	139.72	205.954
458.6	139.78	203.751
458.8	139.84	195.89
459	139.9	185.603
459.2	139.96	177.01
459.4	140.03	171.264
459.6	140.09	167.656
459.8	140.15	163.674
460	140.21	160.759
460.2	140.27	160.581
460.4	140.33	164.595
460.6	140.39	171.862
460.8	140.45	180.57
461	140.51	187.702
461.2	140.57	191.034
461.4	140.63	193.849
461.6	140.7	194.887
461.8	140.76	197.5
462	140.82	203.754
462.2	140.88	209.643
462.4	140.94	213.785
462.6	141	211.418
462.8	141.06	202.499
463	141.12	188.412
463.2	141.18	174.799

463.4	141.24	163.953	
463.6	141.31	154.846	
463.8	141.37	149.876	
464	141.43	145.999	
464.2	141.49	145.829	
464.4	141.55	149.562	
464.6	141.61	157.52	
464.8	141.67	166.808	
465	141.73	179.991	
465.2	141.79	195.896	
465.4	141.85	216.653	
465.6	141.91	240.763	
465.8	141.98	261.696	
466	142.04	271.96	
466.2	142.1	266.96	
466.4	142.16	250.146	
466.6	142.22	227.004	
466.8	142.28	204.15	
467	142.34	189.455	
467.2	142.4	179.122	
467.4	142.46	175.032	
467.6	142.52	175.691	
467.8	142.59	176.673	
468	142.65	179.39	
468.2	142.71	180.203	
468.4	142.77	178.49	
468.6	142.83	171.805	
468.8	142.89	164.006	
469	142.95	154.578	
469.2	143.01	148.151	
469.4	143.07	144.638	
469.6	143.13	144.638	
469.8	143.2	146.693	
470	143.26	149.692	--- Bentonite C
470.2	143.32	154.833	
470.4	143.38	157.918	
470.6	143.44	160.832	
470.8	143.5	159.79	
471	143.56	157.886	
471.2	143.62	155.13	
471.4	143.68	154.338	
471.6	143.74	153.157	
471.8	143.8	153.083	

472	143.87	150.19	
472.2	143.93	148.489	
472.4	143.99	147.633	
472.6	144.05	149.431	
472.8	144.11	154.487	
473	144.17	159.543	
473.2	144.23	165.714	
473.4	144.29	168.799	
473.6	144.35	173.772	
473.8	144.41	181.406	
474	144.48	195.674	
474.2	144.54	219.613	
474.4	144.6	248.228	
474.6	144.66	281.119	
474.8	144.72	303.552	
475	144.78	312.297	--- Bentonite B
475.2	144.84	302.242	
475.4	144.9	273.673	
475.6	144.96	242.135	
475.8	145.02	210.855	
476	145.08	189.933	
476.2	145.15	179.312	
476.4	145.21	175.047	
476.6	145.27	172.2	
476.8	145.33	170.815	
477	145.39	166.44	
477.2	145.45	161.799	
477.4	145.51	158.151	
477.6	145.57	152.497	
477.8	145.63	149.598	
478	145.69	146.223	
478.2	145.76	145.966	
478.4	145.82	146.531	
478.6	145.88	148.067	
478.8	145.94	150.386	
479	146	152.647	
479.2	146.06	155.481	
479.4	146.12	158.77	
479.6	146.18	160.055	
479.8	146.24	161.855	
480	146.3	166.745	--- Bentonite A
480.2	146.36	176.182	
480.4	146.43	191.366	

480.6	146.49	205.262
480.8	146.55	217.957
481	146.61	220.784
481.2	146.67	225.073
481.4	146.73	222.712
481.6	146.79	220.766
481.8	146.85	213.682
482	146.91	201.645
482.2	146.97	188.831
482.4	147.04	180.667
482.6	147.1	175.825
482.8	147.16	175.297
483	147.22	175.284
483.2	147.28	170.43
483.4	147.34	164.236
483.6	147.4	155.992
483.8	147.46	146.027
484	147.52	138.472
484.2	147.58	133.246
484.4	147.65	130.163
484.6	147.71	129.961
484.8	147.77	132.743
485	147.83	136.527
485.2	147.89	144.025
485.4	147.95	153.086
485.6	148.01	166.046
485.8	148.07	180.303
486	148.13	197.196
486.2	148.19	214.846
486.4	148.25	229.629
486.6	148.32	243.456
486.8	148.38	252.406
487	148.44	256.929
487.2	148.5	258.497
487.4	148.56	258.403
487.6	148.62	260.349
487.8	148.68	266.629
488	148.74	276.242
488.2	148.8	284.461
488.4	148.86	291.352
488.6	148.93	291.552
488.8	148.99	288.131
489	149.05	282.056

Bridge Creek Limestone

Hartland Shale

489.2	149.11	274.249
489.4	149.17	267.154
489.6	149.23	262.508
489.8	149.29	258.546
490	149.35	257.152
490.2	149.41	254.454
490.4	149.47	250.514
490.6	149.53	244.843
490.8	149.6	239.749
491	149.66	236.185
491.2	149.72	235.335
491.4	149.78	235.959
491.6	149.84	235.318
491.8	149.9	234.707
492	149.96	233.195
492.2	150.02	232.931
492.4	150.08	235.982
492.6	150.14	240.45
492.8	150.21	245.794
493	150.27	249.843
493.2	150.33	251.873
493.4	150.39	254.138
493.6	150.45	256.615
493.8	150.51	260.732
494	150.57	264.578
494.2	150.63	265.573
494.4	150.69	264.575
494.6	150.75	259.596
494.8	150.82	254.96
495	150.88	251.382
495.2	150.94	249.752
495.4	151	250.334
495.6	151.06	249.67
495.8	151.12	247.738
496	151.18	246.183
496.2	151.24	245.787
496.4	151.3	249.438
496.6	151.36	256.219
496.8	151.42	262.36
497	151.49	267.366
497.2	151.55	269.269
497.4	151.61	270.485
497.6	151.67	271.449

497.8	151.73	271.94
498	151.79	270.201
498.2	151.85	263.623
498.4	151.91	253.74
498.6	151.97	242.177
498.8	152.03	232.436
499	152.1	227.342
499.2	152.16	227.744
499.4	152.22	232.944
499.6	152.28	239.569
499.8	152.34	245.14
500	152.4	246.775
500.2	152.46	245.419
500.4	152.52	241.937
500.6	152.58	239.73
500.8	152.64	235.678
501	152.7	231.714
501.2	152.77	229.297
501.4	152.83	230.215
501.6	152.89	239.217
501.8	152.95	253.887
502	153.01	269.319
502.2	153.07	281.739
502.4	153.13	286.985
502.6	153.19	285.606
502.8	153.25	283.759
503	153.31	275.71
503.2	153.38	273.682
503.4	153.44	267.565
503.6	153.5	261.777
503.8	153.56	257.746
504	153.62	254.813
504.2	153.68	254.039
504.4	153.74	256.558
504.6	153.8	256.595
504.8	153.86	254.753
505	153.92	250.644
505.2	153.98	246.371
505.4	154.05	244.435
505.6	154.11	243.115
505.8	154.17	244.46
506	154.23	245.175
506.2	154.29	245.594

506.4	154.35	246.75
506.6	154.41	249.847
506.8	154.47	250.748
507	154.53	253.708
507.2	154.59	252.076
507.4	154.66	249.052
507.6	154.72	245.793
507.8	154.78	243.644
508	154.84	245.162
508.2	154.9	250.125
508.4	154.96	254.051
508.6	155.02	259.503
508.8	155.08	260.677
509	155.14	259.637
509.2	155.2	256.944
509.4	155.27	252.238
509.6	155.33	246.708
509.8	155.39	244.525
510	155.45	244.374
510.2	155.51	246.154
510.4	155.57	251.297
510.6	155.63	257.914
510.8	155.69	268.837
511	155.75	283.541
511.2	155.81	298.162
511.4	155.87	305.408
511.6	155.94	303.856
511.8	156	294.547
512	156.06	285.384
512.2	156.12	282.267
512.4	156.18	283.412
512.6	156.24	285.455
512.8	156.3	281.758
513	156.36	271.547
513.2	156.42	259.082
513.4	156.48	248.698
513.6	156.55	244.518
513.8	156.61	247.627
514	156.67	253.422
514.2	156.73	259.58
514.4	156.79	263.651
514.6	156.85	265.697
514.8	156.91	269.415

515	156.97	274.356
515.2	157.03	279.587
515.4	157.09	284.73
515.6	157.15	283.791
515.8	157.22	278.76
516	157.28	270.433
516.2	157.34	260.495
516.4	157.4	255.271
516.6	157.46	254.229
516.8	157.52	256.688
517	157.58	260.843
517.2	157.64	262.453
517.4	157.7	261.718
517.6	157.76	257.112
517.8	157.83	251.064
518	157.89	246.624
518.2	157.95	245.704
518.4	158.01	248.865
518.6	158.07	252.858
518.8	158.13	255.779
519	158.19	256.475
519.2	158.25	258.579
519.4	158.31	262.674
519.6	158.37	268.717
519.8	158.44	274.051
520	158.5	275.981
520.2	158.56	275.343
520.4	158.62	272.076
520.6	158.68	270.811
520.8	158.74	270.282
521	158.8	272.433
521.2	158.86	273.62
521.4	158.92	271.418
521.6	158.98	266.626
521.8	159.04	259.305
522	159.11	255.346
522.2	159.17	257.183
522.4	159.23	262.03
522.6	159.29	267.959
522.8	159.35	271.991
523	159.41	269.52
523.2	159.47	265.349
523.4	159.53	257.63

523.6	159.59	247.712
523.8	159.65	241.357
524	159.72	237.166
524.2	159.78	238.066
524.4	159.84	242.068
524.6	159.9	247.581
524.8	159.96	253.018
525	160.02	256.708
525.2	160.08	261.316
525.4	160.14	264.679
525.6	160.2	270.567
525.8	160.26	279.883
526	160.32	286.975
526.2	160.39	292.64
526.4	160.45	289.425
526.6	160.51	283.849
526.8	160.57	276.923
527	160.63	271.275
527.2	160.69	270.982
527.4	160.75	267.175
527.6	160.81	260.551
527.8	160.87	252.199
528	160.93	241.173
528.2	161	233.736
528.4	161.06	232.438
528.6	161.12	232.836
528.8	161.18	235.682
529	161.24	237.132
529.2	161.3	239.438
529.4	161.36	240.488
529.6	161.42	245.187
529.8	161.48	250.411
530	161.54	255.268
530.2	161.6	259.341
530.4	161.67	259.44
530.6	161.73	258.451
530.8	161.79	252.982
531	161.85	248.734
531.2	161.91	242.173

Site 3 – CTB GSSP, CO

Field GRS samples are in counts per minute (cpm).

sample #	height (m)	K(cpm)	U(cpm)	Th(cpm)
1	0.05	408.5	177.6	77.6
2	0.1	379.1	152.4	77.1
3	0.15	409.5	163.9	70.8
4	0.2	395.9	165	75
5	0.25	428.3	157.6	78.1
6	0.3	425.6	161.3	69.2
7	0.35	368	133.5	70.8
8	0.4	354.4	139.8	92.2
9	0.45	371.2	137.7	75.5
10	0.5	324.6	115.8	59.3
11	0.55	289.6	107.9	64.5
12	0.6	275.4	87	57.2
13	0.65	196.8	78.6	54.5
14	0.7	187.9	73.3	39.3
15	0.75	136.7	47.2	32.5
16	0.8	190	68.6	40.4
17	0.85	164.4	66	35.2
18	0.9	158.1	64.4	41.4
19	0.95	173.8	52.9	40.4
20	1	176.9	59.2	36.2
21	1.05	243.3	72.8	49.3
22	1.1	247.5	82.7	52.4
23	1.15	284.1	81.7	73.3
24	1.2	332.9	98.5	73.4
25	1.25	350.7	90.1	72.8
26	1.3	338.7	94.3	84.9
27	1.35	276.4	94.3	66
28	1.4	307.8	97.9	68.7
29	1.45	323.6	93.8	75.5
30	1.5	352.9	96.4	98
31	1.55	394.7	103.7	91.2
32	1.6	352.3	114.7	89.1
33	1.65	381.6	83.8	90.1
34	1.7	498.1	123.7	124.7
35	1.75	495.5	128.4	119.5
36	1.8	496.5	111.1	103.8
37	1.85	396.8	107.9	98.5
38	1.9	385.3	90.6	73.9
39	1.95	360.7	76.5	70.8
40	2	265.4	73.3	68.6
41	2.05	286.2	74.9	51.4

42	2.1	284.6	69.1	44
43	2.15	291.4	68.1	58.2
44	2.2	266.3	71.7	41.4
45	2.25	255.8	57.1	38.3
46	2.3	235.9	58.1	37.2
47	2.35	219.2	71.7	46.7
48	2.4	231.2	60.2	41.4
49	2.45	233.8	61.8	33.6
50	2.5	254.2	73.8	57.6
51	2.55	232.8	58.1	45.6
52	2.6	247.4	64.4	58.1
53	2.65	270.4	73.3	44.6
54	2.7	242.3	74.4	54.5
55	2.75	266.4	71.8	64.4
56	2.8	253.3	72.8	52.9
57	2.85	273.3	74.4	57.1
58	2.9	220.4	73.9	50.3
59	2.95	240.3	67.6	57.1
60	3	210	93.7	63.9
61	3.05	258.6	101.6	66
62	3.1	254.5	104.7	84.4
63	3.15	252.4	108.4	90.1
64	3.2	429.1	194.1	249.1
65	3.25	458.5	183.1	268.5
66	3.3	498.9	214.5	252.3
67	3.35	518.3	213	239.2
68	3.4	401.1	168.8	158.9
69	3.45	355.9	149.4	180.3
70	3.5	297.7	131	128.9
71	3.55	244.6	105.8	116.3
72	3.6	250.8	104.2	69.7
73	3.65	211	85.4	84.3
74	3.7	182.8	82.7	57.7
75	3.75	204.1	83.8	52.4
76	3.8	211.5	75.4	55
77	3.85	177.5	78.6	78.6
78	3.9	145.6	69.1	49.8
79	3.95	163.8	80.1	56.6
80	4	180.1	74.3	45.1
81	4.05	163.8	58.7	32.5
82	4.1	178.5	66	42.5
83	4.15	174.3	77.5	44
84	4.2	161.7	66	35.2
85	4.25	172.7	73.3	40.9
86	4.3	168	67.6	44.6
87	4.35	177.9	60.2	43

88	4.4	164.4	70.7	35.2
89	4.45	149.2	61.3	42.5
90	4.5	140.3	62.3	37.2
91	4.55	121.5	62.3	25.8
92	4.6	136.1	60.2	34.6
93	4.65	142.9	68.6	32.5
94	4.7	124.7	48.7	29.9
95	4.75	119.4	67	29.9

Site 3 – La Junta, CO

Field GRS samples are in counts per minute (cpm).

sample #	height (m)	K (cpm)	Th (cpm)	U(cpm)
1	0	384.1	183.4	70.8
2	0.1	304.8	139.8	53.5
3	0.2	217.4	123.1	52.5
4	0.3	170.7	94.2	29.4
5	0.4	137.7	62.3	29.9
6	0.5	165.4	44.6	45.1
7	0.6	148.2	52.9	32
8	0.7	160.7	71.7	38.3
9	0.8	257.5	90.1	70.7
10	0.9	395.3	99.5	118.4
11	1	367.5	98.5	96.9
12	1.1	236	70.7	59.2
13	1.2	232.3	74.9	44
14	1.3	176.9	44.6	27.3
15	1.4	137.7	51.4	32
16	1.5	143.1	51.5	22
17	1.6	160.2	65.5	25.8
18	1.7	145.6	57.1	29.4
19	1.8	185.8	73.8	44
20	1.9	201.5	75.9	44.6
21	2	212.5	91.1	60.3
22	2.1	373.7	164.1	184.5
23	2.2	298.8	134.2	159.8
24	2.3	277	117.8	98
25	2.4	220.4	92.2	57.7
26	2.5	188.4	73.3	49.3
27	2.6	149.2	76.4	38.8
28	2.7	168	61.8	38.8
29	2.8	163.8	64.4	29.9
30	2.9	136.7	58.7	34.6
31	3	149.2	61.3	34.6
32	3.1	168.5	67	28.9
33	3.2	129.4	50.3	27.3
34	3.3	97.5	58.1	27.3
35	3.4	167	93.7	60.8
36	3.5	311.8	164	140.4

Site 4 – Bounds Core, KS

Well log GRS values are in American Petroleum Industry units (API).

depth (ft)	depth (m)	GRS (API)
966	294.44	73.69
966.25	294.51	77.94
966.5	294.59	82.19
966.75	294.67	84.69
967	294.74	87.19
967.25	294.82	86.56
967.5	294.89	85.94
967.75	294.97	78.53
968	295.05	71.13
968.25	295.12	63.61
968.5	295.2	56.09
968.75	295.28	50.41
969	295.35	44.72
969.25	295.43	44.95
969.5	295.5	45.19
969.75	295.58	48.47
970	295.66	51.75
970.25	295.73	62.09
970.5	295.81	72.44
970.75	295.88	82.09
971	295.96	91.75
971.25	296.04	92.13
971.5	296.11	92.5
971.75	296.19	84.59
972	296.27	76.69
972.25	296.34	68.69
972.5	296.42	60.69
972.75	296.49	59.8
973	296.57	58.91
973.25	296.65	62.64
973.5	296.72	66.38
973.75	296.8	66.09
974	296.88	65.81
974.25	296.95	62.92
974.5	297.03	60.03
974.75	297.1	55.78
975	297.18	51.53
975.25	297.26	47.8
975.5	297.33	44.06

975.75	297.41	44.22	
976	297.48	44.38	--- Bentonite B
976.25	297.56	44.53	
976.5	297.64	44.69	
976.75	297.71	46.22	
977	297.79	47.75	
977.25	297.87	47.75	
977.5	297.94	47.75	
977.75	298.02	48.55	
978	298.09	49.34	
978.25	298.17	50.16	
978.5	298.25	50.97	
978.75	298.32	53.7	
979	298.4	56.44	
979.25	298.48	59.34	
979.5	298.55	62.25	
979.75	298.63	67.78	
980	298.7	73.31	
980.25	298.78	83.38	
980.5	298.86	93.44	
980.75	298.93	95.88	
981	299.01	98.31	
981.25	299.09	91.31	
981.5	299.16	84.31	
981.75	299.24	71.81	
982	299.31	59.31	
982.25	299.39	53.84	
982.5	299.47	48.38	
982.75	299.54	52.33	
983	299.62	56.28	
983.25	299.69	55.34	
983.5	299.77	54.41	
983.75	299.85	53.98	
984	299.92	53.56	
984.25	300	47.7	
984.5	300.08	41.84	
984.75	300.15	40.83	
985	300.23	39.81	
985.25	300.3	39.61	
985.5	300.38	39.41	
985.75	300.46	44.13	
986	300.53	48.84	--- Bentonite A
986.25	300.61	53.7	

986.5	300.69	58.56
986.75	300.76	63.34
987	300.84	68.13
987.25	300.91	66.56
987.5	300.99	65
987.75	301.07	61.31
988	301.14	57.63
988.25	301.22	55.84
988.5	301.29	54.06
988.75	301.37	56.58
989	301.45	59.09
989.25	301.52	62.61
989.5	301.6	66.13
989.75	301.68	66.34
990	301.75	66.56
990.25	301.83	66.53
990.5	301.9	66.5
990.75	301.98	62.81
991	302.06	59.13
991.25	302.13	60.72
991.5	302.21	62.31
991.75	302.29	63.34
992	302.36	64.38
992.25	302.44	68.63
992.5	302.51	72.88
992.75	302.59	76
993	302.67	79.13
993.25	302.74	81.81
993.5	302.82	84.5
993.75	302.9	87.41
994	302.97	90.31
994.25	303.05	89.22
994.5	303.12	88.13
994.75	303.2	86.03
995	303.28	83.94
995.25	303.35	84.03
995.5	303.43	84.13
995.75	303.5	84.88
996	303.58	85.63

Bridge Creek Limestone

Hartland Shale

Site 6 – Cuba, KS

Field GRS samples are in counts per minute (cpm).

sample #	height (m)	K(cpm)	U(cpm)	Th(cpm)
1	0	199.1	178	25.3
2	0.1	264.5	185.9	45.1
3	0.2	285.1	204.8	52.5
4	0.3	334.1	281	83.5
5	0.4	355.1	271	67.2
6	0.5	303	238.9	55.7
7	0.6	276.2	215.8	47.8
8	0.7	336.5	224.3	67.7
9	0.8	343.3	224.2	66.1
10	0.9	373.2	225.8	63.5
11	1	351.1	209	54.1
12	1.1	298.1	176.5	38.9
13	1.2	297.4	170.1	26.8
14	1.3	109.1	45.1	0.7
15	1.4	125.9	37.8	0.7
16	1.5	321	130.9	40.4
17	1.6	230.9	112.1	31.5
18	1.7	234.5	102.6	42
19	1.8	258.6	111.5	38.3
20	1.9	246.1	120.4	40.9
21	2	261.2	107.3	38.8
22	2.1	249.2	105.8	42.5
23	2.2	216.7	96.3	35.2
24	2.3	235	102.1	39.9
25	2.4	231	122.5	59.8
26	2.5	241.5	146.6	60.3
27	2.6	236.2	148.2	75
28	2.7	228.2	152	186.6
29	2.8	264.2	178.7	128.4
30	2.9	250.5	147.2	94.3
31	3	220.5	129.3	62.4
32	3.1	177	101.6	44.6
33	3.2	179.6	106.8	25.2
34	3.3	218.8	114.1	27.9
35	3.4	228.3	120.9	28.4
36	3.5	211.1	138.7	31.5
37	3.6	235.7	146.1	20
38	3.7	192.7	115.2	26.3
39	3.8	193.2	106.3	23.1

40	3.9	190	129.2	23.1
41	4	191	113	23.7
42	4.1	200.5	107.3	33.6
43	4.2	187.5	137.7	38.8
44	4.3	211	110	31
45	4.4	202.7	144	36.2
46	4.5	194.4	146.1	43.6
47	4.6	204.3	153.9	70.2
48	4.7	203.3	144	52.5

Site B – Antonio Canyon, TX

Lab GRS values are reported in counts per gram per hour (cpg/h).

Sample#	height (m)	U (cpg/h)	Th (cpg/h)	K (cpg/h)	Total (cpg/h)
A1	0	0.904597	0.288814	0.756921	1.9503316
A2	0.05	0.978971	0.136083	-0.17452	0.9405328
A3	0.1	0.977669	-0.07668	0.093996	0.9949886
A4	0.15	1.093745	0.027275	0.341057	1.462077
A5	0.2	1.009656	0.354141	1.043739	2.4075359
A6	0.25	1.247508	-0.13583	0.693058	1.8047401
A7	0.3	1.304425	0.193176	0.558034	2.0556346
A8	0.35	1.823639	0.22984	1.402586	3.4560652
A9	0.4	1.350867	0.579936	1.328523	3.2593269
A10	0.45	0.728169	0.160592	1.888832	2.7775928
A11	0.5	0.936172	0.180039	2.566507	3.6827192
A12	0.55	1.440987	0.202323	0.883655	2.526965
A13	0.6	1.761319	0.293328	1.629938	3.684585
A14	0.65	2.966935	0.442339	3.087043	6.4963166
A15	0.7	1.221044	-0.01549	0.462583	1.668136
A16	0.75	1.393419	0.674033	0.573696	2.6411478
A17	0.8	1.35829	0.086928	0.540352	1.98557
A18	0.85	0.738092	0.089669	0.888897	1.7166582
A19	0.9	1.767265	0.507676	1.651029	3.9259696
A20	0.95	0.955559	0.193829	1.141236	2.2906244
A21	1	0.692383	0.162786	1.335814	2.1909829
A22	1.05	1.630249	0.402942	1.362408	3.3955987
A23	1.1	0.43748	0.364119	1.943528	2.7451277
A24	1.15	1.039651	0.35821	1.103394	2.5012549
A25	1.2	0.353171	0.020297	0.368981	0.7424481
A26	1.25	1.342958	0.320701	1.449057	3.1127157
A27	1.3	1.48494	0.42796	1.200842	3.1137419
A28	1.35	1.317095	0.344665	1.695185	3.3569447
A29	1.4	0.537878	0.045252	0.605537	1.1886661
A30	1.45	0.973597	0.08616	1.557264	2.617021
A31	1.5	1.132543	0.276593	2.575755	3.9848909
A32	1.55	1.021759	0.287644	2.057863	3.3672664
1	1.6	1.470581	0.085671	2.402693	3.9589445
2	1.65	1.477782	0.2694	1.252223	2.9994054
3	1.7	1.087176	-0.01757	0.881761	1.9513688
4	1.75	2.157393	0.203563	0.374373	2.7353294
5	1.8	1.41317	0.024139	0.233342	1.6706505
6	1.85	1.5978	0.226383	0.349746	2.1739284
7	1.9	1.254242	0.325375	0.2071	1.7867172
8	1.95	1.49309	0.291064	0.14355	1.9277038
9	2	0.679772	0.245354	0.649907	1.5750328
10	2.05	2.974234	0.337565	0.639857	3.9516565

11	2.1	2.850393	0.234768	1.350353	4.4355142
12	2.15	2.425196	0.116588	1.457482	3.999267
13	2.2	2.200195	0.63111	1.494145	4.3254504
14	2.25	2.569158	0.671454	1.270027	4.510639
15	2.3	2.416565	0.947349	2.683346	6.0472594
16	2.35	1.87238	0.366385	1.191999	3.4307648
17	2.4	1.982157	0.143875	1.26668	3.3927125
18	2.45	1.776395	0.040048	0.387136	2.2035793
19	2.5	1.205417	0.399215	0.87117	2.4758029
20	2.55	1.153689	0.158413	0.667124	1.9792254
21	2.6	0.87604	0.478918	0.343828	1.6987854
22	2.65	1.894285	-0.11362	0.733346	2.5140097
23	2.7	2.500647	0.386882	1.280604	4.1681331
24	2.75	3.113842	0.10999	1.278296	4.5021287
25	2.8	2.090075	0.372215	1.585198	4.0474877
26	2.85	1.055755	0.676581	0.91408	2.6464159
27	2.9	2.401395	1.290048	2.716681	6.4081247
28	2.95	2.348031	0.65027	2.211866	5.2101664
29	3	3.135113	0.196004	3.102434	6.4335504
30	3.05	2.397127	0.451029	1.596559	4.4447148
31	3.1	1.543173	0.285313	1.141004	2.9694892
32	3.15	2.711492	0.826115	1.506381	5.0439885
33	3.2	2.272046	0.142071	2.067799	4.4819163
34	3.25	0.888736	0.051076	1.218376	2.158188
35	3.3	2.691951	0.282813	1.436152	4.4109157
36	3.35	2.210582	0.108194	1.312544	3.6313198
37	3.4	1.038125	0.225488	1.217928	2.4815413
38	3.45	2.628668	1.062776	0.784863	4.4763065
39	3.5	3.270475	0.573064	0.753298	4.5968372
40	3.55	0.908757	0.028769	0.686269	1.6237957
41	3.6	2.026699	0.327865	1.368597	3.7231606
42	3.65	1.245455	0.152463	0.445004	1.8429216
43	3.7	1.87604	0.121775	2.486685	4.4844996
44	3.75	2.081998	0.625855	2.059783	4.7676352
45	3.8	1.233078	0.64342	2.291718	4.1682157
46	3.85	2.842173	0.76609	3.112858	6.7211217
47	3.9	3.228155	0.648779	3.322036	7.1989694
48	3.95	1.775366	0.554656	1.130238	3.4602588
49	4	1.527009	0.971212	0.861255	3.3594765
50	4.05	2.709266	-0.01892	1.590615	4.2809612
51	4.1	0.856029	0.405518	0.990189	2.2517366
52	4.15	0.963834	-0.05607	1.810112	2.7178786
53	4.2	1.070036	0.112161	1.829841	3.0120391
54	4.25	1.049326	0.626119	1.600877	3.2763223
55	4.3	1.222899	0.729688	1.564932	3.5175184
56	4.35	1.408313	0.39211	1.613225	3.4136484

57	4.4	3.577063	0.403002	2.120999	6.1010646
58	4.45	2.66939	0.367293	2.439392	5.4760757
59	4.5	1.817674	0.105891	3.342459	5.2660245
60	4.55	1.670832	0.455526	2.630365	4.7567232
61	4.6	0.813228	0.035243	3.140679	3.9891498
62	4.65	0.794688	0.890386	2.816219	4.5012939
63	4.7	0.669697	-0.01386	1.399699	2.0555397
64	4.75	0.948602	-0.01622	1.033714	1.9660986
65	4.8	1.993611	0.316267	2.915735	5.225613
66	4.85	1.745091	0.253549	3.458382	5.457022
67	4.9	0.922452	0.641659	2.919878	4.4839896
68	4.95	1.075087	0.200206	1.736748	3.0120423
69	5	1.228133	0.21193	1.74836	3.1884232
70	5.05	1.290582	0.308194	2.832544	4.4313198
71	5.1	1.73692	0.261381	3.156311	5.1546108
72-1	5.15	1.011502	0.378472	3.600591	4.990565
72-2	5.2	0.972957	0.086104	3.475434	4.5344947
73	5.25	0.704035	0.481553	2.050849	3.2364372
74	5.3	0.317142	0.102702	1.916481	2.336325
75	5.35	0.483457	0.116088	1.322472	1.922017
76	5.4	0.931571	0.447902	1.331113	2.7105856
77	5.45	1.46326	0.444185	2.896829	4.8042737
78	5.5	0.890954	0.71731	2.429931	4.0381949
79	5.55	2.203074	0.462136	3.562552	6.2277617
80	5.6	1.54775	0.133904	3.060079	4.7417324
81	5.65	1.339552	0.507339	4.161781	6.0086728
82	5.7	2.108092	0.560463	4.440502	7.1090573
83	5.75	1.254699	0.293093	2.384296	3.9320874
84	5.8	1.713385	0.157653	3.098451	4.9694892
85	5.85	1.777693	0.470074	2.522634	4.7704014
86	5.9	1.47244	0.424358	3.469215	5.3660123
87	5.95	1.355075	0.498358	2.57504	4.4284725
88	6	1.957975	1.011706	3.589348	6.5590283
89	6.05	1.723734	0.239459	2.421914	4.385107
90	6.1	1.340028	0.393105	3.051714	4.7848467
91	6.15	1.309628	0.657671	4.48085	6.4481494
92	6.2	2.482087	0.505714	3.793859	6.7816603
93	6.25	Missing			
94	6.3	1.986741	0.502168	2.680379	5.1692883
95	6.35	1.560029	0.757982	3.392453	5.7104637
96	6.4	2.158604	0.57767	5.226999	7.9632735
97	6.45	2.294396	0.665284	7.61231	10.57199
98	6.5	1.527804	0.611084	4.584186	6.7230737
99	6.55	1.319827	0.537932	3.809728	5.6674872
100	6.6	2.833221	0.941747	4.45817	8.233138
101	6.65	2.336594	0.136609	3.677454	6.1506563

102	6.7	1.859239	0.47743	2.851091	5.1877596
103	6.75	0.92384	0.485678	2.523385	3.9329044
104	6.8	0.813446	0.19947	1.392084	2.4049998
105	6.85	0.872577	0.422088	2.186498	3.4811626
106	6.9	1.180022	0.230034	1.645709	3.0557659
107	6.95	2.164761	0.252949	2.946967	5.3646772
108	7	1.506329	0.259937	4.02285	5.7891157
109	7.05	2.795341	0.311332	6.286856	9.393529
110	7.1	1.493729	0.403002	5.593222	7.4899535
111	7.15	1.40695	0.130041	3.789115	5.3261055
112	7.2	1.795371	0.656739	6.307582	8.7596929
113	7.25	2.179214	0.450576	5.369216	7.9990056
114	7.3	2.333239	0.968967	4.277392	7.579598
115	7.35	2.645503	0.563413	4.04282	7.2517366
116	7.4	1.636888	0.403395	5.068774	7.1090573
117	7.45	2.292769	0.583701	3.546484	6.4229542
118	7.5	2.351334	0.418742	3.142043	5.9121193
119	7.55	1.867174	0.710627	2.570751	5.1485518
120	7.6	1.788063	0.733872	3.12213	5.6440652
121	7.65	2.305588	0.180724	3.551882	6.0381949
122	7.7	2.252457	0.851233	4.025689	7.1293786
123	7.75	1.536407	0.224041	3.372076	5.1325236
124	7.8	1.95346	0.283823	4.766845	7.0041291
125	7.85	2.185079	0.439639	3.576444	6.2011614
126	7.9	2.513228	0.885243	4.290679	7.6891498
127	7.95	0.288146	0.18276	1.271188	1.7420943
128	8	2.512479	1.070984	7.113849	10.697311
129	8.05	2.400978	0.426488	4.77345	7.6009161
130	8.1	3.28339	0.406769	3.963252	7.653411
131	8.15	2.811635	0.969163	4.135419	7.9162174
132	8.2	2.478231	1.421742	2.009578	5.9095513
133	8.25	3.609396	0.489743	1.791364	5.8905019

APPENDIX C: TRACE FOSSIL DATA

For each site bed height, height represents 20 mm-wide rows where traces were examined across a slabbed surface of the bed.

Maximum burrow diameter (MBD) is reported as the larges burrow found on a row.

Number of races identified (ID'd) in a random 20 mm^2 section for each row assigns a bioturbation categorization of high (H), medium (M), low (L), or none (N).

Initial bed numbers are from Site 3/CTBGSSP

Bed 63

Height (mm)		Traces Present (counts)							Traces/ 20 mm^2	
st	end	*Chondrites*	*Planolites*	*Taenidium*	*Zoophycus*	*Thalassinoides*	*Teichichnus*	MBD (mm)	ID'd	bioturb
400	380	1		2		1	1	11	2	M
380	360	1	1				1	10	1	H
360	340	2		1				7	2	H
340	320		4	1				5	5	M
320	300			3				5	2	M
300	280	2		1				7		M
260	240			1				7	1	L
240	220						1	7		L
220	200			1			2	8	1	M
180	160						1	7		M
160	140					1	1	9		H
140	120					3	1	20	1	H
120	100					2	2	20	1	H
100	80			1		1		12		H
80	60				1	1	3	13	2	H
60	40				1	1	3	13	2	H
40	20									
20	0									

Bed 67

Height (mm)		Traces Present (counts)							Traces/ 20 mm^2	
st	end	*Chondrites*	*Planolites*	*Taenidium*	*Zoophycus*	*Thalassinoides*	*Teichichnus*	MBD (mm)	ID'd	bioturb
140	120	1		2				5	1	M
120	100			3			1	8	3	H
100	80						2	11	1	M
80	60						2	12	1	M
60	40			1		1	1	20	1	M
40	20		1			2		13	1	H
20	0		1					1		L

Bed 79

Height (mm)		Traces Present (counts)							Traces/20 mm^2	
st	end	*Chondrites*	*Planolites*	*Taenidium*	*Zoophycus*	*Thalassinoides*	*Teichichnus*	MBD (mm)	ID'd	bioturb
170	150			2				3	1	M
150	130		3	1				2	3	H
130	110			2		2		20	2	H
110	90		2	1			1	10	2	M
90	70		3	1				5	2	M
70	50		2					3	2	M
50	30		4	1				5	3	H
30	10		2				1	8	2	H
0			1					3	1	M

Bed 84

Height (mm)		Traces Present							Traces/ 20 mm^2	
st	end	*Chondrites*	*Planolites*	*Taenidium*	*Zoophycus*	*Thalassinoides*	*Teichichnus*	MBD (mm)	ID'd	bioturb
220	200	2		2				5	2	H
200	180	2	4	2		1		20	6	H
180	160	3	4	1		1		5	4	H
160	140	4		2				5	3	H
140	120	7						3	7	H
120	100	3		2		1	1	20	4	H
100	80	2	1	1		1		20	3	H
80	60	2	2			2		20	2	H
60	40	2	1	2			1	20	3	H
40	20		3	1		1	1	20	3	H
20	0		2	1				7	2	H

Bed 86

Height (mm)		Traces Present							Traces/ 20 mm^2	
st	end	*Chondrites*	*Planolites*	*Taenidium*	*Zoophycus*	*Thalassinoides*	*Teichichnus*	MBD (mm)	ID'd	bioturb
25	23						2	15	2	H
23	21		3	1			2	14	3	H
21	19	2		2			1	12	4	H
19	17	3		2				5	3	H
17	15	4						5	2	H
15	13	4						3	2	H
13	11	3						4	2	H
11	9	3	2					3	2	H
9	7	3	1					3	2	H
7	5	2	2	1				7	3	H
5	3	1		1		1	2	20	2	H
3	1		1				1	10	1	H
1	0		1	2		1		20	1	H

Bed 63 equivalent - Site 4

Height (mm)		Traces Present							Traces/ 20 mm^2	
st	end	*Chondrites*	*Planolites*	*Taenidium*	*Zoophycus*	*Thalassinoides*	*Teichichnus*	MBD (mm)	ID'd	bioturb
180	160	1						4	1	M
160	140	1						4	1	M
140	120	1			1?			10	1	L
120	100	1				1		20	1	L
100	80					1	1	20	1	L
80	60			2		1	1	20	1	L
60	40					1	1	20	2	L
40	20			1			1	12	2	M
20	0			2		1	2	20	2	M

Bed 67 equivalent - Site 4

Height (mm)		Traces Present							Traces/ 20 mm^2	
st	end	*Chondrites*	*Planolites*	*Taenidium*	*Zoophycus*	*Thalassinoides*	*Teichichnus*	MBD (mm)	ID'd	bioturb
120	100	1		1		1		20	1	M
100	80	1		1				50	1	M
80	60	1		1			1	10	1	M
60	40	2		1		1		20	1	M
40	20	1					1	10	1	M
20	0			1				5	1	M

Bed 79 equivalent - Site 4

Height (mm)		Traces Present							Traces/ 20 mm^2	
st	end	*Chondrites*	*Planolites*	*Taenidium*	*Zoophycus*	*Thalassinoides*	*Teichichnus*	MBD (mm)	ID'd	bioturb
40	20	6						4	4	M
20	0	6		1				5	4	M

Bed 84 equivalent - Site 4

Height (mm)		Traces Present							Traces/ 20 mm^2	
st	end	*Chondrites*	*Planolites*	*Taenidium*	*Zoophycus*	*Thalassinoides*	*Teichichnus*	MBD (mm)	ID'd	bioturb
20	0	1		3		1		20	2	H
40	20		1	2				10	2	M
60	40		4	2			1	12	2	L
80	60		3	1		1		20	4	H
100	80	2	3	1		1		10	4	H

Bed 86 equivalent - Site 4

Height (mm)		Traces Present							Traces/ 20 mm^2	
st	end	*Chondrites*	*Planolites*	*Taenidium*	*Zoophycus*	*Thalassinoides*	*Teichichnus*	MBD (mm)	ID'd	bioturb
20	0	2	1	1				3	1	L
40	20					1		11	1	L
60	40			3				9	2	L
80	60	1		5				13	3	M
100	80	1	1			4	1	13	4	H
120	100		4			1		11	5	H

Bed 88 equivalent - Site 4

Height (mm)		Traces Present							Traces/ 20 mm^2	
st	end	*Chondrites*	*Planolites*	*Taenidium*	*Zoophycus*	*Thalassinoides*	*Teichichnus*	MBD (mm)	ID'd	bioturb
70	50		1					1		L
50	30		2	2		1		20	2	M
30	10	2	2			1		20	3	H

Bed 63 equivalent - Site 6

Height (mm)		Traces Present							Traces/ 20 mm^2	
st	end	*Chondrites*	*Planolites*	*Taenidium*	*Zoophycus*	*Thalassinoides*	*Teichichnus*	MBD (mm)	ID'd	bioturb
40	60	1				1		13	2	H
20	40	1	2	1				5	3	H
0	20	2	1	1				8	2	M

Bed 79 equivalent - Site 6

Height (mm)		Traces Present							Traces/ 20 mm^2	
st	end	*Chondrites*	*Planolites*	*Taenidium*	*Zoophycus*	*Thalassinoides*	*Teichichnus*	MBD (mm)	ID'd	bioturb
40	60			1				5	0	N
20	40	1		2		1		18	1	L
0	20	2	2					3	1	L

APPENDIX D: GEOCHEMISTRY DATA

Site 3 percent carbonate and uranium concentration data

U data are reported in parts per million (ppm) from two different mass spectrometers.

sample #	height (m)	% CaCO3	[U] ICP-OES	[U] ICP-MS
108	5.35	70.595	7.871490134	7.65
106	5.25	92.866	2.780043254	2
104	5.15		7.867371673	7.3
102	5.05	72.277	8.323491181	6.69
100	4.95	67.173	0.542895472	1.13637
98	4.85	65.28	0.502843443	0.94243
96	4.75	70.722	1.446691644	2.8126
94	4.65	89.431	1.430217802	2.25709
92	4.55	93.796	1.583630458	2.81773
90	4.45	73.201	1.426099342	3.17629
89	4.4		1.70409543	
88	4.35	78.626		3.57125
87	4.3		2.824316705	
85	4.2	68.779	1.484787405	3.33454
83	4.1	64.694		2.311
81	4	87.86	0.425579051	1.07072
80	3.95	91.379	0.52185355	2.16608
78	3.85	63.26	3.268080831	4.96048
76	3.75	64.965	1.669088515	2.43353
74	3.65	58.359	3.530632693	5.30092
72	3.55	69.288	3.105401639	5.02887
70	3.45	86.495	7.627471345	8.52847
68	3.35		16.32051199	15.11167
66	3.25	94.254	5.790637931	6.01388
64	3.15	47.61	2.360989891	2.61308
62	3.05	54.83	2.762539797	3.2083
60	2.95	35.707	2.335249512	2.23831
58	2.85	54.544	1.748368881	2.5943
56	2.75	77.044	1.107948263	1.94848
54	2.65	87.521	1.201643241	1.13614
52	2.55	68.29	1.049260199	0.46716
50	2.45	70.123	1.217087468	1.21289
48	2.35	76.735	0.578417195	0.64617
46	2.25		0.721842584	
45	2.2	19.051		1.29654
44	2.15	27.9	1.664970055	2.50514

42	2.05	86.234	1.985180364	2.71857
40	1.95	61.61	1.77410926	1.0335
38	1.85	76.268	2.998820023	2.19018
36	1.75	35.707	6.591379986	4.55853
34	1.65		6.599915433	
32	1.55			4.08412
30	1.45	-0.08	5.136832315	3.99348
28	1.35	35.139	3.937330674	4.79391
26	1.25	52.37	4.424880858	6.29497
24	1.15	62.927	1.315686825	1.86889
22	1.05	63.432	1.013998622	0.66997
20	0.95	58.567	2.716207115	2.94088
18	0.85	12.016	2.594712528	
17	0.8	73.402	2.991114358	3.65887
15	0.7	64.046	1.172814017	0.75476
13	0.6	54.491	0.555147893	1.78476
11	0.5	64.345	0.363021707	0.22309
9	0.4	69.82	0.318851217	1.05145
7	0.3	84.468	0.749230347	1.57595
5	0.2	76	2.059312654	3.59618
3	0.1	62.32	3.537839999	4.21091
1	0	53.384	5.202727684	5.99496

Portland Core total organic carbon (TOC) data

height (ft)	height (m)	% TOC
470.01	143.26	0.52
470.18	143.31	0.95
470.34	143.36	0.62
470.51	143.41	0.92
470.67	143.46	3.11
470.83	143.51	3.07
471	143.56	0.9
471.19	143.62	0.42
471.33	143.66	0.25
471.49	143.71	0.46
471.65	143.76	0.12
471.82	143.81	0.53
471.98	143.86	0.7
472.15	143.91	1.93
472.31	143.96	1.31
472.47	144.01	0.77
472.64	144.06	0.88
472.8	144.11	1.2
472.93	144.15	1.6
473.06	144.19	2.03
473.26	144.25	0.45
473.43	144.3	0.59
473.59	144.35	1.08
473.75	144.4	1.94
473.92	144.45	2.55
474.02	144.48	5.21
474.18	144.53	0.78
474.31	144.57	0.43
474.51	144.63	0.22
474.64	144.67	0.58
474.84	144.73	0.54
475	144.78	1.64
475.13	144.82	3.33
475.3	144.87	4.68
475.46	144.92	1.64
475.62	144.97	0.9
475.75	145.01	3.01
475.95	145.07	3.61
476.08	145.11	0.66
476.25	145.16	0.62

476.41	145.21	1.89
476.57	145.26	1.2
476.74	145.31	1.96
476.94	145.37	1.29
477.26	145.47	0.05
477.62	145.58	0.47
477.79	145.63	0.31
477.95	145.68	0.67
478.12	145.73	0.57
478.28	145.78	0.64
478.44	145.83	0.74
478.61	145.88	0.9
478.77	145.93	0.73
479	146	1.37
479.13	146.04	1.22
479.3	146.09	0.36
479.43	146.13	0.37
479.59	146.18	0.71
479.76	146.23	0.49
479.92	146.28	0.57
480.12	146.34	0.25
480.28	146.39	0.56
480.45	146.44	1.01
480.61	146.49	0.6
480.77	146.54	0.61
480.97	146.6	0.51
481.14	146.65	0.35
481.3	146.7	0.82
481.46	146.75	0.23
481.63	146.8	0.76
481.79	146.85	0.94
481.96	146.9	0.62
482.02	146.92	1.33
482.19	146.97	0.75
482.35	147.02	0.14
482.51	147.07	0.2
482.68	147.12	0.11
482.84	147.17	0.92
483.01	147.22	1.26
483.17	147.27	1.23
483.33	147.32	0.09
483.5	147.37	0.12
483.66	147.42	0.17

483.83	147.47	0.31
483.96	147.51	0.42
484.12	147.56	0.36
484.28	147.61	0.19
484.45	147.66	0.33
484.61	147.71	0.28
484.78	147.76	0.4
484.97	147.82	0.7
485.14	147.87	0.71
485.3	147.92	0.61
485.47	147.97	0.47
485.63	148.02	1.19
485.79	148.07	0.82
485.93	148.11	0.52
486.09	148.16	0.56
486.25	148.21	0.42
486.42	148.26	0.78
486.58	148.31	0.44
486.75	148.36	0.38
486.91	148.41	0.45
487.04	148.45	0.36
487.2	148.5	0.4
487.37	148.55	0.41
487.53	148.6	0.45
487.66	148.64	0.42
487.86	148.7	0.98
488.02	148.75	0.84
488.19	148.8	1.19
488.35	148.85	1.71
488.52	148.9	1.51
488.68	148.95	3.46
488.85	149	3.47
489.04	149.06	3.17

Bentonite Tests

Ratio plots of rare earth elements in parts per million (ppm).

sample ID	Ba	Sr	Rb	Zr	Ba/Rb	Sr/Rb	Zr/Rb
B69 CTBGSSP	114.1708	572.6291	43.81398	117.2957	2.605807	13.06955	2.67713
B69 Portland	317.0442	685.2215	70.8348	171.133	4.475826	9.673515	2.415946
B80 Portland	377.662	617.5523	70.51107	251.4796	5.356067	8.758231	3.566526
B89 CTBGSSP	111.8159	863.7771	21.78054	36.07918	5.133752	39.65821	1.656487
B89 Port Core	477.1799	562.6777	75.2253	184.4388	6.343343	7.4799	2.451819
1st Bent Ant Cnyn	108.9376	489.2652	37.94649	114.9416	2.870822	12.89356	3.029045
2nd Bent Ant Cnyn	131.3531	555.2853	40.5464	136.7427	3.239576	13.69506	3.372498
3rd Bent Ant Cnyn	182.9873	2301.889	47.85041	134.9003	3.824153	48.10594	2.819209

APPENDIX E: SEDIMENT ACCUMULATION RATE DATA

Listed for each site is the length in meters (m) of half and whole cycles derived from splined χ data curves, where b = black bars on the bar-log, and a whole cycle represents a white and black bar.

Half and whole cycles are scaled to Milankovitch frequencies (P2 or O1) to determine sediment accumulation rate (SAR) depicted here in meters per thousand year (m/kyr; cm/kyr in the dissertation) for that particular cycle.

Site 1

bot	bar	half cycle (m)	whole cycle (m)	P2 (22.5 kyr) SAR half cycle	whole cycle
	b				
		0.203	0.203	0.009028	0.009028
	b	0.188		0.008333	
		0.219	0.406	0.009722	0.018056
	b	0.219		0.009722	
		0.406	0.625	0.018056	0.027778
	b	0.281		0.0125	
		0.297	0.578	0.013206	0.025706
	b	0.141		0.00625	
		0.203	0.344	0.009028	0.015278
	b	0.125		0.005556	
		0.188	0.313	0.008333	0.013889
	b	0.438		0.019444	
		0.406	0.844	0.018056	0.0375
	b	0.375		0.016667	
		0.250	0.625	0.011111	0.027778
	b	0.203		0.009028	
		0.344	0.547	0.015278	0.024306
	b	0.406		0.018056	
		0.625	1.031	0.027778	0.045833

	b	0.250		0.011111	
		0.203	0.453	0.009028	0.020139
	b	0.469		0.020833	
					0.020833
top	tot	6.438	6.438		

Site 2

bot	chron	half cycle (m)	whole cycle (m)	O1 (39 kyr) SAR half cycle	whole cycle
	b				
		0.500	0.500	0.013	0.013
	b	0.350		0.009	
		0.275	0.625	0.007	0.016
	b	0.325		0.008	
		0.375	0.700	0.010	0.018
	b	0.350		0.009	
		0.325	0.675	0.008	0.018
	b	0.425		0.011	
		0.250	0.675	0.006	0.018
	b	0.250		0.006	
		0.350	0.600	0.009	0.016
	b	1.175		0.031	
		0.300	1.475	0.008	0.038
	b	0.500		0.013	
		0.250	0.750	0.006	0.019
top	tot	6.000	6.000		

Site 3/CTB GSSP

bot	chron	half cycle (m)	whole cycle (m)	O1 (39 kyr) SAR half cycle	whole cycle
	b				
		0.563	0.563	0.015	0.015
	b	0.303		0.008	
		0.344	0.646	0.009	0.017
	b	0.250		0.006	
		0.183	0.433	0.005	0.011
	b	0.219		0.006	
		0.156	0.375	0.004	0.010
	b	0.656		0.017	
		0.313	0.969	0.008	0.025
	b	0.188		0.005	
		0.156	0.344	0.004	0.009
	b	0.156		0.004	
		0.156	0.313	0.004	0.008
	b	0.156		0.004	
		0.281	0.438	0.007	0.011
	b	0.281		0.007	
		0.151	0.433	0.004	0.011
	b	0.250		0.006	
			0.250		0.006
top	tot	4.761	4.761		

Site 4

bot	chron	half cycle (m)	whole cycle (m)	O1 (39 kyr) SAR half cycle	whole cycle
	b				
		0.125	0.125	0.003	0.003
	b	0.156		0.004	
		0.156	0.313	0.004	0.008
	b	0.188		0.005	
		0.219	0.406	0.006	0.011
	b	0.563		0.015	
		0.313	0.875	0.008	0.023
	b	0.391		0.010	
		0.219	0.609	0.006	0.016
	b	0.219		0.006	
		0.141	0.359	0.004	0.009
	b	0.203		0.005	
		0.234	0.438	0.006	0.011
	b	0.141		0.004	
		0.125	0.266	0.003	0.007
	b	0.344		0.009	
		0.359	0.703	0.009	0.018
	b	0.094		0.002	
			0.094		0.002
top	tot	4.188	4.188		

Site 6

bot	chron	half cycle (m)	whole cycle (m)	O1 (39 kyr) SAR half cycle	whole cycle
	b				
		0.188	0.188	0.006	0.005
	b	0.234		0.005	
		0.250	0.484	0.006	0.013
	b	0.125		0.003	
		0.125	0.250	0.003	0.006
	b	0.109		0.003	
		0.156	0.266	0.004	0.007
	b	0.125		0.003	
		0.125	0.250	0.003	0.006
	b	0.156		0.004	
		0.156	0.313	0.004	0.008
	b	0.141		0.004	
		0.453	0.594	0.012	0.015
	b	0.234		0.006	
		0.516	0.750	0.013	0.019
	b	0.188		0.005	
		0.172	0.359	0.004	0.009
	b	0.156		0.004	
		0.141	0.297	0.004	0.008
top	tot	3.750	3.750		

Site B (Antonio Canyon)

bot	chron	half cycle (m)	whole cycle (m)	O1 (39 kyr) SAR half cycle	whole cycle
	b				
		0.500	0.500	0.013	0.013
	b	0.219		0.006	
		0.250	0.469	0.006	0.012
	b	0.297		0.008	0.000
		0.260	0.557	0.007	0.014
	b	0.406		0.011	
		0.375	0.781	0.010	0.020
	b	0.344		0.009	
		0.469	0.813	0.012	0.021
	b	0.490		0.013	
		0.313	0.803	0.008	0.021
	b	0.344		0.009	
		0.234	0.578	0.006	0.015
	b	0.203		0.005	
		0.500	0.703	0.013	0.018
	b	0.344		0.009	
		0.281	0.625	0.007	0.016
	b	0.438		0.011	
		0.469	0.906	0.012	0.024
	b	0.313		0.008	
		0.516	0.828	0.013	0.022
	b	0.547		0.014	
		0.344	0.891	0.009	0.028
top	tot	8.453	8.453		

VITA

Jacob Grosskopf was born in Gretna, Louisiana, in May of 1984, to Fred and Beth Grosskopf. He first became interested in science at an early age during summer reading programs. He discovered the field of paleontology in fifth grade when he found fossils in the gravel of his driveway. Later, Discovery Channel's annual Shark Week Broadcast spurred more interest in the subject.

Upon graduation from Mandeville High School in 2002, Jacob enrolled at Louisiana Tech with aspirations to become a paleontologist. He graduated in the summer of 2007 with a bachelor's degree in applied biology and a minor in geology.

Jacob was accepted to Louisiana State University Graduate School, and enrolled in the Spring 2008 semester. While a student there, Jacob became involved in the LSU Geology Club and American Association of Petroleum Geologists - Student Chapter. He acquired funding for research from two scholarships and graduate assistantships. Apart from teaching introductory paleontology labs, Jacob assisted Dr. Laurie Anderson in the summers of 2008 and 2009 at the LSU Freshman Summer Field Camp in Colorado Springs, Colorado.

Upon receiving his MS in May of 2010, Jacob took part in a summer-long field paleontology program at Dinosaur National Monument, through the Geologist in the Parks program sponsored by Geological Society of America. Shortly afterwards Jacob was employed as an adjunct instructor at Tarrant County College - Trinity River campus in Fort Worth, TX. There he honed his teaching skills. He decided he wanted to direct his career toward teaching geology, so he enrolled in the Doctoral program at Louisiana State University in the Spring of 2012. He performed field work over two summer field seasons, where he was allowed to set up base camp and stay overnight at the LSU Field Camp. During the three years it took him to

complete the dissertation project Jacob attended several meetings of the Geological Society of America and was awarded several scholarships. These scholarships and his graduate assistantship aided in paying for his research.

Jacob expects to graduate with his PhD from LSU in 2015. Upon his graduation he plans on moving out west to continue on his career path to become a geology instructor.